EVALUATING SOIL FORMATION PROCESSES IN MEDITERRANEAN GRANITIC SOILS

EVALUACIÓN DE LOS PROCESOS DE FORMACIÓN DE SUELO EN TERRENOS GRANÍTICOS DEL MEDITERRÁNEO

ANDREA ROMÁN SÁNCHEZ

Inter-University PhD Program in Biogeochemical Flow Dynamics and Applications
University of Cordoba
Spain

Supervisors
DR. JUAN VICENTE GIRÁLDEZ CERVERA
DR. TOM VANWALLEGHEM

May, 2018

TITULO: *Evaluating soil formation processes in mediterranean granitic soils*

AUTOR: *Andrea Román Sánchez*

Campus de Rabanales
Ctra. Nacional IV, Km. 396 A
14071 Córdoba

https://www.uco.es/ucopress/index.php/es/
ucopress@uco.es

Instituto de Estudios de Postgrado

TÍTULO DE LA TESIS: EVALUATING SOIL FORMATION PROCESSES IN MEDITERRANEAN GRANITIC SOILS

DOCTORANDO/A: Andrea Román Sánchez

INFORME RAZONADO DEL/DE LOS DIRECTOR/ES DE LA TESIS

(se hará mención a la evolución y desarrollo de la tesis, así como a trabajos y publicaciones derivados de la misma).

La doctoranda ha realizado un excelente trabajo, cumpliendo con satisfacción todos los objetivos propuestos y creemos además que ha desarrollado ampliamente una capacidad docente para impartir clases y dirigir futuras tesis doctorales. Esta tesis ha resultado en la actualidad en dos publicaciones SCI (una de primer autor, y una de segundo autor), y numerosas contribuciones a congresos. Además, está tiene dos manuscritos en segunda revisión y está preparando un manuscrito adicional que en breve será enviado a una revista SCI.

Por todo ello, se autoriza la presentación de la tesis doctoral.

Córdoba, 18 de mayo de 2018

Firma del/de los director/es

Fdo.: _____ Fdo.: _____

A thesis submitted in fulfilment
of the requirements for the degree of
Doctor by the University of Cordoba

Andrea Román Sánchez

This thesis has been carried out within *Hidrología e Hidráulica Agrícola* (AGR 127) research group, department of Agronomy at University of Cordoba, by the projects AGL2012-40128-C03-02 and AGL2015-65036-C3-2-R (MINECO/FEDER, UE).

Andrea Román-Sánchez is funded by:

- Contratos Predoctorales Fellowship with reference BES-2013-067009 by the Ministry of Economy, Industry and Competitiveness, Spanish Government (MINECO).

- Research stay granted by Hidrología e Hidráulica Agrícola group, University of Cordoba at Wageningen University, Soil Geography and Landscape group & Netherlands Centre for Luminescence dating, Environmental Sciences. 3 months.

- Research stay with reference EEBB-I-15-09373 granted by MINECO at Wageningen University, Soil Geography and Landscape group & Netherlands Centre for Luminescence dating, Environmental Sciences. 4 months.

- Research stay with reference EEBB-I-16-11812 granted by MINECO at University of Newcastle, School of Engineering, Australia. 3 months.

- Research stay with reference EEBB-I-17-12547 granted by MINECO at University of Minnesota, Department of Soil, Water and Climate, USA. 4 months.

A) STATEMENT OF ORIGINALITY

This thesis contains no material which has been accepted for the award of any other degree or diploma in any university or other tertiary institution and, to the best of my knowledge and belief, contains no material previously published or written by another person, except where due reference has been made in the text.

B) ACKNOWLEDGEMENT OF AUTHORSHIP

I hereby certify that the work embodied in this thesis contains published paper/s/scholarly work of which I am a joint author. I have included a copy of the paper published as part of the thesis and the all published works derived from it, of which I am a joint author in the Appendix.

ANDREA ROMÁN SÁNCHEZ……. (May, 2018)

AGRADECIMIENTOS

Esta tesis es el resultado de un viaje duro pero extremadamente gratificante. Quisiera agradecer a las siguientes personas por su valiosa contribución y apoyo.

A mis directores de tesis, los Drs. D. Juan Vicente Giráldez Cervera y D. Tom Vanwalleghem por vuestro constante apoyo, duro trabajo, tiempo y valiosos consejos científicos y personales de los cuales me he beneficiado enormemente. Gracias por confiar en mí y darme la oportunidad de formar parte de este equipo.

A Dra. Ana Laguna y Dr. Adolfo Peña por vuestro apoyo y contribuciones que han enriquecido todo este trabajo enormemente.

A Dr. Tony Reimann, Dr. Garry Willgoose, Dr. Kyungsoo Yoo and Dr. Jakob Wallinga por el apoyo, agradable bienvenida, inspiradoras ideas y la estimulante forma de trabajar que me han transmitido durante mis estancias en las Universidades de Wageningen (Holanda), Newcastle (Australia) y Minnesota (EEUU), donde durante catorce meses tuve la gran oportunidad de desarrollar una parte importante de esta tesis.

Al Prof. Jesús Ayuso de la Universidad de Córdoba por facilitarnos el acceso al área experimental y su continua ayuda.

A mi familia, mis padres, hermana y tía, también como a Emilio por su incondicional apoyo y cariño. Soy increíblemente afortunada de tenerlos, ellos han estado en los mejores y peores momentos, confortándome en cada uno de ellos, incluso a veces, desde lejos.

A todos los amigos y compañeros con los que he pasado buenos momentos durante estos años, Blanca, Alicia, Gonzalo, Ana, Teresa, Vanesa, Eva, Antonio, Esteban, Nate, Adrian (y seguro que me dejo a muchos más), gracias vuestra ayuda y hacerme más ameno el camino.

Finalmente, quiero dar las gracias a Dios porque sin él nada de esto hubiera sido posible, quien ha guiado mis pasos y ayudado en cada momento. Muchas gracias.

CONTENTS

LIST OF FIGURES

LIST OF TABLES

APPENDICES

APPENDIX A: SUPPLEMENTARY FIGURES AND TABLES

APPENDIX B: PEER-REVIEWED PUBLICATIONS AND CONFERENCE PUBLICATIONS

JOURNAL PUBLICATIONS

(J1) **Román-Sánchez, A**., Vanwalleghem, T., Peña, A., Laguna, A., Giráldez, J.V. (2018). Controls on soil carbon distribution from solar radiation and topography in rocky, semi-arid landscapes. 311, pp. 159-166. Geoderma. DOI: 10.1016/j.geoderma.2016.10.013

(J2) Reimann T., **Román-Sánchez, A**., Vanwalleghem, T., Jakob Wallinga. (2017). Getting a grip on soil reworking – Single-grain feldspar luminescence as a novel tool to quantify soil reworking rates. 42, pp. 1-14. Quaternary geochronology. DOI: 10.1016/j.quageo.2017.07.002

CONFERENCE PUBLICATIONS

(C1) **Román Sánchez A**., Mediterranean landscape dynamics: soil formation processes long term. Wageningen Soil Conference 2015. Book of abstracts. ISBN: 978-946173-168-5

(C2) **Román Sánchez A**., Single-grain OSL and IRSL dating for reconstruction of soil forming processes in a hillslope catena in Sierra Morena, S Spain. Wageningen Soil Conference 2015. Book of abstracts. ISBN: 978-946173-168-5

(C3) **Román Sánchez A**., Vanwalleghem T., Giráldez JV. Evaluating a spatial soil water balance model under Mediterranean climate and interaction with soil formation. Estudios en la Zona No Saturada 2015. Vol. XII: 111-114. I.S.B.N.: 978-84-16133-91-8

(C4) **Román-Sánchez, A.,** Laguna, A.M., Reimann T., Peña, A., Giráldez, J.V., Wallinga, J., Vanwalleghem T. Estimación de tasas de mezcla vertical y lateral del suelo mediante un modelo analítico. Estudios en la Zona No Saturada 2017. Vol. XIII: 125-132. ISBN: 978-84-947468-9-5.

(C5) **Roman-Sanchez, A.**, Laguna, A., Giraldez, J.V., Reimann, T, Peña, Adolfo, Wallinga, J and Vanwalleghem, T. The potential of luminescence techniques in geomorphological processes. Geological Society of America Abstracts with Programs. Vol. 49, No. 6. DOI:10.1130/abs/2017AM-308541

ATTACHED CD:

ABSTRACT

Soil is one of the most important natural systems that support the development of life and is part of fundamental processes that make our planetary ecosystem work. It is well known that the factors that intervene in the formation of the soil are climate, bedrock, relief, biota and time. However, despite the numerous studies related to soil formation, little is known about these processes due to the immense complexity in which they are integrated.

This study identifies and investigates in detail the different soil-forming processes in the study area located in a rocky Mediterranean landscape. Specifically, the processes that have been studied have been biological such as bioturbation, physical such as erosion-deposit and physical weathering. These processes are related to the spatial distribution of carbon stored in the soil, which has also been part of this study.

The spatial distribution of carbon stocks in the soil is highly variable in the study area, as well as bulk density and stoniness. The variable that controls the spatial distribution of the stoniness is the slope, demonstrating the influence of the erosion. The spatial distribution of the carbon content and carbon stocks in the soil depend on vegetation cover and insolation.

Bioturbation has been studied in soil profiles at different depths along a steeply inclined slope using the IRSL (Infrared Stimulated Luminescence) luminescence technique used on sand sized feldspar grains for the first time for this purpose. This technique has made it possible to identify the age of the sample at different depths and an effective soil mixing rate that takes into account only those grains that have ever been exposed to the soil surface. This has allowed, for the first time, to identify the border between the mobile regolith and the saprolite because the grains close to the border have never visited the surface.The soil age at different depths previously calculated has been used to determine the bioturbation, erosion and deposition rates along the slope through a new analytical solution of the advection-diffusion equation.

Physical weathering has been assessed in the horizons of ten soil profiles by comparing rock fragmentation field data with different models. In this way, the patterns governing

rock fragmentation were established in six profiles. The rest of the profiles did not fit any of these models because they are characterized by armouring effect on the surface, i.e. the surface horizon contains larger size of rocks than the lower one due to the removal of fine particles produced by erosion.

The study presented here is a great advance in the knowledge of these soil-forming processes and can be implemented in other studies of the same type. In the future, this study could be compared with the results that would be obtained from erosion rates using other methods (^{10}Be or ^{137}Cs), completed with an estimation of the chemical processes in the study area and, finally, useful for the calibration and validation of both the new soil formation model that will be developed linked to the work developed in this thesis, as explained in chapter six, and other soil formation and landscape evolution models to better understand the connection between pedology and geomorphological processes.

RESUMEN

El suelo es uno de los sistemas naturales más importantes que sustentan el desarrollo de la vida y forma parte de procesos fundamentales que hacen funcionar nuestro ecosistema planetario. Es bien sabido que los factores que intervienen en la formación del suelo son el clima, la roca madre, relieve, biota y el tiempo. Sin embargo, a pesar de los numerosos estudios relacionados con la formación del suelo, poco es conocido sobre estos procesos debido a la inmensa complejidad en la que se integran.

Este estudio identifica y profundiza en el conocimiento de varios procesos formadores del suelo en la zona de estudio situada en un ambiente Mediterráneo. Específicamente, los procesos que se han estudiado han sido biológicos como la bioturbación, físicos como la erosión-depósito y la meteorización física. Estos procesos están relacionados con la distribución espacial de carbono almacenado en el suelo, la cual también ha formado parte de este estudio.

La distribución espacial del carbono almacenado en el suelo ha resultado ser muy variable en la zona de estudio, caracterizada por ser rocosa, al igual que la densidad aparente y la pedregosidad. Las variables que controlan la distribución espacial de la pedregosidad es la pendiente, demostrándose la influencia de la misma en la erosión. La distribución espacial del contenido de carbono y carbono almacenado en el suelo dependen de la cobertura vegetativa y de la insolación.

La bioturbación se ha estudiado en perfiles de suelo a distintas profundidades a lo largo de una ladera con pronunciada pendiente, a través de la técnica de luminiscencia IRSL (Infrared Stimulated Luminescence) usada en granos de feldespato tamaño arena por primera vez para dicho fin. Esta técnica ha permitido identificar la edad de la muestra a diferentes profundidades y una tasa efectiva de mezcla del suelo que tiene en cuenta sólo los granos que alguna vez vieron la luz en la superficie del suelo. Esto ha hecho posible que, por primera vez, se haya identificado el borde entre el regolito móvil y el saprolito debido a que los granos cercanos a esta franja nunca han visitado la superficie.

La edad del suelo a diferentes profundidades anteriormente calculada ha sido usada para determinar las tasas de bioturbación, erosión y depósito a lo largo de la ladera a través de una nueva solución analítica de la ecuación advección-difusión.

La meteorización física ha sido evaluada en los horizontes de diez perfiles de suelo comparando los datos de campo de fragmentación de rocas con diferentes modelos. De esta forma, se establecieron los patrones que rigen la fragmentación de partículas en seis perfiles. El resto de los perfiles no se ajustaron a ninguno de estos modelos por estar caracterizados por el efecto *armouring* en la superficie, es decir, el horizonte superficial contiene un tamaño de rocas mayor que el inferior debido a la eliminación de las partículas finas producida por la erosión.

El estudio presentado aquí es un gran avance para el conocimiento de estos procesos formadores del suelo y puede ser implementado en otros estudios de la misma índole. En el futuro, este estudio podrá ser comparado con los resultados que se obtendrían de tasas de erosión usando otros métodos (^{10}Be or ^{137}Cs), ser completado con una estimación de los procesos químicos en el área de estudio y, por último, podría ayudar a la calibración y validación tanto del nuevo modelo de formación de suelo que se pretende desarrollar vinculado al trabajo desarrollado en esta tesis, tal y como se explica en el capítulo seis, como de otros modelos de formación de suelo y evolución de paisaje para entender mejor la conexión entre la pedología y los procesos geomorfológicos.

CHAPTER 1

INTRODUCTION

Earth's critical zone is defined as "*a heterogeneous, near surface environment in which complex interactions involving rock, soil, water, air and living organisms regulate the natural habitat and determine availability of life sustaining resources.*" (NRC, 2001). It extends from the top elevation of the vegetation down to the bottom of the aquifer. It is the scenario where some of the fluxes of mass and energy between air, soil, water, bedrock and the relevant organisms which allow for the achievement of sustainable life on earth can be negatively affected by changing environmental conditions. The National Research Council (2001) started a program to improve the current knowledge about those processes, and to preserve and enhance them if this were possible. In the latter study, areas of high priority research were identified, among which appeared for the first time the term *Critical Zone* (CZ). Since this term was coined, the interest, and knowledge, of the processes in the CZ and their interrelationship have been growing.

An important problem in the CZ community is to define the bottom of the CZ and to develop ways of predicting this boundary. Riebe et al. (2017) proposed that the lower CZ boundary is the depth of chemical equilibration between Earth materials and meteoric water in the subsurface. However, they were conscious of some problems with this groundwater-based definition, as even such apparently pristine bedrock might have isotopic signatures from meteoric surface water. The CZ is generally subdivided into two zones. Regolith production converts the fractured, but otherwise unweathered bedrock into the saprolite layer, mainly by chemical weathering. The surface area of weatherable minerals that react with the water from the surface increases towards the surface. Soil production processes then convert the saprolite into the soil or mobile regolith layer, which is affected by the inherent processes of erosion and lowering of the surface. The combination of the processes described above carries rock material from depths where the water, contained in rock

fractures, is in equilibrium with the surrounding mineral assemblage, to the surface, with more fractures and where the minerals are more exposed to reactive fluids (figure 1.1).

Thus, the CZ can be understood as a conveyor-belt, with downward movement of reactive fluids and upward transport of solid materials through the subsurface. The upward conveyor is produced by the surface lowering by erosion that brings materials upward to expose them to chemical, physical and biological processes (Riebe et al. 2017).

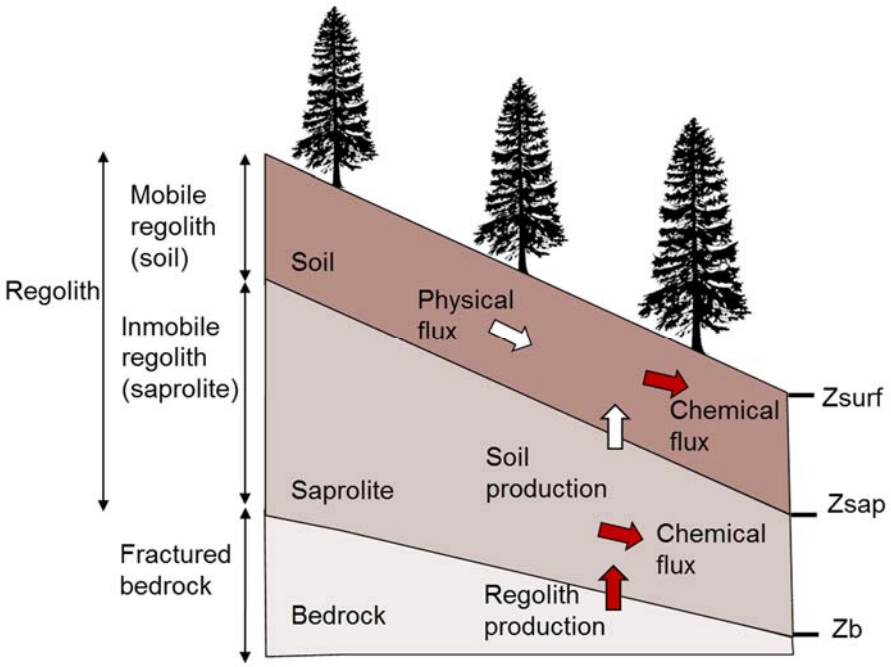

Figure 1.1 Schematic showing mass fluxes on a slope. Conversion of rock to saprolite is the regolith production and conversion of saprolite to soil is the soil production. Regolith is then lost by mineral weathering in the soil and saprolite and by physical erosion of soil. (From Riebe et al. 2017)

The formation and evolution of the deep CZ is supported by several hypotheses, which are summarized by Riebe et al. 2017. These hypotheses are (i) topographic and tectonic forces control open fissures in the subsurface (Slim et al., 2015 and St Clair et al., 2015), (ii) the drainage of chemically equilibrated pore fluids from bedrock initiates chemical weathering at the base of the CZ (Rempe and Dietrich, 2014), (iii) the climate and aspect-driven differences in frost cracking control variations in subsurface rock damage in the CZ (Anderson et al., 2013), (iv) erosion rates and fluid residence times control the thickness and degree of weathering of the CZ.

However, as can be seen, these four hypotheses mainly focus on the process of regolith production that controls the bottom boundary of the CZ. The process of soil production has received relatively less attention. Yet the soil is central in terrestrial ecosystems and its

depth and properties are of critical importance for ecosystem dynamics, food production and overall agricultural sustainability. While it is clear that both regolith and soil production are closely related, soil formation processes have been much less well researched.

This work adopts the concepts and definitions of Egli et al., 2014. 'Soil formation' and 'soil development' are considered synonymous. 'Soil formation' is the net effect while 'soil production' is the gross production. In other words, soil formation is the additions and removals of materials to and from soil profile. On the other hand, soil production consists on the transformation from the parent material to soil (due to physical and chemical weathering and mineral transformation), the lowering of the bedrock (or parent material)-soil boundary (Heimsath et al. 1997, 2009) and the input of the atmospheric deposition (Alewell et al. 2015). Figure 1.2 is a representation formulated by Alewell et al. (2015) for the soil formation, production and denudation as a function of time: In the latter study, another concept was introduced as part of the soil formation, 'soil denudation' as the mass export or import by erosion.

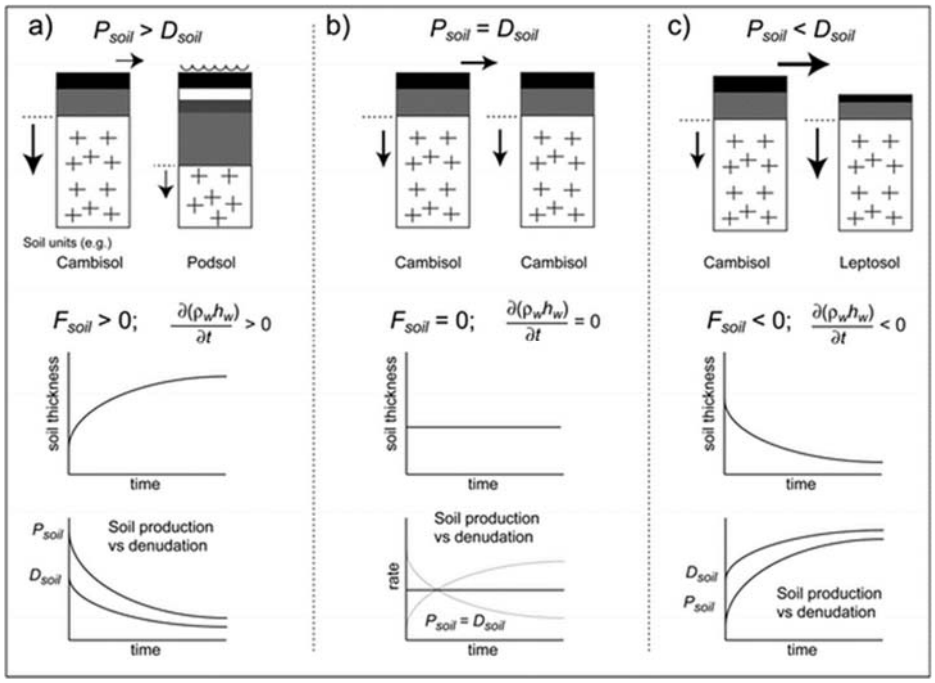

Figure 1.2 Schematic representation of soil formation (F soil), production (P soil) and denudation (D soil) as a function of time for three cases: a) soil production is greater than total denudation over time resulting in soil formation and a positive mass balance; b) denudation and soil production are equal which gives rise to no soil formation; and c) denudation is greater than soil production leading to negative formation rates and a subsequent regressive soil evolution. (From Alewell et al. 2015)

However, it is important to note that this definition by Egli et al. (2014) of soil formation is geomorphologically-oriented and is limited to processes adding or removing soil depth to a profile. However, it is clear that soil formation is much more, and includes processes such as clay eluviation or illuviation, bioturbation, formation of secondary minerals, melanisation, vertization, etc. (Minasny et al., 2015).

At the present time, the models that describe soil formation processes can be broadly grouped in three categories according to Minasny et al. (2015): (i) profile models that include soil formation processes, incorporating a co-evolution of multiple soil properties with depth over timescales, SoilGen (Finke et al., 2008 and Finke, 2012) and Salvador-Blanes et al. (2007), (ii) soil transport models or landscape evolution models (LEMs) which simulate erosion and deposition spatially, and dynamically adjust surface shape and slope for long time scales. While some LEMs are set up for selective fluvial sediment transport, e.g. SIBERIA (Willgoose et al., 1991), very little research has been done on soil feedbacks within these models, (iii) soil-landscape or soilscape models that integrate the soil formation and erosion-deposition processes. One of the first models was mARM3D (Cohen et al., 2010), and its adaptation marm5D (Cohen et al., 2015). One important component of these models was the inclusion of particle breakdown in the conversion of bedrock to soil, which is relevant in this dissertation. Other models are MILESD that integrates landscape evolution and soil formation (Vanwalleghem et al., 2013); LORICA (Temme and Vanwalleghem ,2016) based on LAPSUS and MILESD; and SSSPAM (Welivitiya et al., 2016) that generalized mARM3D.

Depending on the model type specified before, they include different soil or geomorphological processes as shown in figure 1.3. The review by Minasny et al. (2015) identified several problems with the current generation of soil formation models, that, depending on the model type, are:

(i) There is still a lack of identification of representation of important soil formation processes as shown in figure 1.3. Processes such as calcification, and cation leaching are not represented in 3D soilscape models. Even the more detailed profile models are still missing some important soil processes such as salinization or formation of vertic horizons.

(ii) Additionally, the processes included in the models are often not well defined, i.e. in the estimation of bioturbation mixing rates is subject to great uncertainty. The bioturbation, so far, has been estimated using the apparent soil mixing rate, i.e. a mean rate of re-burial of mineral grains, which represents a linear measure and take into account that all mineral grains participate in the soil mixing process (Stockmann et al., 2013; Heimsath

et al., 2002; Wilkinson and Humphreys, 2005). Studies on rates of physical weathering processes are also limited. For example, Wells et al. (2006; 2007) explored mechanisms of salt weathering under laboratory conditions. So, information on other types of physical weathering and under field conditions is still missing.

(iii) The models have only rarely been validated in the field. Currently, more data is becoming available through the CZ Observatories and CZO-like sites to make this possible. The models need calibration and subsequent validation, i.e. the model outcomes must be tested against measured data. Model verification requires checks that all possible situations in the model application domain can be covered in a logical sense by the model (Minasny et al., 2015).

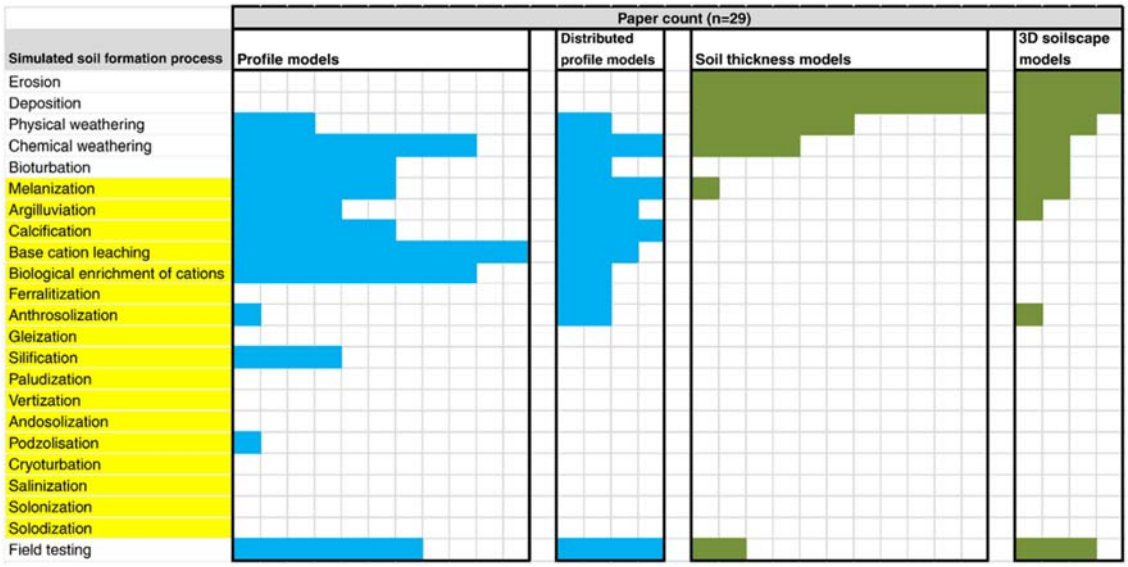

Figure 1.3 Presence (horizontal bars) of 22 soil processes in 29 case studies of profile models and distributed profile models (blue), soil thickness (2D-) models and 3D-Soilscape models (green). (From Minasny et al. 2015)

The main objective of this study is to improve the general knowledge of soil formation processes, specifically focussing on (i) bioturbation and erosion, and (ii) physical weathering.

In the process of solving the main research gaps with respect to our understanding of soil forming and landscape evolution, the specific objectives of this research are: (i) to identify and study the soil formation and landscape evolution processes that intervene in the study area Santa Clotilde Critical Zone Observatory (CZOSC); (ii) to understand the spatial distribution of these processes and the resulting soil properties, as well as the

controlling factors; (iii) to acquire field data on soil properties and process rates to calibrate and validate existing and future models such as mARM3D, MILESD, LORICA.

Figure 1.4 summarizes explicitly the processes and soil properties studied in this research.

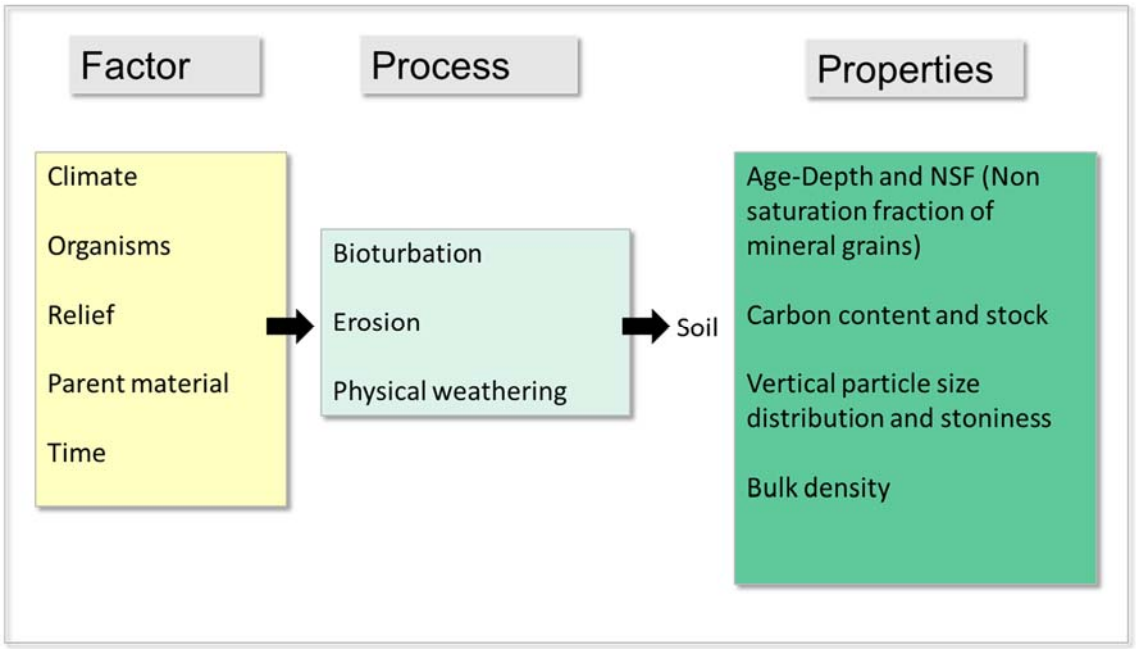

Figure 1.4 Soil formation is conditioned by climate, relief, organisms, parent material and time (Jenny, 1941), which is produced and can be quantified through processes. This chart represents the soil formation processes and resulting soil properties studied in this dissertation.

1. Structure of the thesis

This study is organized in *6 chapters*, which develop in more detail the specific aims.

Chapter 1 is a general introduction to this thesis.

Chapter 2 is dedicated to the factors that control the soil carbon storage in the study area. In this Mediterranean, rocky and mountaneous landscape, located in Sierra Morena, southern Spain, soil carbon distribution is highly heterogeneous. The spatial variability of stoniness, bulk density and soil carbon has been analyzed in order to identify the controls exerted by topographic and vegetation variables. (Román-Sánchez et al. 2018).

In *chapter 3* the effect of bioturbation and erosion on soil formation is analysed by a new method during a research visit at Wageningen University, Netherland. By using feldspar single-grain post-infrared stimulated luminescence techniques (post-IR IRSL), the age-depth distribution in different profiles along a catena was calculated. Statistical parameters calculated from single-grain feldspar age distributions (e.g. number of surface-visiting grains, scatter and shape of the distribution) were used as indicators for vertical

reworking by bioturbation and erosion-deposition related to lateral transport. In this study, we also aimed to elaborate an objective way of identifying the transition between mobile regolith and saprolite using this methodology.

In *chapter 4*, an analytical model was developed to quantify erosion and bioturbation processes along a hillslope based on the age-depth information presented in the previous chapter. This analytical solution of the diffusion-advection equation allows to simultaneously calculate the diffusivity constant and erosion-deposition rates. After this, a global sensitivity analysis was used to assess the relative importance of each model parameter and, finally, to evaluate the uncertainty in the model, the posterior probability density functions of the parameter estimates were calculated.

In *chapter 5* the importance of physical weathering or rock fragmentation is evaluated during a research visit at University of Newcastle, Australia. The surface and subsurface distribution of rock abundance and size in soil profiles along three hillslope catenas are measured. For the first time, the performance of different fragmentation models is compared against this field data, as it is attempted to evaluate if the surface rock grading can be explained from fragmentation of the subsurface material.

In *chapter 6* the overall conclusions and directions for future research are presented.

References

Alewell, C., Egli M., Meusburger, K. (2015). An attempt to estimate tolerable soil erosion rates by matching soil formation with denudation in Alpine grasslands. Journal of Soils and Sediments,15: 1383-1399. DOI: 10.1007/s11368-014-0920-6.

Anderson RS, Anderson SP, Tucker GE. (2013). Rock damage and regolith transport by frost: an example of climate modulation of the geomorphology of the critical zone. Earth Surface Processes and Landforms 38: 299–316.

Cohen, S., Willgoose, G., and Hancock, G. (2010) The mARM3D spatially distributed soil evolution model: Three-dimensional model framework and analysis of hillslope and landform responses, Journal of Geophysical Research-Earth Surface, 115, F04013, DOI:10.1029/2009jf001536, 2010.

Cohen, S., G. Willgoose, T. Svoray, G. Hancock, and S. Sela (2015), The effects of sediment-transport, weathering and aeolian mechanisms on soil evolution, Journal of Geophysical Research, 120: 260–274. DOI: 10.1002/2014JF003186

Egli M, Norton K, Dahms D (2014) Soil formation rates on silicate parent material in high-mountains: different approaches, different results?. Geoderma 213:320–333.

Finke, P.A. and J. Hutson. (2008). Modelling soil genesis in calcareous löss. Geoderma 145:462-479. DOI: 10.1016/j.geoderma.2008.01.017

Finke, P.A. (2012). Modeling the genesis of Luvisols as a function of topographic position in loess parent material. Quaternary International. 265: 3–17.

Heimsath AM, Dietrich WE, Nishiizumi K, Finkel RC (1997) The soil production rate function and landscape equilibrium. Nature 388: 358–361.

Heimsath AM, Fink D, Hancock GR (2009) The 'humped' soil production function: eroding Arnhem Land, Australia. Earth Surface Processes and Landform 34:1674–1684.

Heimsath, A.M., Chappell, J., Spooner, N.A., Questiaux, D.G. 2002. Creeping soil. Geology 30: 111–114. DOI: 10.1130/0091-7613(2002)030<0111:CS>2.0.CO

Jenny H. 1941. Factors of Soil Formation: A System of Quantitative Pedology. McGraw-Hill Book Company: New York.

Minasny, B., Finke P., Stockmann U., Vanwalleghem, T., McBratney, A. (2015). Resolving the integral connection between pedogenesis and landscape evolution. Earth Science Reviews 150: 102-120. DOI:10.1016/j.earscirev.2015.07.004

National Research Council. (2001). Basic research opportunities in Earth Science. National Academies Press.

Rempe DM, Dietrich WE. (2014). A bottom-up control on fresh-bedrock topography under landscapes. Proceedings of the National Academy of Sciences 111: 6576–6581.

Reimann, T., Román-Sánchez, A., Vanwalleghem, T., Wallinga, J. (2017). Getting a grip on soil reworking – Single-grain feldspar luminescence as a novel tool to quantify soil reworking rates. Quaternary Geochronology.42: 1–14. DOI:10.1016/j.quageo.2017.07.002.

Riebe CS, Hahm J, Brantley SL (2017) Controls on deep critical zone architecture: a historical review and four testable hypotheses. Earth Surface Processes and Landform 42:128–156. DOI: 10.1002/esp.4052

Román-Sánchez, A., Vanwalleghem, T., Peña, A., Laguna, A., Giráldez, J.V. (2018). Controls on soil carbon storage from topography and vegetation in a rocky, semi-arid landscapes. Geoderma. 311: 159-166. DOI: 10.1016/j.scitotenv.2018.02.204.

Salvador-Blanes, S., Minasny, B., McBratney, A.B. (2007). Modelling long-term in situ soil profile evolution: application to the genesis of soil profiles containing stone layers. European Journal of Soil Science. 58: 1535–1548.

Slim M, Perron JT, Martel SJ. (2015). Topographic stress and rock fracture: a two-dimensional numerical model for arbitrary topography and preliminary comparison with borehole observations. Earth Surface Processes and Landforms 40: 512–529.

St. Clair J, Moon S, Holbrook WS, Perron JT, Riebe CS, Martel SJ, Carr B, Harman C, Singha K, Richter DD. (2015). Geophysical imaging reveals topographic stress control of bedrock weathering. Science 350: 534–538.

Stockmann, U., Minasny, B., Pietsch, T.J., McBratney, A.B. 2013. Quantifying processes of pedogenesis using optically stimulated luminescence. European Journal of Soil Science 64: 145–160. DOI:10.1111/ejss.12012.

Temme, A.J.A.M., Claessens, L., Veldkamp, A., Schoorl, J.M. (2011). Evaluating choices in multi-process landscape evolution models. Geomorphology. 125: 271–281.

Temme, A. J. A. M., and Vanwalleghem, T. (2016). LORICA– A new model for linking landscape and soil profile evolution: Development and sensitivity analysis, Computers & Geosciences. 90:131–143. DOI:10.1016/j.cageo.2015.08.004.

Vanwalleghem, T., U. Stockmann, B. Minasny, and A. B. McBratney (2013), A quantitative model for integrating landscape evolution and soil formation, Journal of Geophysical Research. Earth Surface. 118: 331–347, DOI:10.1029/2011JF002296.

Welivitiya, W. D. D. P., G. R. Willgoose, G. R. Hancock, and S. Cohen (2016), Exploring the sensitivity on a soil area-slope-grading relationship to changes in process parameters using a pedogenesis model. Earth Surface Dynamics. 4: 607–625. DOI:10.5194/esurf-4-607-2016

Wells, T., Binning, P., Willgoose, G., and Hancock, G. (2006). Laboratory simulation of the salt weathering of schist: I. Weathering of schist blocks in a seasonally wet tropical environment. Earth Surface Processes and Landforms, 31(3): 339–354. DOI: 10.1002/esp.1248.

Wells, T., Willgoose, G., and Binning, P. (2007). Laboratory simulation of the saltweathering of schist: II. Fragmentation of fine schist particles. Earth Surface Processes and Landforms, 32(5): 687– 697. DOI: 10.1002/esp.1450.

Willgoose, G., Bras, R.L., Rodriguez-Iturbe, I. (1991). A coupled channel network growth and hillslope evolution model, 1. Theory. Water Resource Research 27: 1671–1684.

Wilkinson, M.T., Humphreys, G.S. 2005. Exploring pedogenesis via nuclide-based soil production rates and OSL-based bioturbation rates. Soil Research 43: 767–779. DOI:10.1071/SR04158.

CHAPTER 2

CONTROLS ON SOIL CARBON STORAGE FROM TOPOGRAPHY AND VEGETATION IN A ROCKY, SEMI-ARID LANDSCAPES

This work is published in:

Román-Sánchez, A., Vanwalleghem, T., Peña A., Laguna A., Giráldez J.V. 2017. Controls on soil carbon storage from topography and vegetation in a rocky, semi-arid landscapes. Geoderma. 311: 159-166 DOI:10.1016/j.geoderma.2016.10.013

Abstract

Soil properties can exhibit strong spatial variation, even at the small catchment scale. Especially soil carbon pools in semi-arid, mountainous areas are highly uncertain because bulk density and stoniness are very heterogeneous and rarely measured explicitly. The effect of topographic and vegetation variables, on stoniness, bulk density and soil carbon has been explored in a 2.7 km^2 watershed of Sierra Morena in south Spain. Soil core samples were collected from 67 locations at 6 depths up to 0,3 m. Stoniness and bulk density were measured with standard methods, total organic carbon through elemental analysis. These soil properties were then used to calculate carbon stock and related to solar radiation, elevation, slope, curvature, TWI, TPI, SPI and NDVI. Stone content depends on slope, indicating the importance of water erosion on long-term soil development. Spatial distribution of bulk density was found to be highly random. By means of conventional statistical methods, with the help of a random forest method, solar radiation and NDVI proved to be the key variable controlling soil carbon distribution. Total soil organic carbon stocks were 4.38 kg m^{-2} on average, with stocks about double as high on north versus south-facing slopes. These results confirm the importance of the coupled soil moisture and vegetation dynamics on the carbon balance in semi-arid ecosystems. However, validation of the random forest model showed that the different covariates only explained 18% of the variation in the dataset. Apparently, present-day landscape and vegetation properties are not sufficient to fully explain the full variability in the soil carbon stocks in this complex terrain under natural vegetation. This is attributed to a high spatial variability in bulk density and stoniness, key variables controlling carbon stocks. Future improvement of mechanistic soil formation models could help estimating these soil properties better.

1. Introduction

Within a catchment, topography exerts a first-order control over insolation, water and nutrient fluxes, and vegetation patterns, causing differences between south and north facing slopes (Yvanov et al. 2008, Yetemen et al. 2015a), although this is modulated by aridity as, for instance, reported by Mâren et al. (2015). Vegetation and soil moisture dynamics can be expected to control not only landscape shape but also belowground critical zone architecture and properties, especially soil organic carbon (SOC) stocks. Kunkel et al. (2011) showed how NDVI and potential insolation explained 62% of the variation in SOC stocks in the complex semi-arid Dry Creek Observatory, Idaho. However, in complex, rocky terrain, bulk density (BD) and stoniness (ST), soil properties that are often not explicitly measured, exert an important control over SOC stocks. Schrumpf et al. (2011) concluded that SOC stock errors are more dependent on BD and ST than carbon concentration (C) in rocky terrain. Throop et al. (2012) showed that different methods for taking into account the coarse fragment content can lead to differences of up to 26% in carbon stock. As this information is often difficult to measure, many studies assessing SOC stock variability use indirect methods to estimate the latter two variables, using a constant value for BD and ST values from published data (e.g. Kunkel et al.; 2011) or pedotransfer functions (e.g. Bonfatti et al., 2016). While such indirect methods might be a reasonable approximation in simple, agricultural landscapes with low ST, this approach will potentially lead to large errors in complex, stony landscapes. Especially if we are interested in the variables controlling SOC stocks, it is critical to simultaneously assess the spatial variability in C, BD and ST. While C distribution has been linked to vegetation patterns and insolation, as mentioned before, controls over BD and ST are less clear. BD, but especially ST can be expected to vary in response to weathering, transport and biological processes. Geroy et al. (2011) showed how soils in the Dry Creek Observatory, Idaho are typically shallower on south compared to north-facing slopes and the latter can store more water from the wet winter. They also found important differences in SOC, ST, and BD, based on 35 surface samples. Anderson et al. (2013) showed how aspect-related differences in temperature modulate frost cracking and regolith production, leading to distinct weathering rates in the Boulder Creek Critical Zone Observatory, Colorado. Hillslope hydrology and chemical weathering rates are also clearly aspect-related (Anderson et al., 2014). Both global and local studies have shown how transport processes and landscape evolution interact with biological processes (Istanbulluoglu and Bras, 2006; Yetemen et al., 2015a; Yetemen et al., 2015b).

It is clear that there are important interactions between soil properties, water dynamics, plant growth and carbon dynamics. Many of these interactions are not well quantified yet, especially over longer time scales. If we are to develop mechanistic models of soil formation and landscape evolution (Vanwalleghem et al., 2013; Temme and Vanwalleghem, 2016), we need to better understand these interactions and the resulting patterns.

The objectives of this study were: 1) to identify the factors controlling the spatial distribution of carbon concentration, bulk density and stoniness; 2) to use these variables to predict carbon stocks.

2. Materials and methods

2.1. Study area

This study was done in the Santa Clotilde Critical Zone Observatory (SC-CZO), located in Southern Spain (Figure 2.1A). The outline of the study area corresponds with an experimental farm operated by the University of Cordoba and covers 2.7 km^2. The study area is located within the Martin Gonzalo catchment in Sierra of Cardeña and Montoro Natural Park, placed in the Sierra Morena. This mountainous ridge separates the Spanish Central Plateau and the Betic Depression. The bedrock in this area consists of plutonic rock, microadamellita porphyritic and it is part of the Pedroches Batholith. The predominant soils are Regosols, Leptosols and Cambisols under the FAO-Unesco World Reference Base (IUSS Working Group WRB, 2007). The topography is characterized by a gently rolling plateau area and a steeply incised valley towards the south of the study area, with elevations between of 645 and 755 m a.s.l. (Figure 2.1.B). The slopes in this valley area are steep, typically between 20-75%, while in the slopes in the plateau areas are mild, between 0-5%. The climate is True Mediterranean following the Aschmann (1984) criteria, with an average rainfall of 582 mm and a marked wet season during winter. Temperatures vary between 5 and 40ºC. The area is covered by oak-woodland savannah ("dehesa"), which is used for extensive grazing. The stocking densities are very low, i.e. below 0,10 LSU ha^{-1}. The prevailing textural classes in the area are sandy to sandy loam and the observed variation in soil depth is large, generally ranging between 0.5-2.40 m.

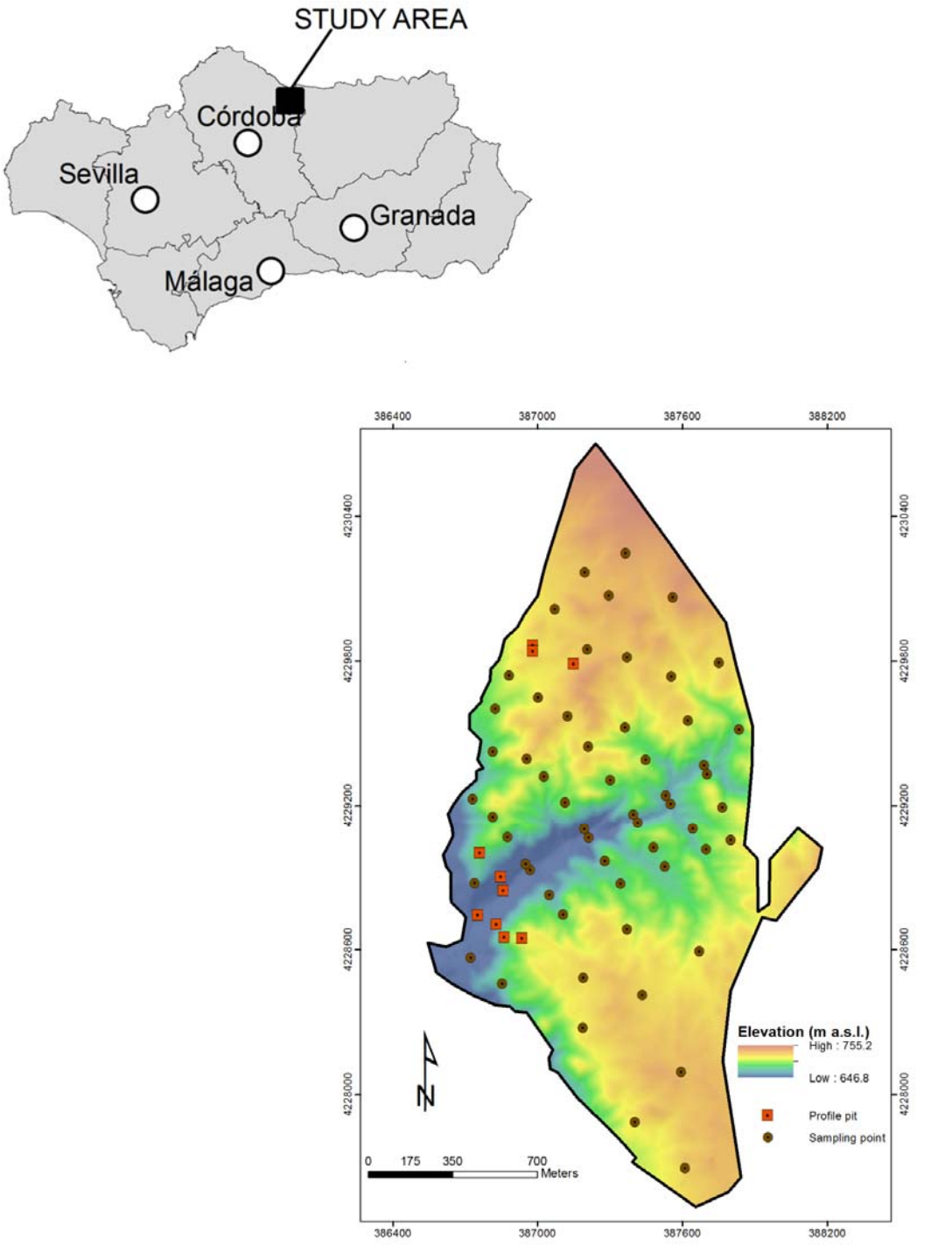

Figure 2.1. Location (left), topography (right) of Santa Clotilde Critical Zone Observatory and sampling points within study area.

2.2. Sampling and measurement

Samples were taken at 67 points, in a combined design-convenience sampling scheme that evenly distributed over the study area in order to cover all different terrains settings using the variables shown in Table 2.1. Sampling points were always located outside the

influence of the tree canopy, in order to avoid local heterogeneities due to the influence of the trees (Simón et al., 2012). At 10 locations, located along 3 transects, profile pits were made and analyzed. At 57 locations, 6 ring samples were taken at 5 cm depth increments down to 30 cm, using a standard Eijkelkamp sample ring kit with a diameter of 5.36 cm. The high stone content prevented sampling below 30 cm and comparison with soil profile data showed that the top 30 cm held on average 70% of the carbon stock. The soil profile pits were sampled along horizon boundaries and subsequently harmonized to 5 cm increments using mass-conserving splines (Malone et al., 2009). A smoothing parameter lambda of 0.1 was used. As sampling up till 30 cm was not always possible in all points due to large rock fragments, a total of 278 samples was obtained.

Samples were stored at -5oC in sealed bags until laboratory analysis. All samples were oven dried at 105ºC and sieved to 2 mm to determine the stone content and bulk density. Next, between 25-30 mg of fine earth was further processed by grounding and a finer sieving to 0.5 mm to measure carbon content. Total organic C and was determined by thermocatalytic oxidation with a temperature of 800ºC using a Elemental CHNS Eurovector EA 3000 (e.g. Giacometti et al. 2013).

Soil organic carbon stocks for each soil layer i, SOC_i, [kg m^{-2}], are calculated with the correction of the stone volume fraction, or material whose representative diameter is greater than 2 mm, S_i [$m^3 m^{-3}$], using the equation of Batjes (1996), as:

$$SOC_i = \frac{1}{1000} C_i h_i \rho_i (1 - S_i) \qquad (1)$$

Where h_i is the layer thickness [m]. ρ_i, the bulk density of the layer [Mg m^{-3}], and C_i its organic carbon fraction [kg C kg^{-1}]. Bulk density, ρ_i, is calculated as the oven-dry mass of solids per sample volume. Stone volume fraction, S_i, is calculated from the measured mass fraction of fragments > 2 mm, and assuming a stone bulk density of 2.65 Mg m^{-3}.

Table 2.1 Variables analyzed as controlling the spatial distribution of bulk density, stoniness and soil carbon.

Abbreviation	Data description	Units	Mean	Median	Stdev	Min	Max
Insolation	Potential incoming solar radiation	10^6Wh m^{-2}	1.36	1.40	0.12	0.91	1.51
Elevation	Elevation above mean sea level	m	713	716	22	653	745
Slope	Local slope gradient	m m^{-1}	0.22	0.18	0.15	0.02	0.66
Curvature	Local hillslope curvature	m	-0.30	-0.16	1.71	-7.12	4.51
TWI	Topographic wetness index (Beven and Kirkby, 1979)	-	5.41	5.00	1.65	3.30	11.95
TPI	Topographic position index (Guisan et al., 1999)	-	-0.36	-0.24	1.60	-4.60	4.09
SPI	Stream power index (Moore et al., 1991)	-	1.79	1.70	1.50	-1.49	7.15
NDVI	Normalized Difference Vegetation Index	-	0.60	0.59	0.07	0.49	0.78

2.3. Predictor variables and data analysis

The predictor variables that were included in the analysis are defined in Table 2.1. Potential insolation depends on aspect, slope gradient, elevation and location and was calculated using the Solar Analyst Tools in ESRI ® Arcmap 10.2 based on the 5 m NGI DEM. Elevation, slope, (S), and curvature were all calculated from the same DEM. Determination of specific contributing area, (A), needed for calculating the Topographic Wetness Index (TWI) and the Stream Power Index (SPI) were calculated in TauDEM using the D-infinity algorithm (Tarboton 1997). Finally, the Topographic Position Index (TPI) is used as a proxy for landscape position, and expressed the elevation of a point with respect to mean elevation. Negative values correspond to lower-lying valley-bottom points, while positive values correspond to ridges and higher elevations.

Vegetative cover reflects ecosystem productivity and controls soil carbon input. The Normalized Difference Vegetation Index (NDVI) is a commonly used, and easily calculated, satellite image-based proxy for vegetative cover. Here, average yearly NDVI was determined from Landsat-5 Thematic Mapper Imagery at 30m resolution (http://earthexplorer.usgs.gov/) for the period 1982-2012. Yearly fluctuations in rainfall are known to affect the spatial distribution of the understory grass vegetation and NDVI (e.g. Lozano-Parra et al., 2014), but studying this variability goes well beyond the scope of this study. It was assumed that the long-term vegetation distribution is adequately represented by the mean NDVI over this thirty year period.

All statistical analysis were performed in R (R Development Core Team, 2008). Firstly, the variation of C, BD, ST and SOC was evaluated against all covariates from Table 2.1. All covariates used in the analysis were checked against cross-correlation, and had a

Variance Inflation Factor below 5. Finally, we calculated cumulative stocks. Missing sampling depths, generally due to field limitations where rock fragments obstructed coring, were reconstructed by fitting a mass-preserving regression fit with depth. A preliminary trial with different regression models was performed, but here we used Random Forests, (RF), which gave the lowest R^2 of the validation data set. The RF is a robust, machine-based learning method which reduces the variance of the regression (e.g. Breiman 2001). RF contains not a single standard regression tree but many regression trees, like a forest. We implemented RF through the package random Forest in R. We performed 100 realizations of the training and validation dataset, using a 75-25 split of the original dataset. Prior to fitting each RF model, the "train" function of the "caret" R package was used to obtain optimal parameter setting. The reported RF results are therefore the average of these different realizations.

3. Results and discussion

3.1. Vertical distribution of bulk density, stoniness, carbon content and carbon stocks

Table 2.2 and Figure 2.2 show how bulk density increases linearly with depth, from a mean value of 1.32 Mg m^{-3} at the surface to 1.58 Mg m^{-3} at the bottom of the sampled profile (25-30 cm). This increase is common to lower C content and higher compaction in depth, but here it is also related to the increase in stoniness. Stoniness increases exponentially with depth, ranging between 14% near to surface to 32% at the bottom. The variation in the dataset is very high, ranging from 0.7% to 84%. Depth is a good predictor of stoniness, explaining 82% of the variation. Phillips et al. (2005) observed a similar pattern in a study of rock fragment distribution in the Ouachita Mountains, Arkansas. They concluded that this increase of ST with depth points to an active production of coarse fragments near the soil-bedrock interface.

Table 2.2 Summary statistics of carbon concentration (C), bulk density (□), stoniness (ST) and soil carbon stocks (SOC).

		Mean	St.Dev.	Min	Max
C (%)	0 - 5 cm	3.1	1.7	1.1	8.1
	5 - 10 cm	1.7	1.2	0.5	6.9
	10 - 15 cm	1.3	0.8	0.4	4.8
	15 - 20 cm	1	0.6	0.2	3.1
	20 - 25 cm	0.8	0.6	0.2	3.4
	25 - 30 cm	0.6	0.4	0.2	2.2
ρ (Mg m^{-3})	0 - 5 cm	1.3	0.2	0.9	2.3
	5 - 10 cm	1.5	0.2	0.9	2.0
	10 - 15 cm	1.5	0.2	1.0	1.9
	15 - 20 cm	1.5	0.2	1.1	2.0
	20 - 25 cm	1.6	0.2	1.2	2.0
	25 - 30 cm	1.6	0.2	1.3	1.9
ST (%)	0 - 5 cm	14.2	8.8	0.8	39.3
	5 - 10 cm	23.6	14.8	4.8	64.8
	10 - 15 cm	26.6	19.6	5.2	83.4
	15 - 20 cm	28.6	18.9	5.7	76.9
	20 - 25 cm	28.8	19.1	4.3	76.9
	25 - 30 cm	31.8	20.0	4.1	82.1
SOC (kg m^{-2})	0 - 5 cm	1.62	0.61	0.69	3.14
	5 - 10 cm	0.96	0.49	0.27	2.59
	10 - 15 cm	0.67	0.35	0.04	1.69
	15 - 20 cm	0.51	0.29	0.06	1.46
	20 - 25 cm	0.41	0.26	0.07	1.44
	25 - 30 cm	0.32	0.20	0.09	1.06
	0 - 30 cm	4.38	1.77	1.70	9.41

C content is relatively low throughout, with mean values decreasing from 3.1% near the surface to 0.6% between 25-30 cm. At the surface, maximum and minimum values are respectively 8.1% and 1.1%. C content follows an exponential decreasing pattern with depth. Depth below the surface is an excellent predictor that explains 96% of the variance, much higher than for BD or ST.

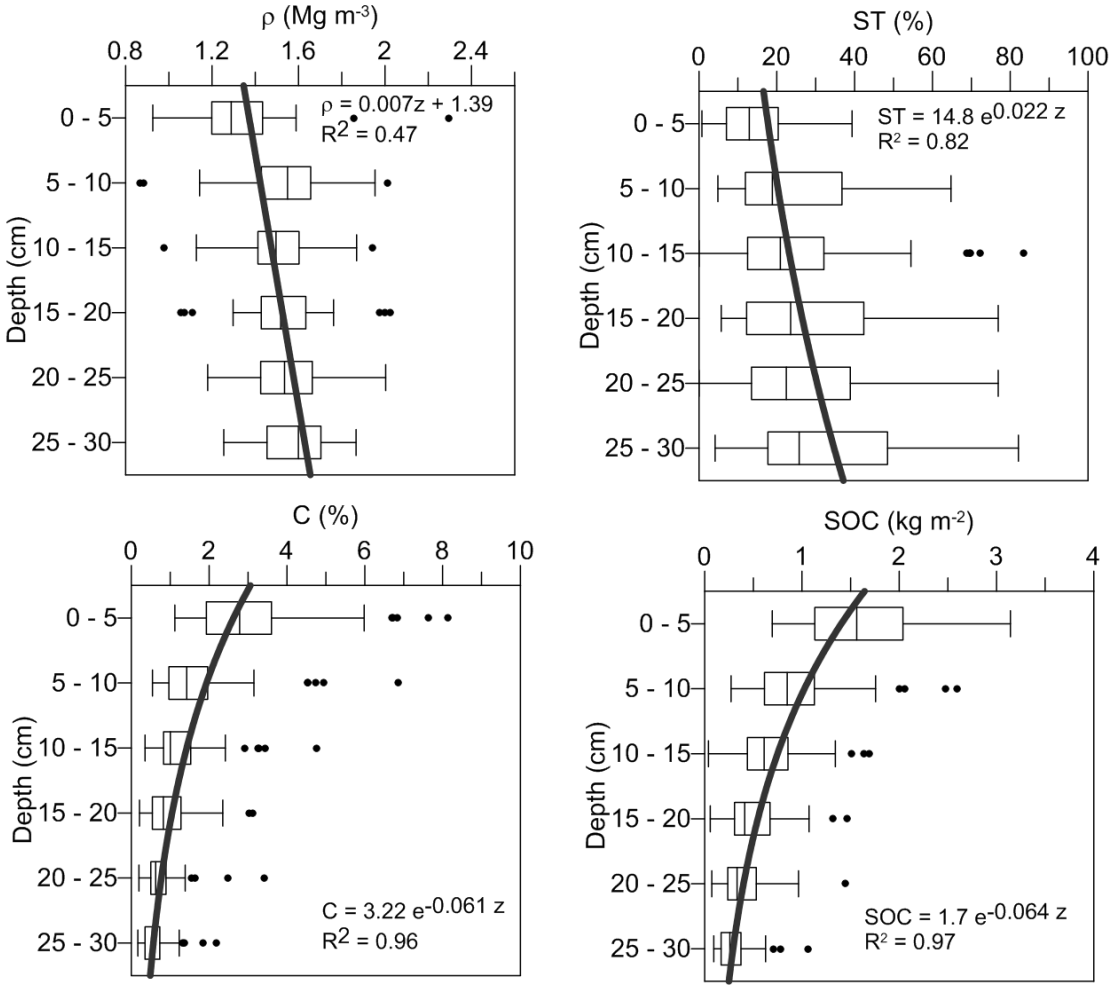

Figure 2.2 Variability of bulk density (ρ), stoniness (ST), carbon concentration (C) and soil carbon stocks (SOC) with depth (z).

Finally, mean calculated SOC stocks range between 1.62 kg m^{-2} for the top 5 cm to 0.32 kg m^{-2} at the bottom of the sampled profiles. Again, SOC stocks decrease exponentially with depth, and the depth-dependence is similar to that of C, explaining 97% of the variation. The total SOC stock for the entire sampled profile sums up to 4.38 kg m^{-2} on average, and varies considerably between 1.70 and 9.41 kg m^{-2}. The values found in this

study are towards the high end of their observed range of 2.28 kg m^{-2} – 4.45 kg m^{-2}. Simón et al. (2012), who studied a similar oak-savanna ecosystem, found SOC stocks in the uppermost 5 cm of 1.05–1.24 kg m^{-2}, about 30% lower than in our study for the same depth, despite yearly precipitation being similar between the two study areas. Howlett et al. (2011) measured SOC stocks up to 1m in oak woodland savannas and reported values of 2.99 kg m^{-2} (Gómez-Rey et al., 2012).

3.2. Relation between bulk density, stoniness, carbon content and carbon stocks

Of the three factors used in calculating carbon stocks, bulk density (BD), stoniness (ST), and carbon content (C), both BD and ST show a significant, negative exponential correlation, Figure 2.3, but the overall R^2 is relatively low, respectively 0.31 and 0.15. This is in contrast with findings from other studies. Based on a study of an agricultural plot in Germany, Bornemann et al., (2011) found that stoniness was linearly related to SOC stock and explained 73% of variability in SOC stock. A possible reason for the difference between the R^2 of our data and that of the latter authors could be that in their study, BD variations were not taken into account. Another reason however is possibly the higher spatial variability of soil properties in natural areas, like our study site. Hoffmann et al. (2014) studied carbon stock variability in the Canadian Rocky Mountains and found a similar low correlation with bulk density and stoniness (explaining respectively 7% and 14% of the observed variability). In agricultural soils, processes such as erosion or tillage tend to drive spatial variability of their properties and to smooth out local heterogeneity. In natural areas however, processes such as tree falls have been widely recognized as key drivers of soil formation (Phillips et al., 2005; Gabet and Mudd, 2010; Roering et al., 2010). Such tree uprooting events mix the soil profile locally and thereby counteract spatial patterns resulting from erosion-deposition or vertical patterns resulting from weathering. By using the soil formation model SoilGen2.0, Finke et al. (2013) were able to show how tree falls caused a much lower correlation with topographic covariates in natural forests of the Belgian loess belt, as opposed to surrounding cropland areas. In our study area, uprooting by tree falls was observed during the field work, but at present no studies have quantified this process.

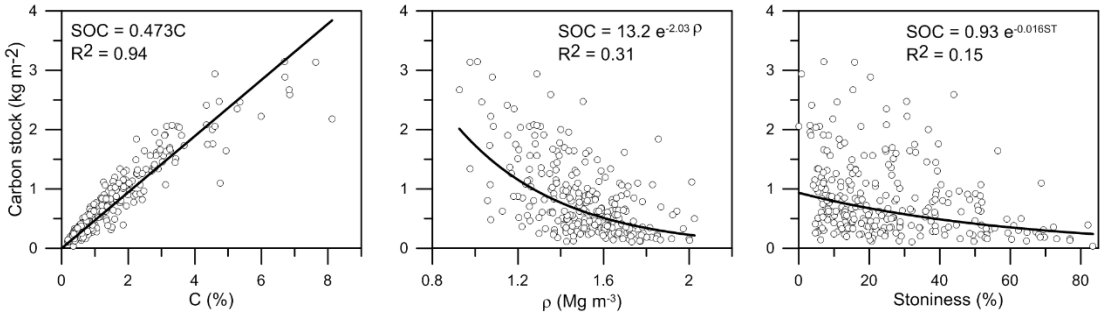

Figure 2.3 Relation between carbon stock and carbon content (%), stone content (%) and bulk density (Mg cm^{-3}).

3.3. Factors controlling the spatial distribution of carbon content, bulk density, stoniness and carbon stocks at different depths

Table 2.3 summarizes the Pearson correlation coefficients of the different environmental covariates with C content, BD, ST and SOC stocks at the 6 six sampled depths.

For C content, insolation is the main variable that is highly significant for all depths. Areas of higher insolation correspond to areas of lower C content. Potential solar radiation will have a direct effect on soil moisture dynamics and plant growth, leading to drier soils and less vegetation on south-facing slopes as opposed to north-facing slopes. This was corroborated by the good correlation of C content with NDVI. This relation was strongest for the deeper soil layers, and decreased towards the surface being non-significant for the 0-5 cm layer. Also slope is significantly correlated to the C content of some layers. Higher C content generally occurs in flatter areas. As current soil erosion rates are low in these natural landscapes, this is more likely to reflect the importance of water dynamics. Infiltration will be higher in flatter areas where all water infiltrates, as opposed to steeper slopes where runoff can occur. There is also an effect, although less clear, of curvature and TPI on C content.

Bulk density is the variable that represents the highest degree of spatial heterogeneity in the study area. As shown in Table 2.3, although some variables can be significantly correlated to BD at different depths, there is no single variable that consistently explains BD variations throughout all sampled depths. In particular for the surface layers, there is no significant relation to be found at all. NDVI is perhaps the most relevant variable here, with lower BD values associated with higher NDVI, implying that higher vegetation covers help to improve soil structure and diminish compaction.

With respect to the spatial distribution of ST, several strong relations become apparent (Table 2.3). First of all however, it is clear that solar radiation does not control the spatial distribution of rock fragments. A significant correlation was only found in the second layer (5 – 10 cm). Also NDVI does not have a strong influence on ST distribution. Only for two depths, a low correlation was found. Also elevation seems to explain ST distribution well, with higher ST content in lower landscape positions. The effect of topography is also reflected in some significant correlation between ST and curvature, TWI and TPI. The strongest and most consistent relation however is between ST and slope, where higher ST content is found on steeper slopes. The good relation with slope in our study clearly indicates that water erosion, a relevant process in these vegetated environments, is strongly related to slope. While absolute erosion rates are low compared to cropland areas, over the long time scales necessary to form soils, erosion will have two effects. Erosion will induce shallower soil profiles, so that the soil-bedrock interface, where an active conversion of bedrock fragments occurs, is closer to the surface. As noted before in section 3.1, this will lead to a higher concentration of rock fragments in the profile. Also Simanton et al. (1994) observed an increase of surface stone cover with slope gradient in the Walnut Gulch Experimental Watershed, Arizona, although they studied larger rock fragments. This semiarid rangeland site is characterized by low vegetation cover and significant runoff and erosion events. These results are in contrast to Phillips et al.'s (2005) findings in the Ouachita Mountains. They analyzed the relation of surface and B-horizon rock fragment concentrations to topographic variables but did not find any statistically significant correlations. They attribute this to the absence of erosion. Our results are however in line with observations from Welivitiya et al. (2016), who predicted with the soil and landscape evolution model SSSPAM a linear dependency of surface slope and contributing area. They found that the interaction between bedrock weathering and armouring due to erosion resulted in a linear increase of median grain size of the coarse fragments with increasing values of area and slope. Their observations remained valid at different depths. In order to confront this hypothesis against our field data, we plotted ST content values against slope and area, Figure 2.4. This figure shows clearly in contrast to the model predictions by Welivitiya et al. (2016), our data only shows a clear dependency of ST on S, but not on A. Higher values of ST will lead to an increase in the median grain size of the soil. This trend is most pronounced for the deeper layers, where ST values are higher. This could suggest that at our site the effect of erosion on ST content is mostly expressed through the lowering of soil profile depth and the exhumation of the actively weathering bedrock interface.

Finally, the spatial distribution of SOC stocks in the SCCZO is statistically well correlated to insolation and NDVI, similar to the spatial patterns in C content. Again, sites with higher potential solar radiation and lower NDVI are characterized by lower SOC stocks. Figure 2.5 illustrates the linear, statistically significant relation for the different depth intervals. Slopes of the regression fit for the top two layers are similar, with the intercept at the origin decreasing with depth due to the damping of the radiation effects.

Table 2.3 Pearson correlation coefficient for the relation between environmental variables and carbon concentration, bulk density, stoniness and soil carbon stocks (SOC). Significant relations are indicated in bold and marked according to their significance level: ***p<0.001; **p<0.05;*p<0.1.

	Carbon concentration per depth interval					
	0 - 5 cm	5 – 10 cm	10 – 15 cm	15 – 20 cm	20 – 25 cm	25 – 30 cm
Insolation	**-0.42*** **	**-0.50*** **	**-0.36*** **	**-0.41*** **	**-0.42*** **	**-0.53*** **
Elevation	-0.01	-0.14	-0.14	-0.07	-0.03	-0.14
Slope	**0.20***	**0.26****	**0.27****	0.20	**0.20***	**0.34*** **
Curvature	**-0.33*** **	**-0.34*** **	-0.12	-0.10	**-0.22***	-0.19
TWI	0.04	-0.06	-0.03	-0.07	0.08	-0.01
TPI	**-0.29****	**-0.29****	-0.20	-0.18	**-0.24****	**-0.25****
SPI	0.06	0.04	0.12	-0.08	-0.03	0.04
NDVI	0.18	**0.27****	**0.26****	**0.30****	**0.36*** **	**0.43*** **

	Bulk density per depth interval					
	0 - 5 cm	5 – 10 cm	10 – 15 cm	15 – 20 cm	20 – 25 cm	25 – 30 cm
Insolation	0.02	0.15	**0.28****	0.12	0.14	**0.26*** **
Elevation	-0.19	0.06	**0.26****	0.16	**0.24*** **	0.07
Slope	-0.14	-0.04	-0.11	0.10	-0.09	0.12
Curvature	0.00	0.19	0.05	0.05	0.11	0.14
TWI	0.08	-0.20	-0.10	**-0.26****	-0.16	**-0.27****
TPI	-0.04	0.03	0.17	0.08	0.16	**0.25*** **
SPI	0.00	-0.19	**-0.21***	-0.13	-0.11	**-0.20***
NDVI	0.17	-0.07	**-0.26****	**-0.22***	**-0.35*** **	**-0.44*** **

	Stoniness per depth interval					
	0 - 5 cm	5 – 10 cm	10 – 15 cm	15 – 20 cm	20 – 25 cm	25 – 30 cm
Insolation	-0.19	**-0.26****	-0.07	-0.17	-0.10	0.00
Elevation	**-0.33*****	**-0.30****	**-0.33*****	**-0.23***	-0.14	**-0.40*****
Slope	**0.37*****	**0.46*****	**0.43*****	**0.41****	**0.37***	**0.58*****
Curvature	-0.17	**-0.25****	-0.05	-0.26**	-0.16	-0.14
TWI	-0.01	-0.13	**-0.23***	-0.19	-0.20	-0.16
TPI	**-0.33*****	**-0.28****	-0.17	-0.08	-0.06	-0.09
SPI	0.19	-0.05	-0.01	0.17	0.02	0.04
NDVI	**0.32****	0.15	**-0.06***	-0.02	-0.07	-0.04

	SOC stock per depth interval					
	0 - 5 cm	5 – 10 cm	10 – 15 cm	15 – 20 cm	20 – 25 cm	25 – 30 cm
Insolation	**-0.30****	**-0.41*****	**-0.32*****	**-0.39*****	**-0.39*****	**-0.47*****
Elevation	0.13	-0.03	0.03	0.01	0.04	-0.02
Slope	0.03	0.10	0.04	0.06	0.03	0.06
Curvature	-0.15	**-0.27****	-0.14	-0.01	-0.15	-0.10
TWI	0.10	0.04	0.13	0.01	**0.21***	0.02
TPI	-0.15	-0.22	-0.11	-0.14	-0.23	-0.18
SPI	0.04	0.04	0.11	-0.15	-0.07	-0.03
NDVI	0.11	**0.25****	**0.26****	**0.34*****	**0.38*****	**0.42*****

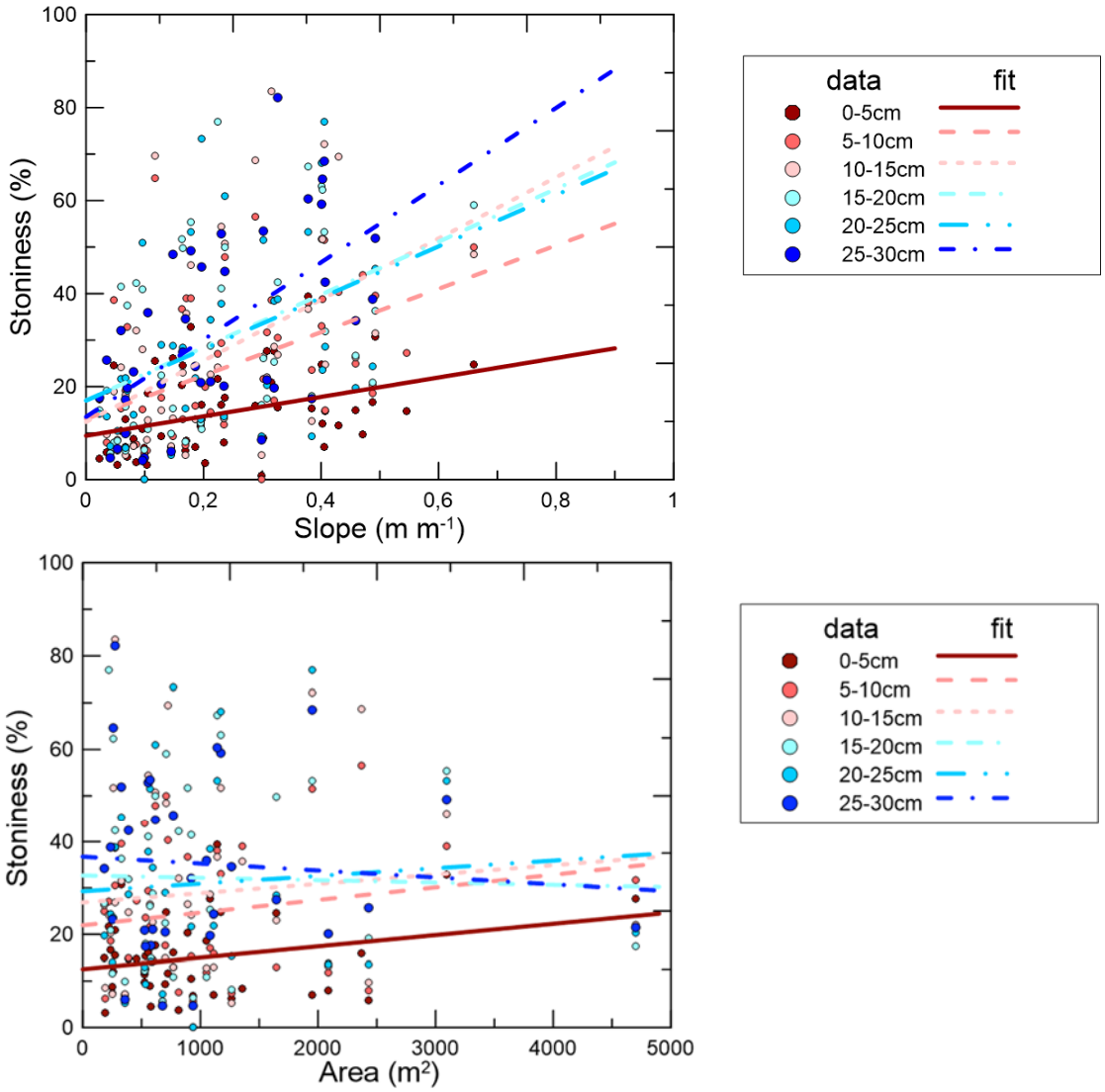

Figure 2.4 Relation between stoniness at different depths with (a) slope and (b) area.

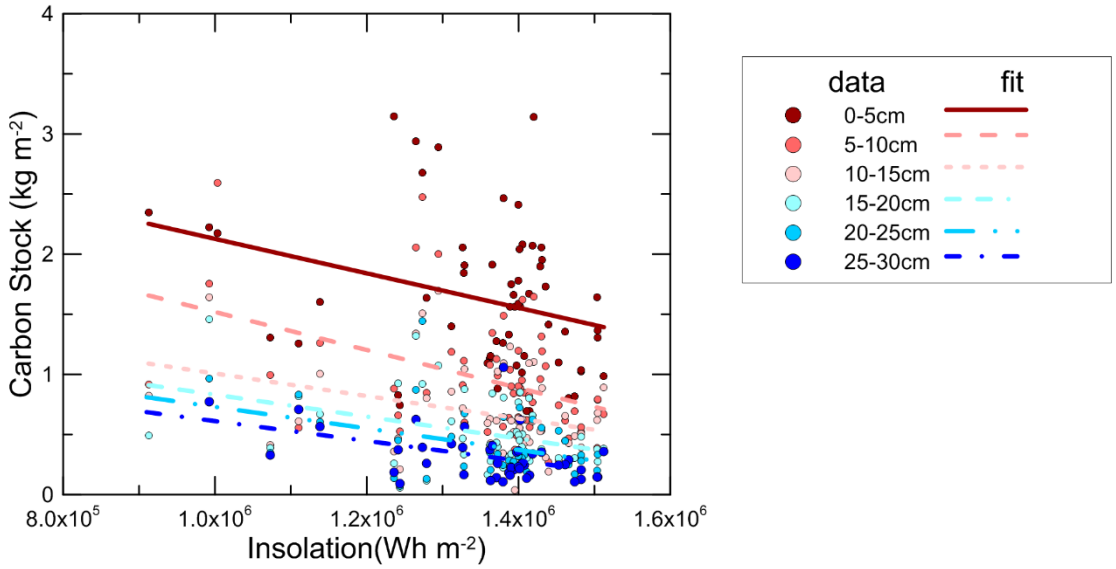

Figure 2.5 Relation between carbon stocks at different depths with insolation.

3.4 Factors controlling the spatial distribution of total carbon stock

Next, a multivariate model was fitted to predict total carbon stocks. Upon analysis of the variograms of the residuals of carbon concentration, bulk density, stoniness and carbon stock, it became clear that in all cases, the data are characterized by either a pure or a very high nugget effect. This implies that there is nothing to gain in terms of modeling the spatial structure of the residuals and therefore no regression kriging was performed.

The RF model could explain 18% of the variation in the validation dataset. This value is relatively modest, although comparable to other recent studies predicting SOC. Bonfatti et al. (2016) found R^2 values for regression kriging between 0.33 and 0.48 for an agricultural area in Brazil, whereas Malone et al. (2009) found R^2 values of 0.20 to 0.27 for validation dataset.

In spite of the low explanatory power of our model, and the absence of spatial autocorrelation, a number of patterns emerge from the analysis of the relative importance of the variables controlling the spatial distribution of SOC stocks in the SCCZO, shown in Figure 2.6. The relative importance is based on the average Gini impurity index (Liaw and Wiener, 2002, Menze et al. 2009) that is used for the calculation of splits during the training phase of the RF model. Figure 2.6 ranks variables from the highest at the top to the lowest at the bottom. Insolation was found to be the most important variable that controls distribution of SOC stocks. This confirms the findings from the simple linear correlation analysis (Table 2.3). After insolation, the following two variables are related to topography, curvature and TPI, and the fourth variable, NDVI, expresses the vegetation effects. Slope, SPI and elevation can be considered less important, as the Gini index of those variables is lower than that of the previous variables although there is not a clear trend break with the previous variables (Figure 2.6). The importance of insolation is clearly reflected in the large differences between the south and north-facing slopes of the valley that dissects the center of the study area. Observations already showed that south-facing slopes, are characterized by SOC stocks of about half those of the opposing north-facing slopes.

The impact of insolation on soil properties is complex. While the direct impact of increased insolation is increased drying on south-oriented slopes and lower vegetation cover, as opposed to north-oriented slopes, Geroy et al. (2011) point out that there is possibly a more important effect on long-term development of soil profiles. They found a marked difference in water retention capacity between north and south slopes, because the first are marked by finer and deeper soils and can therefore store more water. In this study,

we showed that the interaction between C, BD and ST result in complex patterns of SOC stock.

Although SOC stock is controlled mostly by C content, a significant additional term of variability is introduced by explicitly accounting for spatial trends in BD and ST. Trends in BD are markedly random, while ST is significantly correlated to slope gradient. Spatial trends in total SOC stock are characterized by a high small-scale spatial variability.

Several studies have found spatial patterns of soil properties in natural areas to present a higher degree of randomness as compared to areas with a long agricultural history. In agricultural areas, processes such as soil erosion tend to create spatial patterns that vary according to erosion intensity. Dlugoß et al. (2010) for example, were able to predict C content in an agricultural catchment in Germany by erosion modelling. In contrast, in natural areas stochastic processes can be dominant. A first effect inducing spatial variability in this oak savannah ecosystem is the presence of trees. Evaluation of spatial heterogeneity of SOC in oak savannah has clearly shown how tree crowns enhance SOC stocks beneath the canopies (Howlett et al., 2011; Gómez-Rey et al., 2012). In this study, we have attempted to eliminate this effect by sampling outside the influence of the canopy. However, it is not well known how the position of past trees might have a legacy effect on current-day carbon stocks. Another random process that has been discussed before are tree falls. Such events are widely recognized as main soil forming processes in natural areas (Finke et al. 2013). A final, third process that could lead to increased randomness is the effect of extensive grazing. While there is no preestablished grazing pattern in this area, cattle may have preference for certain areas, as shown by Tate et al. (2003). Grazing patterns will influence deposition patterns of cattle feces and might overprint the effects of topographic or vegetation factors. As random events, these three processes will inevitably diminish the extent to which spatial covariates explain soil properties such as SOC stocks.

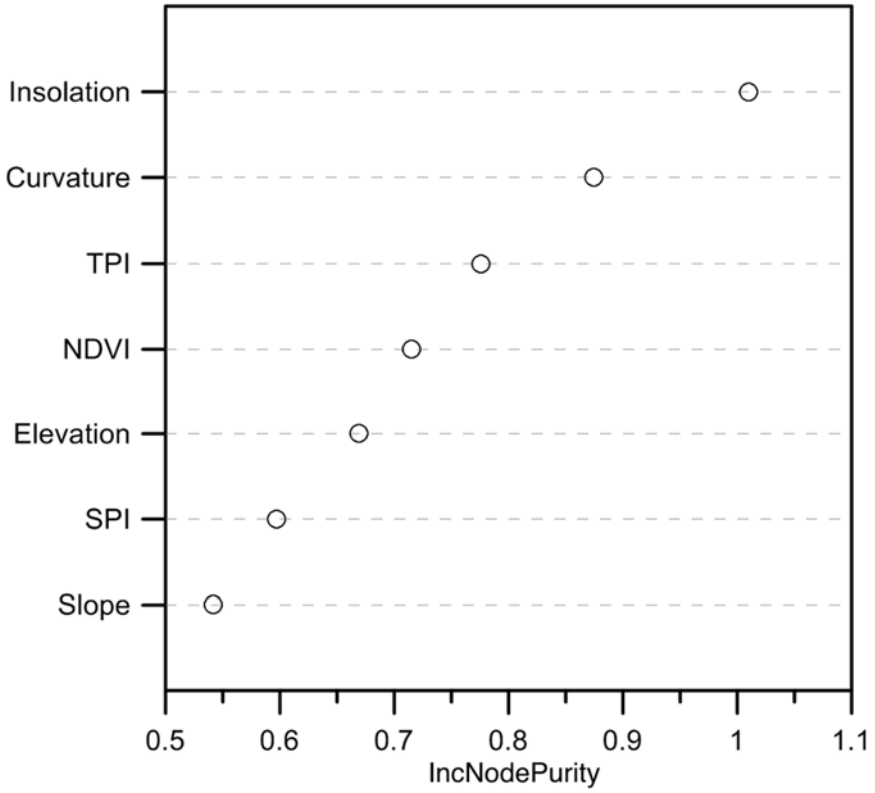

Figure 2.6 Relative importance of the variables used for predicting SOC content with the Random Forest model. The importance is expressed as a function of the mean decrease in the Gini Purity Index, with the most important variables ranked first.

4. Conclusions

The steep topography of the Santa Clotilde Critical Zone Observatory resulted in a high heterogeneity of bulk density, stoniness and soil carbon. Despite this important heterogeneity, clear vertical and spatial patterns emerged, revealing the importance of specific environmental covariates. Slope was found to be a key control over the spatial distribution of stoniness, pointing to the importance of erosion. Solar radiation and vegetation cover, as represented by NDVI, were the main controls over carbon concentration and carbon stocks. A better understanding of the dominant controls over belowground carbon will facilitate soil management in these fragile oak-woodland savannah ecosystems. In the future, a better understanding of the processes involved in soil pedogenesis will boost the understanding of the spatial distribution of soil properties which have proven difficult to predict in digital soil mapping studies, such as stoniness or bulk density, and help to evaluate their variation beyond areas where they were sampled.

Acknowledgements

This work has been funded by projects AGL2012-40128-C03-02 and AGL2015-65036-C3-2-R (MINECO/FEDER, UE). The authors thank Prof Jesús Ayuso for access and support in the Santa Clotilde watershed. We thank F. Cáceres and R. Pédèches for assistance with fieldwork. A. Román-Sánchez is funded by Contratos Predoctorales Fellowship with reference BES-2013-067009.

References

Anderson, R.S., Anderson, S.P., Tucker, G.E., 2013. Rock damage and regolith transport by frost: an example of climate modulation of the geomorphology of the critical zone. Earth Surf. Process. Landf. 38, 299–316. doi:10.1002/esp.3330

Anderson, S.P., Hinckley, E.-L., Kelly, P., Langston, A., 2014. Variation in Critical Zone Processes and Architecture across Slope Aspects. Procedia Earth Planet. Sci., Geochemistry of the Earth's surface GES-10 Paris France, 18-23 August, 2014. 10, 28–33. doi:10.1016/j.proeps.2014.08.006

Aschmann, H., 1984. A restrictive definition of Mediterranean climates. Bull. Société Bot. Fr. Actual. Bot. 131, 21–30.

Batjes, N.H., 1996. Total carbon and nitrogen in the soils of the world. Eur. J. Soil Sci. 47, 151-163.

Beven, K.J., Kirkby, M.J., 1979. A physically based variable contributing area model of basin hydrology. Hydrol. Sci. Bull. 24, 46–69.

Bonfatti, B.R., Hartemink, A.E., Giasson, E., Tornquist, C.G., Adhikari, K., 2016. Digital mapping of soil carbon in a viticultural region of Southern Brazil. Geoderma 261, 204–221. doi:10.1016/j.geoderma.2015.07.016

Bornemann, L., Herbst, M., Welp, G., Vereecken, H., Amelung, W., 2011. Rock Fragments Control Size and Saturation of Organic Carbon Pools in Agricultural Topsoil. Soil Sci. Soc. Am. J. 75, 1898-1907. doi:10.2136/sssaj2010.0454

Breiman, L., 2001. Random forests. Mach. Learn. 45, 5-32.

Darwin, C., 1976. Darwin on Earthworms: The Formation of Vegetable Mould, Through the Action of Worms with Observations on Their Habits. Bookworm Publishing Company, Ontario, California.

Dlugoß, V., Fiener, P., Schneider, K., 2010. Layer-Specific Analysis and Spatial Prediction of Soil Organic Carbon Using Terrain Attributes and Erosion Modeling. Soil Sci. Soc. Am. J. 74, 922. doi:10.2136/sssaj2009.0325

Finke, P.A., Vanwalleghem, T., Opolot, E., Poesen, J., Deckers, J., 2013. Estimating the effect of tree uprooting on variation of soil horizon depth by confronting pedogenetic simulations to measurements in a Belgian loess area. J. Geophys. Res. Earth Surf. 118, 2013JF002829. doi:10.1002/jgrf.20153

Gabet, E.J., Mudd, S.M., 2010. Bedrock erosion by root fracture and tree throw: A coupled biogeomorphic model to explore the humped soil production function and the persistence of hillslope soils. J. Geophys. Res. Earth Surf. 115, F04005. doi:10.1029/2009JF001526

Geroy, I. J., Gribb, M. M., Marshall, H. P., Chandler, D. G., Benner, S. G., McNamara, J. P., 2011. Aspect influences on soil water retention and storage. Hydrol. Process. 25, 3836–3842. doi:10.1002/hyp.8281

Giacometti, C., Demyan, M.S., Cavani, L., Marzadori, C., Ciavatta, C., Kandeler, E., 2013. Chemical and microbiological soil quality indicators and their potential to differentiate fertilization regimes in temperate agroecosystems. Appl. Soil Ecol. 64, 32-48. doi: 10.1016/j.apsoil.2012.10.002

Gómez-Rey, M.X., Garcês, A., Madeira, M., 2012. Soil organic-C accumulation and N availability under improved pastures established in Mediterranean oak woodlands. Soil Use Manag. 28, 497–507. doi:10.1111/j.1475-2743.2012.00428.x

Guisan, A., Weiss, S.B., Weiss, A.D., 1999. GLM versus CCA spatial modeling of plant species distribution. Plant Ecol. 143, 107–122. doi:10.1023/A:1009841519580

Hoffmann, U., Hoffmann, T., Johnson, E.A., Kuhn, N.J., 2014. Assessment of variability and uncertainty of soil organic carbon in a mountainous boreal forest (Canadian Rocky Mountains, Alberta). CATENA 113, 107–121. doi:10.1016/j.catena.2013.09.009

Howlett, D.S., Moreno, G., Mosquera Losada, M.R., Nair, P.K.R., Nair, V.D., 2011. Soil carbon storage as influenced by tree cover in the Dehesa cork oak silvopasture of central-western Spain. J. Environ. Monit. 13, 1897. doi:10.1039/c1em10059a

Istanbulluoglu, E., Bras, R.L., 2006. On the dynamics of soil moisture, vegetation, and erosion: Implications of climate variability and change. Water Resour. Res. vol. 42, W06418. doi:10.1029/2005WR004113.

Ivanov, V.Y., Bras, R.L., Vivoni, E.R., 2008. Vegetation-hydrology dynamics in complex terrain of semiarid areas: 2. Energy-water controls of vegetation spatiotemporal dynamics and topographic niches of favorability. Water Resour. Res. vol. 44, W03430. doi:10.1029/2006WR005595.

Kunkel, M.L., Flores, A.N., Smith, T.J., McNamara, J.P., Benner, S.G., 2011. A simplified approach for estimating soil carbon and nitrogen stocks in semi-arid complex terrain. Geoderma 165, 1–11. doi:10.1016/j.geoderma.2011.06.011

Liaw, A., Wiener, M., 2002. Classification and Regression by randomForest. R News 2, 18–22.

Malone, B.P., McBratney, A.B., Minasny, B., Laslett, G.M., 2009. Mapping continuous depth functions of soil carbon storage and available water capacity. Geoderma 154, 138–152. doi:10.1016/j.geoderma.2009.10.007

Mâren, I.E., Karki, S., Prajapati, C., Yadav, R.K., Shrestha, K.B., 2015. Facing north or south: Does slope aspect impact forest stand characteristics and soil properties in a semiarid trans-Himalayan valley? J. Arid Environ. 121, 112-126, doi: 10.1016/j.jaridenv.2015.06.004

Menze, B.H., Kelm, B.M., Masuch, R., Himmelreich, U., Bachert, P., Petrich, W., Hamprecht, F.A., 2009. A comparison of random forest and its Gini importance with standard chemometric methods for the feature selection and classification of spectral data. BMC Bioinformatics 10:213 doi:10.1186/1471-2105-10-213

Moore, I.D., Grayson, R.B., Ladson, A.R., 1991. Digital terrain modelling: A review of hydrological, geomorphological, and biological applications. Hydrol. Process. 5, 3–30. doi:10.1002/hyp.3360050103

Phillips, J.D., Luckow, K., Marion, D.A., Adams, K.R., 2005. Rock fragment distributions and regolith evolution in the Ouachita Mountains, Arkansas, USA. Earth Surf. Process. Landf. 30, 429–442. doi:10.1002/esp.1152

R Development Core Team, 2008. R: A language and environment for statistical computing. R Foundation for Statistical Computing, Viena, Austria.

Roering, J.J., Marshall, J., Booth, A.M., Mort, M., Jin, Q., 2010. Evidence for biotic controls on topography and soil production. Earth Planet. Sci. Lett. 298, 183–190. doi:10.1016/j.epsl.2010.07.040

Schrumpf, M., Schulze, E.D., Kaiser, K., Schumacher, J., 2011. How accurately can soil organic carbon stocks and stock changes be quantified by soil inventories? Biogeosciences 8, 1193–1212. doi:10.5194/bg-8-1193-2011

Simón, N., Montes, F., Díaz-Pinés, E., Benavides, R., Roig, S., Rubio, A., 2012. Spatial distribution of the soil organic carbon pool in a Holm oak dehesa in Spain. Plant Soil 366, 537–549. doi:10.1007/s11104-012-1443-9

Tarboton, D.G., 1997. A new method for the determination of flow directions and upslope areas in grid digital elevation models. Water Resour. Res. 33, 309-319.

Tate, K.W., Atwill, E.R., McDougald, N.K., George, M.R., 2003. Spatial and temporal patterns of cattle feces deposition on rangeland. J. Range Manage. 56, 432-438.

Temme, A.J.A.M., Vanwalleghem, T., 2016. LORICA – A new model for linking landscape and soil profile evolution: Development and sensitivity analysis. Comput. Geosci., Uncertainty and Sensitivity in Surface Dynamics Modeling 90, Part B, 131–143. doi:10.1016/j.cageo.2015.08.004

Throop, H.L., Archer, S.R., Monger, H.C., Waltman, S., 2012. When bulk density methods matter: Implications for estimating soil organic carbon pools in rocky soils. J. Arid Environ. 77, 66–71. doi:10.1016/j.jaridenv.2011.08.020

Vanwalleghem, T., Stockmann, U., Minasny, B., McBratney, A.B., 2013. A quantitative model for integrating landscape evolution and soil formation. J. Geophys. Res. Earth Surf. 118, 331–347. doi:10.1029/2011JF002296

Welivitiya, W.D.D.P., Willgoose, G.R., Hancock, G.R., Cohen, S., 2016. Exploring the sensitivity on a soil area-slope-grading relationship to changes in process parameters using a pedogenesis model. Earth Surf. Dyn. Discuss. 1–43. doi:10.5194/esurf-2015-54

Yetemen, O., Istanbulluoglu, E., Duvall, A.R., 2015a. Solar radiation as a global driver of hillslope asymmetry: Insights from an ecogeomorphic landscape evolution model. Water Resour. Res. 51, 9843–9861. doi:10.1002/2015WR017103

Yetemen, O., Istanbulluoglu, E., Flores-Cervantes, J.H., Vivoni, E.R., Bras, R.L., 2015b. Ecohydrologic role of solar radiation on landscape evolution. Water Resour. Res. 51, 1127–1157. doi:10.1002/2014WR016169

CHAPTER 3

BIOTURBATION AND EROSION RATES ALONG THE SOIL-HILLSLOPE CONVEYOR BELT, PART 1: INSIGHTS FROM SINGLE-GRAIN FELDSPAR LUMINESCENCE

This work is in review in:

Román-Sánchez, A., Reimann T., Wallinga, J., Vanwalleghem, T. (2017) Bioturbation and erosion rates along the soil-hillslope conveyor belt, part 1: insights from single-grain feldspar luminescence. Earth Surface Processes and Landform. In review

Abstract

The role of bioturbation and long-term soil erosion in soil formation is poorly understood. Feldspar single-grain post-infrared stimulated luminescence measurements (post-IR IRSL) can give us direct information on both processes. Fifteen samples were taken from different depths within four soil profiles along a hillslope catena. The study area is under natural forest and located in the Santa Clotilde Critical Zone Observatory, in the South of Spain. Statistical parameters calculated from single-grain feldspar age distributions (e.g. number of surface-visiting grains, scatter and shape of the distribution) were used as indicators for vertical reworking by bioturbation and erosion-deposition related to lateral transport. Therefore, this work highlights the potential of feldspar single grain techniques to gain quantitative insights into vertical and lateral mixing processes.

Clear differences in age distribution with depth were observed along the catena, with much greater ages at 5-cm depth for hilltop locations (up to 18 ka) compared to hill-base locations (~0.3 ka). The observed variability of the age-depth structure along the hillslope is not in agreement with the assumption of a steady-state landscape. The lower ages and more homogeneous age-depth structure of the hill-base profile, indicates the influence of lateral erosion and deposition processes. We show how our luminescence age-depth profiles along the hillslope catena can be fully explained by the combined effects of bioturbation and erosion-depositional processes. In addition, we propose a new objective measure of the soil depth, based on the occurrence (or absence) of surface visiting grains. This new metric appears to be more reliable than field observations.

1. Introduction

The heart of the critical zone, the heterogeneous, near surface environment in which complex interactions involving rock, soil, water, air, and living organisms regulate the natural habitat and determine the availability of life-sustaining resources (National Research Council, 2001), is the top layer of soil or mobile regolith. Soil formation is driven by the rate at which bedrock or saprolite is converted into soil or mobile regolith. While a lot of progress has been made over the past years quantifying these soil formation rates in different environments (Dixon and Von Blanckenburg, 2012), the process itself remains largely a black box. Firstly, because the key physical and chemical properties of the resulting soil, such as its particle size distribution or horizon distribution, do not yield any quantitative information on soil formation. Secondly, because the exact nature of the

processes involved and their controlling factors are not well characterized. In general, soil production rates are believed to be dependent on local site characteristics such as climate, geology, vegetation and topography. Yet Stockmann et al. (2014) in a review of studies on soil production rates, derived by terrestrial in situ cosmogenic nuclides (TCN) under the assumption of steady state, found no significant effect of geology or climate. No data were available to evaluate vegetation and topography effects. It is therefore clear that more research is needed to elucidate the different processes contributing to soil formation. Physical and especially chemical weathering have received a lot of attention in recent years. Particularly, different studies have reported a clear feedback between chemical weathering and physical erosion rates (Riebe et al., 2003; Larsen et al., 2014). Bioturbation and biological processes in general have received much less attention so far. Nevertheless, bioturbation is increasingly recognized as a key process in soil formation and landscape evolution (Wilkinson and Humphreys, 2005; Wilkinson et al., 2009). It significantly influences the disintegration of the saprolite and bedrock and actively mixes the soil or mobile regolith layer, hereby bringing potentially less weathered material closer to the surface and accelerating physical and chemical weathering.

The soil alteration by biota was probably first studied by Darwin (1881), who reported burial and mounding rates for earthworms. Darwin, following work by Gilbert (1877), was the first to establish the relationship between soil production, i.e. altered saprolite rate, and depth of mobile regolith. He also quantified geomorphological processes such as downslope soil transport. Shaler (1891) studied the effect on soils of bioturbation processes such as tree roots, overturned trees, earthworms, ants and the influence of the inclined hills on the downslope movement of soil and on the spatial distribution of nutrients such as phosphate. Furthermore, he distinguished the bioturbated from the non-bioturbated soil (saprolite) through a stone layer boundary which he explained to have been buried by the mounding action of earthworms and other animals and by the incorporation of organic matter. More recently, Gabet and Mudd (2010) showed how uprooting of trees can bring up parts of the bedrock. They propose a novel paradigm where soil formation is concentrated in patches around hotspots of biological activity as opposed to a homogeneously lowering soil production front. Their model confirms earlier inferences by Phillips and Marion (2004) on the importance of tree throw for soil formation based on field work in the Ouachita Mountains, Arkansas. It is clear that flora and fauna interact with soil, saprolite and bedrock and cause soil reworking through mixing, mounding and burial processes. These processes modify soil depth, produce alteration of soil horizons with a

soil displacement within or between horizons, spatial variation of nutrients concentration, particle size distribution, porosity, carbon content and the formation of a stone layer separating the soil and the saprolite (Wilkinson et al., 2009).

Moreover, biological mixing processes have been shown to actively induce creep, called biogenic creep, produced by uprooting of trees (Lutz, 1960), displacement of soil particles by burrowing voles, gophers and other organisms (Carson and Kirkby, 1972; Lehre, 1987). This process influences not only landscape evolution and relief but also the time particles spend in the weathering zone or the hillslope conveyor belt. These biologically induced sediment fluxes were quantified by Gabet et al. (2003), who established a quantitative model for different processes such as gopher mounding, tree throw and root displacement. By analysing the relation between soil depth and mechanical break-up of bedrock by tree throw, they obtain a humped soil production function, confirming observations by Dietrich et al. (1995) and Wilkinson and Humphreys (2005).

There is a clear need for methods that enable constraining the rate of soil mixing, to improve our understanding of soil formation processes. The pioneering work by Heimsath et al. (2002) has shown that single-grain optically stimulated luminescence (OSL) dating offers an efficient solution for determining burial age of sand-sized mineral grains in soils. Heimsath et al. (2002) also demonstrated that the OSL method allows quantifying long-term pedogenic process such as mixing, erosion or deposition rates, and the approach was adopted in a number of studies in different environments (Stockman et al., 2013; Johnson et al., 2014; Kristensen et al., 2015).

Reimann et al. (2017) recently demonstrated that using feldspar single-grain luminescence techniques has advantages over using quartz when studying the mixing of soils. Feldspar single-grain luminescence measurements are more time-efficient, the technique is more widely applicable and provides more reliable soil reworking rates, especially in settings close to the boundary with the saprolite.

The objective of this paper is to apply this feldspar single-grain luminescence method to reconstruct the vertical and lateral soil mixing processes along a catena. Two important innovations are introduced in this study. The first is that, contrary to previous OSL soil mixing studies, we use luminescence signals from feldspar grains rather than those from quartz. The second innovation is that we make full use of the luminescence signal information provided by feldspar single-grains. We will focus not only on mean ages obtained as a function of depth, but also on the fraction of saturated versus non-saturated grains. The latter is a proxy for surface visiting grains and can be translated into a measure

of the soil reworking intensity (Reimann et al., 2017). This will allow us to correct previously established (apparent) soil reworking estimates and obtain effective soil reworking rates, which take into account only the soil grains that effectively participate in the mixing process. Furthermore, this information will allow us to objectively establish the boundary between the mobile regolith and saprolite-bedrock.

2. Material and Methods

2.1. Study area Cardeña and Montoro Natural Park, Spain

The sampled catena in this study is located in a granitic rock catchment in the Cardeña and Montoro Natural Park (latitude 38,12' N, longitude 4,17' W), Cordoba province, SW Spain (Figure 3.1). The area is influenced by a Mediterranean climate where the annual average rainfall is 600 mm, concentrated during the wet season, and the minimum and maximum temperatures vary between 5 and 40ºC, with medium average values of 15ºC. The climate could be classified as Bsk, (cold semi-arid) within the Köppen-Geiger system (Peel et al., 2007). This climate has allowed the development of Mediterranean sclerophyllous forests in areas with slopes higher than 5%. Generally, flatter areas are covered by oak-woodland savannah ("dehesa"), which is used for extensive grazing with very low stocking densities, i.e. below 0.10 LSU ha^{-1} (livestock units per hectare). The main vegetation is represented by different oak tree species (*Quercus ilex* subsp. *ballota*, *Quercus uber*, *Quercus faginea*). In geological terms, the site is integrated within the Pedroches Batholith, in Sierra Morena, which is a mountain range in southern Spain that separates the Central Plateau from the Baetica Depression. Soil types are Regosols, Cambisols and Phaeozems with Rankers under the FAO-Unesco World Reference Base (IUSS Working Group WRB, 2014).

The sampling area is located along a catena on the north facing hillslope of a steep valley with a permanent creek, covered by natural Mediterranean forest, outside of the area that is extensively grazed (Figure 3.1). The slope range is between 10 and 58% along this catena. The samples were taken from four soil profiles (SC-7, SC-8, SC-9, SC-10), located in distinct landscape positions. The first profile, SC-7, is located at the hill-base, but away from the fluvial influence. Profiles SC-8 and 9 are located near the lower and upper end of the linear hillslope and SC-10 is located on the hilltop.

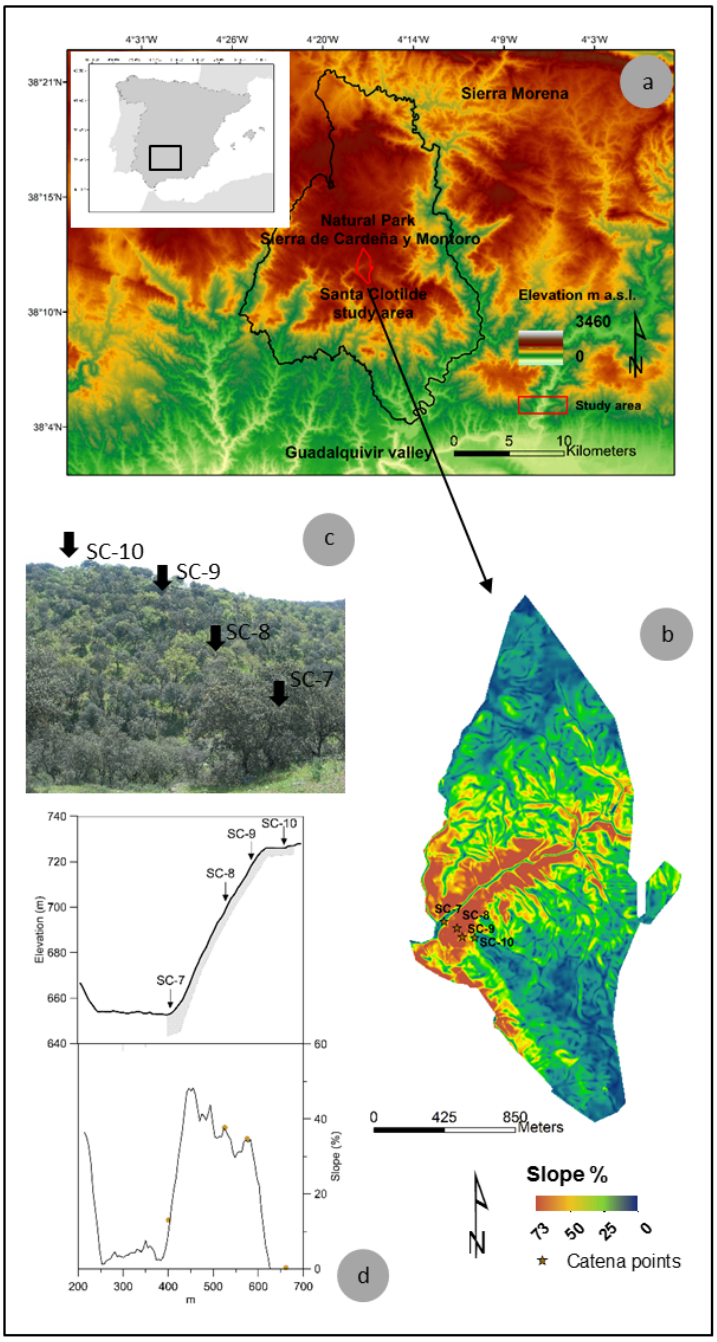

Figure 3.1 (a) Location of the study area within Spain and within the Cardeña and Montoro Natural Park. (b) Slope distribution in the study area with indication of the sampling points. (c) View of the study site with indication of the location of the soil profiles. (d) Transect showing the distribution of the sampled soil profiles along the catena and their slope gradient. The greyed out area indicates the mobile regolith thickness (not indicated for the valley bottom and opposite slope).

2.2. Sample preparation and luminescence analysis

The fifteen samples measured in this study were taken from four soil profiles along the catena described earlier. Within each soil profile different depths were sampled, ranging from near the surface to the bottom of the mobile regolith layer, as identified visually in the field (Table 3.1). The samples were obtained by hammering metal tubes with dimensions of 25x5 centimeters horizontally into the exposure. The material contained in the middle of the tube is not exposed to light during sampling, and is therefore suitable for luminescence analysis (palaeodose estimation). Material from the outer end of the tubes was used to determine the dose rate. Sample preparation was done at the Netherlands Centre for Luminescence (NCL) dating at Wageningen University under subdued orange light.

2.3. Palaeodose and dose rate measurements

For calculating a luminescence age two quantitates need to be determined. The palaeodose, which is the best estimate of the radiation dose a sample received during burial and is obtained by the interpretation of equivalent dose (D_e) distributions. The individual D_e values are obtained by comparing the natural luminescence signal, with the signal induced by laboratory irradiation of the same grain. As the luminescence signal is removed by daylight exposure, the palaeodose provides a best estimate of the ionizing radiation received by the sample since the last daylight exposure. The other quantity is the dose rate, which is the amount of ionizing radiation absorbed by the sample per year.

To determine the palaeodose of our samples we made use of single–grain feldspar luminescence measurements applied to the 212-250 μm sand fraction. We applied the single-grain measurement protocol developed by Reimann et al. (2012), which was recently extended by Reimann et al. (2017) to study soil reworking rates. This measurement protocol measures two feldspar luminescence signals: 1) the infrared stimulated signal at 50 ˚C ($IRSL_{50}$, Hütt et al., 1988) and 2) the post-infrared infrared stimulated signal at 175 ˚C ($pIRIR_{175}$ (Thomsen et al., 2008)). In the previous study both feldspar luminescence signals produced largely consistent results (Reimann et al., 2017), however, in this study we focus solely on the analysis of the $pIRIR_{175}$ signal. The main reason is that the $pIRIR_{175}$ signal is significantly less affected by anomalous fading than the conventional $IRSL_{50}$ signal (Thomsen et al., 2008) and thus less dependable on debatable assumptions regarding state-of-the-art fading correction procedures. More detailed information on the measurement facility, the experimental set-up, corresponding rejection criteria and the performance of

the measurement protocol to determine $pIRIR_{175}$ palaeodoses for these samples is provided in Reimann et al. (2017).

Reimann et al. (2017), showed that the calculation of meaningful soil reworking rates requires the accurate determination of the amount of grains in the soil matrix that likely never (or not since at least the last ~300 ka) reached the surface. These grains have geological luminescence signals close to the saturation threshold, and for identification we made use of the 2 times D_0 saturation threshold (equivalent to ~85% full saturation) suggested by Wintle and Murray (2006). From the proportion of grains above and below this saturation threshold we establish the non-saturation factor (NSF). If all grains have been exposed to light (due to soil reworking or transport), we expect a NSF of 1.0. For a sample from regolith where no grains have been light exposed, we expect all grains to be in saturation, yielding a NSF of 0.0.

The dose rate was assessed from measurements of the activity concentration of isotopes in the ^{232}Th and ^{238}U decay chains as well as ^{40}K employing high-resolution gamma spectrometry. The conversion factors of Guérin et al. (2011) were used to transfer activity concentrations to gamma and beta dose rates. Attenuation due to grain size (Mejdahl, 1979) and moisture and organic matter (Aitken, 1985) were taken into account, and contributions from cosmic radiation (Prescott and Hutton, 1994), and the internal radiation (Smedley et al., 2012) were included (Table 3.S1).

2.4 Luminescence ages and reworking rates

To obtain insight in single-grain De distributions of a sample, the pIRIR175 De measurements were repeated on 300 to 1300 feldspar grains. For the calculation of the palaeodose only grains below the saturation threshold (described above) were taken into account (Reimann et al., 2017). From the distribution of the remaining D_e estimates, i.e. suitable luminescence signal and below saturation, the unweighted average and its 1-sigma standard error was assigned as the sample palaeodose. The sample palaeodose was divided by the corresponding dose rate to obtain the uncorrected apparent luminescence age of the sample. A fading correction (Huntley and Lamothe, 2001) was applied to all uncorrected $pIRIR_{175}$ ages to obtain the corresponding fading corrected apparent luminescence ages. More details regarding age determination are provided in Reimann et al. (2017).

Following previous luminescence studies (Stockmann et al., 2013; Heimsath et al., 2002; Wilkinson and Humphreys, 2005) the apparent soil reworking rate (SR_{app}, mm a^{-1})

can then be calculated by dividing the sample depth by the apparent luminescence age. This rate indicates the displacement rate, or more specifically, the mean rate of re-burial of individual sand grains relative to the soil surface. The disadvantage of this simple measure is that it only provides a linear or average rate of burial. Implications of this approach and suggestions for improvement will be discussed below.

Reimann et al. (2017) pointed out that the apparent soil reworking rate assumes that all grains are participating in the mixing process, as grains with luminescence signals approaching saturation are not taken into account.

The effective soil reworking rate (SR_{eff}) [mm a-1] is a more realistic measure of soil mixing as it takes into account the percentage of grains that participate in the soil mixing process, and thus the intensity of the mixing (Reimann et al., 2017). This mixing intensity is incorporated in the form of the non-saturation factor (NSF) described above, in the calculation of the effective soil reworking rate (Equation 1).

$$SR_{eff} = \left(\frac{sample\ depth\ (mm)}{apparent\ burial\ age\ (years)}\right) xNSF \qquad (3.1)$$

The processes responsible for soil particle exhumation and re-burial can be twofold. If bioturbation is dominant, this measure gives a process rate due to soil mixing. Where lateral surface erosion and deposition is dominant, the process rate will be dominated by sedimentation. Lateral movement due to creep should not have an influence on particle age as particle trajectories are parallel to the slope surface, as shown by Anderson (2015). Whenever these different processes act simultaneously, the resulting age-depth structure becomes more complex. In the next section, a conceptual model is proposed to evaluate the effect of these interacting processes.

A conceptual model for understanding the effect of bioturbation and erosion-deposition on the luminescence age-depth profiles along a hillslope

The effect of different processes causing lateral particle transport along a hillslope is summarized conceptually in Figure 3.2. If one assumes no lateral transport (case a), then the age-depth profile will only form due to bioturbation processes. If bioturbation rates are similar along the hillslope, then similar age-depth profiles will appear from hilltop (left) to hillslope (center) to hill-base (right). Erosion and deposition processes acting on the soil surface (case b), such as sheet or rill erosion, will erode the hillslope profile. As the reference age-depth profile is truncated by a depth Δz, regolith appears at a more shallow

depth and at each depth the age is increased with respect to the reference profile shown in a dotted line. The age observed at each depth z in the eroded hillslope profile corresponds to that of $z+\Delta z$ in the un-eroded reference profile. In this scenario, the soil loss at the hilltop is compensated by soil formation. At the hill-base, freshly deposited sediments will add young grains to the surface, pushing the profile down with respect to the reference profile shown in a dotted line. Note that soil depth is lower on the hillslope and higher at the hill-base, compared to the hilltop reference profile where soil loss is compensated by soil formation. In the third case (c), considering steady-state creep, i.e. creep rates are constant along the hillslope and in equilibrium with soil production and soil erosion rates, the age-depth profiles will be constant along the hillslope, as demonstrated by Anderson et al. (2015). Intuitively, this can be explained by considering a control volume shown at the right in the box (Figure 3.2c). As creep rates are constant, sediment flux in from upslope ($q_{left,in}$) will be equal to sediment flux out of the control volume ($q_{right,\ out}$). Assuming movement parallel to the soil surface, the age of the material flowing in and out is the same as the age of the material in the control volume, and the average age does not change. This hillslope conveyor belt is replenished at the hilltop profile by soil formation and sediment deposits at the hill-base are removed by an incising river. However, in case d, where creep rates increase downslope, the situation changes. Creep flux into the control volume are smaller than the outward flux ($q_{left,in} < q_{right,\ out}$). Although the age of the particles flowing in and out are in principle equal, this causes a deficit in material in the control volume. This deficit lead to particles from overlying layers to "fall down" into the control volume ($q_{down,in}$). As these particles are closer to the surface, their age is younger and they cause an age decrease at the control volume depth with respect to the situation in the reference profile (dotted line). The resulting age-depth profile lies to the left of the reference situation. Note that this also causes a soil surface lowering along the catena. This is expressed as a downslope decrease in soil profile depth along the catena. As this profile is not in steady state, soil formation cannot keep up with the soil loss. The last case (e), then shows the opposite effect, where creep rates decrease along the hillslope. This causes an apparent aging along the hillslope, and the resulting age-depth distribution is displaced to the right with respect to the reference profile (dotted line). As material flux into the control volume exceeds the downslope flux ($q_{left,in} > q_{right,\ out}$), there is an excess of material. Assuming a rigid boundary condition with a bedrock or saprolite layer at the bottom of the mobile regolith, this material is pushed upward ($q_{up,out}$). As this older material is pushed into the overlying, younger layer it leads to older mean particle age.

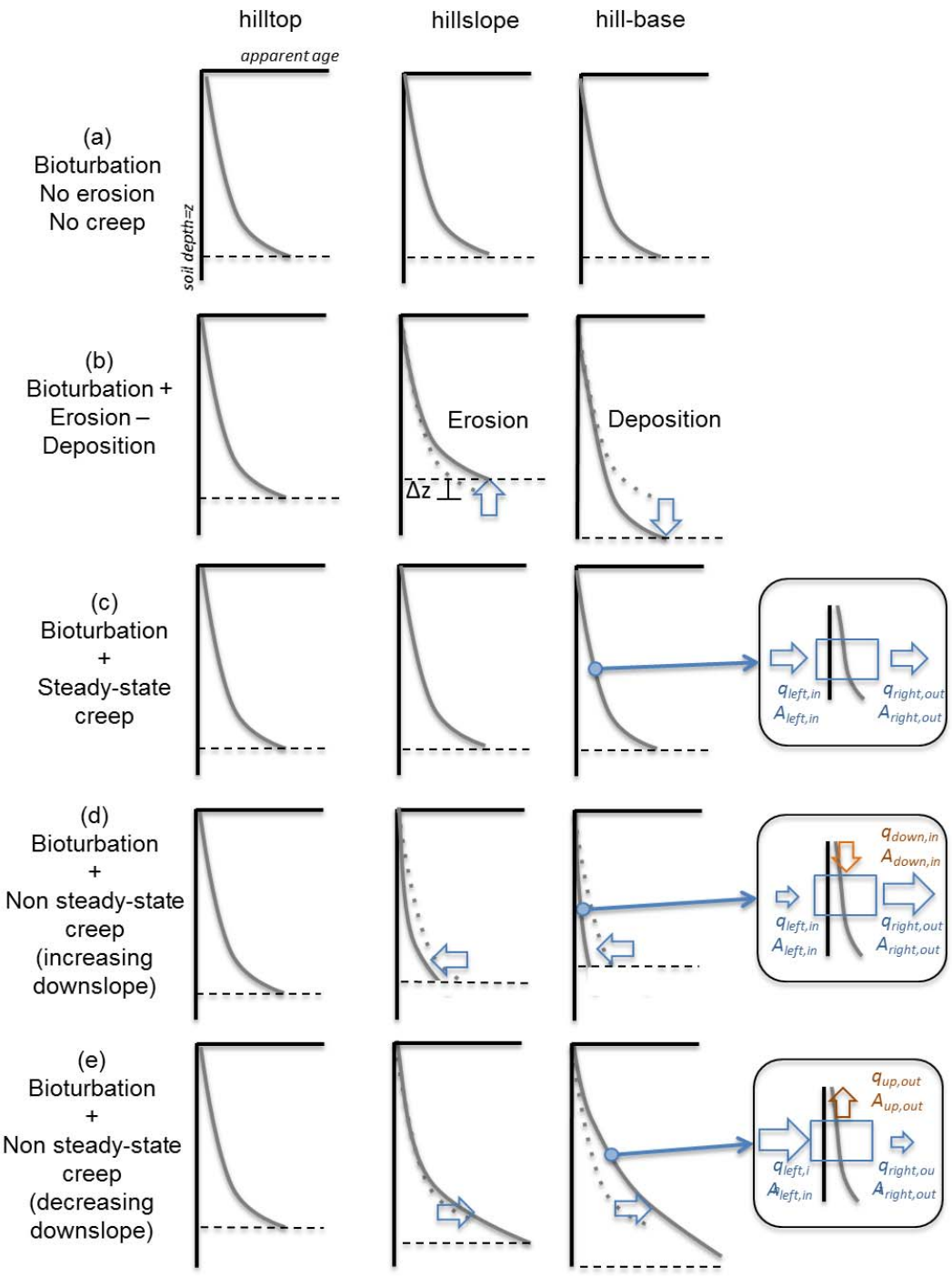

Figure 3.2 Conceptual representation of the effect of bioturbation, erosion-deposition and creep on age-depth profiles along a catena. The horizontal dashed line indicated the mobile regolith boundary. See text for detailed explanation

3. Results

3.1. Soil profile characteristics

The four profiles along the sampled catena, show significant differences, as shown in Figure 3.3. The main soil properties are summarized in table 3.1. Mobile regolith thickness observed in the field is similar for the hilltop and hillslope profiles (SC-10 to 8), varying between 0.47 and 0.57 m. It is almost twice as thick however in the hill-base profile (SC-7), with a depth of 0.97 m. This gives a first indication of accumulation of sediment at the bottom of the hillslope. Soil properties indicate that the hilltop profile SC-10 is the least weathered, as it is characterized by an A horizon directly overlying a less weathered C1 horizon, and it has a higher sand fraction throughout. All other profiles are characterized by a more advanced soil weathering, as they have an A and B horizon overlying the saprolite. Especially the hill-base profile SC-7 and lower hillslope profile SC-8 have noticeably higher clay content, almost double that of the top two profiles, also pointing to a more advanced weathering stage, possibly accentuated by the accumulation of fines due to lateral erosion and deposition processes. In profile SC-10, the C layer is not necessarily undisturbed parent material. It is weathered parent material that has been little affected by pedogenetic processes such as clay illuviation or formation of structure, but the luminescence data clearly shows it has been affected by bioturbation. The hilltop profile is classified as Regosol (IUSS Working Group WRB, 2014), the two hillslope profiles as Cambisols and the hill-base profile as Phaeozem, due to the presence of a dark and organic-rich surface horizon. Bulk density increases linearly with depth in all soil profiles, due to the proximity of the saprolite border and a higher stone fragment content with increasing depth. Organic carbon content decreases exponentially with depth (Román-Sánchez et al., 2018).

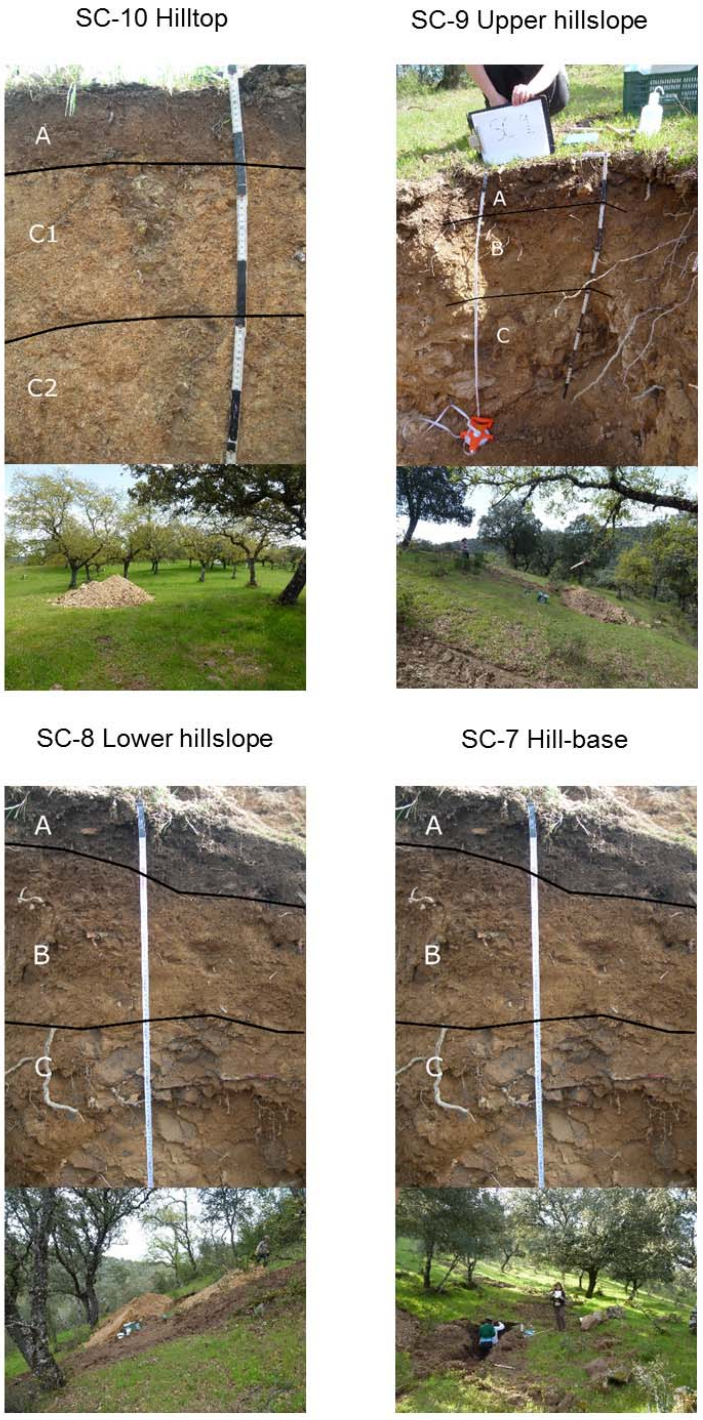

Figure 3.3 Soil profiles sampled along the north-facing hillslope shown in figure 3.1 with indication of soil horizons identified in the field.

Table 3.1 Representative soil properties and topographic variables in the soil profiles along the analysed catena. [a] A negative value indicates that the surface is convex upward in that cell. A positive profile indicates that the surface is concave up in that cell. [b] Taken as fraction 200-2000 µm.

Soil profile and depth, z (cm)	Horizon and soil type	Mobile regolith depth [m]	Slope [%]	Curvature[a] [m]	Bulk density [kg m^{-3}]	Clay [%]	Sand [%][b]	Organic carbon [%]
SC-7	Phaeozems	0.97	13.08	-0.25				
5	Hill-base-A				1355	6.8	74.6	2.91
20	Hill-base-A				1514	9.3	73.4	1.97
37	Hill-base-A				1466	9.3	73.2	0.91
55	Hill-base-B				1753	7.6	79.7	0.63
SC-8	Cambisol	0.47	38.68	0.048				
5	Lower hillslope -A				1468	6.3	75.7	2.76
20	Lower hillslope-B				1382	10.9	57.3	0.59
35	Lower hillslope-B				1422	11.3	49.8	0.57
SC-9	Cambisol	0.57	36.68	-0.03				
5	Upper hillslope -A				1284	5	70.5	3.37
18	Upper hillslope-A				1473	6.8	70.9	1.83
35	Upper hillslope-B				1512	5	78.3	0.37
55	Upper hillslope-B				1628	6.3	73.4	0.27
SC-10	Regosol	0.51	0.58	-0.19				
5	Hilltop-A				1505	6.6	68.5	4.73
20	Hilltop-C1				1771	4.5	83.8	0.59
35	Hilltop-C1				1903	3.3	86.3	0.42
50	Hilltop-C2				1764	3.3	86.4	0.35

3.2. Fraction of saturated feldspar grains

Table 3.2 and Figure 3.4 show the non-saturated factor (NSF) for each sample and reveals important patterns within each profile but also laterally. The data show how NSF is close to one (i.e. most grains visited the surface at some point in the past) for the surface sample at 5 cm depth and rapidly declines with depth. In the profiles where the bottom sample was taken close to the saprolite, SC-9 and SC-10 (respectively at 55 and 50 cm), the corresponding NSF values approach zero (i.e. only a very few or no grains visited the surface at some point in the past). These observations are in line with expectations as they are close to the observed mobile regolith boundary.

Exploring the lateral trends along the catena, a downslope increase in NSF or surface-visiting grain fraction can be seen for the depths of 20 cm and 35 cm (Table 3.2, Figure 3.4). At 20 cm for example, the NSF increases from 0.121 to 0.938 for respectively the hilltop profile SC-10 to the hill-base profile SC-7. At 35 cm, it increases from 0.122 to 0.929. For the surface samples at 5 cm, no clear trend is apparent and all NSF values are above 0.9.

Table 3.2 Summary of the main luminescence results. [a] Non-saturation factor (NSF). The fraction of grains below the saturation threshold with respect to the total number of luminescence grains accepted. [b] Apparent fading corrected feldspar ages. Details provided in section Material and Methods. [c] Apparent soil reworking rate. [d] Effective soil reworking rate. Note that all results are from feldspar single grain $pIRIR_{175}$

Soil profile and depth, z (cm)	NSF[a] [a.u.]	Dose rate [Gy ka^{-1}]	Palaeodose [Gy]	uncorr. Age [ka]	corr. Age[b] [ka]	SR_{app}[c] [mm a^{-1}]	SR_{eff}[d] [mm a^{-1}]
SC-7							
5	0.990	5.71 ± 0.26	2.70 ± 0.56	0.47 ± 0.10	0.54 ± 0.20	0.093 ± 0.034	0.091 ± 0.023
20	0.938	5.59 ± 0.24	20.20 ± 1.21	3.60 ± 0.27	4.00 ± 0.35	0.050 ± 0.004	0.046 ± 0.004
37	0.922	5.87 ± 0.25	29.02 ± 1.14	4.94 ± 0.29	5.51 ± 0.41	0.067 ± 0.005	0.062 ± 0.005
55	0.353	6.58 ± 0.30	54.40 ± 3.08	8.26 ± 0.60	9.24 ± 0.76	0.060 ± 0.005	0.021 ± 0.002
SC-8							
5	0.913	6.16 ± 0.28	9.08 ± 1.95	1.47 ± 0.32	1.60 ± 0.30	0.031 ± 0.006	0.029 ± 0.005
20	0.690	6.16 ± 0.24	109.30 ± 19.8	17.73 ± 3.29	19.9 ± 4.00	0.010 ± 0.002	0.007 ± 0.001
35	0.000	5.85 ± 0.22	-	-	-	-	-
SC-9							
5	0.912	5.50 ± 0.29	6.37 ± 0.62	1.16 ± 0.13	1.3 ± 0.10	0.038 ± 0.003	0.035 ± 0.003
18	0.420	5.08 ± 0.26	21.20 ± 2.8	4.17 ± 0.59	4.7 ± 0.70	0.038 ± 0.006	0.019 ± 0.003
35	0.077	5.64 ± 0.29	25.90 ± 4.2	4.59 ± 0.78	5.1 ± 0.90	0.069 ± 0.012	0.007 ± 0.001
55	0.000	5.12 ± 0.26	-	-	-	-	-
SC-10							
5	0.968	5.19 ± 0.28	8.26 ± 1.40	1.59 ± 0.28	1.76 ± 0.32	0.028 ± 0.005	0.028 ± 0.005
20	0.121	4.10 ± 0.21	76.10 ± 21.8	18.56 ± 5.41	20.9 ± 5.7	0.010 ± 0.003	0.001 ± 0.000
35	0.122	4.21 ± 0.21	108.60 ± 59.4	25.80 ± 14.15	29.1 ± 18.2	0.012 ± 0.008	0.001 ± 0.001
50	0.062	4.54 ± 0.17	203.40 ± 40.4	44.80 ± 9.05	50.7 ± 10.90	0.010 ± 0.002	0.0006 ± 0.000

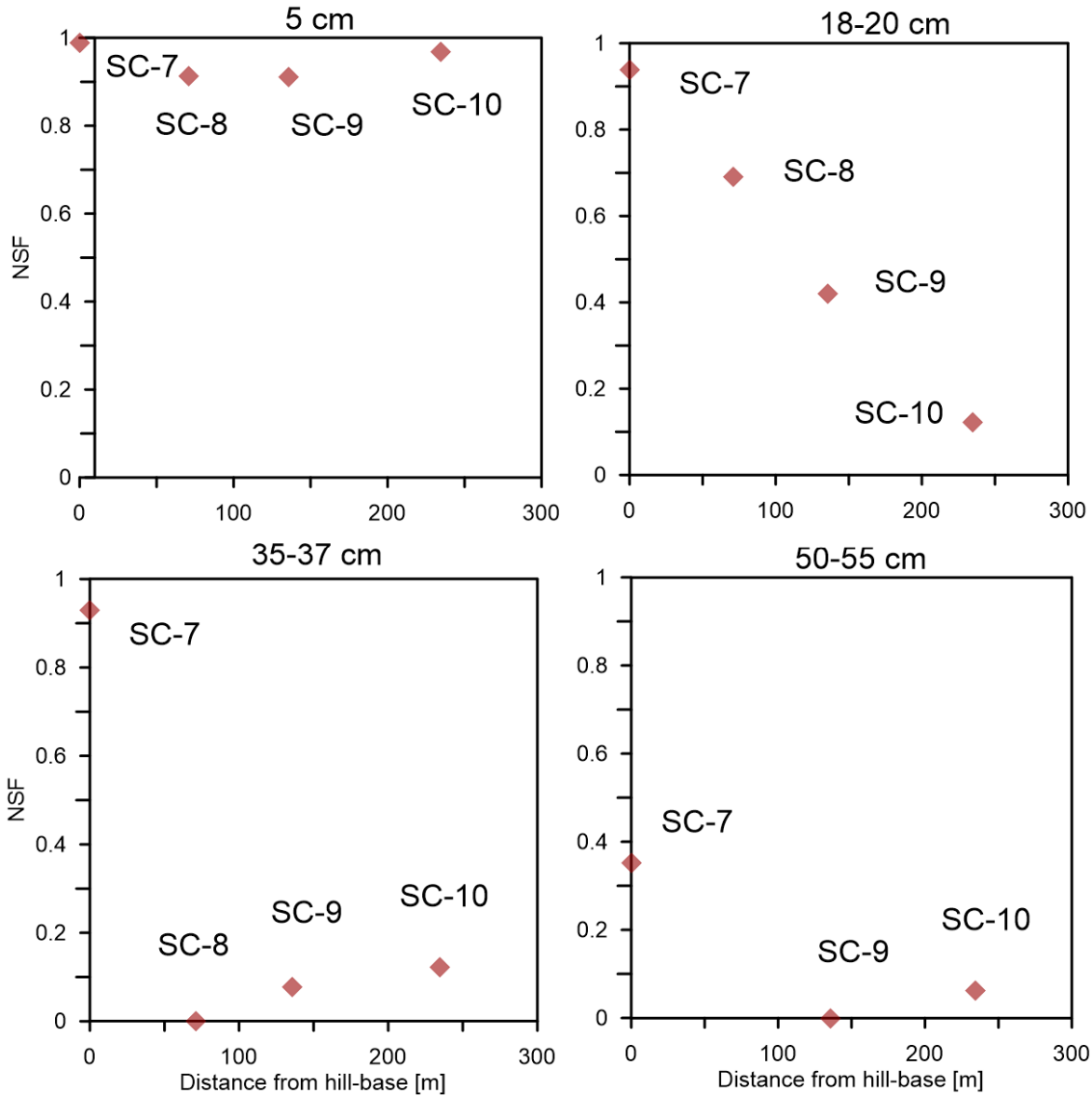

Figure 3.4 Non-saturated factor (NSF) as a function of distance from the hilltop for different depths. The non-saturation factor indicates the ubiquity of grains that have surfaced after being weathered from bedrock.

3.3. Palaeodoses and luminescence ages

The feldspar palaeodoses pIRIR175 signals of each individual soil profile increase with depth (Figure 3.S1 and Table 3.2). For all soil profiles palaeodose increases with depth. At 5 cm depth the vast majority of individual feldspar grains yield an equivalent dose near zero, and the palaeodose is relatively low (< 10 Gy). The analysis of the set of the soil profiles along the catena again reveals a lateral effect with a downslope decrease of the palaeodose, similar to the previously observed increase in NSF in the downslope

direction. The standard error estimated of the palaeodose is higher in the profiles located in the top of the hillslope, due to a higher scatter in the corresponding D_e distribution.

Table 3.2 also shows the resulting fading corrected apparent luminescence ages. Figure 3.5 represents the variation of those ages with depth for the four profiles (SC-7, SC-8, SC-9, SC-10). The boundary between the mobile regolith and the underlying weathered saprolite, as observed in the field, is shown by a dashed line. According to our luminescence results, this boundary is within a transition zone represented with the shaded area (Fig.5 and 6). The boundary must be somewhere inside this transition zone, below the last sample with NSF>0 and above the following sample with NSF=0. For SC-9 the boundary would be somewhere between 35 and 55 cm and in SC-8 between 20 and 35 cm.

If no luminescence age could be determined for the deepest sample, this means that no grains visited the surface and NSF is 0. The sample was therefore taken from below the mobile regolith boundary. Consequently, in the hillslope profiles SC-8 and SC-9, the luminescence-derived mobile regolith boundary was corrected upwards and placed within the transition zone.

Within each individual soil profile, apparent age increases with depth. At 5 cm depth, all profiles exhibit approximately the same recent age, between 0.54 ± 0.2 and 1.76 ± 0.32 ka for profile SC-10 and SC-7 respectively, reflecting recent light exposure of the vast majority of feldspar grains.

The comparison between the four soil profiles along the hillslope shows that the oldest soil profile is the hilltop SC-10 at 50 cm in depth with 50.7 ± 10.9 ka. The age of the soil profiles is decreasing downslope and the hill-base profile SC-7 is the youngest. In this profile, even at 55 cm the measured age is only 9.24 ± 0.76 ka.

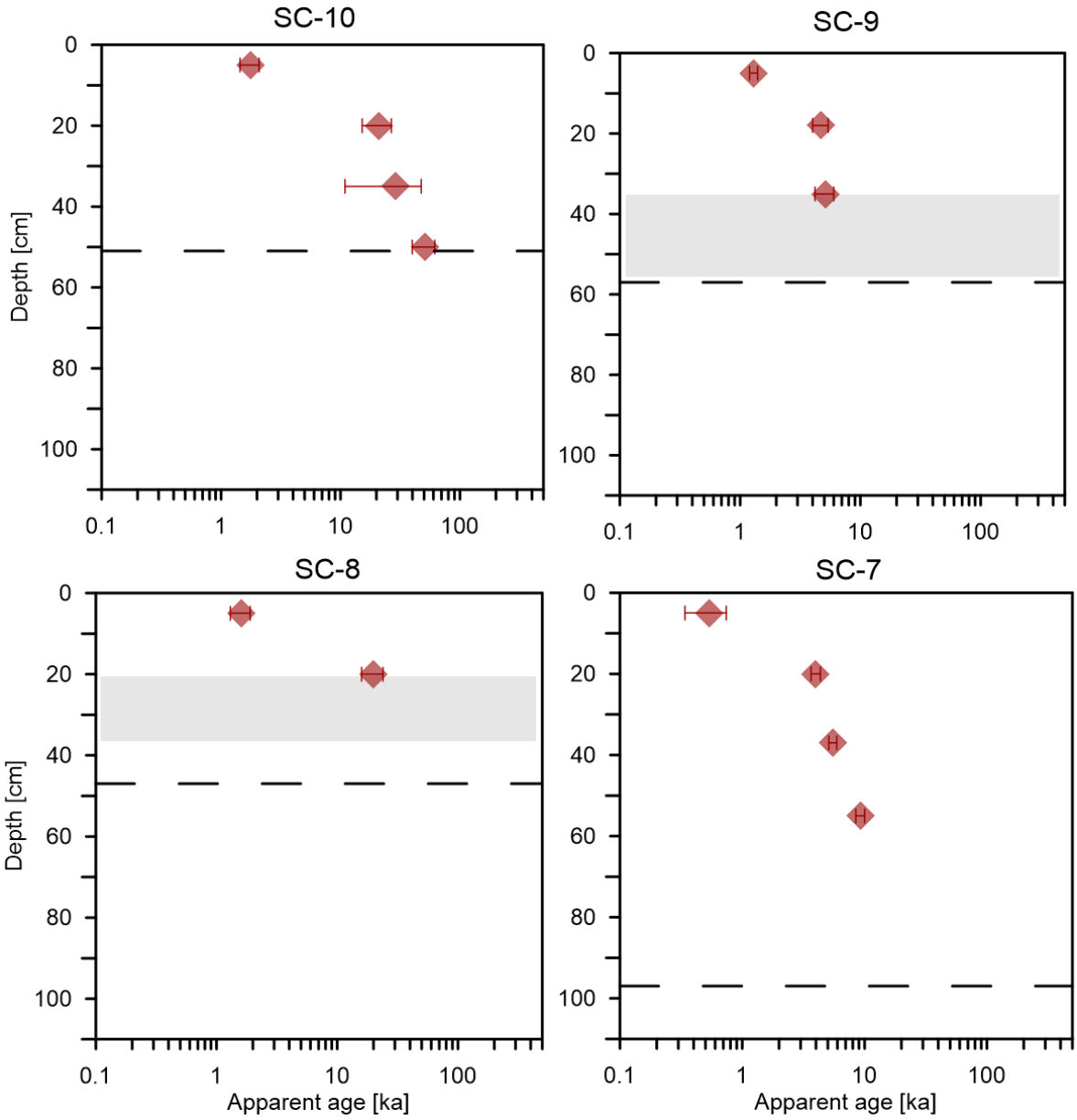

Figure 3.5 Apparent luminescence ages for the four soil profiles (SC-7, SC-8, SC-9, SC-10) obtained with $pIRIR_{175}$. The dashed line indicates the border between mobile regolith and saprolite as identified in the field. The shaded area in profiles SC-8 (lower hillslope) and SC-9 (upper hillslope) shows the transition zone between mobile regolith and saprolite derived from luminescence results. In profiles SC-10 (hilltop) and SC-7 (hill-base) the depth of the mobile regolith observed in the field coincides with the luminescence results. The luminescence results indicate that in the field observations the mobile regolith border has been overestimated in profiles SC-8 and 9.

3.4. Apparent and effective soil reworking rate

Figure 3.6 shows the variation with depth of the apparent soil reworking rates (SR_{app}) [mm a^{-1}] and the effective soil reworking rate SR_{eff} [mm a^{-1}] of the four profiles along the hillslope. SR_{app} were obtained by dividing the sample depth by the apparent burial age, similar to the approach of Heimsath et al. (2002), Wilkinson and Humphreys (2005) and Stockman et al. (2013). SR_{eff} is calculated applying NSF (non-saturation fraction of grains or surface-visiting grains) to apparent soil reworking rate (see equation 1), as proposed by Reimann et al. (2017). Table 3.2 also lists the SR_{app} and the SR_{eff} of our profiles.

Exploring the vertical trends within individual soil profiles, it becomes apparent that in all profiles, the variation of SR_{app} with depth is small. This would suggest similar reworking rates with depth. In contrast to SR_{app}, the recently proposed SR_{eff} declines exponentially with depth in all profiles, translating into a linear decline on the log-axis. SR_{eff} is up to ten times lower compared to SR_{app}, with the most pronounced differences near the saprolite boundary where the NSF is low, indicating that only a small fraction of the grains participates in the mixing process. The decline of SR_{eff} with depth is fastest in the two hillslope profiles SC-8 and SC-9, whereas in the hill-base profile SC-7 and hilltop profile SC-10 it is much less accentuated. Only one sample, at 20 cm in SC-10 seems to deviate from this trend. This difference suggests that the hilltop and hill-base profiles are better mixed compared to the ones on the hillslope. Because of their geomorphologic position, the reasons underlying this better mixing are entirely different however. For the hilltop profile SC-10 it is purely due to bioturbation, while for the hill-base profile deposition processes are dominant, as will be discussed in detail later.

Lateral trends in reworking are shown in Figure 3.7. The hill-base profile SC-7 at 5 cm indicates the highest SR_{eff} value of 0.09 ± 0.023 mma^{-1}, decreasing upward on the hillslope and showing the lowest SR_{eff} value on the hilltop profile SC-10 with 0.028 ± 0.005 mma^{-1}. At 55 cm the hill-base profile SC-7 shows the highest SR_{eff} value of 0.02 ± 0.002- mm a^{-1}, the lowest SR_{eff} on the hilltop profile SC-10 with 0.001 ± 0 mm a^{-1} and in the upper and lower hillslope profiles there is not soil mixing.

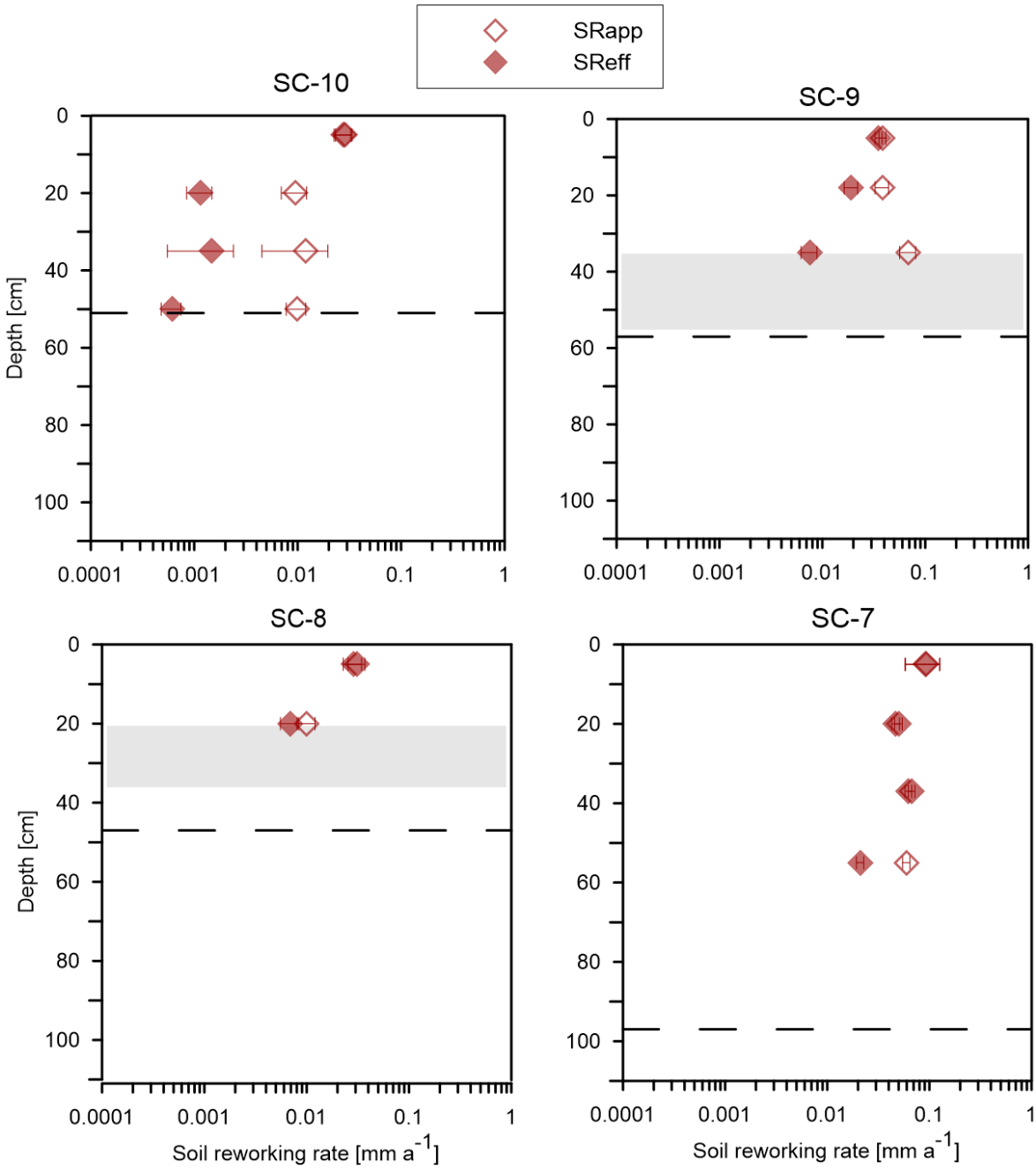

Figure 3.6 Apparent soil reworking rate (SR_{app}) mm a-1 and effective soil reworking rate (SR_{eff}) mm a-1 as a function of depth, for the four soil profiles (SC-7, SC-8, SC-9, SC-10). The dashed line indicates the border between mobile regolith and saprolite as identified in the field. The shaded area in profiles SC-8 (lower hillslope) and SC-9 (upper hillslope) shows the transition zone between mobile regolith and saprolite derived from luminescence results. In profiles SC-10 (hilltop) and SC-7 (hill-base) the depth of the mobile regolith observed in the field coincides with the luminescence results. The luminescence results indicate that in the field observations the mobile regolith border has been overestimated in profiles SC-8 and 9. Note that apparent soil reworking rate tend to be constant with depth, while effective soil reworking rate reflects the decrease in soil reworking with depth that would be expected when bioturbation is the dominant process (SC 8-10).

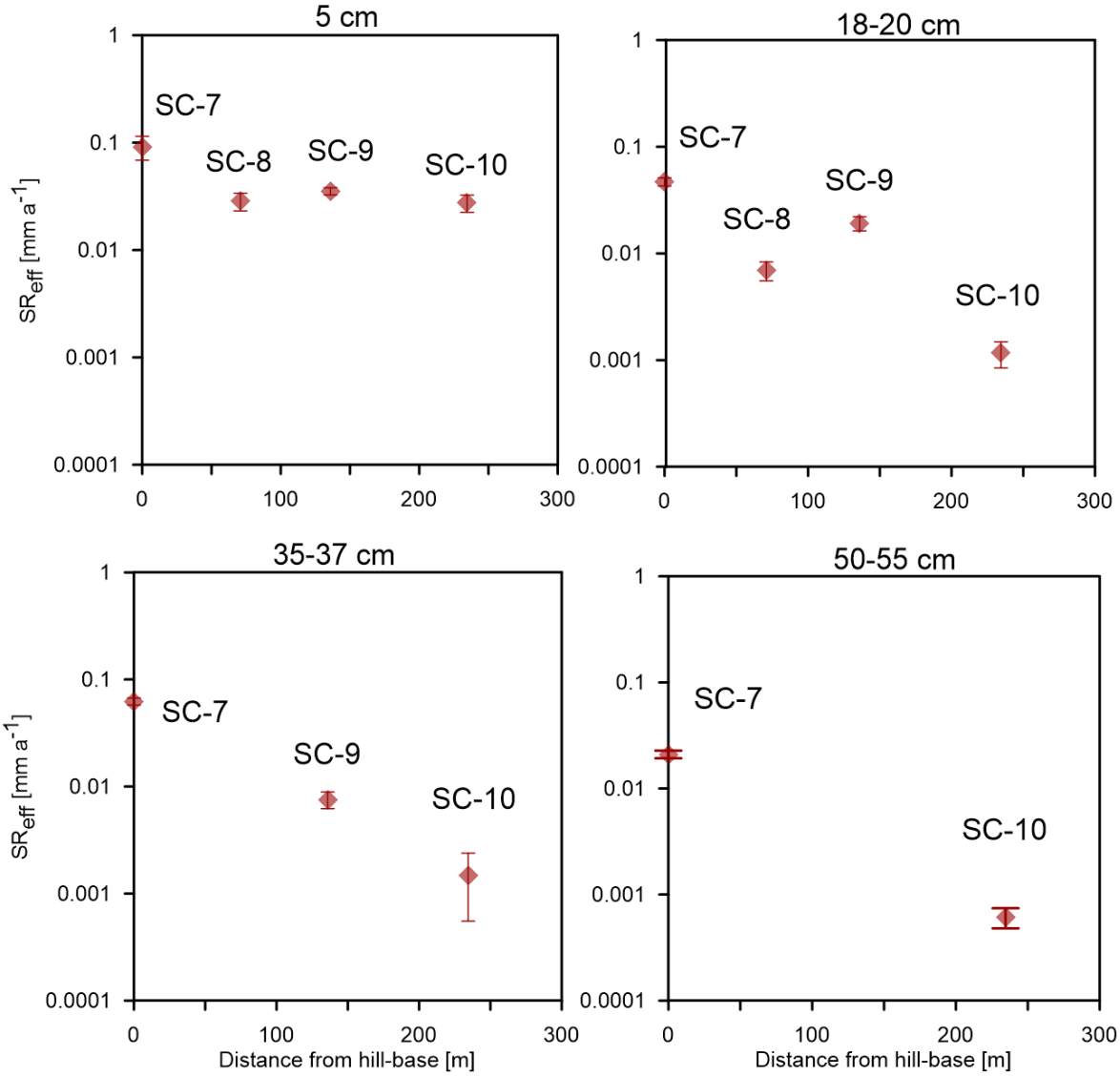

Figure 3.7 Effective soil reworking SR_{eff} as a function of distance from the hilltop for different depths.

4. Discussion

4.1. Reliability of luminescence-derived soil mixing data

The relative uncertainty in the luminescence age calculated increases with depth due to there being fewer grains that have been exposed to light, making the measurement results less precise close to the interface of mobile regolith and saprolite. Also laterally, when comparing the same depth in each soil profile, the paleodose and luminescence age

uncertainty increase upslope for the same reason (Figure 3.5 and Table 3.2). As a consequence, the uncertainty of soil reworking measures (SR_{app} and SR_{eff}) increases with depth and upslope in a similar way.

Our results show a marked difference between the apparent soil reworking rate, as adopted in previous luminescence based soil reworking investigations (Heimsath et al., 2002; Wilkinson and Humphreys, 2005 and Stockmann et al., 2013), and the effective soil reworking rate recently proposed by Reimann et al. (2017). Reimann et al. (2017) already argued that soil reworking rate is expected to decrease with depth, as many biological processes expose this same trend (Wilkinson et al., 2009) and that SR_{app} fails to register this due to methodological limitations. SR_{eff} indeed seems to overcome this shortcoming, providing soil mixing rates which reduce with depth and approach zero near the saprolite. Only for the hill-base profile (SC-7) SR_{app} and SR_{eff} provide similar values, which reflects the depositional nature of these deposits (Figure 3.6). In conclusion, this data shows that within each profile, SR_{eff} with lower values than SR_{app}, is a better indicator of the soil reworking than SR_{app} because it takes into account the non-saturation factor (NSF) or the percentage of grains that have participated in the soil mixing process.

It needs to be noted however that both (SR_{eff} and SR_{app}) are still simple soil reworking measures that only provides a linear measure of the burial rate. A follow-up study will analyze bioturbation rates by calculating the diffusivity constant using this same dataset and compare this to these linear soil reworking measures.

4.2. Reconstruction of soil mixing and erosion-deposition processes along a hillslope catena

We have shown important variations in age within the analyzed profiles, both vertically and laterally (Figure 3.5).

Within each soil profile, apparent luminescence ages increase exponentially with depth from the surface. At the surface, all profiles show relatively young ages and a high fraction of non-saturated grains, indicating that these recently visited the surface and their luminescence signals were reset. The fraction of grains below the saturation threshold (or surface visiting grains) then decreases with depth from the soil surface (Figure 3.4). This is consistent with our current understanding of bioturbation processes. Wilkinson et al. (2009) review data on surface mounding, burial and mixing rates. They conclude that local mounding rates outweigh burial by an order of magnitude. Very often, a large proportion

of the soil is mined from shallow depths. Hence, much higher bioturbation activities are observed at the surface. In depth, bioturbation studies generally observe a decrease of activity with depth below the surface (Wilkinson et al., 2009). Both observations are confirmed by our SR_{eff} data.

Laterally, a systematic downslope decrease in age and an increase in the fraction of non-saturated grains (NSF) are observed when the same depths are considered. This can be explained by the influence of lateral soil redistribution, if it is assumed that bioturbation processes are homogeneous along the hillslope. Lateral soil redistribution can be explained by creep processes or by surface erosion that consist on in this area in splash, sheet and rill erosion produced by water erosion. While rates of surface erosion by water are low for natural vegetation, forest fires have been shown to induce periodically important episodes of erosion (Moody et al., 2013). Erosion, transport and deposition at the surface are likely to induce complete bleaching of the grains. In contrast, creep, whether due to biogenic or physical processes, does not expose grains to light. Anderson (2015) modeled particle trajectories due to creep and showed that them to be parallel to the surface. Generally, creep velocities are higher near the surface and decrease down the profile (Roering et al., 2002; Anderson, 2015). Hence, when creep is the dominant process, the particle ages are expected to depend only upon depth in the soil and not upon horizontal position on the catena (Anderson, 2015).

The hill-base profile SC-7 indicates a low fraction of saturated grains throughout and a gradual increasing age with depth. These features corroborate the depositional context, and indicate that surface erosion is likely more important than creep. The increase in the fraction of saturated grains with depth (from near zero at the surface, to about 30% at 50-55 cm) may reflect mixing of the deposits with underlying regolith through bioturbation, or a dominance of creep rather than surface erosion under different land cover or climate in the past. Visual observations in the field confirm that this is a depositional site at present, as we observed widespread accumulation of sediment next to trees and rocks in the hill-base area (see figure 3.8).

Figure 3.8 Mound formed around a tree trunk indicating active sediment deposition in the area around the hill-base profile.

In our profiles, as we observe a decreasing age-depth trend downslope (Figure 3.5), the hillslope is clearly not in steady state. Our observations correspond either to a hillslope under the influence of surface erosion-deposition processes (scenario b, figure 3.2) or to a scenario with increasing creep downslope (scenario d, figure 3.2). However, the higher soil depth in the hill-base excludes the latter situation. Our luminescence results therefore seem to point to surface erosion-deposition processes as the dominant lateral process along this hillslope. In addition, NSF increases linearly with distance downslope (figure 3.4). If no lateral redistribution would occur, all profiles should exhibit the same NSF trend with depth. In the hilltop profile SC-10, vertical mixing is the dominant soil reworking process. Therefore, as explained above, the lower samples have low NSF values and a high proportion of non-surface visiting grains. This analysis opens interesting perspectives for application of luminescence dating for long-term landscape evolution, as it allows to identify the dominating processes. There exists however the possibility is that our assumption of spatially homogeneous bioturbation is not valid here, but the addition of

extra variable, in our case heterogeneous bioturbation along the hillslope, does not yield better results. In other words, the simplest explanation is usually better and more assumptions make the explanation more unlikely following the law of parsimony or Occam's razor principle. That being said, although the assumption of homogeneous bioturbation is broadly used in literature (e.g. Stockmann et al., 2013), further research will be needed to elucidate this (Román-Sánchez et al., submitted).

4.3. Performance of the feldspar single-grain methodology

Our results show the importance of taking into account the NSF factor. Mixing rates derived from previous luminescence studies, such as Heimsath et al. (2002), Wilkinson and Humphreys (2005) and Stockmann et al. (2013) that did not take this into account, can therefore be expected to be overestimated. This error is especially important for samples with low mixing intensities, i.e. samples that are deep in the soil profile, and that have a low NSF.

Our effective soil reworking rates results are lower compared to values obtained in other studies. Considering the hilltop profile, so as to compare the same topographic position with other studies, the value is 0.028 mm a^{-1} for the surface sample at 5 cm. The vertical mixing value reported by Heimsath et al. (2002) observed in Nunnock River in the upper Bega Valley in southeast NSW, Australia, at 10 cm of depth is 0.26 mm a^{-1}. Our values are more comparable to the vertical mixing values obtained by Stockmann et al. (2013) in Werrikimbe National Park in north-eastern NSW, Australia, of 0.031 and 0.085 and mm a^{-1} at 4 cm depth. We suggest that the low value of soil reworking rates in the superficial layer is due to absence in our environment of great bioturbators such as wombats, termites, high earthworm densities or tree throws.

Our value for the deepest sample, at 50 cm, is 0.0006 mm a^{-1}, while the values reported by Stockmann et al. (2013) at 45 cm depth are between 0.270 and 0.083 mm a^{-1}. Gabet et al. (2003) described from other authors (Michell, 1988; Whitford, 2000) that earthworms move 0.54 mm a^{-1} of soil, ants 0.0045 mm a^{-1} and termites 0.41 mm a^{-1}. Our value is much lower for the deeper sample than previously reported values due to the improvement in the methodology employed in our study that takes into account NSF.

Furthermore, this methodology could be used as a tracer within the soil profile. The basal transition to the underlying granitic saprolite, as observed in the field, is sharp. Our results confirm luminescence as an objective method to establish this border. Our data

suggests that the field identification of the saprolite border might have been overestimated for the hillslope profiles. This has important consequences for estimating soil depth and particularly for calculating soil productivity rates that often depend on a correct identification and sampling in function of this boundary. Luminescence could therefore be important to complement measurements of soil production rates using cosmogenic nuclides or other methods.

5. Conclusions

This study aimed to constrain soil reworking by bioturbation and erosion-deposition along a hillslope catena, using feldspar single grain luminescence. We tested this methodology for the first time at different depths in four soil profiles, located in the Santa Clotilde Critical Zone Observatory in SW Spain.

The apparent burial age in each soil profile marks an expected trend increasing with depth. Effective soil reworking rates range from 0.028 – 0.092 mma^{-1} at 5 cm depth, down to 0.0006-0.0007 mm a^{-1} at 55 cm depth at the hilltop location. The variation of the age-depth trend along the hillslope allows us to identify bioturbation and surface erosion-deposition as the main processes moving grains vertically and laterally. At the hilltop profile, the age-depth trend is caused by slow mixing of the soil through bioturbation. In the two hillslope profiles, this trend is overprinted due to erosion, causing shallower profiles and, in the case of SC-9, a younger profile, whereas in the hill-base profile the age-depth trend clearly reflects the depositional age of the sediments. Effective soil reworking rates at depth are in line with expectations based on proximity to saprolite, and demonstrate the importance of calculating the effective rate taking into account the fraction of non-light exposed grains.

Finally, another potential important application of the fraction of non-visiting surface grains is that it makes it possible to objectively identify the boundary between the mobile regolith and the saprolite. As shown by our data, in two cases this does not correspond with field observations.

Acknowledgement

This work has been funded by projects AGL2012-40128-C03-02 and AGL2015-65036-C3-2-R (MINECO/FEDER, UE). Andrea Román-Sánchez is funded by Contratos

Predoctorales Fellowship with reference BES-2013-067009 and by research stay funding with reference EEBB-I-15-09373 (MINECO) in Wageningen University, Soil Geography and Landscape group & Netherlands Centre for Luminescence dating, Environmental Sciences. The authors would also like to thank Professor Jesús Ayuso for providing access to the experimental area and help with the field work.

References

Aitken, M.J. 1985. Thermoluminescence dating, U.S. ed. London : Academic.

Anderson, R.S. 2015. Particle trajectories on hillslopes: Implications for particle age and 10Be structure. Journal of Geophysical Research: Earth Surface 120: 2015JF003479. DOI:10.1002/2015JF003479

Carson, M.A. and Kirkby M.J. 1972. Hillslope Form and Process. Cambridge University Press: Cambridge.

Darwin, C. 1881. The formation of vegetable mould through the action of worms : with observations on their habits. London: John Murray.

Dietrich, W.E., Reiss, R., Hsu, M.-L., Montgomery, D.R. 1995. A process-based model for colluvial soil depth and shallow landsliding using digital elevation data. Hydrological Processes 9: 383–400. DOI:10.1002/hyp.3360090311

Dixon, J. L., and F. von Blanckenburg 2012. Soils as pacemakers and limiters of global silicate weathering. Comptes Rendus Geoscience 344(11–12): 597–609. DOI:10.1016/j.crte.2012.10.012.

Gabet, E.J., Reichman, O.J., Seabloom, E.W. 2003. The Effects of Bioturbation on Soil Processes and Sediment Transport. Annual Review of Earth and Planetary Sciences 31: 249–273. DOI:10.1146/annurev.earth.31.100901.141314

Gabet, E.J., Mudd, S.M. 2010. Bedrock erosion by root fracture and tree throw: A coupled biogeomorphic model to explore the humped soil production function and the persistence of hillslope soils. Journal of Geophysical Research: Earth Surface115: F04005. DOI:10.1029/2009JF001526

Gilbert, G.K. 1877. Geology of the Henry Mountains (USGS Unnumbered Series), Monograph. Government Printing Office, Washington, D.C.

Guérin, G., Mercier, N., Adamiec, G. 2011. Dose-rate conversion factors: update. Ancient TL 29: 5–8.

Heimsath, A.M., Chappell, J., Spooner, N.A., Questiaux, D.G. 2002. Creeping soil. Geology 30: 111–114. DOI: 10.1130/0091-7613(2002)030<0111:CS>2.0.CO

Huntley, D.J., Lamothe, M. 2001. Ubiquity of anomalous fading in K-feldspars and the measurement and correction for it in optical dating. Canadian Journal of Earth Sciences 38: 1093–1106. DOI:10.1139/e01-013

Hütt, G., Jaek, I., Tchonka, J.1988: Optical dating – K-feldspars optical-response stimulation spectra. – Quaternary Science Reviews 7: 381-385. DOI:10.1016/0277-3791(88)90033-9

IUSS Working Group 2014. World Reference Base for Soil Resources 2014. International soil classification system for naming soils and creating legends for soil maps (3rd ed.). FAO, Rome

Larsen, I.J., Almond, P.C., Eger, A., Stone, J.O., Montgomery, D.R., Malcolm, B. 2014. Rapid Soil Production and Weathering in the Southern Alps, New Zealand. Science 343: 637–640. DOI:10.1126/science.1244908

Lehre, A.K. 1987. Rates of soil creep on colluvium-mantled hillslopes in north-central California. Erosion and Sedimentation in the Pacific Rim. Proceedings of the Corvallis Symposium, August: IAHS 165: 91–100

Lutz, H.J. 1960. Movement of rocks by uprooting of forest trees. American Journal Science 258: 752–756. DOI:10.2475/ajs.258.10.752

Mejdahl, V. 1979. Thermoluminescence Dating: Beta-Dose Attenuation in Quartz Grains. Archaeometry 21: 61–72. DOI:10.1111/j.1475-4754.1979.tb00241.x

Michell, PB. 1988. The influences of vegetation, animals, and micro-organisms on soil processes. In: Viles, H.A. (Ed.), Biogeomorphology. Basil Blackwell Ltd, Oxford, UK: 43 - 82.

Moody, J.A., Shakesby, R.A., Robichaud, P.R., Cannon, S.H., Martin, D.A. 2013. Current research issues related to post-wildfire runoff and erosion processes. Earth-Science Reviews 122: 10-37. DOI: 10.1016/j.earscirev.2013.03.004

National Research Council 2001. Basic research opportunities in Earth science. National Academies Press, Washington, D.C.

Peel, M.C., Finlayson, B.L., McMahon, T.A. 2007. Updated world map of the Köppen-Geiger climate classification. Hydrology and Earth System Science 11: 1633–1644. DOI:10.5194/hess-11-1633-2007

Phillips, J.D., Marion, D.A. 2004. Pedological memory in forest soil development. Forest Ecology and Management 188: 363 – 380.

Prescott, J.R., Hutton, J.T. 1994. Cosmic ray contributions to dose rates for luminescence and ESR dating: large depths and long-term time variations. Radiation Measurements 23: 497–500. DOI: 10.1016/1350-4487(94)90086-8

Reimann, T., Thomsen, K.J., Jain, M., Murray, A.S., Frechen, M. 2012. Single-grain dating of young feldspars using the pIRIR procedure. Quaternary Geochronology 11: 28-41. DOI: 10.1016/j.quageo.2012.04.016

Reimann, T., Román-Sánchez, A., Vanwalleghem, T., Wallinga, J. 2017. Getting a grip on soil reworking – Single-grain feldspar luminescence as a novel tool to quantify soil reworking rates. Quaternary Geochronology 42: 1–14. DOI:10.1016/j.quageo.2017.07.002

Riebe, C.S., Kirchner, J.W., Finkel, R.C. 2003. Long-term rates of chemical weathering and physical erosion from cosmogenic nuclides and geochemical mass balance. Geochimica et Cosmochimica Acta 67: 4411–4427. DOI: 10.1016/S0016-7037(03)00382-X

Roering, J.J., Almond, P., Tonkin, P., McKean, J. 2002. Soil transport driven by biological processes over millennial time scales. Geology 30: 1115–1118. DOI: 10.1130/0091-7613(2002)030<1115:STDBBP>2.0.CO;2

Román-Sánchez, A., Vanwalleghem, T., Peña A., Laguna A., Giráldez J.V. 2017. Controls on soil carbon storage from topography and vegetation in a rocky, semi-arid landscapes. Geoderma. DOI:10.1016/j.geoderma.2016.10.013

Román-Sánchez, A., Laguna, A., Reimann, T., Giráldez, J.V., Peña, A., Vanwalleghem, T. Bioturbation and erosion rates along the soil-hillslope conveyor belt, part 2: quantification using an analytical solution of the diffusion-advection equation. Earth Surface Processes and Landforms. Submitted

Shaler, N. S. 1891. The origin and nature of soils. U.S. Geological Survey 12th Annual Report, part 1: 213-345

Smedley, R.K., Duller, G. a. T., Pearce, N.J.G., Roberts, H.M. 2012. Determining the K-content of single-grains of feldspar for luminescence dating. Radiation Measurements. 47: 790–796. DOI:10.1016/j.radmeas.2012.01.014

Stockmann, U., Minasny, B., Pietsch, T.J., McBratney, A.B. 2013. Quantifying processes of pedogenesis using optically stimulated luminescence. European Journal of Soil Science 64: 145–160. DOI:10.1111/ejss.12012

Stockmann, U., Minasny, B., McBratney, A.B. 2014. How fast does soil grow?. Geoderma 216: 48–61. DOI:10.1016/j.geoderma.2013.10.007

Thomsen, K.J., Murray, A.S., Jain, M., Bøtter-Jensen, L. 2008. Laboratory fading rates of various luminescence signals from feldspar-rich sediment extracts. Radiation Measurements 43: 1474–1486. DOI:10.1016/j.radmeas.2008.06.002

Whitford, W.G. 2000. Keystone arthropods as webmasters in desert ecosystems. Invertebrates as Webmasters in Ecosystems: 25–41. DOI: 10.1079/9780851993942.0025

Wilkinson, M.T., Humphreys, G.S. 2005. Exploring pedogenesis via nuclide-based soil production rates and OSL-based bioturbation rates. Soil Research 43: 767–779. DOI:10.1071/SR04158

Wilkinson, M.T., Richards, P.J., Humphreys, G.S. 2009. Breaking ground: Pedological, geological, and ecological implications of soil bioturbation. Earth-Science Reviews 97: 257–272. DOI:10.1016/j.earscirev.2009.09.005

Wintle, A.G., Murray, A.S. 2006. A review of quartz optically stimulated luminescence characteristics and their relevance in single-aliquot regeneration dating protocols. Radiation Measurements 41: 369–391. DOI:10.1016/j.radmeas.2005.11.001

CHAPTER 4

BIOTURBATION AND EROSION RATES ALONG THE SOIL-HILLSLOPE CONVEYOR BELT, PART 2: QUANTIFICATION USING AN ANALYTICAL SOLUTION OF THE DIFFUSION-ADVECTION EQUATION

This work is in review in:

Román-Sánchez, A., Laguna, A., Reimann T., Peña, A., Giráldez, J.V., Vanwalleghem, T. (2017) Bioturbation and erosion rates along the soil-hillslope conveyor belt, part 2: quantification using an analytical solution of the diffusion-advection equation. Earth Surface Processes and Landform. In review.

Abstract

Erosion and bioturbation move soil particles down along hillslopes and change the vertical and horizontal distribution of soil properties. Both are key processes for understanding landscape evolution and soil formation, and affect the functioning of the critical zone. We show here how the depth-age information, derived from feldspar-based single grain post Infrared Stimulated Luminescence (post-IR IRSL), can be used to simultaneously quantify erosion and bioturbation processes along a hillslope. In this study, we propose, for the first time, an analytical solution for the diffusion-advection equation to calculate the diffusivity constant and erosion-deposition rates. We fit this model to age-depth data derived from fifteen soil samples from four soil profiles along a catena located under natural grassland in the Santa Clotilde Critical Zone Observatory, in the South of Spain. Next, a global sensitivity analysis was used to assess the relative importance of each model parameter in the output. Finally, the posterior probability density functions were calculated to evaluate the uncertainty in the model parameter estimates.

The results show that the diffusivity constant at the surface varies from 11.4 to 81.9 $mm^2\ a^{-1}$ for the hilltop and hill-base profile respectively, and between 7.4 and 64.8 $mm^2\ a^{-1}$ at 50 cm depth. The uncertainty in the estimation of the erosion-deposition rates is found to be too high to make a reliable estimate, probably because erosion- deposition rates are very low in this environment. This is confirmed by a global sensitivity analysis that shows how the most important parameters controlling the age-depth structure are the diffusivity constant and regolith depth.

Finally, the soil reworking rates proposed by earlier studies, only taking into account particle age and depth, are compared with diffusivity. We find a good agreement of our calculated diffusivity constants with soil reworking rates, given these rates are corrected for the proportion of particles actually participating in the reworking process, i.e. using effective soil reworking rates.

1. Introduction

The architecture of the critical zone, including its surface topography, soil properties, depth of the weathering zone and ecosystem properties, is controlled by the balance of weathering, transport and biological processes (Anderson, 2015). Recent studies have highlighted important interactions between chemical weathering and physical erosion processes (Riebe et al., 2003; Maher, 2010; Larsen et al., 2014). However, biological

processes have received much less attention although biota is a fundamental part of the critical zone (Gabet et al., 2003). According to Lin (2010), the coupling of geological cycles and biological cycles is essential in understanding how the critical zone functions and eventually in developing predictive models. Bioturbation is a key process in soil formation and landscape evolution. Historically, the action of biota reworking sediment was first described by Darwin (1881), who believed firmly that it was a fundamental process in the formation of soils and landscapes. Schäfer (1952) defined the term bioturbation for the first time in the discipline of ichnology. Richter (1952) distinguished between phytoturbation due to growing plants and zooturbation caused by burrowing of animals. Blum and Ganssen (1972) then defined bioturbation in pedology as a biological process produced by plants and animals that alter soil properties and interrupt horizon layers. Wilkinson et al. (2009) detailed this process like a biotic mixing or displacement in the soil and recognized its importance to link different Earth system sciences.

Bioturbation processes have a clear impact on soil or mobile regolith, as they continuously move their particles vertically and laterally. This movement will have important effects on the development of weathering profiles and soil horizons. Commonly, the limit between the soil or mobile regolith and the underlying chemically weathered saprolite or unweathered bedrock is a sharp one. Such a sharp boundary cannot be explained by chemical weathering reactions, but is rather the result of tree throws and burrowing animals, such as earthworms, ants or termites (Heimsath et al., 1999). Other clear examples of biogenic effects on soil particle grading are subsurface stone lines, often attributed to bioturbation based on field studies (e.g. Johnson, 1989). Salvador-Blanes et al. (2007) developed a soil formation model able to reproduce such stone lines. Roering et al. (2010) showed with geophysical methods that the classical soil formation model, with a soil-bedrock interface lowering homogenously over the landscape, might not be valid. They showed how uprooting of the saprolite by tree throws resulted in a feedback mechanism creating hotspots of soil formation and localized pockets of deep soil. Gabet and Mudd (2010) developed a coupled biogeomorphic model based on this tree-throw controlled regolith production, which resulted in a humped soil production function, consistent with field observations based on Terrestrial Cosmogenic Nuclides (TCN).

Recent research also recognizes the importance of bioturbation processes for downslope sediment transport, or biogenic creep (Wilkinson et al., 2009). Hillslopes can be seen as conveyor belts as suggested Anderson et al. (2013), in analogy to river systems (Kondolf, 1994), where soil is loaded onto at a particular rate depending on formation and

transported downwards depending on erosion and bioturbation processes. In many studies, the former have received much more attention than the latter, while in many natural vegetation-covered landscapes, rain splash and overland flow are not effective, apart from short periods after occasional forest fires. However, uprooting of trees, mound generation and constant mixing of soils result in a significant net downslope movement on hillslopes. Soil biota displace great volumes of soil and, in many environments, bioturbation has been shown to be dominant over mechanical effects - such as freeze-thaw or drying-wetting cycles- in controlling creep flux rates (Wilkinson et al., 2009). Gabet et al. (2003) developed theoretical models for sediment flux rates due to different biogenic processes, and obtained values between 0.001 and 0.004 $m^3\ m^{-1}\ a^{-1}$ for tree throw and values of almost an order of magnitude higher for bioturbation by gophers. Such values are of the same order of magnitude as those reported by Small et al. (1999) for an alpine landscape in Wyoming, who measured creep fluxes 0.0024 m a-1 using in situ TCN.

In spite of its importance, data on bioturbation rates and its contribution to sediment fluxes are rare. In part, this is due to the fact that such sediment flux rates are slow and therefore difficult to measure. Many studies have used TCN for this purpose, but this technique is laborious and expensive, especially when applied over many points of the landscape. Also, TCN do not allow tracking particle behaviour within soils or constraining bioturbation rates. Very often, bioturbation rates have been determined by simple methods such as measuring the amount of surface casts, biomounds or tree falls (Meysman et al., 2006). Another alternative has been to characterize bioturbation as a diffusive process and use short-lived radioisotope profiles to obtain the diffusion coefficient (Lecroart et al., 2010; Yoo et al., 2011). Heimsath et al. (2002) and Stockmann et al. (2013) used Optically Stimulated Luminescence (OSL) dating techniques but only determined linear mixing rates, i.e. simply dividing depth by burial age, without taking into account the non-linear behavior of the mixing process. More recently, Johnson et al. (2014) applied the diffusion-advection equation proposed by Kirkby (1985), in combination with OSL to calculate bioturbation on the one hand and TCN to determine erosion rates on the other hand for a study site northeast Queensland. The use of luminescence techniques in soil formation and geomorphic studies allows to study the effect of bioturbation and biogenic creep over longer time scales. Current applications have been limited so far however. The analysis by Johnson et al. (2014) for example was limited to a single soil profile and used numerical methods to solve the diffusion-advection equation.

We show here how age-depth information from single-grain feldspar luminescence can be used to simultaneously quantify bioturbation and erosion-deposition rates along a hillslope. First, we propose an analytical solution for the diffusion–advection equation to simultaneously calculate bioturbation and long-term soil transport rates within four profiles along this catena. While analytical solutions for the simple diffusion case are widely available, this is not the case for the combined equation. We then apply uncertainty and global sensitivity analysis to constrain the optimal values and uncertainty on these rates, and to determine the relative importance of the model's parameters.

2. Material and Methods

2.1. Site description

The study area is located in the Santa Clotilde Critical Zone Observatory, within the Cardeña and Montoro Natural Park, Cordoba province, SE Spain (Figure 4.1 a). The site is in the Martin Gonzalo headwater catchment (latitude 38° 12′ N, longitude 4° 17′ W) in Sierra Morena, which belongs to the SW Iberian Massif and separates the Spanish Central Plateau and the Baetic Depression. The edge of the plateau is fractured and lifted by Alpine thrust forces on the Hercynian base of the plateau. This explains on the one hand, the formation of permanent creeks flowing to the Baetic Depression with steep slopes that are covered by natural Mediterranean sclerophyll forests, and on the other hand, higher-lying plateau areas covered by oak-woodland grassland savannah. The most representative tree species are *Quercus ilex* subsp. *Ballota*, *Quercus suber*, *Quercus faginea*, *Quercus pirenaica*, *Arbutus unedo* and shrubs are *Quercus coccifera*, *Phlomys purpurea*, *Pistacia lentiscus*, *Smilax aspera*, *Rubus ulmifolius*. The geology is composed of granites (Geological and Mining Institute of Spain, 2013) and the main soil types are Regosols, Cambisols and Phaeozems with Rankers under the FAO-Unesco World Reference Base (IUSS Working Group WRB, 2014). The mean annual rainfall is 600 mm, concentrated in the wet season, and the mean annual air temperature is 15 ^{0}C, with minimum and maximum extreme values of 5 and 40 ^{0}C, respectively. The climate is classified as Bsk, (cold semi-arid) within the Köppen-Geiger system (Peel et al., 2007).

In this study we sampled four soil profiles along the north facing slope of a catena (Figure 4.1 b, c, d) in different soil landscape position, SC-7 (hill-base), SC-8 (lower hillslope), SC-9 (upper hillslope) and SC-10 (hilltop) and at different depths from the surface to the top to saprolite layer (Table 4.1). The limit between the mobile regolith and the saprolite layer was identified visually in the field.

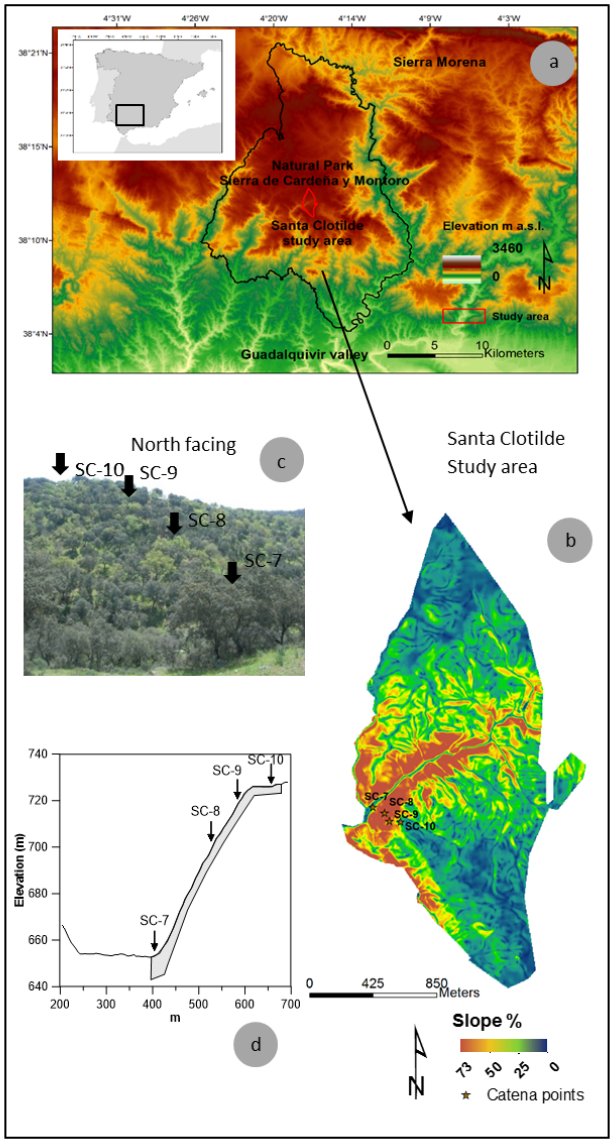

Figure 4.1 (a) Location of the study area within Spain and Cardeña and Montoro Natural Park. (b) Slope distribution in the study area. (c) General view and location of the four soil profiles along the hillslope. (d) Cross-sectional profile of the valley and location of the catena points

2.2. Sampling and luminescence measurements

In total 15 samples were collected for luminescence analysis. The samples were taken at four different depths in four soil profiles along a catena, from the surface to the upper boundary of the regolith: 5, 18-20, 35-37, 50-55 cm (Table 4.1). Details about sampling, sample preparation and pre-testing of those samples are provided in Reimann et al., (2017) and Román-Sánchez et al. (submitted); the focus of this paper is to use the luminescence

data that has been described already in the above mentioned paper to analytically solve the diffusion-advection equation.

Luminescence dating determines the last time mineral grains such as quartz or feldspar were exposed to the surface and this method is widely used in Quaternary research and archaeology which is for example reviewed in Rhodes (2011) and Duller (2008), respectively. For a luminescence age two quantities have to be determined: (i) the palaeodose estimate (P), which is the dose (in Gray, Gy) a mineral grain has been received since burial by natural occurring radioactivity and (ii) the rate at which this palaeodose accumulates, known as the dose rate. It was recently suggested by Reimann et al. (2017) that the luminescence analysis of feldspar single sand-sized grains is the most promising method to determine meaningful luminescence based soil mixing rates.

One main advantage of the feldspar single-grain luminescence method over the more conventional quartz OSL single-grain method is that we can more reliably determine the number of grains that have not participated in the soil mixing process. However, an accurate estimate of these "out of competition" grains per sample is key to calculate effective soil reworking rates (Reimann et al. 2017). Here, we follow up on these suggestion and findings and we will specifically focus on the luminescence data gained by single-grain feldspar measurement using the post-IR IRSL signal measured at 175 °C. For more details about the comparison between the feldspar single-grain luminescence signals and the single-grain OSL signal from quartz as well as the respective measurement protocols and the calculation of effective soil reworking rates, we refer to Reimann et al. (2017) and Román-Sánchez et al. (submitted).

2.3. Determination of burial age and reworking rate

Once palaeodose, P, and the dose rate, *DR*, are estimated, the burial age, *A*, can be determined according to Equation 1

$$A = \frac{P}{DR} \tag{4.1}$$

A linear soil reworking rate (*SR*) can be determined dividing the soil depth of the sample, *z*, by the burial age (Heimsath et al., 2002; Stockmann et al., 2013; Wilkinson and Humphreys, 2005). However, as shown by Reimann et al. (2017), this *SR* or also called apparent SR (SR_{app}) can be an overestimation of the real rate.. These authors propose an linear effective soil reworking (SR_{eff}) (equation 2, Table 4.1), taking into account only the

fraction of sand grains that have participated in the soil mixing, i.e. the grains that have been dug up and subsequently reburied at some point, (expressed by the non-saturated factor, NSF listed in Table 4.1). Román-Sánchez et al. (submitted) present, for the studied catena, the values of SR_{app} and SR_{eff}. They find SR_{eff} to be a better estimator of the velocity of soil reworking than SR_{app}.

$$SR_{eff} = \frac{z}{A}\ NSF \tag{4.2}$$

Table 4.1 Luminescence results. [a] Non-saturation factor (NSF). Proportion of grains below the saturation threshold. [b] Burial age. [c] Effective soil reworking rate. More details can be found in Materials and Methods. Note that all results are from feldspar single grain $pIRIR_{175}$

Soil profile and depth, z (cm)	Mobile regolith depth [m]	Slope [%]	NSF[a] [a.u.]	Burial Age [b] [ka]	SR_{eff}[c] [mm a^{-1}]	Diffusivity [mm^2 a^{-1}]
SC-7	0.97	13.08				
5			0.990	0.54 ± 0.20	0.093 ± 0.034	81.9
20			0.938	4.00 ± 0.35	0.050 ± 0.004	75.7
37			0.922	5.51 ± 0.41	0.067 ± 0.005	69.4
55			0.353	9.24 ± 0.76	0.060 ± 0.005	64.8
SC-8	0.47	38.68				
5			0.913	1.60 ± 0.30	0.031 ± 0.006	13.2
20			0.690	19.9 ± 4.00	0.010 ± 0.002	11.0
35			0.000	-	-	9.2
SC-9	0.57	36.68				
5			0.912	1.3 ± 0.10	0.038 ± 0.003	23.3
18			0.420	4.7 ± 0.70	0.038 ± 0.006	21.6
35			0.077	5.1 ± 0.90	0.069 ± 0.012	19.5
55			0.000	-	-	17.4
SC-10	0.51	0.58				
5			0.968	1.76 ± 0.32	0.028 ± 0.005	11.4
20			0.121	20.9 ± 5.7	0.010 ± 0.003	9.9
35			0.122	29.1 ± 18.2	0.012 ± 0.008	8.6
50			0.062	50.7 ± 10.90	0.010 ± 0.002	7.4

2.4. Analytical solution of the diffusion-advection equation

The diffusivity equation representing the effect of bioturbation, that decreases with depth as mentioned below by several authors (e.g. Humphreys and Field, 1998), on the soil particle burial age, A, can be expressed as

$$\frac{\partial A}{\partial t} = \frac{\partial}{\partial z}\left(D(z)\frac{\partial A}{\partial z}\right) \tag{4.3}$$

where t is time; D is diffusivity coefficient and z is depth. The diffusivity coefficient can be expected to decrease exponentially with depth, in correspondence with a decreasing biological activity.

$$D(z) = D_o e^{-z/zb} \tag{4.4}$$

where D_0 is the diffusivity coefficient at the surface and z_b is the e-folding length scale. This latter parameter is the *depth* interval in which *diffusivity* decreases by a factor of e. This parameter therefore affects the shape of the age-depth curve obtained. For lower z_b values, the decrease of diffusivity with depth is slower. The result is a better mixed profile with a more slowly decreasing exposure age with depth. The suggested exponential decline of diffusivity with depth is supported by different studies. Darwin (1881) proposed that vertical mixing in the soil is produced by biological activity and its intensity decays with depth. Kirkby (1985) assumed that the diffusion coefficient decreases exponentially with depth. Canti (2003) confirmed this exponential trend in an experiment with earthworms. Studies by Humphreys and Field (1998), Cousins et al. (1999), Vanwalleghem et al. (2013) also argument that the soil bioturbation decreases with increasing depth due to reduced biological activity (roots, earthworms, termites, gophers). Johnson et al. (2014) explore both a linear as an exponential expression for D.

Including the aging of particles over time, equation 3 becomes

$$\boldsymbol{\frac{\partial A}{\partial t} = \frac{\partial}{\partial z}\left(D(z)\frac{\partial A}{\partial z}\right) + 1} \tag{4.5}$$

In addition, erosion-deposition processes need to be included. This lateral movement is represented by an advection process, resulting in equation 6, where T is the erosion-deposition rate.

$$\boldsymbol{\frac{\partial A}{\partial t} = \frac{\partial}{\partial z}\left(D(z)\frac{\partial A}{\partial z}\right) - T\frac{\partial A}{\partial z} + 1} \tag{4.6}$$

Equation 6 can then be solved analytically under three different conditions: (i) no erosion (T = 0); (ii) net erosion (positive values of T) and (iii) net deposition (negative values of T, or by renaming -T=W with W being deposition).

(i) Under the absence of erosion-deposition, equation 6 reduces to equation 5. Under steady-state conditions, $\frac{\partial A}{\partial t} = 0$, this equation allows to deduce a relation between the particle age and depth. Integration with the boundary conditions, at the surface, $z = 0$, $A = 0$, and a null gradient, $\frac{\partial A}{\partial z} = 0$, at the bottom of the profile, $z = z_{bp}$. The solution is

$$A = -\frac{{z_b}^2}{D_o}\left\{e^{\frac{z}{z_b}}\left[\frac{z}{z_b} - \left(\frac{z_b + z_{bp}}{z_b}\right)\right] + \left(\frac{z_b + z_{bp}}{z_b}\right)\right\} = -\xi\zeta\left[1 - \left(1 - \frac{z/z_b}{\zeta}\right)e^{z/z_b}\right] \qquad (4.7)$$

with

$$\xi = \frac{z_b^2}{D_o} \qquad \zeta = 1 + \frac{z_{bp}}{z_b} \qquad (4.8)$$

where

Do is the diffusion coefficient at the surface and zbp is related to the maximum depth at which the mixing process takes place and may be associated with the depth of the mobile regolith.

(ii) In the case of net erosion, T, the boundary conditions, with the parameters Do and z_o, are

$$\left(D\frac{dA}{dz}\right)_o = D_o\left(\frac{dA}{dz}\right)_o = z_o \; ; \quad A=0 \qquad z=0 \qquad (4.9)$$

If there is no erosion, $T=0$, and as in case (i) under the condition of null gradient, $\frac{\partial A}{\partial z} = 0$, then $z_o = z_{bp}$ and the solution of the equation 6 is

$$A = \frac{z - z_o}{T} + \frac{z_b}{T}exp\left(\frac{Tz_b}{D_o}e^{z/z_b}\right)\left\{\left[E_1\left(\frac{Tz_b}{D_o}e^{z/z_b}\right) - E_1\left(\frac{Tz_b}{D_o}\right)\right] + \frac{z_o}{z_b}exp\left(\frac{Tz_b}{D_o}\right)\right\} \qquad (4.10)$$

E_1 is the exponential integral, defined as

$$E_1 = \int_z^\infty \frac{e^{-\xi}}{\xi}\,d\xi \qquad |\arg z| < \pi \qquad (4.11)$$

(iii) In the case of deposition with negative values of T, now represented as $W = -T$, the equation 6 is expressed as

$$\frac{\partial A}{\partial t} = \frac{\partial}{\partial z}\left(D\frac{\partial A}{\partial z}\right) + W\frac{\partial A}{\partial z} + 1 \tag{4.12}$$

The solution is

$$A = \frac{z_o - z}{W} + \frac{z_b}{W} exp\left(-\frac{Wz_b}{D_o}e^{z/z_b}\right)\left\{\left[E_i\left(\frac{Wz_b}{D_o}e^{z/z_b}\right) - E_i\left(\frac{Wz_b}{D_o}\right)\right] - \frac{z_o}{z_b} exp\left(\frac{Wz_b}{D_o}\right)\right\} \tag{4.13}$$

E_i is another expression of the exponential integral with negative argument, written as

$$E_{i(x)} = -\int_{-x}^{\infty}\frac{e^{-t}}{t}\,dt = \int_{-\infty}^{x}\frac{e^{t}}{t}\,dt \qquad x < 0 \tag{4.14}$$

The results of equations 10 and 13 are shown in Figure 4.2, illustrating the effect of increasing erosion and deposition on the age-depth behaviour within a soil profile. It can be seen how for a given bioturbation setting, as defined by the parameters D_0, z_0, and z_b, the age-depth profile becomes more accentuated with increasing erosion rates. Higher erosion rates lead to more rapidly increasing grain ages with depth. Increasing the deposition rates then result in an apparent homogenization of the age-depth profile, where age only increases slowly with depth. This figure extends the case of erosion shown in the study of Johnson et al. (2014).(see Appendix for the complete mathematical development of this solution of the diffusion-advection equation)

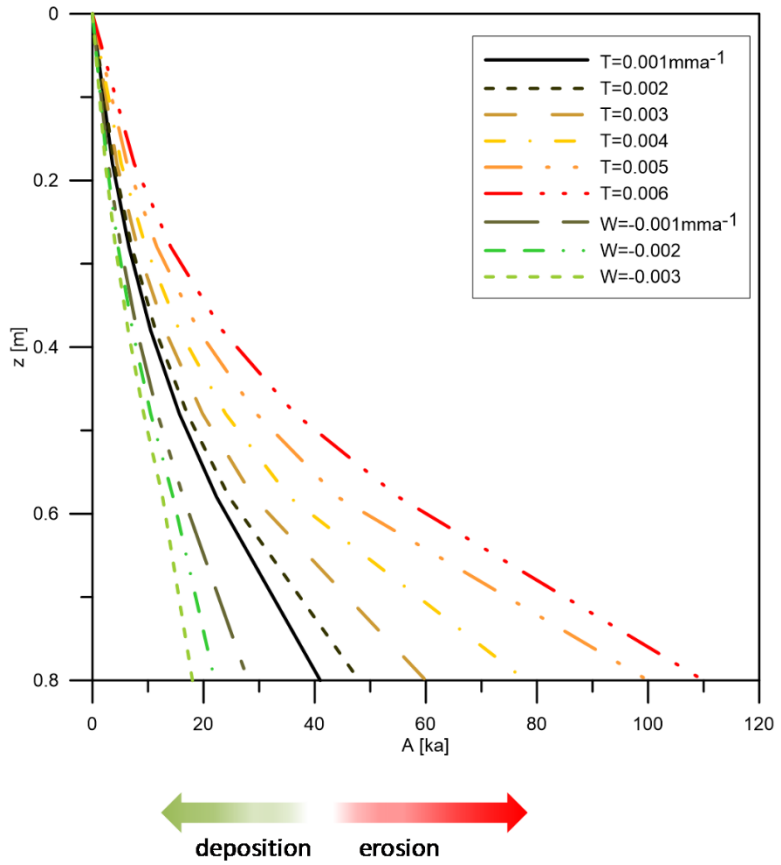

Figure 4.2 Steady-state age-depth profiles illustrating the effect of erosion (T)-deposition (W) on the analytical solution of the advection-diffusion equation.

2.5. Parameter identification and uncertainty analysis

The model coefficients were obtained by fitting this analytical solution against age-depth data derived from the four sampled profiles described in Table 4.1 and an uncertainty analysis was performed using the General Likelihood Uncertainty Estimator (GLUE) methodology (Beven and Binley, 1992). The value of z_0 used for each profile was fixed at the regolith depth measured in the field. For the other three parameters, z_b, D_0 and T or W (with deposition W being equivalent to negative T values), the limits and probability distribution functions, PDFs, included in Table 4.2 were used. We used uniform PDFs for all parameters which, according to Ratto and Saltelli (2001), are appropriate when making an exploratory analysis and no prior information is readily available, as is the case here. SimLab 2.2 (Saltelli et al., 2004) was used to generate 16384 random parameters sets with the Sobol sampling method. The model was run with each parameter set and was compared with the measured age for the four profiles, calculating the respective Nash-Sutcliffe efficiency (NSE) as likelihood function. Finally, the GLUEWIN methodology (Ratto and Saltelli, 2001) was used to obtain the posterior probability density functions (Posterior PDF). The Posterior PDFs are obtained by retaining all the simulations with a likelihood

greather then a predetermined value and rescaling the likelihoods values. The posterior PDF gives an idea of the uncertainty in the estimation of the parameters.

The choice of the likelihood function is somewhat arbitrary, the only requirement is that it should be zero for all simulations that are considered to exhibit behavior dissimilar to the system under study, and it should increase monotonically as the similarity in behavior increases (Beven and Binley, 1992).

The likelihood function used, equation (15), is a function of the variance of the residuals, σ_s, and the variance of observations, σ_o, for each parameter set, θ, and observation set y (e.g. (Beven and Binley, 1992; Kisekka et al., 2013).

$$\begin{aligned} L(\theta / y) &= \left(1 - \frac{\sigma_\varepsilon^2}{\sigma_o^2}\right) \qquad \sigma_\varepsilon^2 < \sigma_o^2 \\ L(\theta / y) &= 0 \qquad\qquad\quad \sigma_\varepsilon^2 \geq \sigma_o^2 \end{aligned} \tag{4.15}$$

This function matches NSE for values greater than zero. When NSE is less than zero, the model is not a better predictor than the data average and a zero value is assigned to the likelihood function.

2.6. Global sensitivity analysis (GSA)

The Morris' method has been used to explore the global sensitivity of the analytical model to variation of the input parameters. In this analysis, z_0 was not constrained by field observations and was allowed to vary as well, as the objective of the GSA was to evaluate the general behaviour of the model, not limited to this specific case study. The same limits and PDFs included in Table 4.2 were used.

Subsequently, input parameter sets were randomly generated covering the whole range of input parameter space, according to the selected global method (Morris method). Then buried age at 0.05, 0.20, 0.35 and 0.50 m was calculated for each input parameter set, and local effects (one factor at a time, OAT) were calculated with equation 16, that quantifies the local response of output (Y, particle age, A, in this case) to a particular input factor x_i at a selected point x^0 in the hyperspace of the input factors (with the total number of input factors = I).

$$S_{i\,(x^0)} = \left\{\frac{\partial Y}{\partial x_i}\right\}_{x^0} = \frac{Y\left(x_1^0,\ldots,x_i^0+\partial x_i,\ldots,x_I^0\right) - Y\left(x^0\right)}{\partial x_i} \tag{4.16}$$

Finally, the mean of absolute values of local effects, μ^*_i, and standard deviation, σ_i, is determined for each parameter *i*. A high μ^*_i indicates a significant overall effect of the parameter *i* on model output and a large standard deviation indicates that the effect depends very much on the input values or that its effect is nonlinear (Morris, 1991). Sensitivity analysis was implemented using SimLab 2 (Saltelli et al., 2004).

Table 4.2. Range of input parameters and probability distribution function (PDF) used to perform the Global Sensitivity Analysis. To calibrate the model and to perform Uncertainty Analysis, mobile regolith depth (z_0) was fixed to its observed value. Positive T values indicate erosion and negative values deposition rate (W). Note that z_0 was fixed at the observed regolith depth during the uncertainty analysis. Z_b is the e-folding or shape parameter, D_0 is the surface diffusivity constant.

Parameter	Interval	PDF	Literature value	Reference
z_0, m	0.1 - 2	Uniform		
z_b, m	0.1 - 2	Uniform	0.28	Johnson et al., 2014
D_0, m^2 ka^{-1}	0.01 - 0.4	Uniform	$1.8\text{-}2.1 \times 10^{-2}$	Johnson et al., 2014
T-W, m ka^{-1}	-0.01 - 0.01	Uniform	0.005-0.0068	Johnson et al., 2014

3. Results

3.1. Sensitivity analysis and variable importance

As a result of the global sensitivity analysis, the mean and standard deviation of the local effects of each factor on the age- depth results, were calculated with Morris' method and are shown in Figure 4.3. Results of the sensitivity analysis are given in terms of the ranking of the input parameters as a function of their effect on the modeled particle ages. The further away from the origin a factor in this diagram is, the greater its influence on the output. As shown in Figure 4.3, the most influential parameters at all depths are the diffusion coefficient at the surface, D_0, and regolith depth, z_0. Therefore, it is important to make a good measure of z_0 in the field because the model is highly sensitive to this parameter. In all cases the erosion-deposition parameter, T-W (with T representing erosion and W, being equivalent to negative T values, representing deposition), was not very influential. The e-folding length scale, z_b, becomes more important with increasing depth.

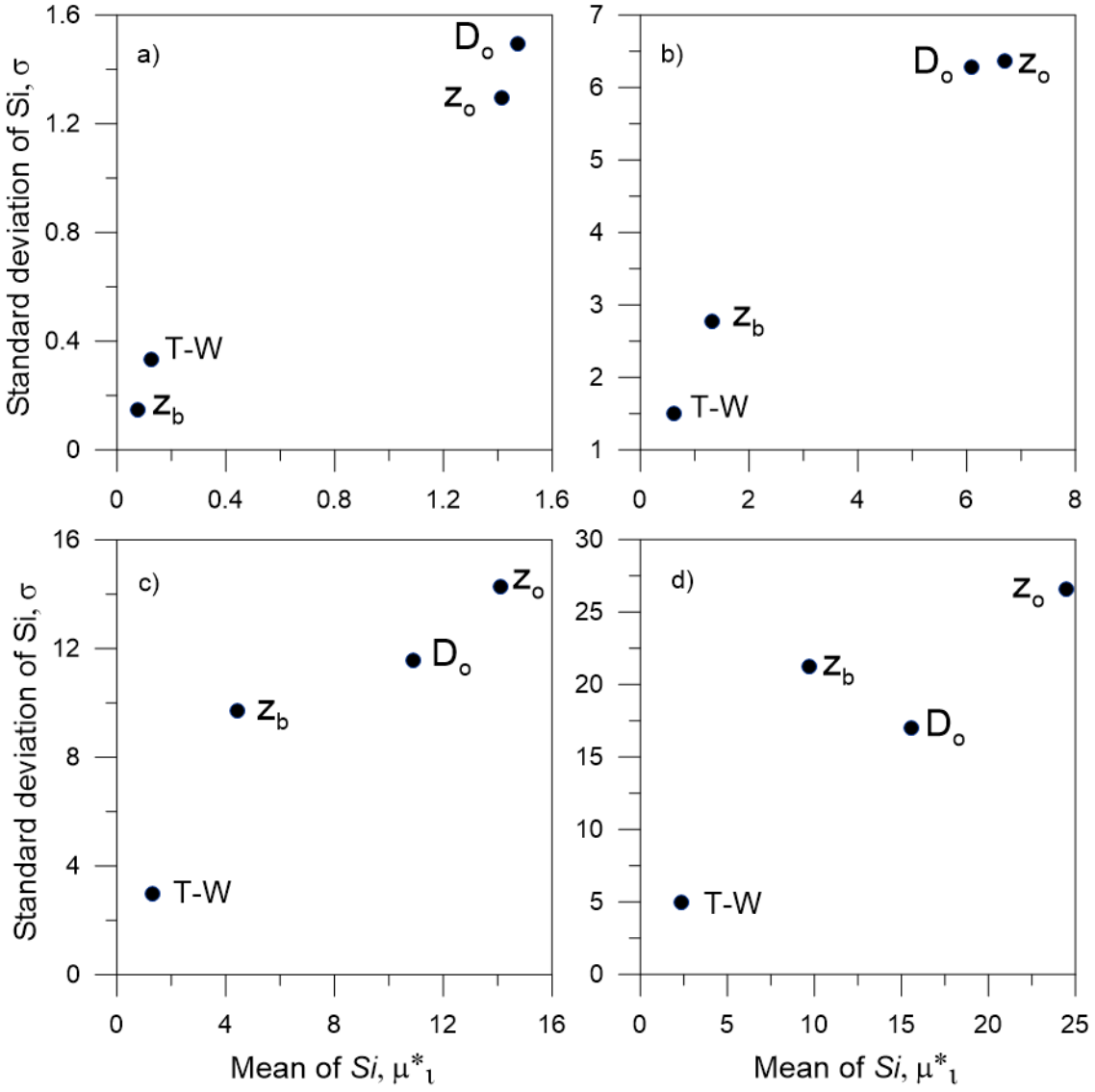

Figure 4.3 Global sensitivity analysis results at four different depths: a) 0.05 m; b) 0.20 m; c) 0.35 m; d) 0.50 m, obtained using the Morris method. Range of input parameters is shown in Table 4.2.

3.2. Uncertainty analysis

Posterior PDF of the diffusion coefficient at the surface, D_0, e-folding length scale, z_b and erosion-deposition parameter, *T-W*, was determined for the four profiles (Figure4.4). As a measure of uncertainty, 5% and 95% quantiles of the posterior PDF are shown in Table 4.3. The shape of the posterior probability density function indicates the degree of uncertainty in the parameter estimation. A flat distribution indicates considerable uncertainty while a distribution with a sharp peak indicates better parameter identifiability.

As Figure 4.4 and Table 4.3 illustrate, the uncertainty is great for the z_b parameter, it can take any value of the interval with almost equal probability of finding a good agreement

with the experimental data. However, there is a maximum in likelihood for values of z_b ~0.1-0.2 m in SC-7, SC-8 and SC-10 profiles. There is much less uncertainty in the estimation of the diffusion coefficient at the surface, D_0, as observed in Figure 4.4. For the erosion-deposition term, T-W, the uncertainty is absolute for the profiles SC-9 and SC-7 (respectively the upper hillslope and hill-base profile), as it is impossible to distinguish between erosion and deposition. Both negative and positive values are equally likely. This is highly unlikely to correspond to reality for the hill-base profile SC-7, that –due to its geomorphological position at the bottom of the catena- is likely to be depositional. The erosion-deposition uncertainty is lower for the hilltop profile SC-10 and lower hillslope profile SC-8, in which only positive values of T, i.e. with erosion, are likely. Nevertheless, the range of variation is important and spans approximately an order of magnitude.

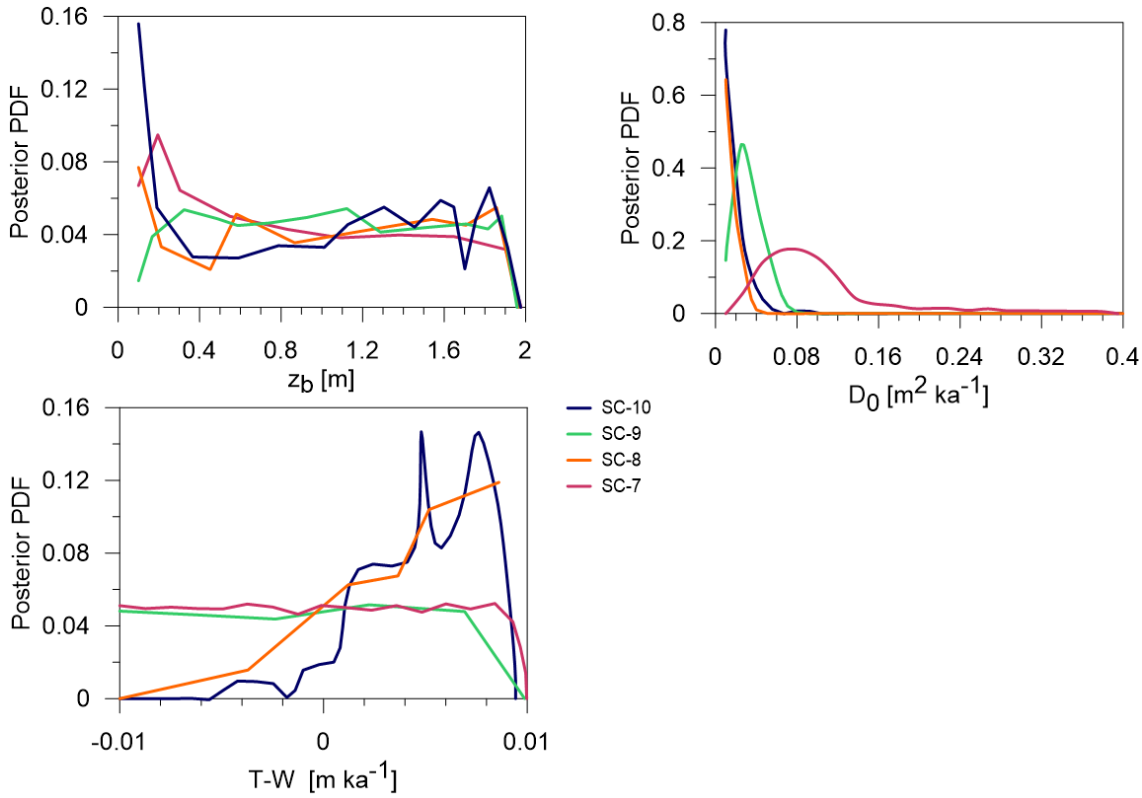

Figure 4.4 Posterior probability density functions of the diffusion-advection model parameters (D0=surface diffusivity; T=erosion rate, with negative values expressing deposition (W); zb= e-folding depth) for all four profiles. Mobile regolith depth z0 is fixed in these simulations. Table 4.3. Main results of the Uncertainty Analysis of the advection-diffusion equation (6). n is the number of parameter sets that yield a NSE between 0-1. Mobile regolith depth, z_0, is fixed based on field observations. For each profile and estimated parameter the values in the simulated set with highest NSE, opt, and the 5% and 95% quantile of the posterior probability density functions are given. Positive T-values indicate erosion and negative values deposition (W)

Table 4.3 Main results of the Uncertainty Analysis of the advection-diffusion equation (6). n is the number of parameter sets that yield a NSE between 0-1. Mobile regolith depth, z0, is fixed based on field observations. For each profile and estimated parameter the values in the simulated set with highest NSE, opt, and the 5% and 95% quantile of the posterior probability density functions are given. Positive T-values indicate erosion and negative values deposition (W)

Profile		**SC-10**	**SC-9**	**SC-8**	**SC-7**
$\mathbf{n_{NSE>0.0}}$		218	959	286	4029
$\mathbf{z_0}$ **[m]**		0.51	0.57	0.47	0.97
$\mathbf{z_b}$ **[m]**	opt	1.05	1.7	0.824	1.931
	5%quantile	0.13	0.33	0.16	0.18
	95% quantile	1.91	1.93	1.91	1.88
$\mathbf{D_0}$ **[m^{2}ka^{-1}]**	opt	0.012	0.024	0.014	0.084
	5% quantile	0.012	0.022	0.011	0.044
	95% quantile	0.036	0.061	0.032	0.245
T-W [m ka^{-1}]	opt	0.004	-0.008	0.008	0.008
	5% quantile	0.001	-0.009	0.001	-0.009
	95% quantile	0.01	0.009	0.01	0.009
NSE	opt	0.976	0.805	0.959	0.975

3.3. Modelling bioturbation, erosion and deposition

For each profile, experimental luminescence burial age data and the best-fit simulation are plotted in Figure 4.5. Table 4.3 contains the fitted parameters values and NSE. The advection-diffusion model adequately predicts the age-depth distribution in the four soil profiles, with high model efficiencies, between 0.805 and 0.976. These results illustrate that our physical model captures the main processes, i.e. bioturbation and erosion-deposition, acting on these hillslopes and controlling the observed age-depth patterns. As written above, the depth of the mobile regolith, z_o, was fixed based on field observations, while optimizing the parameter space (D_o, z_b, T or W). The depth of the mobile regolith is indicated in grey in Figure4. 5. It should be noted that in the profiles SC-9 and SC-8, located on the upper and lower hillslope respectively, the actual border based on the luminescence dating analysis is in somewhere inside a transition zone, below the last sample with NSF>0 and above the following sample with NSF=0, that is to say, more proximal to the surface than in the data of Figure 4.5. For SC-9 the boundary would be somewhere between 35 and 55 cm and in SC-8 between 20 and 35 cm. The last sample analyzed was at 55 and 35 cm depth respectively, but these points are not plotted as in those samples, the mineral grains are above the saturation threshold with a proportion of 100% in both profiles, meaning they

have neither reached the surface and nor participated in the soil mixing process. The use of luminescence techniques for mapping the mobile regolith-saprolite border is discussed in further detail in Román-Sánchez et al. (submitted). The values obtained for the diffusivity coefficient at the surface, D_0, do not show a clear tendency along the catena and optimal values vary between the lowest value, 12 $mm^2\ a^{-1}$, at the hilltop profile, SC-10, and the highest value, 84 $mm^2\ a^{-1}$, at the hill-base profile, SC-7. The optimal values of the e-folding parameter z_b are of the same order of magnitude along the hillslope, varying between 0.824 and 1.931 m. Finally, in terms of erosion-deposition rates, the model fits indicate that the profiles SC-10 (hilltop), SC-8 (lower hillslope) and SC-7 (hill-base) are characterized by erosion , *T*, while the upper hillslope profile, SC-9, is characterized by deposition, *W*, (Table 4.3). However, as it was already noted, the uncertainty regarding the T-W parameter is too large in this case study to give a reliable estimate. For profiles SC-9 and SC-7, the 5% and 95% quantile values even range from negative to positive values, meaning the model cannot discern whether or not the profile in question is characterized by erosive or depositional conditions. For the other two profiles, erosion values range by one order of magnitude within the 5 and 95% quantile range.

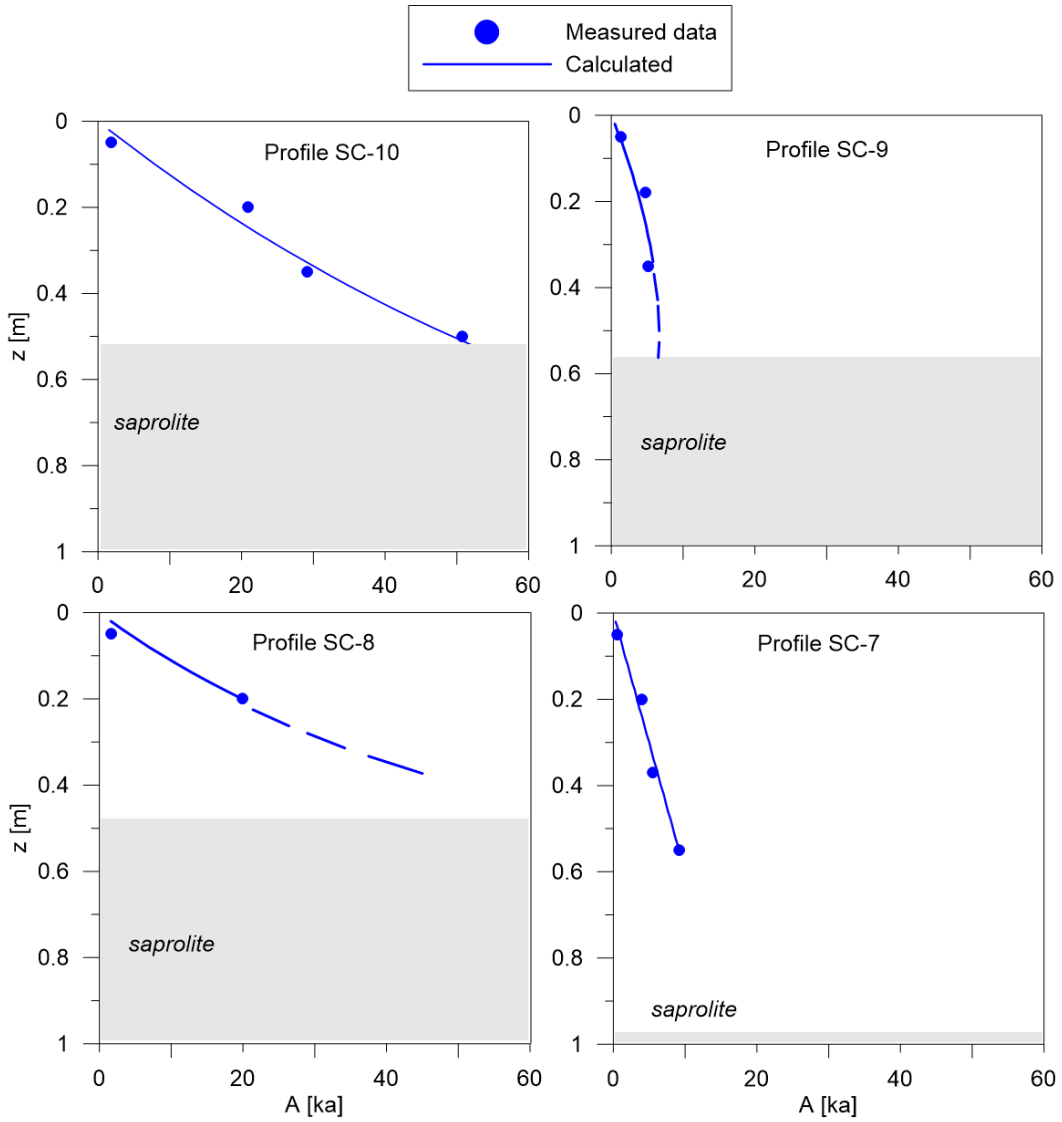

Figure 4.5 Measured age-depth distribution for the four sampled profiles, from the hill-base (SC-7) to the hilltop (SC-10). The best-fit simulation using the analytical solution of the advection-diffusion equation with fixed mobile regolith depth z0 is also shown. Observed saprolite depth is shown in grey. Dashed line in profiles SC-8 and SC-9 (upper and lower hillslope) indicates the simulation of the analytical solution of the advection-diffusion equation until the sample collected close to mobile regolith boundary observed in the field (35 cm in SC-8 and 55 cm in SC-9). The luminescence method demonstrated that the latter samples are feldspar grains saturated (grains that have not been exposed to the surface) and they do not emit accepted luminescence and cannot be used to the model. This suggests that in these profiles the mobile regolith is more shallow and the border is within a transition zone located below the last sample with NSF>0 and above the following sample with NSF=0. For SC-9 the boundary would be somewhere between 35 and 55 cm and in SC-8 between 20 and 35 cm.

3.4. Diffusivity constant and effective soil reworking

The diffusion-advection model used in this study offers a more accurate representation of actual soil reworking processes compared to linear soil reworking rates (*SR*), calculated

by dividing depth by particle age, as reported by earlier luminescence studies (Heimsath et al., 2002; Stockmann et al., 2013). As mentioned in Román-Sánchez et al. (submitted), here we corrected these soil reworking rates by NSF to obtain effective soil reworking rates (SR_{eff}). Figure 4.6a shows how these linear effective soil reworking rates compare to the diffusion coefficient, obtained from fitting the advection-diffusion model to the age-depth data. Observations are shown by symbols and grouped by soil profile. It can be seen how within each individual profile the correspondence between D and SR_{eff} is only moderate. A linear regression through the origin, shown by lines, allows establishing the slope of the relation SReff – D listed in Table 4.4.

Table 4.4 Summary statistics (Slope (a) and R2) of the linear relation between diffusion constants and soil reworking, shown in figure 4. 6a

Profile	a	R^2	$a=0.5L^{-1}$
	$[mm^{-1}]$	equation $S_{Reff}=a\ D$ (through the origin)	$[mm^{-1}]$
SC-7	0.00067	0.92	0.00067
SC-8	0.0013	0.6337	0.0013
SC-9	0.00082	0.6766	0.00082
SC-10	0.00096	0.1755	0.00096

Using a simple model to calculate the vertical grain displacement velocities, as described by Kaste et al. (2007), the obtained diffusion coefficient D can be used to simulate soil depths and calculate average turnover times. Kaste et al. (2007) proposed to use the diffusion coefficient to calculate the mixing time constants (t) for a soil depth, L, ($t=L^2D^{-1}$). Assuming that a grain travels 0.5L during the mixing time (t), the vertical velocity of the mixing process can be calculated as $SR=0.5L^{-1}D$. This relation can then be used to predict soil depth from the observed slope of the regression line in Figure 4.6a, as shown in Figure 4.6b. This figure shows that, only based on considerations of biological soil mixing, the predicted soil depths are reasonably close to the observed values. This is especially true for the upper three profiles SC-8, SC-9 and SC-10. Only the hill-base profile SC-7 is considerably deeper than simulated. This probably indicates the importance of its geomorphological position at the bottom of the hillslope, where sediment deposition is likely to occur. Furthermore, the SC-7 profile is characterized by the highest uncertainty and lowest R^2 values. This could explain the fact that it moves away from line 1: 1 (Figure 4.6b).

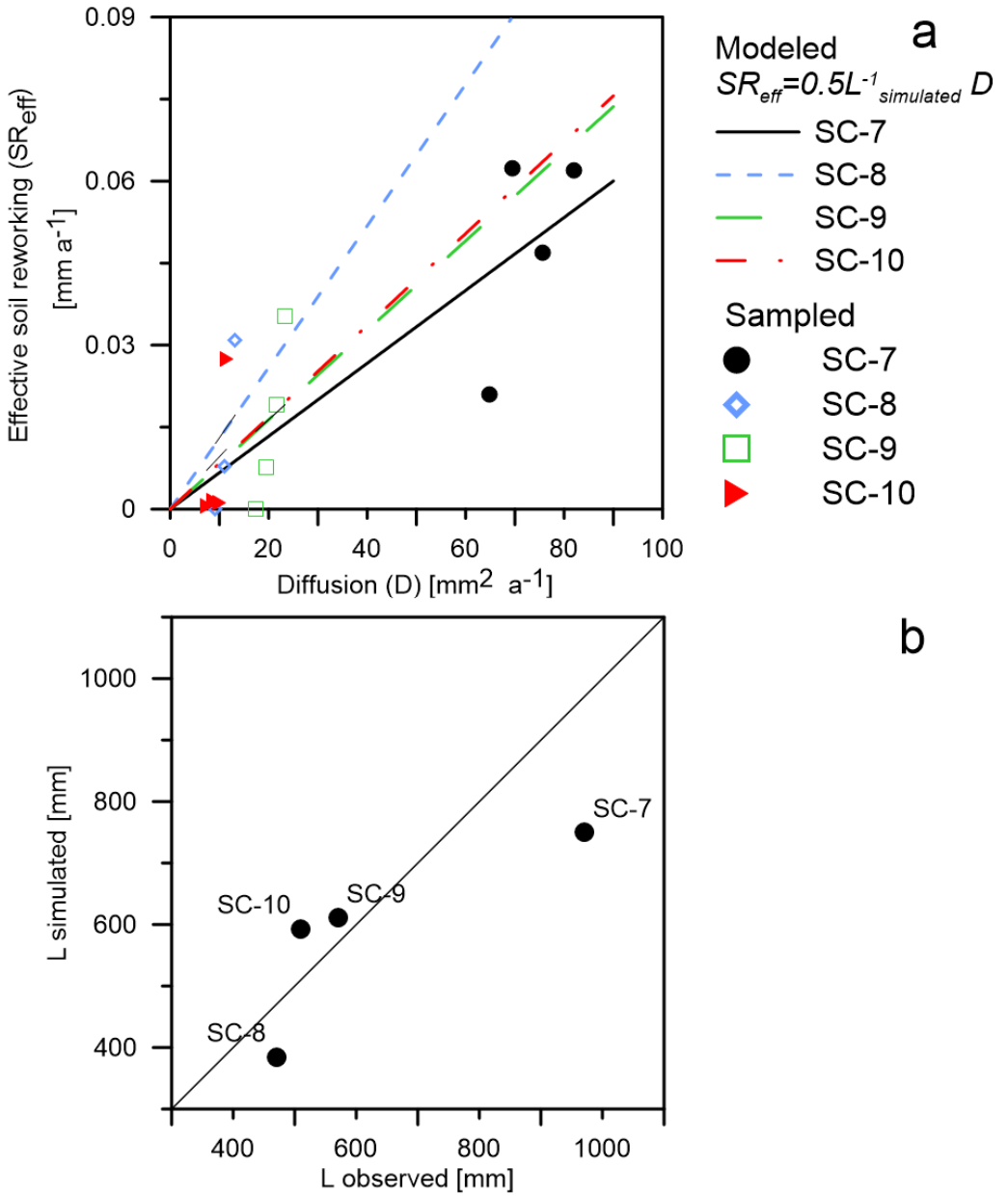

Figure 4.6 (a) Symbols indicate observations and fitted lines are model fits following Kaste et al. (2007). (b) Comparison of observed versus predicted soil depth, based on the bioturbation diffusivity coefficient, following Kaste et al. (2007).

4. Discussion

Combining the experimental luminescence data of Román-Sánchez et al. (2017 In review) with the analytical solution of the diffusion-advection equation (ec. 7, 10 and 13), presented in this study, allows simultaneous determination of bioturbation and erosion-deposition rates.

Although it is widely recognized that bioturbation is well described by diffusion processes, especially coupled to an advective term as is the case here, quantitate

measurements of this diffusion coefficient are rare. This coefficient has so-far been determined by fitting the diffusion-advection- equation to vertical distributions of natural radioactive tracers (see for example Kaste et al. (2007)), radioisotopes or introduced particles. This study, using luminescence allows determining these processes over much longer time scales. Also, to our knowledge, this study is the first to directly establish soil diffusivity coefficients and erosion-deposition rates using an analytical model from particle burial ages only. The only other similar study by Johnson et al. (2014) uses a combination of luminescence and cosmogenic nuclides, and a numerical solution of the advection-diffusion equation. The results obtained in this study show that bioturbation intensity does not is homogeneous along the hillslope, the surface diffusivity coefficient D_o varies between 12 and 24 $mm^2\ a^{-1}$ in the profiles SC-8, SC-9, SC-10 and considerably higher D_o value of 84 $mm^2\ a^{-1}$ in the hill-base profile SC-7. Figure 4.7 compares to other studies. As shown in this figure, our results confirm a positive trend diffusion coefficients and erosion. In absolute values, in our environment with Mediterranean sclerophyll forests the optimum values for the surface diffusivity coefficient D_o of between 12 and 24 $mm^2\ a^{-1}$ in profiles SC-8, SC-9, SC-10 are in the same range as those found by Kaste et al. (2007) for coniferous forest in the New England Mnts. In the hill-base profile SC-7 the D_o optimum value is significantly higher, 84 $mm^2\ a^{-1}$. Its value is comparable with the study of Johnson et al. (2014) for open savanna woodland in Hughenden Region (Queensland, Australia) who report a value of 98.1 $mm^2\ a^{-1}$ and with the study of Kaste et al. (2007) for sclerophyll forest in Bega Valley, Australia (Figure 4.7). Although in our study area there is not presence of great bioturbators as wombats, tree throws, great earthworm densities like occur in the latter study areas of Australia, the diffusivity coefficient D_o of SC-7 in our study area is in the same range to its geomorphological position at the bottom of the hillslope. This leads to a deeper and more humid profile, with higher organism activity and deeper root penetration. Although there is considerable uncertainty regarding the erosion-deposition rates, optimum values range between -0.008 and 0.008 mm a^{-1}. These values are in the same range as the results by Kaste et al. (2007) for coniferous forest, New England Mtn., measured with sediment traps and those of Johnson et al. (2014) measured with cosmogenic nuclides in open savanna woodland in Queensland, Australia.

Other studies report soil production rates between 0.001-0.246 mm a^{-1} (Stockmann et al., 2014) and physical denudation between 0.014-0.645 mm a^{-1} (Riebe et al., 2004). Total denudation, equal to soil production rate under the assumption of steady state, integrates the combined effect of physical erosion and chemical weathering (Riebe et al., 2003;

Larsen et al., 2014), so the values reported by Stockmann et al. (2014) should be considered as an upper limit. From a global compilation, Montgomery (2007) reported a range of soil erosion rates of 0.0002-0.5 mm a^{-1} for native vegetation. Wilkinson and McElroy (2007) report an average erosion rate in the continental US of 0.021 mm a^{-1}. In the light of these results, our erosion-deposition rates are low, but given that they are located in a forest area with tree cover, they are within the range described by Montgomery (2007).

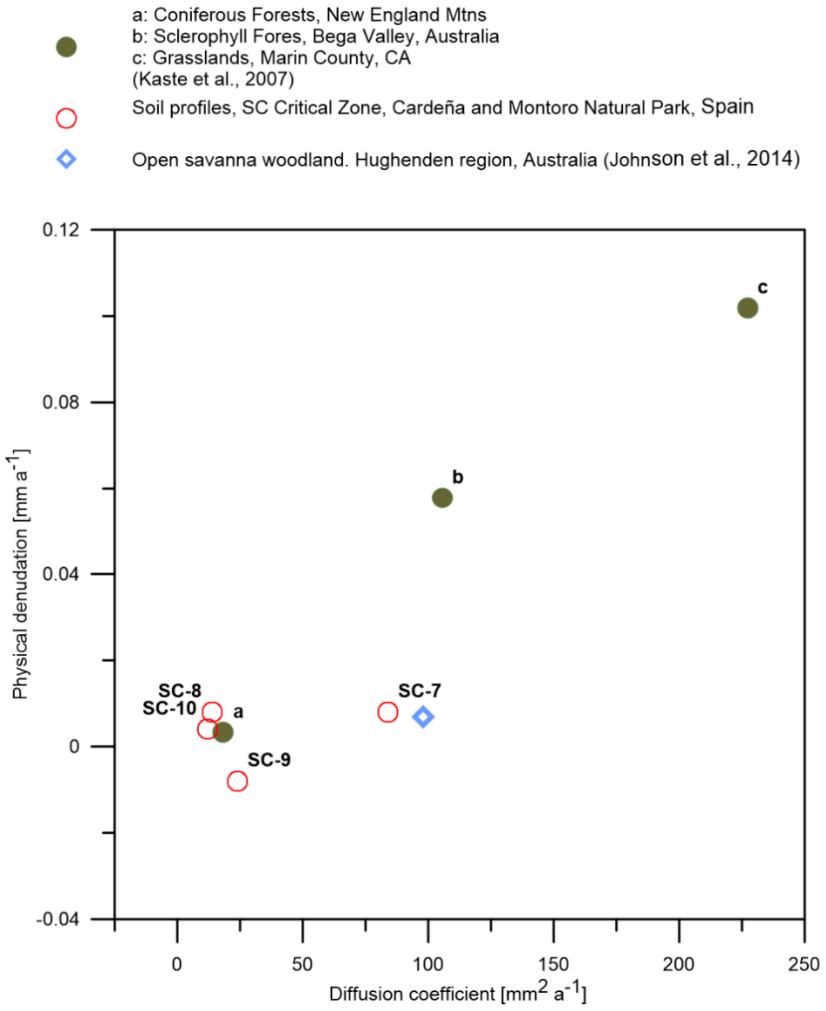

Figure 4.7 Landscape physical denudation rates versus soil mixing rates, compiled from different studies. (Values of physical denudation for literature studies are measured by cosmogenic nuclides. Values for soil mixing in Kaste et al. (2007) are short-term, Johnson et al. (2014) and this study are long-term).

These low erosion rates are the first reason why at our study site, there exists a high uncertainty regarding the determination of erosion-deposition rates. A new study in a more actively incising or eroding area should be able out to single out the erosion effect and age-depth distributions. A second reason, which should be taken into account in future studies, is that the number of samples that was analyzed in each profile was limited to four different

depths. In profiles SC-8 and SC-9, the actual number of samples returning a useable luminescence signal was even lower (respectively two and three). Increasing the sampling intensity to at least five or six samples per profile would allow to fit the analytical solution of the advection-diffusion model with a lower degree of uncertainty.

The relation between our results of linear soil reworking rates and diffusivity obtained from the analytical diffusion-advection solution in each soil profile is moderate, as shown in Figure 4.6a. This high dispersion in this linear fit is clearly related to depth. Although the depth of each sample is not shown in this graph, within each profile, the shallow samples are characterized by the highest SR_{eff}-D values, and plot above the regression line. The points that plot below the regression line are deeper samples with the lowest SR_{eff}-D values. This suggests that the actual grain travel distances for shallow grains are larger and lower for deeper samples. The assumption by Kaste et al. (2007) that t=0.5L is clearly not constant and should be adapted in function of depth. These results corroborate the exponential decline of diffusivity with depth, proposed by different studies (Canti, 2003; Humphreys and Field, 1998; Cousins et al., 1999; Vanwalleghem et al., 2013; Johnson et al., 2014), as discussed in the material and methods section, and as adopted in equation 4. On the other hand, this simple assumption, averaging out travel distance, allowed us to compare our observed soil depths to simulated soil depths (Figure 4.6b). In general terms, this simple model performs well, except for the case of the hill-base profile SC-7. The high deviation for this profile shows how considerations based only on bioturbation underestimate the actual soil profile depth. This suggests that deposition is important here, as can be expected from its geomorphic position.

5. Conclusions

The new analytical model proposed in this study using the advection-diffusion equation allows in theory simultaneous estimation of bioturbation and erosion-deposition rates. With this analytical solution, we have obtained a good fit of the measured age-depth data in four profiles along a hillslope under Mediterranean forest. Our data allows a good estimation of diffusivity but shows that the uncertainty in the estimated erosion-deposition rates is too high to make a reliable estimate.

The diffusivity coefficients at the surface are similar between the hilltop and the two hillslope profiles, between 11.4 and 23.3 $mm^2\ a^{-1}$ and higher for the hill-bottom profile, 81.9 $mm^2\ a^{-1}$, although the uncertainty in the estimation of this value has been much greater

than the previous ones. An exponential decline of diffusivity constants with depth fits the data well.

Using GLUE methodology, there is great uncertainty in estimating the parameters *T-W* and z_b. The uncertainty range estimating D_0 is much narrower. For future work, this uncertainty can be reduced by taking a higher number of sampling points within each profile. In this work we sampled up to four soil depths, and for some profiles did not obtain a luminescence signal for the deepest samples. Analyzing at least 5 to 6 soil depths per profile should overcome this.

The Global sensitivity analysis, using Morris' method, of the full advection-diffusion model of the combined effect of bioturbation and soil erosion-deposition, showed that the vertical particle age distributions are very sensitive to surface diffusivity and mobile regolith depth (D_0 and z_0) and almost insensitive to the erosion-deposition (*T-W*) parameter. The e-folding length, z_b, becomes more important with depth in the profile. In this way, it can be concluded that D_0 and z_0 parameters control the shape of the age-depth relation. The low sensitivity of the model to the erosion-deposition parameter *T-W* indicates that the diffusion process dominates over advection.

Given its importance, prior knowledge of the mobile regolith depth is key. This value is generally derived from field work as it is easily detectable, however, the luminescence dating allows objective and accurate determination of the depth of the mobile regolith boundary and should be used as reference technique for this purpose.

Finally, the diffusivity coefficients are linearly related to the effective soil reworking rate SR_{eff} (that takes into account the grains that participate in the soil mixing process), a linear measure of soil reworking. Although the correlation is only moderate, and appears to vary with depth, this relation can be used to estimate mobile regolith depth successfully.

Appendix

i) Diffusion

In steady state conditions, $\frac{\partial A}{\partial t} = 0$, and the equation 1 allows to deduce a relation between the degree of alteration, *A*, and depth, *z*.

$$d\left(D\frac{dA}{dz}\right) = 0 \Longrightarrow \qquad dA = \frac{C_1\, dz}{D} \tag{4.17}$$

The integration constant, C_1, is evaluated in boundary conditions with a null value at the surface, $A=0$ if $z=0$, and null gradient $\left(\frac{dA}{dz}\right) = 0$, at the bottom of the profile, $z=z_{bp}$. The solution with exponential diffusion coefficient (equation 2) is the equation 18.

$$A = \frac{C_1 z_b}{D_o}\left(e^{\frac{z}{z_b}} - 1\right) \tag{4.18}$$

If it is considered the aging of the particles (equation 3), the relationship between degree of alteration, *A*, and depth, *z* is the equation 19

$$d\left(D\frac{dA}{dz}\right) = -dz \Longrightarrow \qquad D\frac{dA}{dz} = z_{bp} - z \tag{4.19}$$

The solution with exponential diffusion coefficient is the equation 5.

ii) Erosion

Starting with the complete equation 4, the integration is

$$d\left(D\frac{dA}{dz}\right) - TdA = -dz \tag{4.20}$$

The boundary conditions are, with the parameters, D_o and z_o

$$\left(D\frac{dA}{dz}\right)_o = D_o\left(\frac{dA}{dz}\right)_o = z_o \quad ; A=0 \text{ and } z=0 \tag{4.21}$$

In the case that there is no erosion, $T = 0$, the equality $z_o = z_{bp}$ is met, by equation 17.

Then the ordinary linear equation (20) that can be easily integrated

$$\left(\frac{dA}{dz} - \frac{T}{D_o}e^{\frac{z}{z_b}}A\right) = -\frac{z-z_o}{D_o}\, e^{\frac{z}{z_b}} \tag{4.22}$$

The equation homogeneous of the equation 22 is

$$\frac{dA_h}{dz} = \frac{T}{D_o} e^{\frac{z}{z_b}} A_h \tag{4.23}$$

and the solution is

$$A_h = \exp\left(\frac{Tz_b}{D_o} e^{\frac{z}{z_b}}\right) \tag{4.24}$$

The complete solution, A, is composed of homogeneous solution, *Ah*, and particular solution, *Ap*, $A = A_h A_p$.

Substituting *A* value in the complete equation 22, the equation 25 is obtained

$$\frac{dA_p}{dz} = -\frac{z - z_o}{A_h D_o} e^{\frac{z}{z_b}} \tag{4.25}$$

and the particular solution is from the integral

$$A_p = -\int \frac{z - z_o}{D_o} \frac{e^{\frac{z}{z_b}}}{\exp\left[(Tz_b \;\; D_o^{-1}) e^{\frac{z}{z_b}}\right]} dz =$$

$$-\int \frac{z - z_o}{D_o \;\exp\left(\alpha e^{\frac{z}{z_b}}\right)} dz \tag{4.26}$$

where $\alpha = \frac{Tz_b}{D_o}$ (4. 27)

The equation 26 can be decomposed by the sum of the numerator in two parts,

$$A_p = \frac{z_b z_o}{D_o} \int \frac{e^{\frac{z}{z_b}} dz/z_b}{\exp\left(\alpha\, e^{\frac{z}{z_b}}\right)} - \frac{z_b^2}{D_o} \int \frac{\left(\frac{z}{z_b}\right) e^{\frac{z}{z_b}} dz/z_b}{\exp\left(\alpha e^{\frac{z}{z_b}}\right)} = A_{p1} + A_{p2} = \frac{z_b z_o}{D_o} I_1 -$$

$$\frac{z_b^2}{D_o} I_2 \tag{4.28}$$

Solving the first integral of equation 28, I_1

$$I_1 = \int \frac{e^y dy}{\exp(\alpha\, e^y)} = \int e^{-\alpha u} du = -\frac{1}{\alpha} e^{-\alpha u} = -\frac{1}{\alpha} \exp\left(-\alpha e^{\frac{z}{z_b}}\right) \tag{4.29}$$

And the second integral, I_2 with the successive changes of variables $u = e^y, dy = \frac{du}{u}, and\ v = \alpha u$

$$\boldsymbol{I_2 = \int y\, e^{y} \exp(-\alpha e^{y})\, dy = \int \ln(u)\, e^{-\alpha u} du = -\frac{e^{-\alpha u}\ln(u)}{\alpha} + \frac{1}{\alpha}\int \frac{e^{v}}{v}\, dv} \quad (4.30)$$

The last integral in equation 30 is the exponential integral

$$\boldsymbol{E_1 = \int_z^{\infty} \frac{e^{-\xi}}{\xi}\, d\xi \qquad |\arg z| < \pi} \quad (4.31)$$

So the solution of the second integral is

$$\boldsymbol{I_2 = -\frac{y}{\alpha}\, exp(-\alpha e^{y}) + \frac{1}{\alpha}\, E_1(\alpha e^{y})} \quad (4.32)$$

The particular solution is

$$\boldsymbol{A_p = \frac{z - z_o}{T}\, exp\left(-\alpha e^{\frac{z}{z_b}}\right) + \frac{z_b}{T}\, E_1\left((T z_b \;\; D_o^{-1}) e^{\frac{z}{z_b}}\right)} \quad (4.33)$$

The complete solution is

$$\boldsymbol{A = A_p\, A_h + c_1\, A_h = \frac{z - z_o}{T} + \frac{z_b}{T} exp\left((T z_b \;\; D_o^{-1}) e^{\frac{z}{z_b}}\right) E_1\left((T z_b \;\; D_o^{-1}) e^{\frac{z}{z_b}}\right) + c_1\, exp\left((T z_b \;\; D_o^{-1}) e^{\frac{z}{z_b}}\right)} \quad (4.34)$$

The constant $\boldsymbol{c_1}$ is with the boundary conditions on the surface, $A=0$, and $z=0$.

$$\boldsymbol{c_1 = \frac{z_o}{T} \exp(-T z_b \;\; D_o^{-1}) - \frac{z_b}{T} E_1\,(T z_b \;\; D_o^{-1})} \quad (4.35)$$

Finally, the equation 34 is simplified and it is obtained the equation 10 that represents the erosion.

iii) Deposition

In the case of deposition, the equation 4 can be expressed with negative values of T, expressed as $W=-T$ according the equation 36

$$\boldsymbol{\frac{\partial A}{\partial t} = \frac{\partial}{\partial z}\left(D(z)\frac{\partial A}{\partial z}\right) + W\frac{\partial A}{\partial z} + 1} \quad (4.36)$$

In steady state, integrating the equation 36,

$$\boldsymbol{d\left(D\frac{dA}{dz}\right) + W dA = -dz} \quad (4.37)$$

The boundary conditions are the same that in the erosion case (equation 21)

$$\left(\boldsymbol{D}\frac{\boldsymbol{dA}}{\boldsymbol{dz}}\right)_{\boldsymbol{o}} = \boldsymbol{D_o}\left(\frac{\boldsymbol{dA}}{\boldsymbol{dz}}\right)_{\boldsymbol{o}} = \boldsymbol{z_o} \qquad ; A=0 \text{ and } z=0 \tag{4.38}$$

The differential equation is

$$\left(\frac{\boldsymbol{dA}}{\boldsymbol{dz}} + \frac{\boldsymbol{W}}{\boldsymbol{D_o}}\boldsymbol{e}^{\frac{\boldsymbol{z}}{\boldsymbol{z_b}}}\boldsymbol{A}\right) = -\frac{\boldsymbol{z-z_o}}{\boldsymbol{D_o}}\,\boldsymbol{e}^{\frac{\boldsymbol{z}}{\boldsymbol{z_b}}} \tag{4.39}$$

The solution of the homogeneous equation is

$$\boldsymbol{A_{sh}} = \mathbf{exp}\left(-\frac{\boldsymbol{Wz_b}}{\boldsymbol{D_o}}\boldsymbol{e}^{\frac{\boldsymbol{z}}{\boldsymbol{z_b}}}\right) \tag{4. 40}$$

The solution of the particular equation is with a new parameter $\boldsymbol{\beta} = \boldsymbol{W z_b}\ \boldsymbol{D_o^{-1}}$

$$\boldsymbol{A_{sp}} = -\int \frac{\boldsymbol{z-z_o}}{\boldsymbol{D_o}}\boldsymbol{e}^{\frac{\boldsymbol{z}}{\boldsymbol{z_b}}}\boldsymbol{exp}\left[(W z_b\ \ D_o^{-1})e^{\frac{z}{z_b}}\right]dz =$$

$$-\int \frac{(z-z_o)e^{\frac{z}{z_b}}\,exp\left(\beta e^{\frac{z}{z_b}}\right)}{D_o}dz \tag{4.41}$$

Preceding analogously that in the erosion case, the solution of the particular equation is

$$A_{sp} = \frac{z-z_o}{W}\exp\left(\beta e^{\frac{z}{z_b}}\right) + \frac{z_b}{W}E_i\left(\beta e^{\frac{z}{z_b}}\right) \tag{4.42}$$

In the equation 42 there is another form of the exponential integral

$$E_{i(x)} = -\int_{-x}^{\infty}\frac{e^{-t}}{t}\,dt = \int_{-\infty}^{x}\frac{e^{t}}{t}\,dt \qquad x<0 \tag{4.43}$$

The complete solution of the equation 36 is

$$A = \frac{z-z_o}{W} + \frac{z_b}{W}exp\left((-W z_b\ \ D_o^{-1})e^{\frac{z}{z_b}}\right)E_i\left((W z_b\ \ D_o^{-1})e^{\frac{z}{z_b}}\right) +$$

$$C_2\,exp\left((-W z_b\ \ D_o^{-1})e^{\frac{z}{z_b}}\right) \tag{4.44}$$

With the constant C_2

$$C_2 = -\frac{z_o}{W}\exp(W z_b\ \ D_o^{-1}) - \frac{z_b}{W}E_i\,(W z_b\ \ D_o^{-1}) \tag{4.45}$$

Acknowledgement

This work has been funded by projects AGL2012-40128-C03-02 and AGL2015-65036-C3-2-R (MINECO/FEDER, UE). Andrea Román-Sánchez is funded by a Contratos Predoctorales Fellowship with reference BES-2013-067009 and by research stay funding with reference EEBB-I-15-09373 (MINECO) in Wageningen University, Soil Geography and Landscape group & Netherlands Centre for Luminescence dating, Environmental Sciences. The authors would also like to thank Prof. Jesús Ayuso of the University of Cordoba for providing access to the experimental area and his continuous support.

References

Abramowitz, M., Stegun, I. 1964. Handbook of Mathematical Functions Dover New York

Anderson, R.S., Anderson, S.P., Tucker, G.E. 2013. Rock damage and regolith transport by frost: an example of climate modulation of the geomorphology of the critical zone: Rock damage and regolith transport by frost. Earth Surface Processes and Landforms38: 299–316. DOI:10.1002/esp.3330

Anderson, R.S. 2015. Particle trajectories on hillslopes: Implications for particle age and 10Be structure. Journal of Geophysical Research: Earth Surface. 120: 1626-1644. DOI:10.1002/2015JF003479

Beven, K., Binley, A. 1992. The future of distributed models: Model calibration and uncertainty prediction. Hydrological Processes 6: 279–298. DOI:10.1002/hyp.3360060305

Boas, M.L. 1983.Mathematical methods in the physical sciences. 2nd ed. Wiley. New York.

Canti, M.G. 2003. Earthworm Activity and Archaeological Stratigraphy: A Review of Products and Processes. Journal of Archaeological Science 30: 135–148. DOI:10.1006/jasc.2001.0770

Cousins, I.T., Gevao, B., Jones, K.C. 1999. Measuring and modelling the vertical distribution of semi-volatile organic compounds in soils. I: PCB and PAH soil core data. Chemosphere 39: 2507–2518. DOI:10.1016/S0045-6535(99)00164-2

Darwin, C. 1881. The formation of vegetable mould through the action of worms : with observations on their habits. London: John Murray.

Duller, G.A.T. 2008. Single-grain optical dating of Quaternary sediments: why aliquot size matters in luminescence dating. Boreas 37: 589-612. DOI: 10.1111/j.1502-3885.2008.00051.x

Gabet, E.J., Reichman, O.J., Seabloom, E.W., 2003. The Effects of Bioturbation on Soil Processes and Sediment Transport Annual Review of Earth and Planetary Sciences 31: 249–273. DOI:10.1146/annurev.earth.31.100901.141314

Gabet, E.J., Mudd, S.M. 2010. Bedrock erosion by root fracture and tree throw: A coupled biogeomorphic model to explore the humped soil production function and the persistence of hillslope soils. J. Geophys. Res. Earth Surf. 115: 1–14. DOI:10.1029/2009JF001526

Geological and Mining Institute of Spain. 2013

Heimsath, A.M., E. Dietrich, W., Nishiizumi, K., Finkel, R.C. 1999. Cosmogenic nuclides, topography, and the spatial variation of soil depth. Geomorphology 27: 151–172. DOI:10.1016/S0169-555X(98)00095-6

Heimsath, A.M., Chappell, J., Spooner, N.A., Questiaux, D.G. 2002. Creeping soil. Geology 30: 111–114. DOI: 10.1130/0091-7613(2002)030<0111:CS>2.0.CO

Humphreys, GS, Field, R. 1998. Mixing, mounding and other aspects of bioturbation: implications for pedogenesis. In Proceedings, 16th World Congress of Soil Science, International Society of Soil Science, Montpellier, Registered paper no. 18.

IUSS Working Group, 2014. World Reference Base for Soil Resources 2014. International soil classification system for naming soils and creating legends for soil maps (3rd ed.), FAO, Rome

Johnson, D.L. 1989. Subsurface stone lines, stone zones, artifact-manuport layers, and biomantles produced by bioturbation via pocket gophers (Thomomys Bottae). American Antiquity 54: 370–389. DOI:10.2307/281712

Johnson, M.O., Mudd, S.M., Pillans, B., Spooner, N.A., Keith Fifield, L., Kirkby, M.J., Gloor, M. 2014. Quantifying the rate and depth dependence of bioturbation based on optically-stimulated luminescence (OSL) dates and meteoric ^{10}Be: Quantifying the rate and depth dependence of

bioturbation. Earth Surface Processes and Landforms 39: 1188–1196. DOI:10.1002/esp.3520

Kaste, J.M., Heimsath, A.M., Bostick, B.C. 2007. Short-term soil mixing quantified with fallout radionuclides. Geology 35: 243–246. DOI:10.1130/G23355A.1

Kirkby, M.J. 1985. A basis for soil profile modelling in a geomorphic context. European Journal of Soil Science 36: 97–121. DOI:10.1111/j.1365-2389.1985.tb00316.x

Kisekka, I., Migliaccio, K.W., Muñoz-Carpena, R., Khare, Y., Boyer, T.H. 2013. Sensitivity analysis and parameter estimation for an approximate analytical model of canal-aquifer interaction applied in the C-111 basin. Transactions of the ASABE 56: 977-992. DOI: 10.13031/trans.56.10037

Larsen, I.J., Almond, P.C., Eger, A., Stone, J.O., Montgomery, D.R., Malcolm, B. 2014. Rapid Soil Production and Weathering in the Southern Alps, New Zealand. Science 343: 637–640. DOI:10.1126/science.1244908

Lecroart, P., Maire, O., Schmidt, S., Grémare, A., Anschutz, P., Meysman, F.J.R. 2010. Bioturbation, short-lived radioisotopes, and the tracer-dependence of biodiffusion coefficients. Geochimica et Cosmochimica Acta 74: 6049–6063. DOI:10.1016/j.gca.2010.06.010

Lin, H., 2010. Earth's Critical Zone and hydropedology: concepts, characteristics, and advances. Hydrology and Earth System Sciences 14: 25–45. DOI:10.5194/hess-14-25-2010

Maher, K. 2010. The dependence of chemical weathering rates on fluid residence time. Earth and Planetary Science Letters 294: 101–110. DOI:10.1016/j.epsl.2010.03.010

Meysman, F.J.R., Middelburg, J.J., Heip, C.H.R. 2006. Bioturbation: a fresh look at Darwin's last idea. Trends in Ecology & Evolution 21: 688–695. DOI:10.1016/j.tree.2006.08.002

Montgomery, D.R., 2007. Soil erosion and agricultural sustainability. Proceedings of the National Academy of Sciences of the United States of America104: 13268–13272. DOI:10.1073/pnas.0611508104

Morris, M.D. 1991. Factorial Sampling Plans for Preliminary Computational Experiments. Technometrics 33: 161–174. DOI:10.2307/1269043

Peel, M.C., Finlayson, B.L., McMahon, T.A. 2007. Updated world map of the Köppen-Geiger climate classification. Hydrology and Earth System Sciences 11: 1633–1644. DOI:10.5194/hess-11-1633-2007

Ratto, M., and A. Saltelli. 2001. Model assessment in integrated procedures for environmental impact evaluation: Software prototypes. IMPACT Project (SCA,DG-IST,1999-11313), Deliverable 18. Brussels, Belgium: Joint Research Center of the European Commission

Reimann, T., Román-Sánchez, A., Vanwalleghem, T., Wallinga, J. 2017. Getting a grip on soil reworking – Single-grain feldspar luminescence as a novel tool to quantify soil reworking rates. Quaternary Geochronology. 42: 1–14. DOI:10.1016/j.quageo.2017.07.002

Rhodes, E.J., 2011. Optically stimulated luminescence dating of sediments over the past 200,000 years. Annual Review of Earth and Planetary Sciences 39: 461-488. DOI: 10.1146/annurev-earth-040610-133425

Riebe, C.S., Kirchner, J.W., Finkel, R.C. 2003. Long-term rates of chemical weathering and physical erosion from cosmogenic nuclides and geochemical mass balance. Geochimica et Cosmochimica Acta 67: 4411–4427. DOI:10.1016/S0016-7037(03)00382-X

Riebe, C.S., Kirchner, J.W., Finkel, R.C. 2004. Erosional and climatic effects on long-term chemical weathering rates in granitic landscapes spanning diverse climate regimes. Earth and Planetary Science Letters 224: 547–562. DOI:10.1016/j.epsl.2004.05.019

Roering, J.J., Marshall, J., Booth, A.M., Mort, M., Jin, Q. 2010. Evidence for biotic controls on topography and soil production. Earth and Planetary Science Letters 298: 183–190. DOI:10.1016/j.epsl.2010.07.040

Román-Sánchez, A., Reimann, T., Wallinga, J., Vanwalleghem, T. Bioturbation and erosion rates along the soil-hillslope conveyor belt, part 1: insights from single-grain feldspar luminescence. Earth Surface Processes and Landforms. Submitted

Saltelli, A., Tarantola, S., Campolongo, F., Ratto, M. 2004. Sensitivity Analysis in Practice: A Guide to Assessing Scientific Models. Halsted Press, New York, NY, USA.

Salvador-Blanes, S., Minasny, B., McBratney, A.B. 2007. Modelling long-term in situ soil profile evolution: application to the genesis of soil profiles

containing stone layers. European Journal of Soil Science 58: 1535–1548. DOI:10.1111/j.1365-2389.2007.00961.x

Schäfer W (1952) Biogene Sedimentation im Gefolge von Bioturbation. Senckenbergiana 33: 1−12

Small, E.E., Anderson, R.S., Hancock, G.S. 1999. Estimates of the rate of regolith production using 10Be and 26Al from an alpine hillslope. Geomorphology 27: 131–150. DOI:10.1016/S0169-555X(98)00094-4

Stockmann, U., Minasny, B., Pietsch, T.J., McBratney, A.B. 2013. Quantifying processes of pedogenesis using optically stimulated luminescence. European Journal of Soil Science 64: 145–160. DOI:10.1111/ejss.12012

Stockmann, U., Minasny, B., McBratney, A.B. 2014. How fast does soil grow? Geoderma 216: 48–61. DOI:10.1016/j.geoderma.2013.10.007

Vanwalleghem, T., Stockmann, U., Minasny, B., McBratney, A.B. 2013. A quantitative model for integrating landscape evolution and soil formation: Modelling landscape and soil formation. Journal of Geophysical Research: Earth Surface. 118: 331–347. DOI:10.1029/2011JF002296

Wilkinson, B.H., McElroy, B.J. 2007. The impact of humans on continental erosion and sedimentation. Geological Society of America Bulletin 119: 140–156. DOI:10.1130/B25899.1

Wilkinson, M.T., Humphreys, G.S. 2005. Exploring pedogenesis via nuclide-based soil production rates and OSL-based bioturbation rates. Soil Research 43: 767–779. DOI:10.1071/SR04158

Wilkinson, M.T., Richards, P.J., Humphreys, G.S. 2009. Breaking ground: Pedological, geological, and ecological implications of soil bioturbation. Earth-Science Reviews 97: 257–272. DOI:10.1016/j.earscirev.2009.09.005

Yoo, K., Weinman, B., Mudd, S.M., Hurst, M., Attal, M., Maher, K. 2011. Evolution of hillslope soils: The geomorphic theater and the geochemical play. Applied Geochemistry 26: 149–153. DOI:10.1016/j.apgeochem.2011.03.054

CHAPTER 5

THE EFFECT OF FRAGMENTATION ON THE DISTRIBUTION OF HILLSLOPE ROCK SIZE AND ABUNDANCE: INSIGHTS FROM CONTRASTING FIELD AND MODEL DATA

Abstract

The disintegration of rocks into soil plays an important role in geomorphological processes, such as the evolution of hillslopes and river valleys. Nevertheless, the factors and processes controlling the physical weathering of rock particles is poorly understood. In this study, the surface and subsurface distribution of rock abundance and size is measured in ten soil profiles along three hillslopes transects. For the surface horizons, we observed a significant linear relation between d90 and slope gradient and a significant logarithmic relation between the ninth decile of the diameter, d90, and rock fragment abundance. For the first time, the performance of different fragmentation models is compared against field data to evaluate if the surface rock distribution can be explained from fragmentation of the subsurface material only. In six profiles these fragmentation models adequately reproduced the observed particle size distribution. In the other four profiles, all located on eroding hillslopes, armouring dominates over fragmentation and the surface rock distribution is coarser compared to the subsurface. The modelling results indicate two different zones in terms of fragmentation mechanism. The profiles in transect 1, located along a gently sloping hillslope, are best fit with the px-98-1-spread model, while the profiles in transects 2 and 3, along a steep river valley, are best fit with the px-98-1-3*0-1 model.

In the models, we consider physical weathering as the main factor and combined with a bulk chemical weathering of the fine fraction in two models, px-98-1 and px-98-1-x, although this chemical weathering is not specifically to explore soil water chemistry or mineralogy in detail. The observed discrepancies between field data and the results of this study, especially in the fine fraction, reveal the possible relevance of chemical or biological weathering.

1. Introduction

The abundance and size of rock fragments in soils influence several key processes, such as its water erosion and transport, thermal expansion or contraction, chemical dissolution, external crystal growth and soil productivity (Poesen and Laveee, 1994). Unfortunately, the processes causing the lateral and vertical distribution of rock fragments are poorly understood at present. While that the influence of the factors climate, vegetation, relief, bedrock, organisms and time intervene in the soil formation is widely acknowledged (Jenny, 1941), the underlying processes on the parent rock are not well ascertained. Especially the physical weathering or fragmentation of rocks into finer soil material, which

has been barely explored. Rock fragmentation was first characterized fitting several simple probability distribution functions to experimental data, as, for instance, Sanchidrian et al. (2014) proposed using rock blasting fragments. However, Brown (1989), considering the complexity of the fragmentation process, propose the sequential fragmentation as a cascade of fragmentation and re-fragmentation, a continued comminution in his own words. The next step was given by Wohletz et al. (1989) with the sequential fragmentation/transport theory, where fragmentation and transport were coupled with a Green function. More recently Fowler and Scheu (2016) have corrected these models for the case of explosive rock fragmentation concluding that one gamma distribution function could describe the uniform fragmentation leading to the production of coarse particles and another gamma function could describe the production of finer particles. This result agrees with the observations of Russell (1976) on the particle size distribution for the coarse fraction of granite soils in Zimbawe. Sklar et al. (2017) proposed a conceptual modelling framework relating the initial setting of the rocks in the hillslope to the particle size distribution of the sediment delivered to the river draining the valley. Accepting the analogue factors of soil formation of Jenny they formulated several functions for the local particle size distribution, the weathering intensity, the residence time, and even the possibility of by-passes in the path of the sediments toward the river.

Legros and Pedro (1985) analyzed particle size distributions of over 600 profiles. They proposed a weathering model with a limited number of weathering pathways, which they related to soil type and rock source. Wells et al. (2006; 2007) explored the mechanisms of salt weathering under laboratory controlled conditions detecting the importance of the sequence of wet and dry seasons in the fragmentation of the rocks, as well as the effect of temperature accelerating the processes. This experimental information was integrated in the elaboration of a rock fragmentation model based on a simple fracture geometry, a particle breaks down into two particles of similar volume, and on a fracture probability increasing with time (Wells et al., 2008).

Several field studies (e.g. Marshal and Sklar, 2012; Román-Sanchez et al., 2018) found slope to be a key factor controlling the spatial distribution of stoniness, and the size of particles (Attal et al. 2015). These results enhance the importance of detachment and transport on the final distribution of rocks fragments in the landscape. Where water and aeolian erosion rates are fast compared to soil formation, these processes will control the surface distribution of stoniness, removing the fine soil material on the surface and leaving a coarse layer forming an armour. The mechanism of armouring was studied by several

authors at least since Einstein (1950), and later by Parker and Klingeman, (1982), Parker et al. (1982) and Parker and Toro-Escobar (2002); Willgoose and Sharmeen (2006) developed the ARMOUR model, which is a physically based armouring and weathering model. The model inputs are soil grading, slope and runoff hydrograph. However, this is a computationally complex model and it cannot simulate large areas or over long periods of time; Later, Cohen et al. (2009) developed a computationally more efficient one-dimensional model, mARM. This model allows to easily explore the relationship between erosion and physical weathering rates on a hillslope by varying the scales of time and space. On erosion-dominated hillslopes, the armouring process creates a surface layer with coarse rock fragments, while on weathering-dominated hillslopes, fine particles accumulate on the surface. They calibrated mARM to output from ARMOUR. Cohen et al. (2010) later presented a new three-dimensional landscape evolution model, mARM3D, which simulates soil evolution combining erosion and pedogenic processes on long term and large spatial scale. It simulates discretized soil profiles on a spatial grid to examine the evolution of the full soil profile and not only the armour of the soil surface. They studied the rate of soil particle breakdown and of conversion of bedrock to soil. Welivitiya et al. (2016) extended their model SSSPAM to more general conditions than mARM3D and explored a more extensive range of parameters. They simulated soil evolution in two horizontal dimensions (x and y), depth down the soil profile and soil grading with depth over time.

Due to the very few data available for hillslopes and their soils and considering the importance of understanding the temporal evolution of soil grading for the prediction of long-term landscape evolution, the general purpose of this work is to gather particle size distribution data obtained in a Mediterranean climate, to establish the patterns or models that fit to them, as well as to explain the evolution of the rock grading in the soil profiles sampled along three hillslope transects.

2. Material and Methods

2.1.Site description

The study was conducted in the headwater of Martin Gonzalo catchment, in Santa Clotilde Critical Zone Observatory, Sierra Morena, Cordoba province, SW Spain (Figure 5.1). The climate is Mediterranean, Temperate with dry and hot summers, Csa in the Köppen-Geiger scheme (Peel et al. 2007), with annual average rainfall of 800 mm,

concentrated between the fall and early spring, with temperatures in the range (5-40ºC), and a medium value of 15ºC.

Ten soil profiles were studied distributed in three transects. The transect 1 (SC-1, SC-2, SC-3) is in mostly flat area with slopes between 0-10%. The vegetation is mainly represented by tree species of Quercus ilex, Quercus suber and natural and cultivated grasslands, forming an oak-woodland savannah, “dehesa system”, used for extensive grazing with very low stocking densities, i.e. below 0.10 LSU ha-1 (livestock units per hectare). The transect 2 (profiles SC-4, SC-5, SC-6) and 3 (profiles SC-7, SC-8, SC-9 and SC-10) are in a steep topography, in the south and north facing, respectively, of a hillslope. The abrupt topography, with slopes between 5-40%, has allowed the development of Mediterranean sclerophyllous forests and has impeded access to the area of human resources for grassland cultivation. The vegetation in both transects is characterized by three vegetation strata, tree species formed mainly of Quercus ilex, Quercus suber, Mediterranean scrub (Arbutus unedo, Phlomis purpurea, Pistacia lentiscus), and grassland. The north facing slope with higher vegetation density and tree cover than the south facing slope, preserves a higher soil moisture content throughout the year.

Figure 5.1 shows the different landscape positions of the different profiles: on hilltop: SC-4 and SC-10; on hillslope; SC-1, SC-3, SC-5, SC-8 and SC-9; and on hill-base: SC-2, SC-6 and SC-7. The hill-base profile, SC-2 is located within a valley bottom, but does not have a permanent creek or river. Also, profiles SC-6 and SC7 are not affected by fluvial dynamics.

Specifically, in the geological context the site lies within the Central-Iberian Zone (ZCI) of the Spanish Hercynian Massif, where large volumes of granitoids emerge. The predominant granitic types are called "granitoid characters mixed" in some areas with epizonal intrusions forming individual units of batolytic dimensions (Capdevila et al. 1973; Corretge et al. 1977). Granitoids contain peralumin minerals in variable amounts and its composition varies from granodiorites and monzogranites, many times porphyric comegacrystals of K-Fd to leukogranites. The study area is located in the granitic area called Los Pedroches batolith that is spatially connected with biotite granodiorites and amphibole (Garcia-Casco et al. 1989). Two datings place this batholith in 305±10 m.a and 291±15.m.a (Penha and Arribas, 1974). Two differentiated igneous units constitute Los Pedroches batolith in our study area that are included in the lithological granodioritic group (Mapa Geológico de España, 1990): (1) Microgranites and leucogranites undifferentiated, which involves the profiles of the transect 1, with grey colour, fine-medium grain size with

myarolytic cavities and formed by quartz (in the larger grain size phase), K-feldspar (interstitial in the form of phenocrystals), plagioclase (albitic composition with phenocrystals of albite-oligoclase) and muscovite (from K-feldspar replacement, plagioclase and biotite) as the main mineral structure, and biotite, cordierite as sporadic minerals, (2) Porphyric microadamellite, which includes the profiles of the transect 2 and 3, with fine grain size and formed by quartz (represents late interstitial phase, burst appearance, poiquilitic texture and abundant plagioclase, biotite and apatite inclusions), K-feldspar (represents late interstitial phase, formed by phenocrystals and poiquilitic texture), plagioclase (formed by phenocrystals with inclusions in quartz and feldspar) and biotite (in the form of phenocrystals and in small crystals included in plagioclase, quartz and potassium feldspar).

Is important to point out that, as has been described above, there are two differentiated mineralogy groups in the area, transect 1 on one side, and transects 2 and 3 on the other. Their mineralogy will determine, between others factors as physical and biological, the patterns in the rock fragmentation on the sublayer (horizon B). The sensitivity to chemical weathering of the minerals of each group might be variable, e.g. the biotite content in the transects 2 and 3 is higher than in the transect 1, this means that the chemical reactions between biotite with carbon, hydrogen, oxygen, iron, etc, and its transformational weathering products (clay) has higher rate in transects 2 and 3. This aspect will be argued in more detail in the discussion section.

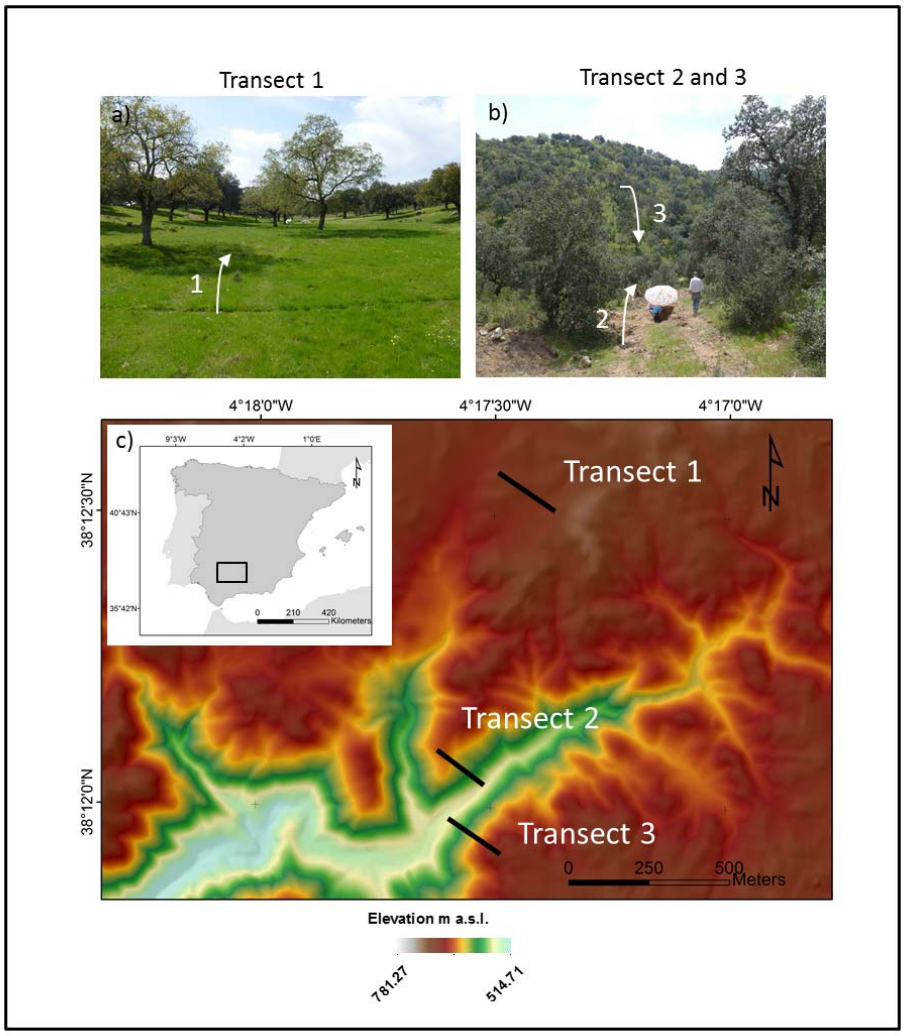

Figure 5.1 Study area. (a) Overview of transect 1 looking west direction towards profiles SC-2 and SC-3. (b) Overview of transect 2 and 3 that join in the valley. (c) Regional location of the study area in SW Spain and elevation map of the study area with indication of the 3 studied transects

2.2. Sampling and measurement

Twenty samples were taken from the surface (horizon A) and subsurface (horizon B) to determine their particle size distribution (PSD).

A specific analysis protocol was developed in the laboratory as shown in figure 5.2. First, the samples were separated in the fraction > 2mm and < 2mm by sieving. The soil's fine fraction (diameter < 2 mm) was then measured by a conventional particle size analysis using the hydrometer method (Gee and Or, 2002). To further separate the coarse fraction (diameter > 2mm), first, they were washed to remove any fine fraction adhering to rock fragments, and to break up aggregates of fine soil, organic matter, etc. and then dried. Secondly, the rock fragments were separated in fourteen sizes (2, 4, 5, 6.3, 8, 11.2, 12.5,

16, 20, 31.5, 40, 50, 60, and 70 mm) by dry sieving using a mechanical method. Finally, mass and volumetric percentage of stoniness was computed, using the bulk density of each layer.

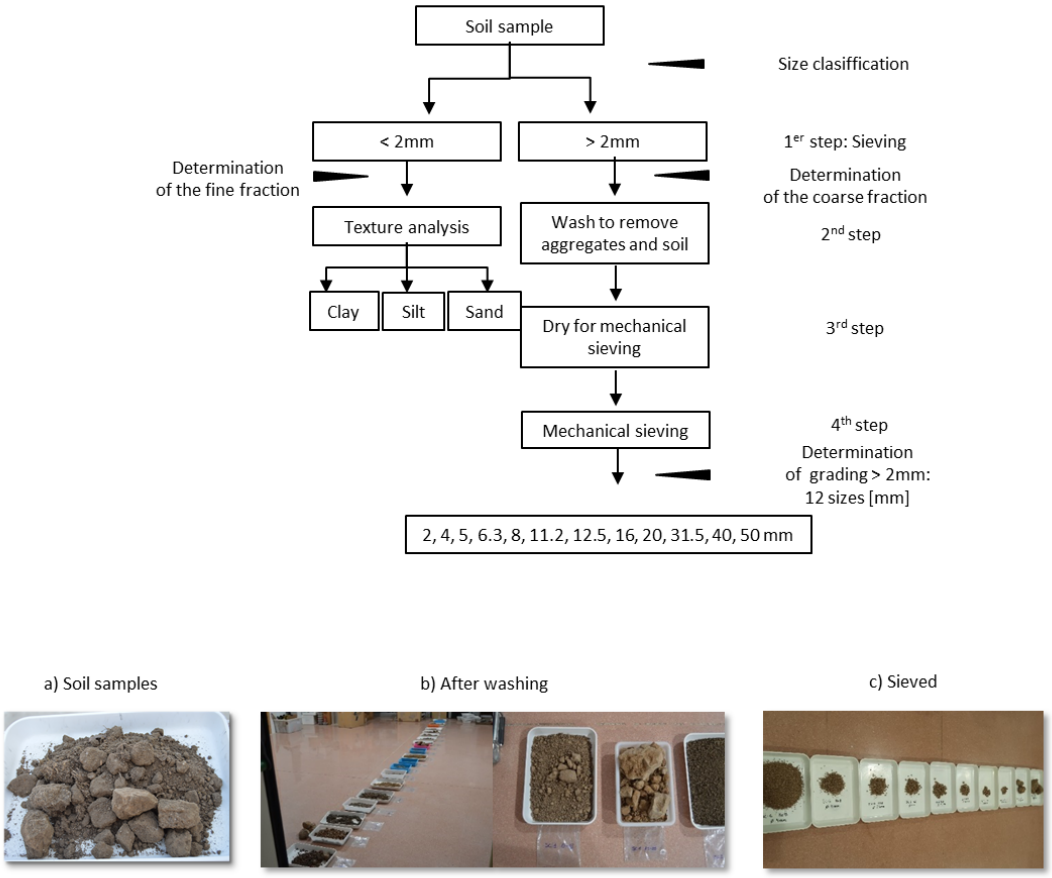

Figure 5.2 Sample preparation design to obtain the particle size distribution.

2.3. Rock fragmentation model

Rock fragmentation or the generation of smaller daughter particles from larger parent particles can be promoted by physical, biological and chemical processes in the soil layer or mobile regolith. Physical processes can include rock damage by frost cracking, crystal growth, or thermal expansion. Recent studies (e.g. Ruiz et al., 2017) have also stressed the importance of earthworms and plant roots in wedging open smaller cracks. and breaking up smaller rocks from bedrocks, for example due to tree falls (Brantley et al., 2017). Fractures also open in the deep critical zone under topographic and tectonic stresses (St Clair et al., 2015), but here these effects are considered to be included in the latent particle size distribution. In the case of this study, this latent particle size distribution is then

represented by the subsurface horizon grading, while the surface grading represents the end member or the result of physical weathering processes. Chemical weathering can also disturb the bedrock particle size distribution reducing the dimension of the particles as described by Sklar et al. (2017). Physical weathering is the dominant soil formation process near the surface, although the chemical weathering has also been included in two models as a disintegrating process acting on the fine fraction (table 5.1). Indeed, temperature and moisture gradients are higher near the surface than in deep layers. Any deviance of the field data from this expected trend could then be attributed to armouring effect produced by erosion or biological weathering processes, as it will be discussed below.

The framework rock fragmentation models assume mechanisms of rock disintegration with all particles spherical, constant density distribution within each particle fraction. They all consider the mass, or volume, conservation principle, where the total volume of the daughter particles is the same as the volume of the parent particle. In all weathering or fragmentation mechanisms considered here, the daughter particles size obtained from the parent particle is not usually fitted to a single size fraction. Instead it needs to be interpolated througha number of size fractions, depending on the final size of the daughter particles..

Specifically, the rock fragmentation models consider a fragmentation geometric function based on the distribution of the volume of daughter particles assuming a size grading where the diameter of the daughter particles is (1/N)1/3 times the diameter of the parent particle, with N as the number of equal particles resulting from the fracture of the parent particle. In general, the geometry adopted is pX-AAA-BBB-CCC-DDD where X is the number of daughter particles that have been defined in the grading fraction, AAA is the volume percentage of the particles that remain in the parent particle, BBB is the volume percentage in the next size grading smaller, CCC is the volume percentage in the next size grading smaller, etc. (Sharmeen and Willgoose, 2006; Willgoose, 2018).

The models were run for 6 profiles. Nash-Sutcliffe efficiency (NSE) (Nash-Sutcliffe ,1970) was used as a goodness-of-fit indicator for the different models.

Table 5.1 Rock fragmentation models

Model notation	Description of fragmentation patterns
p2-0-100	2 fragments; 2 x 1/2 the volume (Wells et al., 2008)
p2-0-0-0-100	8 fragments; 8 fragments of 1/8, 0 fragments of 1/2 and 1/4 the volume. Used by Finke et al. (2012) in SOILGEN model.
p2-0-50-50	3 fragments; 1 x 1/2, 2 x 1/4 the volume
p2-0-50-0-50	5 fragments; 1 x 1/2, 4 x 1/8 volume
px-98-1-2*0-1	x fragments; particles spall, lots of small particles and large particles decline slightly in size (model 1)
px-98-1-3*0-1	x fragments; particles spall, more small particles and large particles than in the model 1 decline slightly in size (model 2)
px-98-1-n*0-1	x fragments; particles spall, all small particles to smallest grading and large particles decline slightly in size (model 3)
px-98-1	x fragments; particles spall, the smallest fraction captures all the fines and chemically weathers them. The large particles decline slightly in size (model 4)
px-98-1-x	x fragments; the smallest fraction captures only a part of the fines and chemically weathers them (model 5)
px-98-1-spread	x fragments; as for model 4 but the finest fraction uniformly spread over the next 'spread' smaller fractions (model 6)
p2-stoch	2 fragments; 2 fragments uniformly randomly distributed between the original volume and zero (random fracture of a cube)

3. Results

3.1. Observed vertical and spatial variation in rock fragments

Figure 5.3 A (i) and (ii) illustrates the spatial and vertical particle size distribution in the study area, based on the data given in Table 5.2. The vertical distribution of the soil profiles follows a common trend. The profiles located on the hill-base and on the hilltop hold larger rock fragments in the subsurface compared to the surface (horizon B vs horizon A), while the profiles on the hillslopes exhibit the opposite trend. It is likely that all soil profiles are affected by physical weathering in a similar degree. However, in the case of the hillslope profiles (SC-3, SC-5, SC-8 and SC-9), this process is masked by erosion, resulting in surface armouring. Figures 5.3 B, C, D describe the spatial trends in the rock´s size and abundance as a function of hillslope gradient and d_{90} and indicate Pearson correlation coefficient with a significance level for each relation on horizon A. Rock abundance is significantly related to rock size, d_{90}, for horizon A, but not for the subsurface horizon B. Figure 5.3 B shows this logarithmic trend, similar to the relation found for d50 by Sklar et al. (2016). Rock abundance is linearly related to hillslope gradient (Figure 5.3C). Again, the relationship is highly significant for the surface layer (horizon A), but not for the subsurface B horizon. Also, rock fragment size, d90, was found to be linearly related

to hillslope gradient within the surface horizon A (Figure 5.3 D). Again, this is not the case for the subsurface horizon

Table 5.2 shows the observed particle size distribution in abundance or mass percentage in each soil profile, d90 and descriptive statistics of the data. In general, horizon B is characterized by the presence of larger rock fragments compared to the surface horizon A, indicating that the subsurface fragments are weathered into finer daughter particles in the overlying layer. However, there is an exception in the profiles SC-3, SC-5, SC-8, SC-9 where the rocks fragments in horizon A are larger than in horizon B. These profiles have in common that they are all located on steep (SC-8 and 9) or gentle slopes (SC-3, SC-5), so this effect can be attributed to erosion and armouring. The highest rock fragment sizes, expressed by the d90 values (the diameter at which 90% of the sample´s mass is smaller that this value), for the surface and subsurface horizon are found in profile SC-8 and SC-1 respectively (Table 5.2). The parameter d90 was selected as the representative diameter because, in general, the largest percentage of mass in these samples is distributed in sizes > 2 mm and, therefore, there is little variation in the d50, making it less suitable as a representative diameter.

Exploring the spatial patterns and distribution of the rock fragments, there are notable differences between transect 2 and 3, on the south and north facing of the hillslope respectively. On the one hand, it is interesting to point out that the d90 and slope values are increasing downslope (as reported by Attal et al. 2015), except for the profile on the hill-base SC-6 and SC-7, where the slope decreases in both but the d90 increases in SC-6 (transect 2) and decreases in SC-7 (transect 3). On the other hand, the south-facing transect 2 has lower d90 and slope values than the north-facing transect 3, excluding the hill-base profiles, where SC-6 in the transect 2 has higher d90 than SC-7 in the transect 3 (table 5.2). On this south-facing slope, solar radiation and the consequent evapotranspiration is higher than on the north-facing, transect 3 (Román-Sanchez et al. 2014; 2015). Dryer slopes at the start of a rainfall event induce higher infiltration rates and reduced or none soil water erosion. These south-facing slopes also have a lower vegetation cover which further limits bioturbation and resulting biogenic creep.

The data of all profiles show positively skewed, right tailed, distributions and high kurtosis values, heavy tailed distributions. The particle size distributions of the samples of these profiles approach a Weibull distribution with good fit. Their shape and scale parameters are listed in table 5.2. Figure 5.3 E presents the relation between the shape and scale parameters for each profile and horizons. In most profiles, the scale and shape

parameters are greater for the A horizon than for the B horizon, except in SC-1, SC-2, SC-4 and SC-10, where the opposite trend happens. There is a significant linear relation between the scale parameter and the slope gradient in A horizon while there is no significant relation of both parameters in B horizon (figure 5.3 F), the greater the hillslope gradient, the greater the scale value, implying that on steeper slopes the particle size distribution is wider. At the same time, these high scale values on the steeper slopes, correspond with high d90 values for the A horizon as observed earlier. This effect reinforces the hypothesis that these high scale values are caused by armouring of the surface layer produced by erosion on the steeper slopes.

A (i)

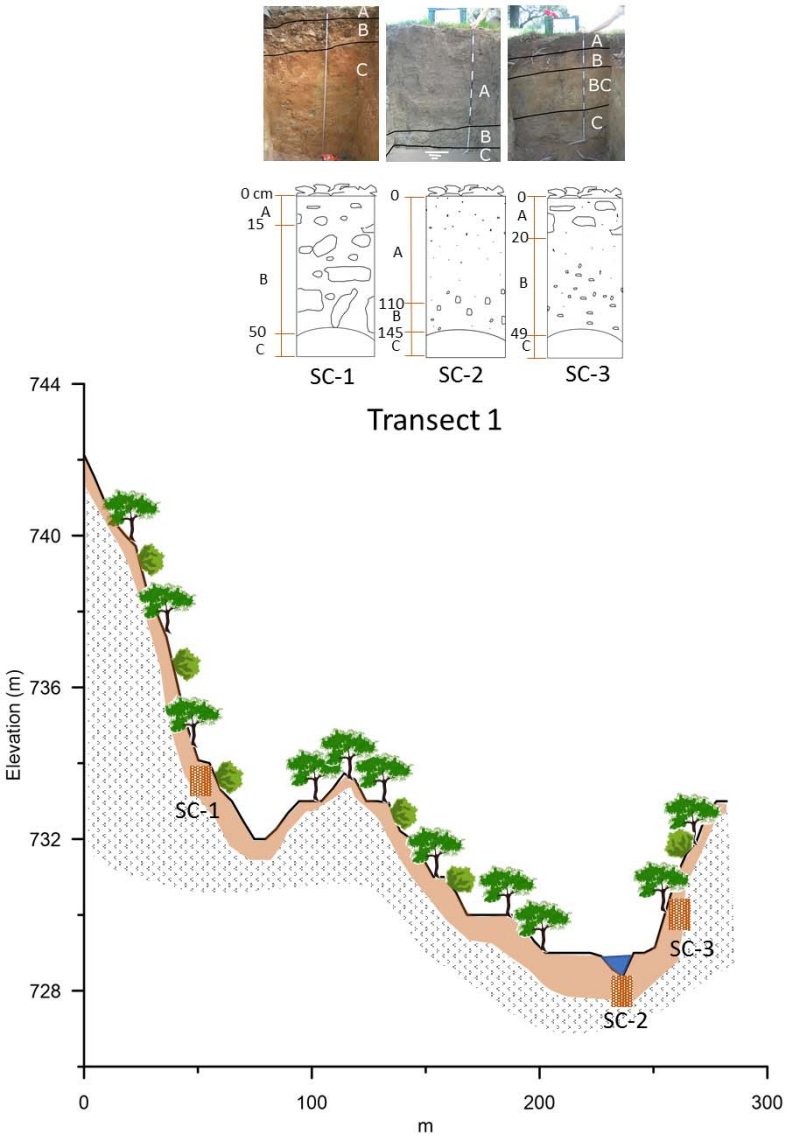

A (ii)

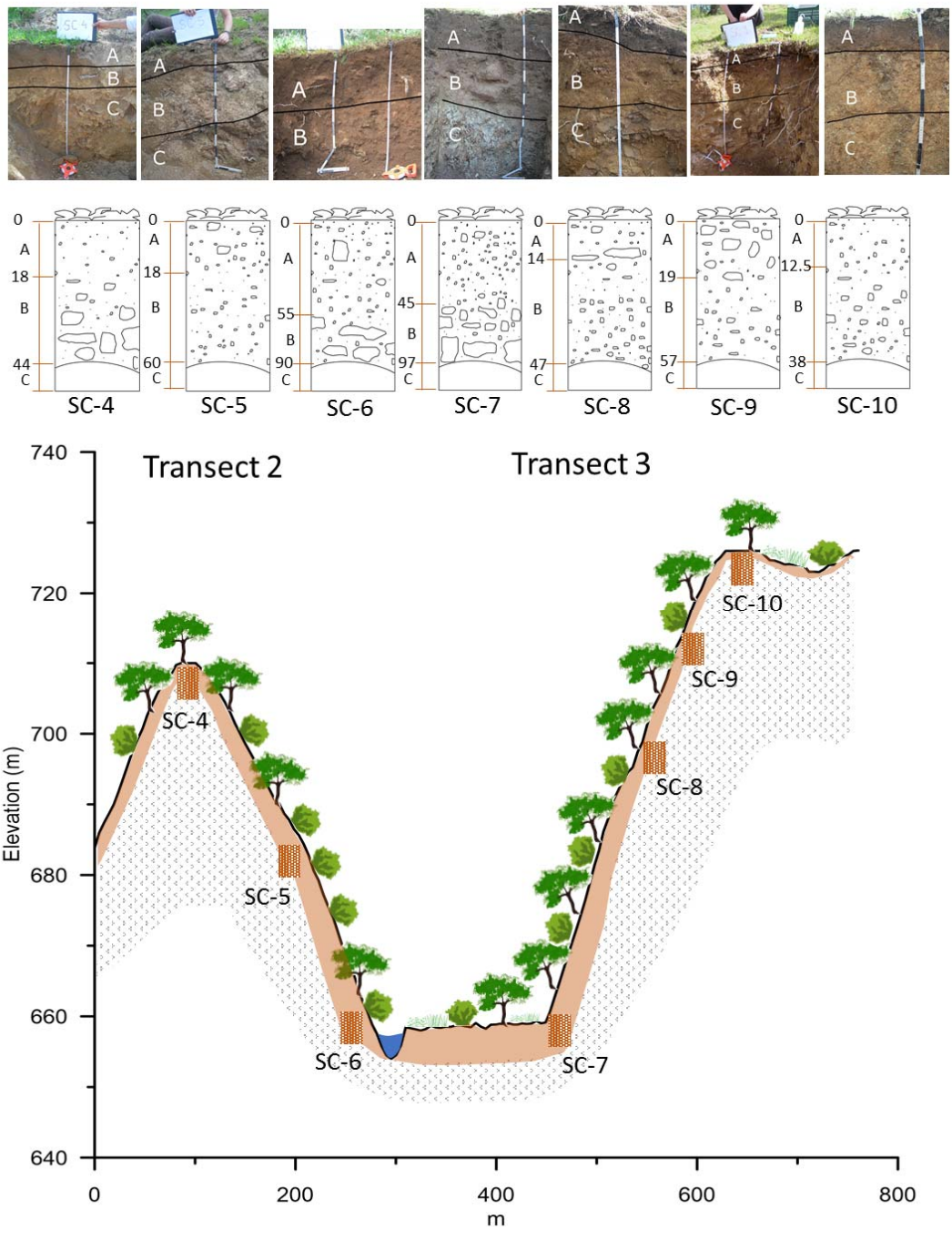
A
B
C
0
18
44
60
55
90
45
97
14
47
19
57
12.5
38
SC-4
SC-5
SC-6
SC-7
SC-8
SC-9
SC-10
Transect 2
Transect 3
Elevation (m)
740
720
700
680
660
640
0
200
400
600
800
m

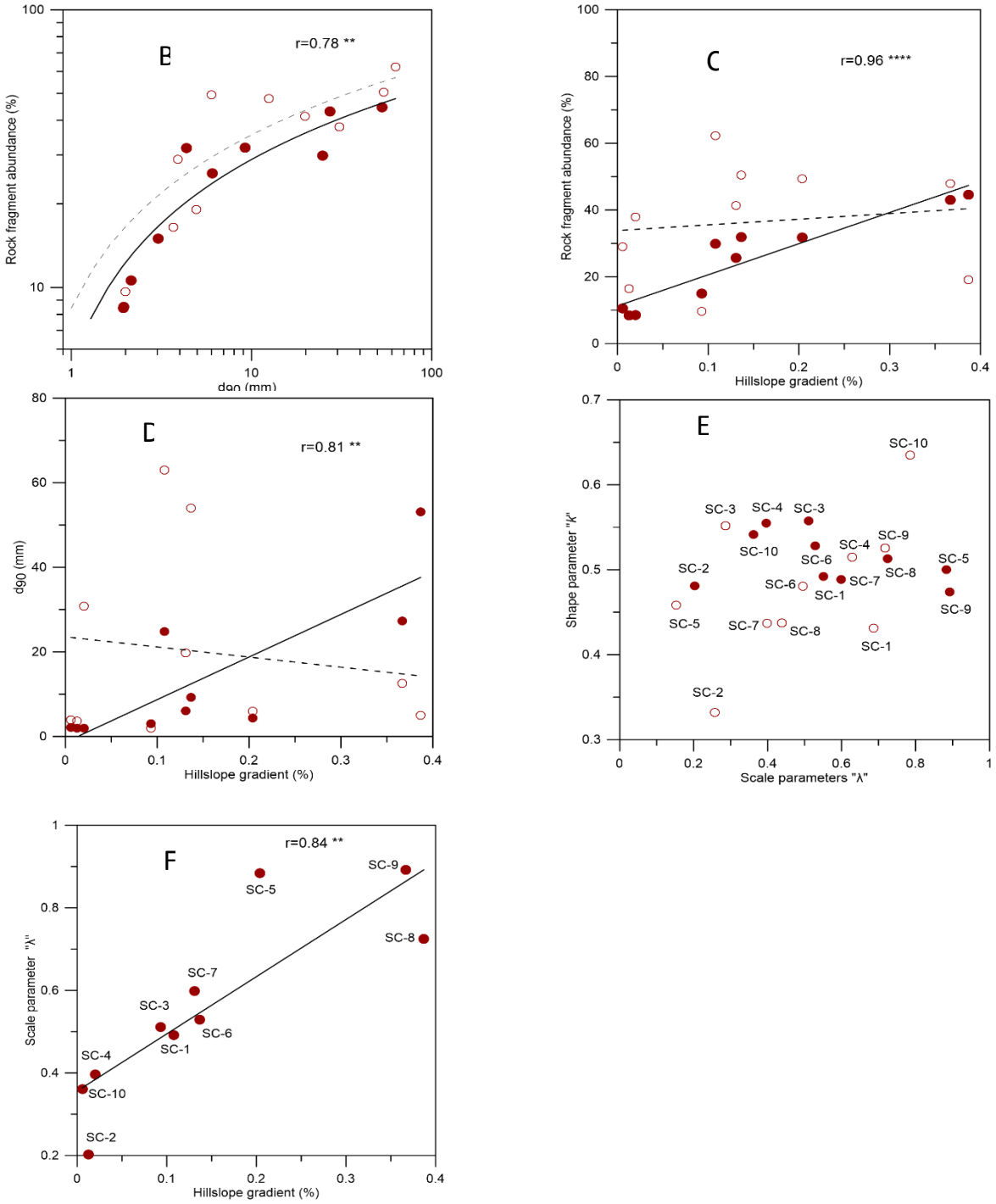

Figure 5.3 A (i) and (ii) Rock fragments distribution in each horizon for all soil profiles in the three studied transects. B) Variation between d90 and rock fragmentation abundance percentage on horizon A and B for all profiles, C) Relation between hillslope gradient and rock fragmentation abundance percentage on horizon A and B for all profiles, D) Relation between hillslope gradient and d90 on horizon A and B for all profiles, E) Graphical representation of Weibull distribution parameters; scale and shape for all profiles, F) Variation between hillslope gradient and Weibull distribution scale parameter on horizon A for all profiles.

Table 5.2 Measured particle size distributions in surface (A horizon) and subsurface (B horizon) and statistical parameters

Soil profile and slope [%]	Horizon depth [cm]	Diameter [mm] 0.002	0.05	2	4	5	6.3	8	11.2	12.5	16	20	31.5	40	50	60	70
		% abundance															
SC-1	A (0-15)	100	95.58	74.05	29.86	21.85	20.64	19.41	18.17	16.25	15.15	14.55	11.80	7.54	5.60	-	-
(10.80)	B (15-50)		96.75	86.59	62.30	56.81	55.77	54.66	53.40	50.73	47.70	45.83	43.55	-	35.19	30.90	27.31
SC-2	A (0-110)	100	88.63	65.66	8.44	1.55	0.98	0.69	0.55	0.41	0.18	-	-	-	-	-	-
(1.28)	B (110-145)		92.75	72.67	16.47	2.27	1.43	0.95	0.71	-	-	0.46	0.30	-	-	-	-
SC-3	A (0-20)	100	95.19	80.33	15.01	5.35	4.59	3.92	3.51	3.00	2.47	2.34	2.11	1.91	-	-	-
(9.30)	B (20-49)		92.59	74.10	9.63	1.09	0.56	0.28	0.09	-	-	-	-	-	-	-	-
SC-4	A (0-18)	100	94.60	75.56	8.50	3.34	2.67	2.15	1.59	1.03	0.67	0.45	-	-	-	-	-
(2)	B (18-44)		95.73	83.77	37.88	25.09	23.66	21.99	20.54	18.51	16.83	15.24	11.77	7.85	6.27	-	-
SC-5	A (0-18)	100	95.79	83.31	31.76	11.06	8.10	6.00	4.81	3.50	2.89	2.19	1.54	-	-	-	-
(20.38)	B (18-60)		97.41	92.54	49.37	20.65	11.12	5.42	1.71	0.59	0.48	0.28	-	-	-	-	-
SC-6	A (0-55)	100	95.18	78.95	31.89	14.26	12.58	11.31	10.35	9.44	8.64	8.33	7.57	6.60	5.86	-	-
(13.65)	B (55-90)		95.46	85.11	50.48	38.89	37.33	36.05	34.68	32.98	31.79	30.75	-	-	29.77	27.88	-
SC-7	A (0-45)	100	93.65	80.16	25.73	13.16	11.34	9.70	8.16	5.93	4.30	3.41	2.62	1.43	-	-	-
(13.08)	B (45-97)		95.20	87.10	41.34	24.29	21.74	19.50	17.10	14.68	13.35	11.72	-	-	8.88	4.21	-
SC-8	A (0-14)	100	96.51	86.53	44.57	34.56	32.74	31.06	29.28	26.18	24.66	23.67	-	21.52	18.28	14.52	-
(38.68)	B (14-47)		91.86	65.35	19.07	11.07	9.02	7.11	5.21	3.00	1.75	1.06	0.58	-	-	-	-
SC-9	A (0-19)	100	96.60	83.32	43.05	33.99	32.15	30.21	28.01	26.06	22.85	21.43	18.95	4.82	3.10	-	-
(36.68)	B (19-57)		97.27	88.75	47.91	31.70	27.97	24.21	19.91	13.93	9.97	6.88	4.28	-	-	-	-
SC-10	A (0-12.5)	100	94.10	71.84	10.60	2.67	2.03	1.60	1.29	0.73	0.41	0.27	-	-	-	-	-
(0.58)	B (12.5-38)		97.38	88.84	28.98	7.85	5.66	3.96	3.41	1.74	0.63	0.29	-	-	-	-	-

4 **Table 5.2.** Measured particle size distributions in surface (A horizon) and subsurface (B horizon) and statistical parameters

5

Soil profile and slope [%]	Horizon depth [cm]	Rock fragments >2mm %abundance	d_{90}	skewness	kurtosis	shape	scale	R-squared
SC-1	A (0-15)	29.86	24.86	2.446	7.862	0.492	0.550	0.995
(10.80)	B (15-50)	62.30	63.00	1.738	4.349	0.431	0.686	0.994
SC-2	A (0-110)	8.44	1.94	2.210	5.985	0.481	0.203	0.987
(1.28)	B (110-145)	16.47	3.68	1.995	5.818	0.332	0.257	0.991
SC-3	A (0-20)	15.01	3.03	2.749	8.742	0.558	0.511	0.996
(9.30)	B (20-49)	9.63	1.99	1.726	4.077	0.552	0.286	0.991
SC-4	A (0-18)	8.50	1.95	2.499	7.766	0.555	0.396	0.998
(2)	B (18-44)	37.88	30.76	2.797	9.752	0.515	0.629	0.997
SC-5	A (0-18)	31.76	4.35	2.286	7.084	0.500	0.884	0.997
(20.38)	B (18-60)	49.37	5.99	1.696	4.415	0.458	0.153	0.991
SC-6	A (0-55)	31.89	9.21	2.391	7.854	0.528	0.529	0.992
(13.65)	B (55-90)	50.48	54	1.625	4.162	0.481	0.496	0.996
SC-7	A (0-45)	25.73	6.06	2.733	9.244	0.489	0.598	0.994
(13.08)	B (45-97)	41.34	19.75	2.628	8.684	0.437	0.399	0.99
SC-8	A (0-14)	44.57	53.11	2.615	8.955	0.513	0.725	0.998
(38.68)	B (14-47)	19.07	4.94	1.997	5.662	0.437	0.439	0.996
SC-9	A (0-19)	43.05	27.28	2.490	8.382	0.474	0.892	0.997
(36.68)	B (19-57)	47.91	12.49	2.477	7.867	0.526	0.718	0.996
SC-10	A (0-12.5)	10.60	2.15	2.296	6.958	0.541	0.361	0.999
(0.58)	B (12.5-38)	28.98	3.9	2.345	7.137	0.635	0.786	0.984

6

3.2.Rock fragmentation models

Observed patterns of rock distribution, resulting from fragmentation of the parent material during the weathering process, were then modelled. The particle size distribution in each soil profile for horizon A was modelled starting from that of the underlying subsurface horizon B, using different rock fragmentation models. Table 5.1 simplifies the fragmentation geometry of the different models used, detailing how the volume of particles will be distributed after each fragmentation episode. Figure 5.4 shows the cumulative particle size distribution of field data (dots) and the fit to different rock fragmentation models (continuous lines) in each soil profile. In this figure, the initial conditions are the measured PSD of horizon B, and the final condition is the measured PSD of horizon A. These simple models are based on the physical weathering or fragmentation, but some models include chemical weathering as well for the fine fraction changes. In particular, the models px-98-1 and px-98-1-x. In any case, none of the models performs well under erosive or armour-generating conditions. Therefore, it has only been applied to 6 profiles: SC-1, SC-2, SC-4, SC-6, SC-7 and SC-10. Four profiles, all located on steep or gentle slopes, were excluded: SC-3, SC-5, SC-8 and SC-9. Profiles SC-3 and SC-8 have a higher abundance of rock fragments (> 2mm) in the horizon A than in horizon B. Also, in profiles SC-5 and SC-9 such an inversion exists, with more rock fragments in the surface A layer, but only down to a size class of respectively 6.3 mm and 4 mm.

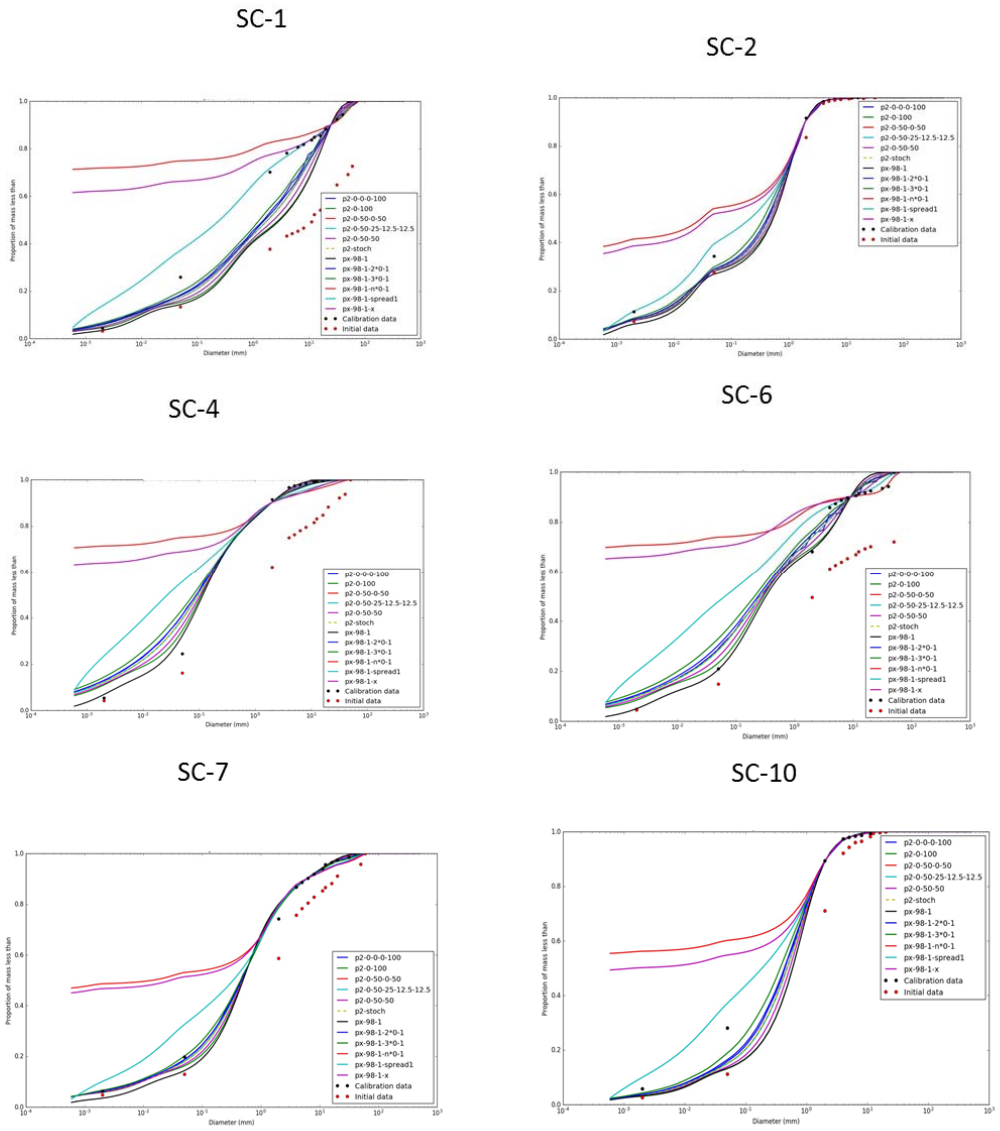

Figure 5.4 Fit of 11 different rock fragmentation models (continuous lines) to field data (dots). Subsurface horizon B particle size distribution represents the initial situation (initial data). Surface horizon A data represents the end situation (calibration data).

3.3. Model efficiency

Following NSE efficiency, in the transect 1: profiles SC-1 and SC-2, the best model is px-98-1-spread where the particles are divided in x fragments, the particles spall and all small particles are dissolved but the finest fraction spreads over the fine fractions. The profile SC-4, on the hilltop of the transect 2, is fit best to the model px-98-1. This means that x fragments; particles spall, the particles are broken in x fragments, the particles spall and the smallest fraction captures all the fines and chemically weathers them. The large particles decline slightly in size. Finally, the best model fits for transects 2 and 3: profiles SC-6, SC-7, SC-10, is px-98-1-3*0-1 where the rocks are divided in x fragments, the

particles spall, lots of small particles are created and large particles decline slightly in size. The likelihoods values of the rest of the models are also shown in Table 5.3.

In summary, the rock fragment models are capable of adequately simulating the evolution of particle size distribution from the subsurface B horizon to the surface A horizon for all profiles. Once the profiles have been simulated, there seem to emerge some differences between the three transects, as the best model is different as it was mentioned before (table 5.3). All profiles modelled are connected with physical fragmentation and in the case of the profile SC-4, furthermore, is related with chemical weathering.

Table 5.3 Test of goodness of fit of the different fragmentation models applied to soil profiles SC-1, 2, 4, 6, 7 and 10. The best model for each profile and according to NSE is shown in bold.

	Soil profile					
Model notation	SC-1	SC-2	SC-4	SC-6	SC-7	SC-10
p2-0-0-0-100	0.8732	0.9952	0.9717	0.9713	0.9975	0.9851
p2-0-100	0.6598	0.9943	0.9895	0.9619	0.9959	0.9784
p2-0-50-0-50	0.8220	0.9951	0.9769	0.9713	0.9975	0.9833
p2-0-50-50	0.7452	0.9946	0.9844	0.9667	0.9968	0.9803
px-98-1	0.6442	0.9913	**0.9951**	0.9557	0.9937	0.9788
px-98-1-2*0-1	0.8475	0.9958	0.9710	0.9697	0.9980	0.9865
px-98-1-3*0-1	0.8986	0.9970	0.9614	**0.9783**	**0.9982**	**0.9913**
px-98-1-n*0-1	0.2226	0.8622	0.3882	0.3267	0.7386	0.6778
px-98-1-spread	**0.9766**	**0.9972**	0.8844	0.9414	0.9820	0.9919
px-98-1-x	0.4593	0.8881	0.5207	0.4416	0.7622	0.7578
p2-stoch	0.8177	0.9951	0.9773	0.9745	0.9975	0.9834

4. Discussion

The rock fragmentation patterns studied in our soil profiles show that six out of 10 profiles have higher rock fragment sizes and abundance in the subsurface than in the surface, indicating that these profiles are dominated by fragmentation. Only four profiles have a higher rock fragment size and abundance in the surface compared to the underlying material. Three of these profiles are on steep slopes and one on a gentler slope, indicating that erosion and armouring processes are dominant over fragmentation here. Their effect on landscape and soil evolution was studied and modelled by Willgoose and Sharmeen (2006), Cohen et al. (2009, 2010) and Welivitiya et al. (2016).

The subsurface material (horizon B), which immediately overlies the saprolite, represents the inherited particle size distribution as defined by Sklar et al. (2016). In Sklar's

review, the PSD of this material is described as being influenced by two factors: the latent sizes and its susceptibility to weathering. In our study area, with granodioritic bedrock, the latent size is controlled by the size distribution of individual mineral grains and is relatively homogenous over the study area. While the susceptibility of these minerals is also -relatively- homogenous, the extent of weathering could be different in different landscape positions. In this respect, the mineralogy of the study area is divided in two groups as described in the site description section: transect 1 versus transects 2 and 3. The sensibility to the chemical weathering is different in each group, e. g. biotite has several weathering sequences, such changes can occur in the interlayer of the mineral (removal K, oxidation) resulting in the formation of mica-vermiculite, vermiculite, smectite, Al-clorite, etc. In the transformation of biotite to clay, an expansion in volume is produced that deforms the outline of the mineral and can disturb the bedrock where it is originated (Bisdom et al., 1982). This phenomenon is likely to cause differences between the areas where the biotite is more abundant, in our case, the transects 2 and 3, and the area of transect 1. In the model results there are indeed two distinct areas where different fragmentation patterns can be identified. Transect 1 follows the physical fragmentation model px-98-1-spread, while transects 2 and 3 follow a different physical fragmentation model, px-98-1-3*0-1. One exception is the profile SC-4 profile in transect 2 that follows model px-98-1, a fragmentation model that includes chemical weathering of the fine fraction.

These results point to a potential contribution of chemical weathering on our observed PSD. Although several studies (Riebe et al. 2017) indicate that chemical weathering is dominant in the deep critical zone, while physical weathering is expected to more important near the surface, we cannot totally exclude an added effect of chemical weathering on particle size evolution from subsurface to surface. This should be subject of further study. While in general a good model fit is obtained, with relatively high model efficiencies (for example, NSE> 0.99) for most profiles, the finer particle sizes (< 2mm) are less well predicted compared to the coarser size classes (figure 5.4). Generally, the model overpredicts the abundance of fines. Different reasons can be sought for this: First, these finer size classes are most susceptible to erosion-deposition, process that is not specifically addressed in our models, secondly, two models px-98-1 and px-98-1-x include a bulk chemical weathering term of the fine fraction but it is not specifically designed to explore soil water chemistry or mineralogy in detail, and finally, there is lower accuracy of the number of fine fraction classes established and measured than in the coarse fraction, making it more difficult to obtain a good model fit to the field data. Further studies,

employing holistic models such as Miles3D (Vanwalleghem et al., 2013), LORICA (Temme and Vanwalleghem, 2016), SSSPAM (Welivitiya et al., 2016) should be conducted to help clarify the relative importance of each of the processes, i.e. chemical and physical weathering, erosion-deposition, armouring and the impact of biology on these.

5. Conclusions

For the first time, this study tests different rock fragmentation models with field data from three transects in a Mediterranean environment. We show how for six profiles the grading of the surface horizon can be modelled from the grading of the subsurface material or mobile regolith. For the remaining four profiles, all located on steep hillslopes, we observe surface armouring due to erosion.

Following different model efficiency parameters (Nash-Sutcliffe) there are two different areas that can be identified in terms of best-performing model: the model px-98-1-spread in the transect 1 (SC-1 and SC-2 profiles) and the model px-98-1-3*0-1 in the transect 2 (SC-6, SC-7 and SC-10 profiles) both with physical weathering. There is an exception with SC-4 profile in transect 2 where the fine fraction is chemically weathered and follows the model px-98-1.

In spite of the good model fit, some deviations between modelled and observed particle size grading were observed, especially for the smaller size fractions. These results suggest that these differences could be associated to other factors such as erosion-deposition processes and the chemical weathering of the fine fraction, which although is included in two models, is not enough to investigate the soil water chemistry or mineralogy in detail. However, the measured number of size classes in the fine fraction range is lower than in the coarse fraction, which difficult more detailed interpretation and, therefore, narrower measurement ranges would improve the results of model fits. Further research is needed to determine the extent of these processes.

Acknowledgement

This work has been funded by projects AGL2012-40128-C03-02 and AGL2015-65036-C3-2-R (MINECO/FEDER, UE). Andrea Román-Sánchez is funded by a Contratos Predoctorales Fellowship with reference BES-2013-067009 and by research stay funding with reference EEBB-I-16-11812 (MINECO) in University of Newcastle, Australia. The

authors would also like to thank Prof. Jesús Ayuso of the University of Cordoba for providing access to the experimental area and his continuous support.

References

Attal, M., Mudd, S.M., Hurst, M.D., Weinmann, D., Yoo, K., Naylor, M. 2015. Impact of change in erosion rate and landscape steepness on hillslope and fluvial sediments grain size in the Feather River basin (Sierra Nevada, California). Earth Surface Dynamics 3:201-222.

Bisdom, E.B.A., Stoops, G., Delvigne, J., Kurmi, P., Altemuller, H.-J. (1982) Micromorphology of weathering biotite and its secondary products. Pedologie 33, 225-252.

Brantley, S. L., Eissenstat, D. M., Marshall, J. A., Godsey, S. E., Balogh-Brunstad, Z., Karwan, D. L., Papuga, S. A., Roering, J., Dawson, T. E., Evaristo, J., Chadwick, O., McDonnell, J. J., and Weathers, K. C. (2017). Reviews and syntheses: on the roles trees play in building and plumbing the critical zone, Biogeosciences, 14: 5115-5142. DOI: 10.5194/bg-14-5115-2017.

Brown, W.K. 1989. A theory of sequential fragmentation and its astronomical applications. Journal of Astrophysics and Astronomy. 10:89-112.

Capdevila, R., Corretge, G., Floor P. (1973). Les granitoides vansques de la Meseta lbérique. Bull. Soco Géol. Fr 15:209-228

Corretge, L.G.; Ugidos, J. M. y Martínez, F. J. (1977). Les séries granitiques varisques du secteur Centre-occidental espagnol. La Chaine varisque d'Europe Moyenne et Occidentale. CoIlection Interna. CNRS, 243:453-461.

Cohen, S., G. Willgoose, and G. Hancock (2009). The mARM spatially distributed soil evolution model: A computationally efficient modelling framework and analysis of hillslope soil surface organization. Journal of Geophysical Research: Earth Surface, 114, F03001. DOI: 10.1029/2008JF001214

Cohen, S., Willgoose, G., and Hancockm, G. (2010). The mARM3D spatially distributed soil evolution model: three-dimensional model framework, and analysis of hillslope and landform responses, Journal of

Geophysical Research: Earth Surface 115, F04013. DOI:10.1029/2009JF001536.

Einstein, H. A., 1950. The bedload function for sediment transport in open channel flows, Tech. Bull. 1026, U.S. Dep. of Agric., Soil Conservation Service, Washington, D.C.

Finke, P. (2012). Modeling the genesis of luvisols as a function of topographic position in loess parent material. Quaternary International, 266: 3-17. DOI: 10.1016/j.quaint.2011.10.016

Fowler, A.C., Scheu, B. 2016. A theroretical explanation of grain size distributions in explosive rock fragmentation. Proc. R. Soc. A 472: 20150843.

Garcia-Casco, A., Pascual, E., Fenoll Hach-Alí, P. (1989). Petrogénesis del pluton monzogranitico peraluminico Santa Eufemia (Batolito de Los Pedroches, Córdoba). Estudios geológicos, 45:3-20.

Gee, G.E., Or, D. 2002. Particle size analysis. In J. H. Dane, C. G. Topp,(eds.), Methods of Soil Analysis: Part 4 Physical Methods. SSSA Book Ser. 5.4. SSSA, Madison, WI. § 2.4.

Larrea, F.J., Cueto, L.A., Quesada, C., Fernández, F.J., Larrea, F.J (2013). "Mapa Geológico de España, escala 1:50.000, 2ª serie (MAGNA). Hoja nº 882: Cardeña". Instituto Geológico y Minero de España, Madrid. Cartografía finalizada en 1990. Memoria finalizada y revisada en 2008

Jenny, H. (1941). Factors of soil formation. a system of quantitative pedology. McGraw-Hill, New York.

Legros, J. P., and G. Pedro (1985). The causes of particle-size distribution in soil profiles derived from crystalline rocks. Geoderma, 36:15–25.

Marshall, J.A., Sklar, L.S. 2012. Mining soil databases for landscape-scale patterns in the abundance and size distribution of hillslope rock fragments. Earth Surface Processes and Landform. 37:287-300.

Nash, J. E.; Sutcliffe, J. V. (1970). "River flow forecasting through conceptual models part I — A discussion of principles". Journal of Hydrology. 10 (3): 282–290. DOI:10.1016/0022-1694(70)90255-6.

Parker, G., Klingeman,P.C. 1982. On why gravel bed streams are paved, Water Resources Research. 18: 1409–1433.

Parker, G., Klingeman, P.C., McLean, D.G. 1982. Bed load and size distribution in paved gravel-bed streams, Journal Hydraulic Engineering. ASCE 108:544–571.

Parker, G., Toro-Escobar, C.M. 2002. Equal mobility of gravel in streams: The remains of the day. Water Resources Research. 38. DOI:10.1029/2001WR000669.

Peel, M.C., Finlayson, B.L., McMahon, T.A. 2007. Updated world map of the Koppen-Geiger climate classification. Hydrology Earth System Science 11:1633-1644.

Penha and Arribas, A. (1974). Datación geocronológica de algunos granitos uraníferos españoles". Boletín Geológico y Minero, 85: 271-273.

Poesen, J., Lavee, H. (1994). Rock fragments in top soils: significance and processes. Catena 23: 1–28. DOI: 10.1016/0341-8162(94)90050-7

Riebe, C. S., Hahm, W. J., and Brantley, S. L. (2017). Controls on deep critical zone architecture: a historical review and four testable hypotheses. Earth Surface Processes and Landforms, 42: 128–156. DOI: 10.1002/esp.4052.

Román-Sánchez, A., Giráldez, J.V. and Vanwalleghem, T. (2014). Modelling the effect of climate and relief on soil formation on granites. Avances de la Geomorfología en España 2012-2014. XIII Reunión Nacional de Geomorfología, Cáceres, 246.

Román-Sánchez, A., Giráldez, J.V. and Vanwalleghem, T. (2015). Evaluating a spatial soil water balance model under mediterranean climate and interaction with soil formation. XII Jornadas de lnvestigación en Ia Zona No Saturada (ZNS'15), Alcalá de Henares.

Román-Sánchez, A., Vanwalleghem, T., Peña A., Laguna A., Giráldez J.V. (2018). Controls on soil carbon storage from topography and vegetation in a rocky, semi-arid landscapes. Geoderma, 311: 159-166. DOI: 10.1016/j.geoderma.2016.10.013.

Russell, D.A. 1976. Particle-size distribution characterization for the coarse fraction of a granite soil. I. A model. Soil Science Society of America Journal 40:409-413.

Ruiz, S., Schymanski, S.J., Or, D. 2017. Mechanics and energetics of soil penetration by earthworms and plant roots: higher rates cost more, Vadose Zone Journal 16(8) DOI:10.2136/vzj2017.01.0021.

Sanchidrián, J.A., Ouchterlony, F., Segarra, P. and Moser, P. (2014). Size distribution functions for rock fragments. International Journal of Rock Mechanics and Mining Sciences, 71: 381-394

Schaetzl, R., & Anderson, S. (2005). Soils: Genesis and Geomorphology. Cambridge: Cambridge University Press. DOI:10.1017/CBO9780511815560

Sharmeen, S., and Willgoose G. R. (2006). The interaction between armouring and particle weathering for eroding landscapes. Earth Surface Processes and Landform, 31: 1195–1210. DOI:10.1002/esp.1397

Sklar, L.S., Riebe, C.S., Marshall, J.A., Genetti, J., Leclere, S., Lukens, C.L., Merces, V., (2017). The problem of predicting the size distribution of sediment supplied by hillslopes to rivers. Geomorphology.277:31-49 DOI: 10.1016/j.geomorph.2016.05.005

St.Clair, J., Moon, S., Holbrook, W.S., Perron, J.T., Riebe, C.S., Carr, B., Harman, C., Singha, K., Richter, D. de B. 2015. Geophysical imaging reveals topographic stress control of bedrock weathering. Science 350:534-538.

Temme, A. J. A. M., and Vanwalleghem, T. (2016). LORICA – A new model for linking landscape and soil profile evolution: Development and sensitivity analysis, Computers & Geosciences 90: 131–143. DOI:10.1016/ j.cageo.2015.08.004.

Vanwalleghem, T., Stockmann, U., Minasny, B., and McBratney, A. B. (2013). A quantitative model for integrating landscape evolution and soil formation, Journal of Geophysical Research: Earth Surface, 118: 331–347. DOI:10.1029/2011JF002296.

Welivitiya, W. D. D. P., Willgoose, G. R., Hancock, G. R., and Cohen, S. (2016). Exploring the sensitivity on a soil area-slope-grading relationship to changes in process parameters using a pedogenesis model, Earth Surface and Dynamics, 4: 607-625. DOI:10.5194/esurf-4-607.

Wells, T., Binning, P., Willgoose, G., and Hancock, G. (2006). Laboratory simulation of the salt weathering of schist: I. Weathering of schist

blocks in a seasonally wet tropical environment. Earth Surface Processes and Landforms, 31(3): 339– 354. DOI: 10.1002/esp.1248

Wells, T., Willgoose, G., and Binning, P. (2007). Laboratory simulation of the salt weathering of schist: II. Fragmentation of fine schist particles. Earth Surface Processes and Landforms, 32(5): 687– 697. DOI: 10.1002/esp.1450

Wells, T., Willgoose, G, and Hancock, G. (2008). Modeling weathering pathways and processes of the fragmentation of salt weathered quartz-chlorite schist, Journal of Geophysical Research: 113, F01014, DOI:10.1029/2006JF000714.

Willgoose, G. (2018). Principles of Soilscape and Landscape Evolution. Cambridge University Press. Online ISBN: 9781139029339.

Willmott, C. J., Robeson, S.M., Matsuura, K. 2012. A refined index of model performance. Int. J. Climatol. 32: 2088–2094.

Wohletz, K.H., Sheridan, M.F., Brown, W.K. 1989. Particle size distributions and the sequential fragmentation/transport theory applied to volcanic ash. Journal of. Geophysical Research 94:15,703-15,721.

CHAPTER 6

CONCLUSIONS

This study expands our knowledge on soil forming processes. This information will contribute to get a broader and clearer perspective of soil formation and landscape evolution, and improve our capability to model these processes numerically.

Specifically, the soil forming processes studied here are bioturbation, erosion-deposition and physical weathering. These processes are associated with the variables controlling soil carbon storage in a rocky Meditteranean landscape in chapter 2. Chapter 3 describes soil profile dating and effective soil mixing rates in order to calculate bioturbation and erosion-deposition rates in the chapter 4 and, finally, the vertical and lateral rock fragmentation patterns are described in chapter 5.

It was shown in chapter 2 that the study area of Santa Clotilde is characterized by a high spatial variability in carbon stocks, stoniness and bulk density. The main variable controlling the spatial distribution of stoniness is slope, demonstrating the importance of the erosion. Solar radiation and vegetation cover control carbon concentration and carbon stocks. Although the validation of the random forest used shows that only 18% of the variation in the dataset is explained, there are evidences that the soil moisture and vegetation dynamics are important on the carbon balance in these semi-arid areas (Román-Sánchez et al. 2018).

Chapter 3 presents a novel method for dating soil particles. Bioturbation and surface erosion-deposition are the main vertical and lateral soil mixing processes, which are identified by the variation of the age-depth trend along the hillslope using this novel feldspar-based single grain post Infrared Stimulated Luminescence (post-IR IRSL) technique. The effective mixing rate, described for the first time in the study of Reimann et al. (2017) and incorporated in the study of the *chapter 3*, is an important metric measure, which take into account only the soil grains that effectively participate in the mixing process. This study shows that the portion of surface-visiting grains is in some cases quite low, and the effective mixing rate presents a significant improvement over previously published soil mixing rates. This study concludes that the observed luminescence age-depth profiles along the hillslope catena can be explained from the combined effects of bioturbation and erosion-depositional processes. Lastly, for the first time, it was also shown how this luminescence methodology can be used as an objective method to establish the boundary between the mobile regolith and saprolite, as it takes into account the fraction of non-light exposed mineral grains. While this boundary corresponds in most cases to the soil-saprolite boundary that was identified in the field, in some profiles this was not the case.

The new analytical solution of the diffusion-advection equation described in the *chapter 4* is used to calculates bioturbation and erosion-deposition rates. Pre-existing luminescence models were based on quartz rather than feldspar, or numerical instead of analytical, or addressing only the flat or eroding sections of the hillslope, while this model addresses both simultaneously. The results show how the rates of bioturbation and erosion-deposition can be estimated by means of the variation of the age-depth trend along the hillslope calculated using feldspar-based single grain post Infrared Stimulated Luminescence (post-IR IRSL) technique. The assessment of the uncertainty reveals the most uncertainty in the erosion-deposition rates, probably because the absolute rates are quite low. The global sensitivity analysis shows that the most important parameters controlling the age along the hillslope are the diffusivity constant and mobile regolith depth, hereby indicating the importance of correctly identifying the soil-saprolite boundary. As was discussed in chapter 3, the luminescence technique provides an objective way of doing this.

The rock fragmentation study described in the chapter 5 analyzes the physical weathering processes, comparing different rock fragmentation models against field data. In six of the ten studied profiles, these models are able to adequately simulate the surface grading from the subsurface grading. However, in the remaining four profiles, all located in sloping areas, the erosion and resulting surface armouring dominates over the fragmentation processes and does not make it possible to apply the rock fragmentation models. The results of the six profiles allowed to identify two different zones in the study area, with contrasting fragmentation behaviour. Although the model results in a good fit to the vertical particle size distribution of each soil profile, some deviations are observed, especially for the smaller size fractions. In order to explain the discrepancies between the field data and the model results, especially in the fine fraction, two reasons are proposed. One possibility is the possible relevance of biological processes or chemical weathering of the fine fraction. Although the latter process is included in two models, it is not represented with much detail. A second reason could be found in the lower accuracy of the data available in the fine fraction, as the number of classes established and measured is lower than in the coarse fraction, making it more difficult to obtain a good model fit to the field data.

This research provides important advances in our knowledge of the soil forming processes, so that it can be specifically applied into soil formation studies. Specifically, an important finding is to know the objective transition between mobile regolith and saprolite

based on luminescence. Given the importance of this transition for determining soil formation rates using for example cosmogenic nuclides, that are sampled along the soil-saprolite boundary, correctly identifying this boundary is paramount. Also, to establish the spatial and vertical distribution of the rock fragmentation patterns yields important information on not only physical weathering but also other processes such as physical processes (erosion-deposition, armouring) or chemical weathering. These results allow the calibration and validation of soil formation and landscape evolution models in the future, so as to better our understanding of pedogenesis and geomorphological processes on long time scales.

In future work, this work should be complemented with an evaluation of the chemical weathering processes in our study area, in order to understand their contribution to soil formation. This process should be carried out in soil profiles along two hillslopes with opposite orientation (north and south) to evaluate the relevance of this exposition and soil water dynamics in chemical weathering.

To complete the understanding of the physical processes should be analysed with the radioactive isotope ^{10}Be or ^{137}Cs the rates of erosion-deposition along the hillslopes to contrast the results with those obtained in this study using feldspar-based single grain post Infrared Stimulated Luminescence (post-IR IRSL) technique.

Finally, a new spatially explicit model will be generated which integrates water infiltration and redistribution, climate with daily paleoclimatic reconstruction of 25.000 years, topographical variables (slope, aspect) and physical, biological and chemical processes in the soil.

APPENDICES

APPENDIX A: SUPPLEMENTARY FIGURES AND TABLES

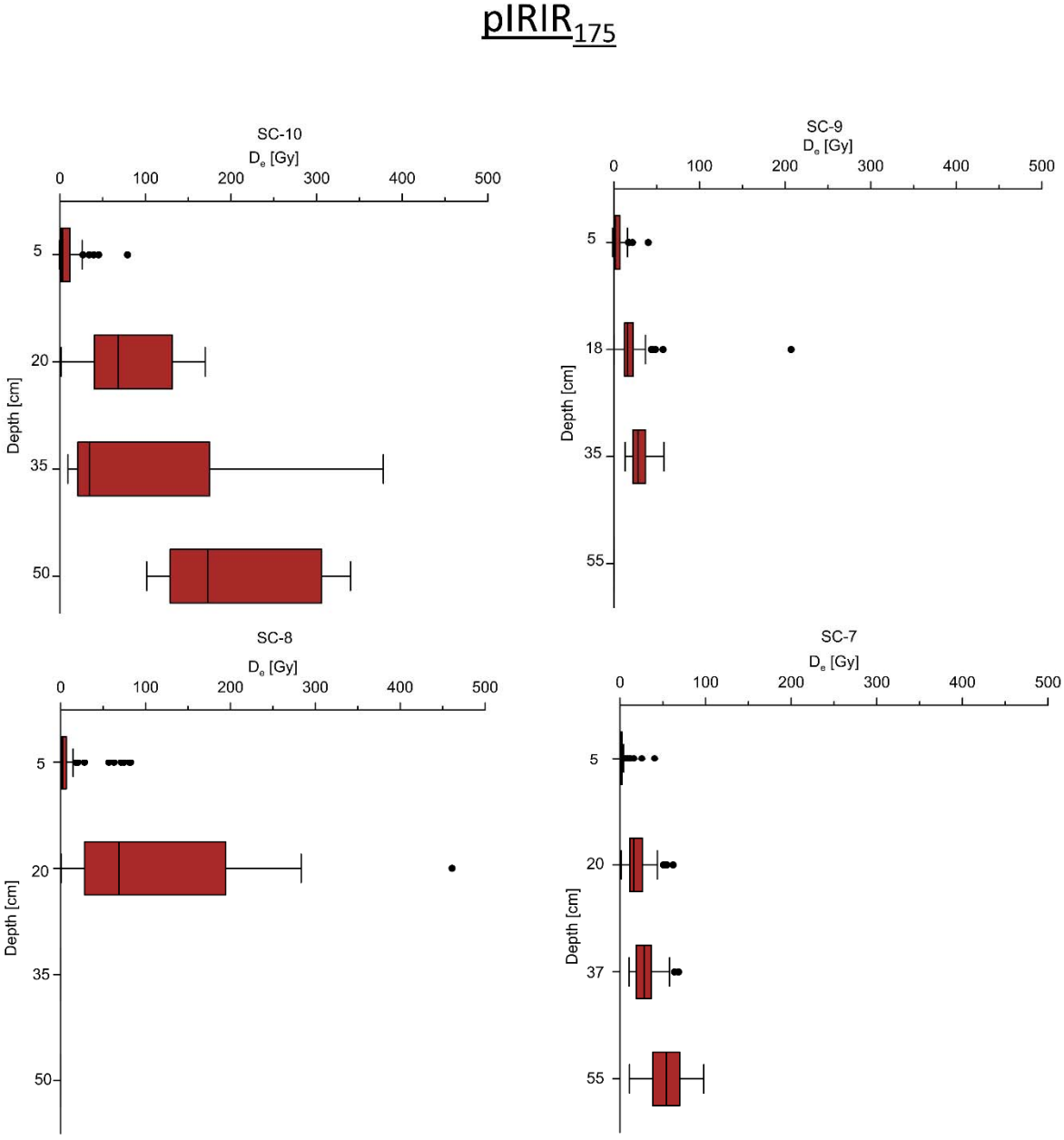

Figure 3.S1 Equivalent dose (De) for the four soil profiles (SC-7, SC-8, SC-9, SC-10) at different depths for the pIRIR175 signal. The box encompasses the lower and upper quartile, with the line in the middle representing the median. The whiskers represent measurements that are still within a 1.5 interquartile range from the quartiles of the distribution. Outliers from this distribution are plotted as individual points. Note that no points are shown for the $pIRIR_{175}$ signal in SC-8 and 9 at the deepest sampling level because all grains were saturated.

Table 3.S1 Dose rate

Soil profile and depth, z (cm)	Cosmic ray	Grain size and water attenuated external gamma	Internal Alpha	Grain size and water attenuated external Beta	Internal Beta	^{238}U	^{232}Th	^{40}K	Total dose rate
	[Gy ka^{-1}]	[Gy ka^{-1}]	[Gy ka^{-1}]	[Gy ka^{-1}]	[Gy ka^{-1}]	[Bq kg^{-1}]	[Bq kg^{-1}]	[Bq kg^{-1}]	[Gy ka^{-1}]
SC-7									
5	0.27 ± 0.014	1.28 ± 0.082	0.01 ± 0.005	3.19 ± 0.228	0.94 ± 0.10	51.95 ± 0.569	66 ± 1.400	1238 ± 23	5.71 ± 0.260
20	0.27 ± 0.013	1.53 ± 0.093	0.01 ± 0.005	2.84 ± 0.201	0.93 ± 0.10	49.44 ± 0.539	57.40 ± 1.129	1106 ± 20.74	5.59 ± 0.242
37	0.25 ± 0.012	1.70 ± 0.099	0.01 ± 0.005	2.95 ± 0.206	0.93 ± 0.10	57.89 ± 0.603	64.75 ± 1.378	1168 ± 21.73	5.86 ± 0.248
55	0.24 ± 0.012	2.03 ± 0.137	0.01 ± 0.005	3.34 ± 0.244	0.93 ± 0.10	52.11 ± 0.640	68.688 ± 1.454	1256 ± 26	6.58 ± 0.296
SC-8									
5	0.27 ± 0.013	1.497 ± 0.106	0.01 ± 0.005	3.43 ± 0.238	0.93 ± 0.10	64.02 ± 0.75	77.105 ± 1.577	1339 ± 27.62	6.16 ± 0.279
20	0.27 ± 0.013	1.87 ± 0.093	0.01 ± 0.005	3.09 ± 0.201	0.93 ± 0.10	79.78 ± 0.778	93.52 ± 1.740	1228 ± 22.79	6.18 ± 0.242
35	0.25 ± 0.012	1.92 ± 0.100	0.01 ± 0.005	2.72 ± 0.18	0.93 ± 0.10	89.23 ± 0.86	95.08 ± 1.78	970.9 ± 18.43	6.61 ± 0.220
SC-9									
5	0.28 ± 0.014	1.30 ± 0.071	0.01 ± 0.005	3.11 ± 0.174	0.78 ± 0.14	42.24 ± 0.496	64.06 ± 1.357	1103 ± 20.71	5.5 ± 0.290
18	0.26 ± 0.013	1.42 ± 0.069	0.01 ± 0.005	2.51 ± 0.137	0.78 ± 0.14	32.34 ± 0.405	55.885 ± 1.219	958.9 ± 18.10	5.08 ± 0.260
35	0.25 ± 0.012	1.62 ± 0.085	0.01 ± 0.005	2.79 ± 0.155	0.78 ± 0.14	33.00 ± 0.445	58.81 ± 1.280	1070 ± 22.27	5.64 ± 0.290
55	0.24 ± 0.012	1.47 ± 0.071	0.01 ± 0.005	2.57 ± 0.140	0.78 ± 0.14	29.59 ± 0.368	53.361 ± 1.144	1013 ± 18.88	5.12 ± 0.260
SC-10									
5	0.27 ± 0.013	1.47 ± 0.100	0.01 ± 0.005	3.43 ± 0.193	0.93 ± 0.10	48.63 ± 0.612	64.00 ± 1.398	1241 ± 25.72	6.13 ± 0.238
20	0.27 ± 0.013	1.35 ± 0.085	0.01 ± 0.005	2.58 ± 0.186	0.93 ± 0.10	28.63 ± 0.381	51.20 ± 1.186	1051 ± 19.80	5.17 ± 0.227
35	0.25 ± 0.012	1.42 ± 0.099	0.01 ± 0.005	2.51 ± 0.189	0.93 ± 0.10	28.67 ± 0.397	49.94 ± 1.206	944 ± 18.88	5.15 ± 0.235
50	0.24 ± 0.012	1.55 ± 0.078	0.01 ± 0.005	2.72 ± 0.151	0.93 ± 0.10	29.76 ± 0.357	54.41 ± 1.116	1034 ± 19.11	5.478 ± 0.196

Table 3.S2 Saturated and non-saturated feldspar grains. nmeasured: number of grains measured, nluminescent: number of grains that emit luminescence, naccepted: number of grains accepted following the luminescence protocol (Reimann et al., 2017), nnon-saturated: number of grains no saturated, nabove saturation: number of grains above saturation

Soil profile and depth, z (cm)	nmeasured	nluminescent	%	naccepted	%	nnon-saturated	nabove saturation	%
SC-7								
5	300	124	0.41	97	0.32	96	1	0.01
20	300	137	0.46	112	0.37	105	7	0.06
37	500	232	0.46	141	0.28	130	11	0.08
55	300	209	0.70	153	0.51	54	99	0.65
SC-8								
5	400	148	0.37	103	0.26	94	9	0.09
20	500	139	0.28	71	0.14	49	22	0.31
35	1300	11	0.01	9	0.01	0	9	1.00
SC-9								
5	300	141	0.47	113	0.38	103	10	0.09
18	300	224	0.75	156	0.52	65	91	0.58
35	300	185	0.62	65	0.22	5	60	0.92
55	300	229	0.76	131	0.44	0	131	1.00
SC-10								
5	300	135	0.45	94	0.31	91	3	0.03
20	300	156	0.52	107	0.36	13	94	0.88
35	900	173	0.19	90	0.10	11	79	0.88
50	300	201	0.67	145	0.48	9	136	0.94

APPENDIX B: PEER-REVIEWED PUBLICATIONS AND CONFERENCE PUBLICATIONS

Geoderma 311 (2018) 159–166

Contents lists available at ScienceDirect

Geoderma

journal homepage: www.elsevier.com/locate/geoderma

Controls on soil carbon storage from topography and vegetation in a rocky, semi-arid landscapes

A. Román-Sánchez [a], T. Vanwalleghem [a,*], A. Peña [b], A. Laguna [c], J.V. Giráldez [a,d]

[a] Department of Agronomy, University of Cordoba, Spain
[b] Department of Rural Engineering, University of Cordoba, Spain
[c] Department of Applied Physics, University of Cordoba, Spain
[d] Institute for Sustainable Agriculture, (IAS), CSIC, Spain

ARTICLE INFO

Article history:
Received 26 May 2016
Received in revised form 1 October 2016
Accepted 12 October 2016
Available online 18 October 2016

Keywords:
Soil carbon
Stoniness
Critical zone
Random forest
Solar radiation
Vegetation

ABSTRACT

Soil properties can exhibit strong spatial variation, even at the small catchment scale. Especially soil carbon pools in semi-arid, mountainous areas are highly uncertain because bulk density and stoniness are very heterogeneous and rarely measured explicitly. The effect of topographic and vegetation variables, on stoniness, bulk density and soil carbon has been explored in a 2.7 km^2 watershed of Sierra Morena in south Spain. Soil core samples were collected from 67 locations at 6 depths up to 0,3 m. Stoniness and bulk density were measured with standard methods, total organic carbon through elemental analysis. These soil properties were then used to calculate carbon stock and related to solar insolation, elevation, slope, curvature, TWI, TPI, SPI and NDVI. Stone content depends on slope, indicating the importance of water erosion on long-term soil development. Spatial distribution of bulk density was found to be highly random. By means of conventional statistical methods, with the help of a random forest method, solar radiation and NDVI proved to be the key variable controlling soil carbon distribution. Total soil organic carbon stocks were 4.38 kg m^{-2} on average, with stocks about double as high on north versus south-facing slopes. These results confirm the importance of the coupled soil moisture and vegetation dynamics on the carbon balance in semi-arid ecosystems. However, validation of the random forest model showed that the different covariates only explained 18% of the variation in the dataset. Apparently, present-day landscape and vegetation properties are not sufficient to fully explain the full variability in the soil carbon stocks in this complex terrain under natural vegetation. This is attributed to a high spatial variability in bulk density and stoniness, key variables controlling carbon stocks. Future improvement of mechanistic soil formation models could help estimating these soil properties better.

1. Introduction

Within a catchment, topography exerts a first-order control over insolation, water and nutrient fluxes, and vegetation patterns, causing differences between south and north facing slopes (Ivanov et al. 2008, Yetemen et al. 2015a), although this is modulated by aridity as, for instance, reported by Mâren et al. (2015). Vegetation and soil moisture dynamics can be expected to control not only landscape shape but also belowground critical zone architecture and properties, especially soil organic carbon (SOC) stocks. Kunkel et al. (2011) showed how NDVI and potential insolation explained 62% of the variation in SOC stocks in the complex semi-arid Dry Creek Observatory, Idaho. However, in complex, rocky terrain, bulk density (BD) and stoniness (ST), soil properties that are often not explicitly measured, exert an important control over SOC stocks. Schrumpf et al. (2011) concluded that SOC stock errors are more dependent on BD and ST than carbon concentration (C) in rocky terrain. Throop et al. (2012) showed that different methods for taking into account the coarse fragment content can lead to differences of up to 26% in carbon stock. As this information is often difficult to measure, many studies assessing SOC stock variability use indirect methods to estimate the latter two variables, using a constant value for BD and ST values from published data (e.g. Kunkel et al. 2011) or pedotransfer functions (e.g. Bonfatti et al. 2016). While such indirect methods might be a reasonable approximation in simple, agricultural landscapes with low ST, this approach will potentially lead to large errors in complex, stony landscapes. Especially if we are interested in the variables controlling SOC stocks, it is critical to simultaneously assess the spatial variability in C, BD and ST. While C distribution has been linked to vegetation patterns and insolation, as mentioned before, controls over BD and ST are less clear. BD, but especially ST can be expected to vary in response to weathering, transport and biological processes. Geroy et al. (2011) showed how soils in the Dry Creek Observatory,

* Corresponding author at: Edificio Leonardo da Vinci, Campus de Rabanales, University of Cordoba, Cra Madrid km 396, 14014,Córdoba, Spain.
E-mail address: ag2vavat@uco.es (T. Vanwalleghem).

http://dx.doi.org/10.1016/j.geoderma.2016.10.013
0016-7061/

Idaho are typically shallower on south compared to north-facing slopes and the latter can store more water from the wet winter. They also found important differences in SOC, ST, and BD, based on 35 surface samples. Anderson et al. (2013) showed how aspect-related differences in temperature modulate frost cracking and regolith production, leading to distinct weathering rates in the Boulder Creek Critical Zone Observatory, Colorado. Hillslope hydrology and chemical weathering rates are also clearly aspect-related (Anderson et al. 2014). Both global and local studies have shown how transport processes and landscape evolution interact with biological processes (Istanbulluoglu and Bras 2006; Yetemen et al. 2015a; Yetemen et al. 2015b).

It is clear that there are important interactions between soil properties, water dynamics, plant growth and carbon dynamics. Many of these interactions are not well quantified yet, especially over longer time scales. If we are to develop mechanistic models of soil formation and landscape evolution (Vanwalleghem et al. 2013; Temme and Vanwalleghem 2016), we need to better understand these interactions and the resulting patterns.

The objectives of this study were: 1) to identify the factors controlling the spatial distribution of carbon concentration, bulk density and stoniness; 2) to use these variables to predict carbon stocks.

2. Materials and methods

2.1. Study area

This study was done in the Santa Clotilde Critical Zone Observatory (SC-CZO), located in Southern Spain (Fig. 1A). The outline of the study area corresponds with an experimental farm operated by the University of Cordoba and covers 2.7 km^2. The study area is located within the Martin Gonzalo catchment in Sierra of Cardeña and Montoro Natural Park, placed in the Sierra Morena. This mountainous ridge separates the Spanish Central Plateau and the Betic Depression. The bedrock in this area consists of plutonic rock, microadamellita porphyritic and it is part of the Pedroches Batholith. The predominant soils are Regosols, Leptosols and Cambisols under the FAO-Unesco World Reference Base

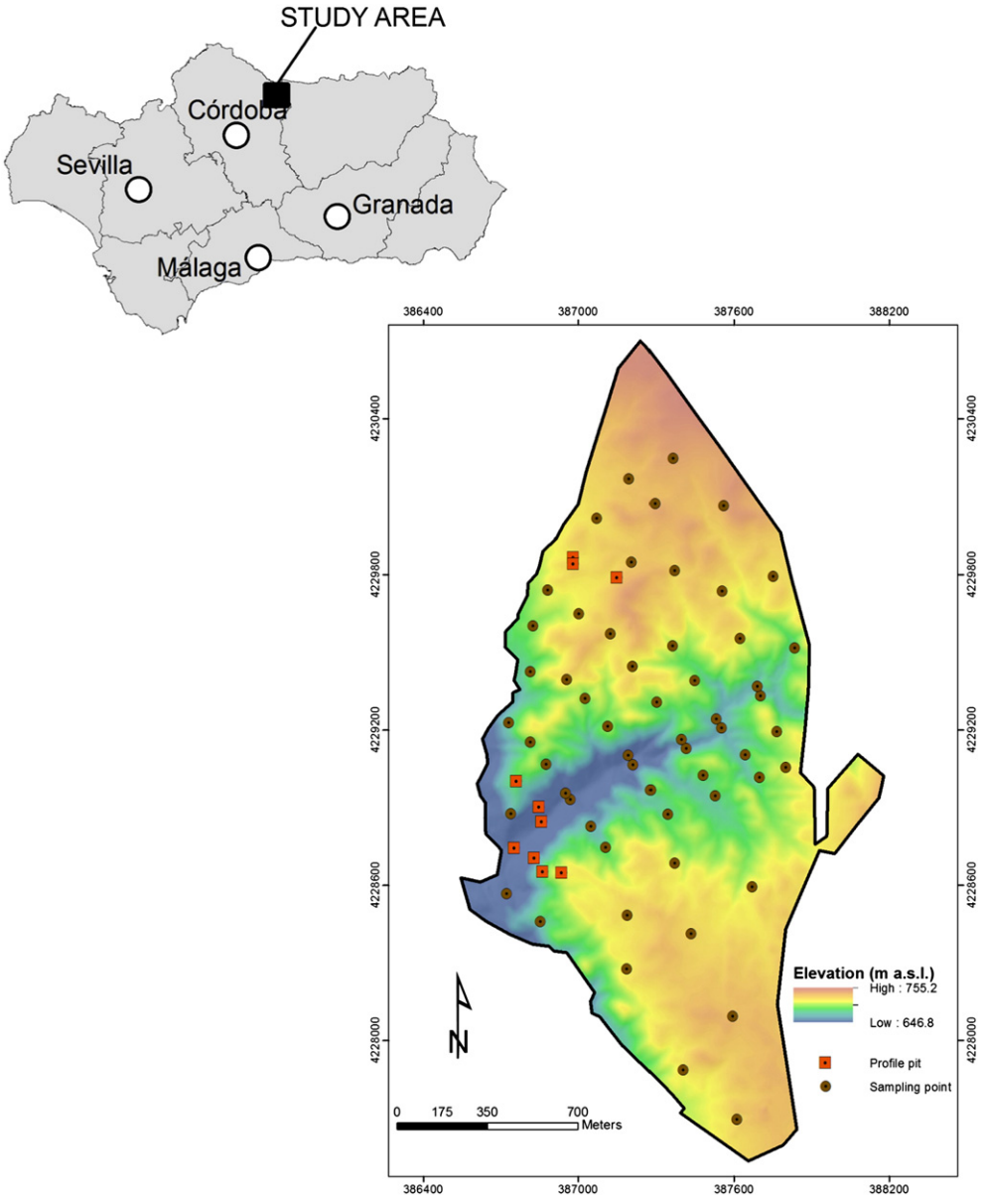

Fig. 1. Location (left), topography (right) of Santa Clotilde Critical Zone Observatory and sampling points within study area.

(IUSS Working Group WRB, 2014). The topography is characterized by a gently rolling plateau area and a steeply incised valley towards the south of the study area, with elevations between of 645 and 755 m asl (Fig. 1. B). The slopes in this valley area are steep, typically between 20 and 75%, while in the slopes in the plateau areas are mild, between 0 and 5%.. The climate is True Mediterranean following the Aschmann (1984) criteria, with an average rainfall of 582 mm and a marked wet season during winter. Temperatures vary between 5 and 40 °C. The area is covered by oak-woodland savannah ("dehesa"), which is used for extensive grazing. The stocking densities are very low, i.e. below 0,10 LSU ha^{-1}. The prevailing textural classesin the area are sandy to sandy loam and the observed variation in soil depth is large, generally ranging between 0.5 and 2.40 m.

2.2. Sampling and measurement

Samples were taken at 67 points, in a combined design-convenience sampling scheme that evenly distributed over the study area in order to cover all different terrains settings using the variables shown in Table 1. Sampling points were always located outside the influence of the tree canopy, in order to avoid local heterogeneities due to the influence of the trees (Simón et al. 2012). At 10 locations, located along 3 transects, profile pits were made and analyzed. At 57 locations, 6 ring samples were taken at 5 cm depth increments down to 30 cm, using a standard Eijkelkamp sample ring kit with a diameter of 5.36 cm. The high stone content prevented sampling below 30 cm and comparison with soil profile data showed that the top 30 cm held on average 70% of the carbon stock. The soil profile pits were sampled along horizon boundaries and subsequently harmonized to 5 cm increments using mass-conserving splines (Malone et al. 2009). A smoothing parameter lambda of 0.1 was used. As sampling up till 30 cm was not always possible in all points due to large rock fragments, a total of 278 samples was obtained.

Samples were stored at −5 °C in sealed bags until laboratory analysis. All samples were oven dried at 105 °C and sieved to 2 mm to determine the stone content and bulk density. Next, between 25 and 30 mg of fine earth was further processed by grounding and a finer sieving to 0.5 mm to measure carbon content. Total organic C and was determined by thermocatalytic oxidation with a temperature of 800 °C using a Elemental CHNS Eurovector EA 3000 (e.g. Giacometti et al. 2013).

Soil organic carbon stocks for each soil layer i, SOC_i, [kg m^{-2}], are calculated with the correction of the stone volume fraction, or material whose representative diameter is >2 mm, S_i [m^3 m^{-3}], using the following equation:

$$SOC_i = \frac{1}{1000} C_i h_i \rho_i (1 - S_i) \quad (1)$$

where h_i is the layer thickness [m]. ρ_i, the bulk density of the layer [Mg m^{-3}], and C_i its organic carbon fraction [kg C kg^{-1}]. Bulk density, ρ_i, is calculated as the oven-dry mass of solids per sample volume. Stone volume fraction, S_i, is calculated from the measured mass fraction of fragments >2 mm, and assuming a stone bulk density of 2.65 Mg m^{-3}.

2.3. Predictor variables and data analysis

The predictor variables that were included in the analysis are defined in Table 1. Potential insolation depends on aspect, slope gradient, elevation and location and was calculated using the Solar Analyst Tools in ESRI ® Arcmap 10.2 based on the 5 m NGI DEM. Elevation, slope, (S), and curvature were all calculated from the same DEM. Determination of specific contributing area, (A), needed for calculating the Topographic Wetness Index (TWI) and the Stream Power Index (SPI) were calculated in TauDEM using the D-infinity algorithm (Tarboton 1997). Finally, the Topographic Position Index (TPI) is used as a proxy for landscape position, and expressed the elevation of a point with respect to mean elevation. Negative values correspond to lower-lying valley-bottom points, while positive values correspond to ridges and higher elevations.

Vegetative cover reflects ecosystem productivity and controls soil carbon input. The Normalized Difference Vegetation Index (NDVI) is a commonly used, and easily calculated, satellite image-based proxy for vegetative cover. Here, average yearly NDVI was determined from Landsat-5 Thematic Mapper Imagery at 30 m resolution (http://earthexplorer.usgs.gov/) for the period 1982–2012. Yearly fluctuations in rainfall are known to affect the spatial distribution of the understory grass vegetation and NDVI (e.g. Lozano-Parra et al., 2014), but studying this variability goes well beyond the scope of this study. It was assumed that the long-term vegetation distribution is adequately represented by the mean NDVI over this thirty year period.

All statistical analyses were performed in R (R Development Core Team 2008). Firstly, the variation of C, BD, ST and SOC was evaluated against all covariates from Table 1. All covariates used in the analysis were checked against cross-correlation, and had a Variance Inflation Factor below 5. Finally, we calculated cumulative stocks. Missing sampling depths, generally due to field limitations where rock fragments obstructed coring, were reconstructed by fitting a mass-preserving regression fit with depth. A preliminary trial with different regression models was performed, but here we used Random Forests, (RF), which gave the lowest R^2 of the validation data set. The RF is a robust, tree-based Machine learning method (e.g. Breiman 2001). RF contains not a single standard regression tree but many regression trees, like a forest. We implemented RF through the package randomForest in R. We performed 100 realizations of the training and validation dataset, using a 75-25 split of the original dataset. Prior to fitting each RF model, the "train" function of the "caret" R package was used to obtain the optimal number of trees to grow. The reported RF results are therefore the average of these different realizations.

3. Results and discussion

3.1. Vertical distribution of bulk density, stoniness, carbon content and carbon stocks

Table 2 and Fig. 2 show how bulk density increases linearly with depth, from a mean value of 1.32 Mg m^{-3} at the surface to 1.58 Mg m^{-3} at the bottom of the sampled profile (25–30 cm). This increase is common to lower C content and higher compaction in depth, but here it is also related to the increase in stoniness. Stoniness increases

Table 1
Variables analyzed as controlling the spatial distribution of bulk density, stoniness and soil carbon.

Abbreviation	Data description	Units	Mean	Median	Stdev	Min	Max
Insolation	Potential incoming solar radiation	10^6W h m^{-2}	1.36	1.40	0.12	0.91	1.51
Elevation	Elevation above mean sea level	m	713	716	22	653	745
Slope	Local slope gradient	m m^{-1}	0.22	0.18	0.15	0.02	0.66
Curvature	Local hillslope curvature	m	−0.30	−0.16	1.71	−7.12	4.51
TWI	Topographic wetness index (Beven and Kirkby 1979)	–	5.41	5.00	1.65	3.30	11.95
TPI	Topographic position index (Guisan et al. 1999)	–	−0.36	−0.24	1.60	−4.60	4.09
SPI	Stream power index (Moore et al. 1991)	–	1.79	1.70	1.50	-1.49	7.15
NDVI	Normalized Difference Vegetation Index	–	0.60	0.59	0.07	0.49	0.78

Table 2
Summary statistics of carbon concentration (C), bulk density (ρ), stoniness (ST) and soil carbon stocks (SOC).

		Mean	St.Dev.	Min	Max
C (%)	0–5 cm	3.1	1.7	1.1	8.1
	5–10 cm	1.7	1.2	0.5	6.9
	10–15 cm	1.3	0.8	0.4	4.8
	15–20 cm	1	0.6	0.2	3.1
	20–25 cm	0.8	0.6	0.2	3.4
	25–30 cm	0.6	0.4	0.2	2.2
ρ (Mg m^{-3})	0–5 cm	1.3	0.2	0.9	2.3
	5–10 cm	1.5	0.2	0.9	2.0
	10–15 cm	1.5	0.2	1.0	1.9
	15–20 cm	1.5	0.2	1.1	2.0
	20–25 cm	1.6	0.2	1.2	2.0
	25–30 cm	1.6	0.2	1.3	1.9
ST (%)	0–5 cm	14.2	8.8	0.8	39.3
	5–10 cm	23.6	14.8	4.8	64.8
	10–15 cm	26.6	19.6	5.2	83.4
	15–20 cm	28.6	18.9	5.7	76.9
	20–25 cm	28.8	19.1	4.3	76.9
	25–30 cm	31.8	20.0	4.1	82.1
SOC (kg m^{-2})	0–5 cm	1.62	0.61	0.69	3.14
	5–10 cm	0.96	0.49	0.27	2.59
	10–15 cm	0.67	0.35	0.04	1.69
	15–20 cm	0.51	0.29	0.06	1.46
	20–25 cm	0.41	0.26	0.07	1.44
	25–30 cm	0.32	0.20	0.09	1.06
	0–30 cm	4.38	1.77	1.70	9.41

exponentially with depth, ranging between 14% near to surface to 32% at the bottom. The variation in the dataset is very high, ranging from 0.7% to 84%. Depth is a good predictor of stoniness, explaining 82% of the variation. Phillips et al. (2005) observed a similar pattern in a study of rock fragment distribution in the Ouachita Mountains, Arkansas. They concluded that this increase of ST with depth points to an active production of coarse fragments near the soil-bedrock interface.

C content is relatively low throughout, with mean values decreasing from 3.1% near the surface to 0.6% between 25 and 30 cm. At the surface, maximum and minimum values are respectively 8.1% and 1.1%. C content follows an exponential decreasing pattern with depth. Depth below the surface is an excellent predictor that explains 96% of the variance, much higher than for BD or ST.

Finally, mean calculated SOC stocks range between 1.62 kg m^{-2} for the top 5 cm to 0.32 kg m^{-2} at the bottom of the sampled profiles. Again, SOC stocks decrease exponentially with depth, and the depth-dependence is similar to that of C, explaining 97% of the variation. The total SOC stock for the entire sampled profile sums up to 4.38 kg m^{-2} on average, and varies considerably between 1.70 and 9.41 kg m^{-2}. The values found in this study are towards the high end of their observed range of 2.28 kg m^{-2}–4.45 kg m^{-2}. Simón et al. (2012), who studied a similar oak-savanna ecosystem, found SOC stocks in the uppermost 5 cm of 1.05–1.24 kg m^{-2}, about 30% lower than in our study for the same depth, despite yearly precipitation being similar between the two study areas. Howlett et al. (2011) measured SOC stocks up to 1 m in oak woodland savannas and reported values of 2.99 kg m^{-2} (Gómez-Rey et al. 2012).

3.2. Relation between bulk density, stoniness, carbon content and carbon stocks

Of the three factors used in calculating carbon stocks, bulk density (BD), stoniness (ST), and carbon content (C), both BD and ST show a significant, negative exponential correlation, Fig. 3, but the overall R^2 is relatively low, respectively 0.31 and 0.15. This is in contrast with findings from other studies. Based on a study of an agricultural plot in Germany, Bornemann et al., (2011) found that stoniness was linearly related to SOC stock and explained 73% of variability in SOC stock. A possible reason for the difference between the R^2 of our data and that of the latter authors could be that in their study, BD variations were not taken into account. Another reason however is possibly the higher spatial

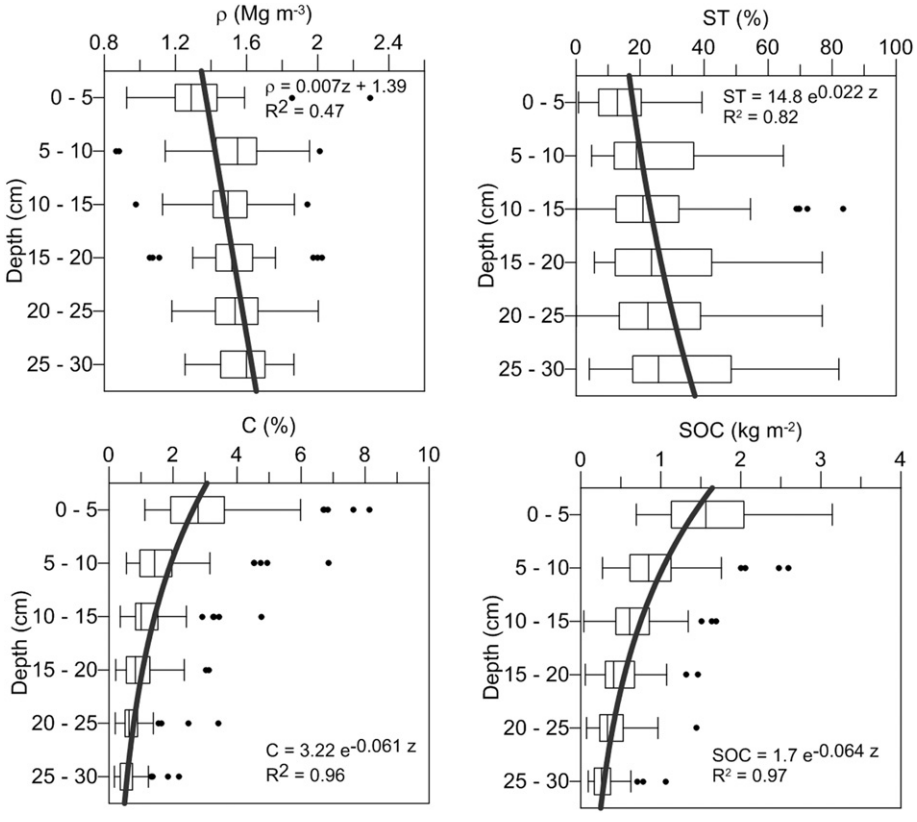

Fig. 2. Variability of bulk density (ρ), stoniness (ST), carbon concentration (C) and soil carbon stocks (SOC) with depth (z).

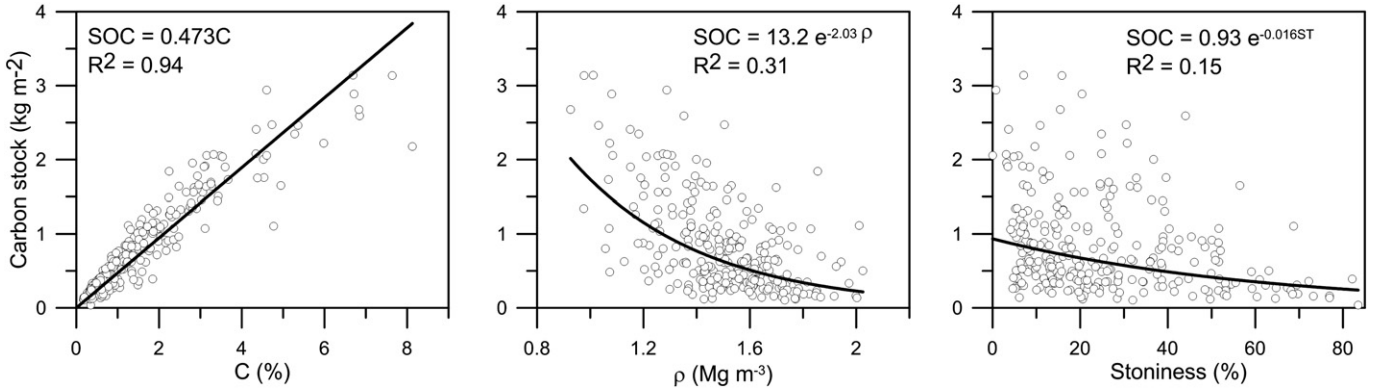

Fig. 3. Relation between carbon stock and carbon content (%), stone content (%) and bulk density (Mg cm^{-3}).

variability of soil properties in natural areas, like our study site. Hoffmann et al. (2014) studied carbon stock variability in the Canadian Rocky Mountains and found a similar low correlation with bulk density and stoniness (explaining respectively 7% and 14% of the observed variability). In agricultural soils, processes such as erosion or tillage tend to drive spatial variability of their properties and to smooth out local heterogeneity. In natural areas however, processes such as tree falls have been widely recognized as key drivers of soil formation (Phillips et al. 2005; Gabet and Mudd 2010; Roering et al. 2010). Such tree uprooting events mix the soil profile locally and thereby counteract spatial patterns resulting from erosion-deposition or vertical patterns resulting from weathering. By using the soil formation model SoilGen2.0, Finke et al. (2013) were able to show how tree falls caused a much lower correlation with topographic covariates in natural forests of the Belgian loess belt, as opposed to surrounding cropland areas. In our study area, uprooting by tree falls was observed during the field work, but at present no studies have quantified this process.

3.3. Factors controlling the spatial distribution of carbon content, bulk density, stoniness and carbon stocks at different depths

Table 3 summarizes the Pearson correlation coefficients of the different environmental covariates with C content, BD, ST and SOC stocks at the 6 six sampled depths.

For C content, insolation is the main variable that is highly significant for all depths. Areas of higher insolation correspond to areas of lower C content. Potential solar radiation will have a direct effect on soil moisture dynamics and plant growth, leading to drier soils and less vegetation on south-facing slopes as opposed to north-facing slopes. This was corroborated by the good correlation of C content with NDVI. This relation was strongest for the deeper soil layers, and decreased towards the surface being non-significant for the 0–5 cm layer. Also slope is significantly correlated to the C content of some layers. Higher C content generally occurs in flatter areas. As current soil erosion rates are low in these natural landscapes, this is more likely to reflect the importance of water dynamics. Infiltration will be higher in flatter areas where all water infiltrates, as opposed to steeper slopes where runoff can occur. There is also an effect, although less clear, of curvature and TPI on C content.

Bulk density is the variable that represents the highest degree of spatial heterogeneity in the study area. As shown in Table 3, although some variables can be significantly correlated to BD at different depths, there is no single variable that consistently explains BD variations throughout all sampled depths. In particular for the surface layers, there is no significant relation to be found at all. NDVI is perhaps the most relevant variable here, with lower BD values associated with higher NDVI, implying that higher vegetation covers help to improve soil structure and diminish compaction.

With respect to the spatial distribution of ST, several strong relations become apparent (Table 3). First of all however, it is clear that solar radiation does not control the spatial distribution of rock fragments. A significant correlation was only found in the second layer (5–10 cm). Also NDVI does not have a strong influence on ST distribution. Only for two depths, a low correlation was found. Also elevation seems to explain ST distribution well, with higher ST content in lower landscape positions. The effect of topography is also reflected in some significant correlation between ST and curvature, TWI and TPI. The strongest and

Table 3
Pearson correlation coefficient for the relation between environmental variables and carbon concentration, bulk density, stoniness and soil carbon stocks (SOC). Significant relations are indicated in bold and marked according to their significance level: ***p < 0.001; **p < 0.05;*p < 0.1.

	0–5 cm	5–10 cm	10–15 cm	15–20 cm	20–25 cm	25–30 cm
Carbon concentration per depth interval						
Insolation	**−0.42*** **	**−0.50*** **	**−0.36*** **	**−0.41*** **	**−0.42*** **	**−0.53*** **
Elevation	−0.01	−0.14	−0.14	−0.07	−0.03	−0.14
Slope	**0.20***	**0.26****	**0.27****	0.20	**0.20***	**0.34*** **
Curvature	**−0.33*** **	**−0.34*** **	−0.12	−0.10	**−0.22***	−0.19
TWI	0.04	−0.06	−0.03	−0.07	0.08	−0.01
TPI	**−0.29****	**−0.29****	−0.20	−0.18	**−0.24****	**−0.25****
SPI	0.06	0.04	0.12	−0.08	−0.03	0.04
NDVI	0.18	**0.27****	**0.26****	**0.30****	**0.36*** **	**0.43*** **
99						
Bulk density per depth interval						
Insolation	0.02	0.15	**0.28****	0.12	0.14	**0.26*** **
Elevation	−0.19	0.06	**0.26****	0.16	**0.24*** **	0.07
Slope	−0.14	−0.04	−0.11	0.10	−0.09	0.12
Curvature	0.00	0.19	0.05	0.05	0.11	0.14
TWI	0.08	−0.20	−0.10	**−0.26****	−0.16	**−0.27****
TPI	−0.04	0.03	0.17	0.08	0.16	**0.25*** **
SPI	0.00	−0.19	**−0.21***	−0.13	−0.11	**−0.20***
NDVI	0.17	−0.07	**−0.26****	**−0.22***	**−0.35*** **	**−0.44*** **
Stoniness per depth interval						
Insolation	−0.19	**−0.26****	−0.07	−0.17	−0.10	0.00
Elevation	**−0.33*** **	**−0.30****	**−0.33*** **	**−0.23***	−0.14	**−0.40*** **
Slope	**0.37*** **	**0.46*** **	**0.43*** **	**0.41****	**0.37***	**0.58*** **
Curvature	−0.17	**−0.25****	−0.05	−0.26**	−0.16	−0.14
TWI	−0.01	−0.13	**−0.23***	−0.19	−0.20	−0.16
TPI	**−0.33*** **	**−0.28****	−0.17	−0.08	−0.06	−0.09
SPI	0.19	−0.05	−0.01	0.17	0.02	0.04
NDVI	**0.32****	0.15	**−0.06***	−0.02	−0.07	−0.04
SOC stock per depth interval						
Insolation	**−0.30****	**−0.41*** **	**−0.32*** **	**−0.39*** **	**−0.39*** **	**−0.47*** **
Elevation	0.13	−0.03	0.03	0.01	0.04	−0.02
Slope	0.03	0.10	0.04	0.06	0.03	0.06
Curvature	−0.15	**−0.27****	−0.14	−0.01	−0.15	−0.10
TWI	0.10	0.04	0.13	0.01	**0.21***	0.02
TPI	−0.15	−0.22	−0.11	−0.14	−0.23	−0.18
SPI	0.04	0.04	0.11	−0.15	−0.07	−0.03
NDVI	0.11	**0.25****	**0.26****	**0.34*** **	**0.38*** **	**0.42*** **

most consistent relation however is between ST and slope, where higher ST content is found on steeper slopes. The good relation with slope in our study clearly indicates that water erosion, a relevant process in these vegetated environments, is strongly related to slope. While absolute erosion rates are low compared to cropland areas, over the long time scales necessary to form soils, erosion will have two effects. Erosion will induce shallower soil profiles, so that the soil-bedrock interface, where an active conversion of bedrock fragments occurs, is closer to the surface. As noted before in section 3.1, this will lead to a higher concentration of rock fragments in the profile. Also Simanton et al. (1994) observed an increase of surface stone cover with slope gradient in the Walnut Gulch Experimental Watershed, Arizona, although they studied larger rock fragments. This semiarid rangeland site is characterized by low vegetation cover and significant runoff and erosion events. These results are in contrast to Phillips et al.'s (2005) findings in the Ouachita Mountains. They analyzed the relation of surface and B-horizon rock fragment concentrations to topographic variables but did not find any statistically significant correlations. They attribute this to the absence of erosion. Our results are however in line with observations from Welivitiya et al. (2016), who predicted with the soil and landscape evolution model SSSPAM a linear dependency of surface slope and contributing area. They found that the interaction between bedrock weathering and armouring due to erosion resulted in a linear increase of median grain size of the coarse fragments with increasing values of area and slope. Their observations remained valid at different depths. In order to confront this hypothesis against our field data, we plotted ST content values against slope and area, Fig. 4. This figure shows clearly in contrast to the model predictions by Welivitiya et al. (2016), our data only shows a clear dependency of ST on S, but not on A. Higher values of ST will lead to an increase in the median grain size of the soil. This trend is most pronounced for the deeper layers, where ST values are higher. This could suggest that at our site the effect of erosion on ST content is mostly expressed through the lowering of soil profile depth and the exhumation of the actively weathering bedrock interface.

Finally, the spatial distribution of SOC stocks in the SCCZO is statistically well correlated to insolation and NDVI, similar to the spatial patterns in C content. Again, sites with higher potential solar radiation and lower NDVI are characterized by lower SOC stocks. Fig. 5 illustrates the linear, statistically significant relation for the different depth intervals. Slopes of the regression fit for the top two layers are similar, with the intercept at the origin decreasing with depth due to the damping of the radiation effects.

3.4. Factors controlling the spatial distribution of total carbon stock

Next, a multivariate model was fitted to predict total carbon stocks. Upon analysis of the variograms of the residuals of carbon concentration, bulk density, stoniness and carbon stock, it became clear that in all cases, the data are characterized by either a pure or a very high nugget effect. This implies that there is nothing to gain in terms of modeling

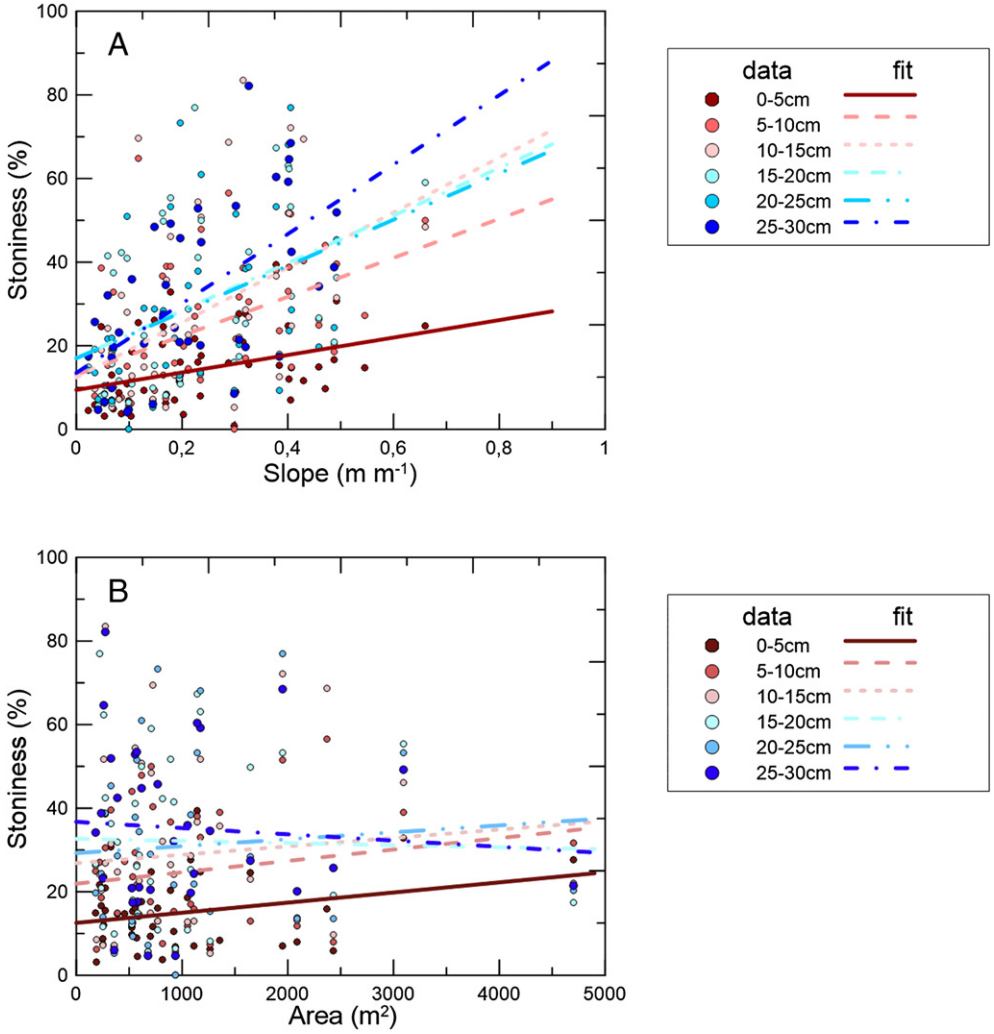

Fig. 4. Relation between stoniness at different depths with (a) slope and (b) area.

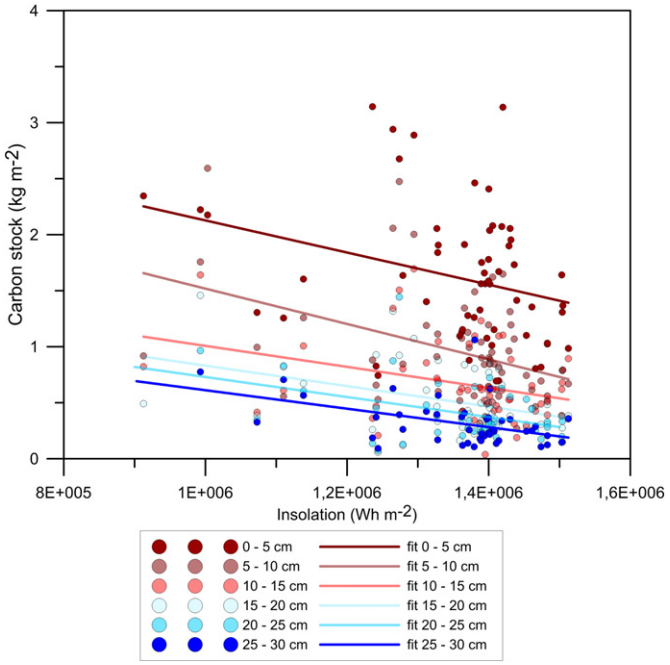

Fig. 5. Relation between carbon stocks at different depths with insolation.

the spatial structure of the residuals and therefore no regression kriging was performed.

The RF model could explain 18% of the variation in the validation dataset. This value is relatively modest, although comparable to other recent studies predicting SOC. Bonfatti et al. (2016) found R^2 values for regression kriging between 0.33 and 0.48 for an agricultural area in Brazil, whereas Malone et al. (2009) found R^2 values of 0.20 to 0.27 for validation dataset.

In spite of the low explanatory power of our model, and the absence of spatial autocorrelation, a number of patterns emerge from the analysis of the relative importance of the variables controlling the spatial distribution of SOC stocks in the SCCZO, shown in Fig. 6. The relative importance is based on the average Gini impurity index (Liaw and Wiener 2002; Menze et al. 2009) that is used for the calculation of splits

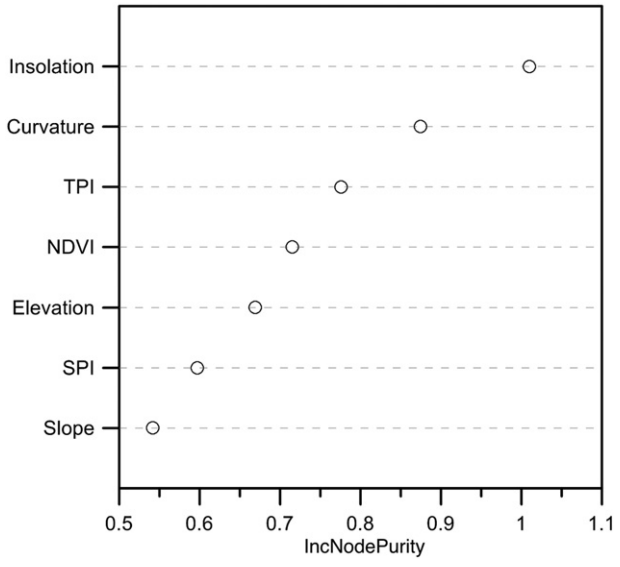

Fig. 6. Relative importance of the variables used for predicting SOC content with the Random Forest model. The importance is expressed as a function of the mean decrease in the Gini Purity Index, with the most important variables ranked first.

during the training phase of the RF model. Fig. 6 ranks variables from the highest at the top to the lowest at the bottom. Insolation was found to be the most important variable that controls distribution of SOC stocks. This confirms the findings from the simple linear correlation analysis (Table 3). After insolation, the following two variables are related to topography, curvature and TPI, and the fourth variable, NDVI, expresses the vegetation effects. Slope, SPI and elevation can be considered less important, as the Gini index of those variables is lower than that of the previous variables although there is not a clear trend break with the previous variables (Fig. 6). The importance of insolation is clearly reflected in the large differences between the south and north-facing slopes of the valley that dissects the center of the study area. Observations already showed that south-facing slopes, are characterized by SOC stocks of about half those of the opposing north-facing slopes.

The impact of insolation on soil properties is complex. While the direct impact of increased insolation is increased drying on south-oriented slopes and lower vegetation cover, as opposed to north-oriented slopes, Geroy et al. (2011) point out that there is possibly a more important effect on long-term development of soil profiles. They found a marked difference in water retention capacity between north and south slopes, because the first are marked by finer and deeper soils and can therefore store more water. In this study, we showed that the interaction between C, BD and ST result in complex patterns of SOC stock.

Although SOC stock is controlled mostly by C content, a significant additional term of variability is introduced by explicitly accounting for spatial trends in BD and ST. Trends in BD are markedly random, while ST is significantly correlated to slope gradient. Spatial trends in total SOC stock are characterized by a high small-scale spatial variability.

Several studies have found spatial patterns of soil properties in natural areas to present a higher degree of randomness as compared to areas with a long agricultural history. In agricultural areas, processes such as soil erosion tend to create spatial patterns that vary according to erosion intensity. Dlugoß et al. (2010) for example, were able to predict C content in an agricultural catchment in Germany by erosion modeling. In contrast, in natural areas stochastic processes can be dominant. A first effect inducing spatial variability in this oak savannah ecosystem is the presence of trees. Evaluation of spatial heterogeneity of SOC in oak savannah has clearly shown how tree crowns enhance SOC stocks beneath the canopies (Howlett et al. 2011; Gómez-Rey et al. 2012). In this study, we have attempted to eliminate this effect by sampling outside the influence of the canopy. However, it is not well known how the position of past trees might have a legacy effect on current-day carbon stocks. Another random process that has been discussed before are tree falls. Such events are widely recognized as main soil forming processes in natural areas (Finke et al. 2013). A final, third process that could lead to increased randomness is the effect of extensive grazing. While there is no preestablished grazing pattern in this area, cattle may have preference for certain areas, as shown by Tate et al. (2003). Grazing patterns will influence deposition patterns of cattle feces and might overprint the effects of topographic or vegetation factors. As random events, these three processes will inevitably diminish the extent to which spatial covariates explain soil properties such as SOC stocks.

4. Conclusions

The steep topography of the Santa Clotilde Critical Zone Observatory resulted in a high heterogeneity of bulk density, stoniness and soil carbon. Despite this important heterogeneity, clear vertical and spatial patterns emerged, revealing the importance of specific environmental covariates. Slope was found to be a key control over the spatial distribution of stoniness, pointing to the importance of erosion. Solar radiation and vegetation cover, as represented by NDVI, were the main controls over carbon concentration and carbon stocks. A better understanding of the dominant controls over belowground carbon will facilitate soil management in these fragile oak-woodland savannah ecosystems. In

the future, a better understanding of the processes involved in soil pedogenesis will boost the understanding of the spatial distribution of soil properties which have proven difficult to predict in digital soil mapping studies, such as stoniness or bulk density, and help to evaluate their variation beyond areas where they were sampled.

Acknowledgements

This work has been funded by projects AGL2012-40128-C03-02 and AGL2015-65036-C3-2-R (MINECO/FEDER, UE). The authors thank Prof Jesús Ayuso for access and support in the Santa Clotilde watershed. We thank F. Cáceres and R. Pédèches for assistance with fieldwork. A. Román-Sánchez is funded by Contratos Predoctorales Fellowship with reference BES-2013-067009.

References

Anderson, R.S., Anderson, S.P., Tucker, G.E., 2013. Rock damage and regolith transport by frost: an example of climate modulation of the geomorphology of the critical zone. Earth Surf. Process. Landf. 38, 299–316. http://dx.doi.org/10.1002/esp.3330.

Anderson, S.P., Hinckley, E.-L., Kelly, P., Langston, A., 2014. Variation in critical zone processes and architecture across slope aspects. Procedia Earth Planet. Sci., Geochemistry of the Earth's surface GES-10 Paris France 10, 28–33. http://dx.doi.org/10.1016/j.proeps.2014.08.006 18–23 August, 2014.

Aschmann, H., 1984. A restrictive definition of Mediterranean climates. Bull. Société Bot. Fr. Actual. Bot. 131, 21–30.

Beven, K.J., Kirkby, M.J., 1979. A physically based variable contributing area model of basin hydrology. Hydrol. Sci. Bull. 24, 46–69.

Bonfatti, B.R., Hartemink, A.E., Giasson, E., Tornquist, C.G., Adhikari, K., 2016. Digital mapping of soil carbon in a viticultural region of southern Brazil. Geoderma 261, 204–221. http://dx.doi.org/10.1016/j.geoderma.2015.07.016.

Bornemann, L., Herbst, M., Welp, G., Vereecken, H., Amelung, W., 2011. Rock fragments control size and saturation of organic carbon pools in agricultural topsoil. Soil Sci. Soc. Am. J. 75, 1898–1907. http://dx.doi.org/10.2136/sssaj2010.0454.

Breiman, L., 2001. Random forests. Mach. Learn. 45, 5–32.

Development Core Team, R., 2008. R: A Language and Environment for Statistical Computing. R Foundation for Statistical Computing, Viena, Austria.

Dlugoß, V., Fiener, P., Schneider, K., 2010. Layer-specific analysis and spatial prediction of soil organic carbon using terrain attributes and erosion modeling. Soil Sci. Soc. Am. J. 74, 922. http://dx.doi.org/10.2136/sssaj2009.0325.

Finke, P.A., Vanwalleghem, T., Opolot, E., Poesen, J., Deckers, J., 2013. Estimating the effect of tree uprooting on variation of soil horizon depth by confronting pedogenetic simulations to measurements in a Belgian loess area. J. Geophys. Res. Earth Surf. 118. http://dx.doi.org/10.1002/jgrf.20153 2013JF002829.

Gabet, E.J., Mudd, S.M., 2010. Bedrock erosion by root fracture and tree throw: a coupled biogeomorphic model to explore the humped soil production function and the persistence of hillslope soils. J. Geophys. Res. Earth Surf. 115, F04005. http://dx.doi.org/10.1029/2009JF001526.

Geroy, I.J., Gribb, M.M., Marshall, H.P., Chandler, D.G., Benner, S.G., McNamara, J.P., 2011. Aspect influences on soil water retention and storage. Hydrol. Process. 25, 3836–3842. http://dx.doi.org/10.1002/hyp.8281.

Giacometti, C., Demyan, M.S., Cavani, L., Marzadori, C., Ciavatta, C., Kandeler, E., 2013. Chemical and microbiological soil quality indicators and their potential to differentiate fertilization regimes in temperate agroecosystems. Appl. Soil Ecol. 64, 32–48. http://dx.doi.org/10.1016/j.apsoil.2012.10.002.

Gómez-Rey, M.X., Garcês, A., Madeira, M., 2012. Soil organic-C accumulation and N availability under improved pastures established in Mediterranean oak woodlands. Soil Use Manag. 28, 497–507. http://dx.doi.org/10.1111/j.1475-2743.2012.00428.x.

Guisan, A., Weiss, S.B., Weiss, A.D., 1999. GLM versus CCA spatial modeling of plant species distribution. Plant Ecol. 143, 107–122. http://dx.doi.org/10.1023/A:1009841519580.

Hoffmann, U., Hoffmann, T., Johnson, E.A., Kuhn, N.J., 2014. Assessment of variability and uncertainty of soil organic carbon in a mountainous boreal forest (Canadian Rocky Mountains, Alberta). Catena 113, 107–121. http://dx.doi.org/10.1016/j.catena.2013.09.009.

Howlett, D.S., Moreno, G., Mosquera Losada, M.R., Nair, P.K.R., Nair, V.D., 2011. Soil carbon storage as influenced by tree cover in the Dehesa cork oak silvopasture of central-western Spain. J. Environ. Monit. 13, 1897. http://dx.doi.org/10.1039/c1em10059a.

Istanbulluoglu, E., Bras, R.L., 2006. On the dynamics of soil moisture, vegetation, and erosion: implications of climate variability and change. Water Resour. Res. vol. 42, W06418. http://dx.doi.org/10.1029/2005WR004113.

IUSS Working Group, W.R.B., 2014. World Reference Base for Soil Resources 2014. International soil classification system for naming soils and creating legends for soil maps, (3rd ed.). FAO, Rome.

Ivanov, V.Y., Bras, R.L., Vivoni, E.R., 2008. Vegetation-hydrology dynamics in complex terrain of semiarid areas: 2. Energy-water controls of vegetation spatiotemporal dynamics and topographic niches of favorability. Water Resour. Res. 44. http://dx.doi.org/10.1029/2006WR005595 W03430.

Kunkel, M.L., Flores, A.N., Smith, T.J., McNamara, J.P., Benner, S.G., 2011. A simplified approach for estimating soil carbon and nitrogen stocks in semi-arid complex terrain. Geoderma 165, 1–11. http://dx.doi.org/10.1016/j.geoderma.2011.06.011.

Liaw, A., Wiener, M., 2002. Classification and regression by random Forest. R News 2, 18–22.

Lozano-Parra, J., Maneta, M.P., Schnabel, S., 2014. Climate and topographiccontrols on simulated pasture production in a semiarid Mediterranean watershed with scattered tree cover. Hydrol. Earth Syst. Sci. 18, 1439–1456. http://dx.doi.org/10.5194/hess-18-1439-2014.

Malone, B.P., McBratney, A.B., Minasny, B., Laslett, G.M., 2009. Mapping continuous depth functions of soil carbon storage and available water capacity. Geoderma 154, 138–152. http://dx.doi.org/10.1016/j.geoderma.2009.10.007.

Mâren, I.E., Karki, S., Prajapati, C., Yadav, R.K., Shrestha, K.B., 2015. Facing north or south: does slope aspect impact forest stand characteristics and soil properties in a semiarid trans-Himalayan valley? J. Arid Environ. 121, 112–126. http://dx.doi.org/10.1016/j.jaridenv.2015.06.004.

Menze, B.H., Kelm, B.M., Masuch, R., Himmelreich, U., Bachert, P., Petrich, W., Hamprecht, F.A., 2009. A comparison of random forest and its Gini importance with standard chemometric methods for the feature selection and classification of spectral data. BMC Bioinformatics 10, 213. http://dx.doi.org/10.1186/1471-2105-10-213.

Moore, I.D., Grayson, R.B., Ladson, A.R., 1991. Digital terrain modelling: a review of hydrological, geomorphological, and biological applications. Hydrol. Process. 5, 3–30. http://dx.doi.org/10.1002/hyp.3360050103.

Phillips, J.D., Luckow, K., Marion, D.A., Adams, K.R., 2005. Rock fragment distributions and regolith evolution in the Ouachita Mountains, Arkansas. USA. Earth Surf. Process. Landf. 30, 429–442. http://dx.doi.org/10.1002/esp.1152.

Roering, J.J., Marshall, J., Booth, A.M., Mort, M., Jin, Q., 2010. Evidence for biotic controls on topography and soil production. Earth Planet. Sci. Lett. 298, 183–190. http://dx.doi.org/10.1016/j.epsl.2010.07.040.

Schrumpf, M., Schulze, E.D., Kaiser, K., Schumacher, J., 2011. How accurately can soil organic carbon stocks and stock changes be quantified by soil inventories? Biogeosciences 8, 1193–1212. http://dx.doi.org/10.5194/bg-8-1193-2011.

Simanton, J.R., Renard, K.G., Christiansen, C.M., 1994. Spatial distribution of surface rock fragments along catenas in semiarid Arizona and Nevada, USA. Catena 23 pp. 29–42.

Simón, N., Montes, F., Díaz-Pinés, E., Benavides, R., Roig, S., Rubio, A., 2012. Spatial distribution of the soil organic carbon pool in a holm oak dehesa in Spain. Plant Soil 366, 537–549. http://dx.doi.org/10.1007/s11104-012-1443-9.

Tarboton, D.G., 1997. A new method for the determination of flow directions and upslope areas in grid digital elevation models. Water Resour. Res. 33, 309–319.

Tate, K.W., Atwill, E.R., McDougald, N.K., George, M.R., 2003. Spatial and temporal patterns of cattle feces deposition on rangeland. J. Range Manag. 56, 432–438.

Temme, A.J.A.M., Vanwalleghem, T., 2016. LORICA – a new model for linking landscape and soil profile evolution: Development and sensitivity analysis. Comput. Geosci., Uncertainty and Sensitivity in Surface Dynamics Modeling 90, 131–143. http://dx.doi.org/10.1016/j.cageo.2015.08.004 Part B.

Throop, H.L., Archer, S.R., Monger, H.C., Waltman, S., 2012. When bulk density methods matter: implications for estimating soil organic carbon pools in rocky soils. J. Arid Environ. 77, 66–71. http://dx.doi.org/10.1016/j.jaridenv.2011.08.020.

Vanwalleghem, T., Stockmann, U., Minasny, B., McBratney, A.B., 2013. A quantitative model for integrating landscape evolution and soil formation. J. Geophys. Res. Earth Surf. 118, 331–347. http://dx.doi.org/10.1029/2011JF002296.

Welivitiya, W.D.D.P., Willgoose, G.R., Hancock, G.R., Cohen, S., 2016. Exploring the sensitivity on a soil area-slope-grading relationship to changes in process parameters using a pedogenesis model. Earth Surf. Dyn. Discuss. 1–43. http://dx.doi.org/10.5194/esurf-2015-54.

Yetemen, O., Istanbulluoglu, E., Duvall, A.R., 2015a. Solar radiation as a global driver of hillslope asymmetry: insights from an ecogeomorphic landscape evolution model. Water Resour. Res. 51, 9843–9861. http://dx.doi.org/10.1002/2015WR017103.

Yetemen, O., Istanbulluoglu, E., Flores-Cervantes, J.H., Vivoni, E.R., Bras, R.L., 2015b. Ecohydrologic role of solar radiation on landscape evolution. Water Resour. Res. 51, 1127–1157. http://dx.doi.org/10.1002/2014WR016169.

Quaternary Geochronology 42 (2017) 1–14

Contents lists available at ScienceDirect

Quaternary Geochronology

journal homepage: www.elsevier.com/locate/quageo

Research paper

Getting a grip on soil reworking – Single-grain feldspar luminescence as a novel tool to quantify soil reworking rates

Tony Reimann [a, *], Andrea Román-Sánchez [a, b], Tom Vanwalleghem [b], Jakob Wallinga [a]

[a] Soil Geography and Landscape Group, Netherlands Centre for Luminescence Dating, Wageningen University, Droevendaalsesteeg 3, 6708 PB Wageningen, The Netherlands
[b] Group for Rural Hydrology and Hydraulics, Department of Agronomy, University of Cordoba, Spain

ARTICLE INFO

Article history:
Received 23 December 2016
Received in revised form
14 July 2017
Accepted 17 July 2017
Available online 19 July 2017

Keywords:
Feldspar single-grains
Bioturbation
Creep
Soil mixing
Post-IR IRSL feldspar

ABSTRACT

Soil reworking, e.g. due to bioturbation, is an important aspect of soil and landscape evolution. Yet, rates of soil mixing are poorly constrained, especially on pedological and geomorphological relevant time scales of decades to millennia. This study presents a novel method to reconstruct soil reworking rates on such timescales by utilising luminescence signals from individual sand-sized feldspar grains as soil reworking tracers. We propose a post-IR IRSL procedure to harvest two luminescence signals from individual feldspar grains. We applied this method to four soil samples from a single soil profile in Spain, and compared our results to those derived through a more conventional approach based on single-grain quartz luminescence analysis. We also propose novel ways of deriving effective soil reworking rates from luminescence data, using not only apparent burial ages of mineral grains but also the proportion of mineral grains that never reached the soil surface.

Our results confirm the general suitability of feldspar post-IR IRSL as soil reworking tracer in terms of measurement performance, luminescence signal resetting and eventually the determination of soil reworking rate. We furthermore demonstrate that the feldspar based method is more time and labour efficient than quartz based methods, and we expect it to be more widely applicable. Most importantly, the method provides a reliable measures of the soil reworking intensity, which was not possible with quartz based methods. We conclude that feldspar single-grain luminescence analysis has the potential to become the method of choice for investigating soil reworking rates.

1. Introduction

Soils are the living skin of our planet and the ecosystem services they provide are crucial for our wellbeing (e.g. Keesstra et al., 2016). The importance of (fertile) soils and the challenges humankind faces with regard to soil resources were recently highlighted by Amundson et al. (2015). In spite of growing awareness of the relevance, soil-forming processes such as bioturbation are poorly understood and especially poorly quantified. The architecture of the critical zone, i.e. the heterogeneous and complex near-surface environment, is controlled by the balance between soil production from saprolite (chemically weathered bedrock) or deposition, chemical weathering, physical denudation and biological or anthropogenic soil mixing. From the time soil particles are converted from bedrock, they are continuously reworked within the soil by fauna and flora, but also by other processes such as freeze-thaw or wetting–drying processes. On hillslopes, this reworking results in a net downhill movement of the soil, known as creep (Heimsath et al., 2002). Bioturbation is one of the main contributors to soil creep (Gabet et al., 2003). The term 'biomantle' or 'mobile regolith' is often used to differentiate this physically disrupted layer that is available for sediment transport from the underlying saprolite (Mudd et al., 2013). Bioturbation is potentially the most active soil-forming process (Wilkinson and Humphreys, 2005). At the same time it is also the main geomorphological process on diffusive soil-mantled hillslopes, which may control the form of entire landscapes (Dietrich and Perron, 2006). However, the rates involved in this crucial soil-forming process of bioturbation are only poorly constrained and we are still far from quantifying them accurately, especially on pedological relevant time scales of decades to millennia. One main reason for this knowledge gap is the limited availability of suitable reconstruction methods for long-

* Corresponding author.
E-mail address: tony.reimann@wur.nl (T. Reimann).

http://dx.doi.org/10.1016/j.quageo.2017.07.002
1871-1014/

term soil reworking.

Several studies have used radioisotopes to investigate soil mixing on timescales of decades by monitoring the distribution of short-lived isotopes (e.g. ^{137}Cs, ^{7}Be) through the soil profile (e.g. Kaste et al., 2007; Tsukata et al., 2008). However, as the radioisotopes so far used yield relative short half-life's and are mainly associated to finer soil particles (soil organic matter or clay) (e.g. Tsukata et al., 2008) these techniques cannot be used for reconstructions on longer timescales where down-profile clay migration (clay eluviation) becomes a significant process.

Luminescence dating has been proposed as a potentially suitable method for the reconstruction of long-term soil reworking (Heimsath et al., 2002). Luminescence dating estimates the time since the last light exposure of quartz and feldspar mineral grains. While the grains are buried, luminescence signals build up due to absorption of ionizing radiation (e.g. Preusser et al., 2008). When a grain is brought to the surface (e.g. through bioturbation), it is exposed to light and its luminescence signal is reset. Thus, luminescence age–depth profiles potentially provide measures of both the time of deposition and burial, as well as soil mixing/reworking. Optically Stimulated Luminescence (OSL) of quartz minerals (quartz OSL) was recently used to study lugworm bioturbation in a tidal flat in Denmark (Madsen et al., 2011a), terrestrial soil mixing rates in Australia (Heimsath et al., 2002; Wilkinson and Humphreys, 2005; Stockmann et al., 2013; Johnson et al., 2014) and termite soil reworking in Ghana (Kristensen et al., 2015). Thus, bearing in mind that luminescence dating is determine the time since the last daylight exposure, it can therefore be assumed that the obtained reworking rates can be mainly attributed to bioturbation. Other mixing processes (e.g. freeze-thaw, drying-wetting) will not consistently bring particles to the soil surface to be bleached. Soil reworking rates derived from luminescence dating analysis thus mainly refer to soil reworking by bioturbation and/or anthropogenic reworking (e.g. ploughing).

In general, the luminescence measurements on quartz single grains are required to obtain meaningful luminescence age–depth profiles (e.g. Heimsath et al., 2002; Kristensen et al., 2015). The measurement of quartz single-grains, however, is cumbersome and tedious as typically only a few percent of quartz grains (1–5%) show suitable OSL behaviour (Duller, 2008). It is therefore no surprise that quartz single grains as soil reworking tracers were so far exclusively applied to regions with extraordinary good quartz OSL properties. Australia for example, where most of these studies were carried out, is famous in the luminescence dating community for its unusual well behaving quartz (e.g. Murray and Roberts, 1997, 1998). So far, single-grain quartz OSL is still a rare niche application in studying soil reworking, likely due to a combination of the relatively recent development and the time and labour intensive nature of the method.

The goal of this study is to develop and test an alternative luminescence-based method for the reconstruction of soil reworking, which is more widely applicable and less labour intensive. For this purpose we will systematically test the use of feldspar single grains as soil reworking tracers; we will build upon recently developed feldspar luminescence dating protocols (Thomsen et al., 2008; Reimann et al., 2011) and feldspar single-grain techniques (Reimann et al., 2012a). The advantage of using feldspar compared to quartz is that feldspar typically shows superior luminescence sensitivity with typically ~50% of the grains emitting a suitable luminescence signal (e.g. Duller, 2006; Reimann et al., 2012a). Hence, single grains of feldspar can potentially be used as soil reworking tracers in regions where quartz OSL properties are poor (e.g. European and New Zealand Alps, NE America, Himalaya, Andes, Scandinavia, Scotland, Turkey) (e.g. Duller, 2006; Preusser et al., 2006; Klasen et al., 2007; Lukas et al., 2007; Steffen et al., 2009; Madsen et al., 2011b; van Gorp et al., 2013; Preusser et al., 2014).

2. Luminescence method

2.1. Background on luminescence dating in soils

Luminescence signals of natural minerals provide a powerful means for examining daylight exposure at the soil surface and continuous re-burial by new soil particles on a decadal to millennial time scale (Heimsath et al., 2002; Kristensen et al., 2015) and thus long-term rates of soil reworking mainly due to bioturbation. Within the luminescence dating community, soil reworking and especially bioturbation have been mainly given attention as processes that potentially destroy the stratigraphic integrity of deposits through vertical movement of particles and thus may lead to inaccurate luminescence ages when attempting to determine the time of deposition. Therefore, the vast majority of luminescence research recognizes soil mixing as a potential contamination problem that has to be overcome by the OSL measurement of single mineral grains and by applying sophisticated statistical models (e.g. Roberts et al., 2000; Bateman et al., 2003, 2007a,b; Jacobs and Roberts, 2007; Rink et al., 2013; Gliganic et al., 2015). However, inspired by the pioneering work of Heimsath et al. (2002), some studies recently also explored the added value of quartz single-grain OSL data for the quantification of soil processes (Stockmann et al., 2013; Johnson et al., 2014; Kristensen et al., 2015; Gliganic et al., 2016) or reconstruction of phases of enhanced pedoturbation (Gliganic et al., 2015). These studies successfully applied quartz OSL single-grain techniques for this purpose; a comprehensive review of quartz OSL single-grain techniques is given by Duller (2008), a general quartz OSL review is provided in Preusser et al. (2009).

Single-grain luminescence of K-rich feldspar as soil reworking tracers has three potential advantages compared to quartz: (i) a much larger percentage of grains show suitable luminescence properties (e.g. Reimann et al., 2012a,b); (ii) feldspar luminescence sensitivity seems to be largely independent of the provenance and reworking history of the grains (e.g. Lukas et al., 2007; Pietsch et al., 2008; see also section 1), and (iii) due to a significant component of the environmental dose from ^{40}K inside the grain, the age estimate is less depended on critical assumptions regarding the annual dose rate (e.g. Reimann et al., 2011).

However, conventional feldspar infrared stimulated luminescence (IRSL) signals have drawbacks that need to be considered. First, feldspar IRSL signals suffer from anomalous fading (Spooner, 1994). Anomalous fading is an a-thermal loss of trapped charge due to quantum mechanical tunnelling, which can lead to severe age underestimation (e.g. Huntley and Lamothe, 2001; Wallinga et al., 2007). Secondly, IRSL and post IR-IRSL (pIRIR) feldspar signals reset (or bleach) more slowly upon daylight exposure than quartz OSL (Godfrey-Smith et al., 1988; Murray et al., 2012). As a consequence, feldspar luminescence signals are more likely to be poorly bleached upon grain burial, which may provoke age overestimation.

One of the main challenges in this study is to overcome these drawbacks of feldspar luminescence dating, and to develop a feldspar-based method for quantifying soil reworking that is complementary to previously applied approaches based on quartz luminescence as well as other non-luminescence methods. We will focus on low-temperature (<200 °C) IRSL and post-IR IRSL (pIRIR) feldspar signals, as they are better bleachable than their high-temperature equivalents (>200 °C; Kars et al., 2014). The pIRIR signals have the benefit that they are less affected by anomalous fading (e.g. Thomsen et al., 2008; Reimann et al., 2011).

Furthermore, we aim to use feldspar single-grain analysis to obtain information at the scale of the individual sand-sized particles that are involved in the mixing process. We work on a number of samples from a hillslope in SW Spain (Section 2.2), and will validate our results by comparing them to single-grain quartz OSL results from the same samples.

2.2. Luminescence samples and setting

The sampling area is located in the Cordoba province, SW Spain, in the Martin Gonzalo headwater catchment (latitude 38.12′ N, longitude 4.17’ W), with an altitude between 660 and 740 m above sea level (see Fig. 1). This catchment is part of the Sierra de Cardeña y Montoro Natural Park, located in the Sierra Morena, which is part of the SW Iberian Massif and separates the Spanish Central Plateau and the Betic Depression. The edge of the plateau is fractured and lifted by Alpine thrust forces on the Hercynian base of the plateau. The parent material in the area consists of granitic rock (Geological and Mining Institute of Spain, 2013) and belongs to the Los Pedroches Batholith. Rocks are porphyritic monzogranites with 73 wt % SiO_2 and high K_2O values of 5 wt % on average (Carracedo et al., 2009). Soil types are Regosols, Leptosols and Cambisols with Rankers under the FAO-Unesco World Reference Base (IUSS Working Group WRB, 2007). The soil texture in the research area is sandy to sandy loam.

The sampled catena is on the north-facing slope of a steep south-west to north-east oriented V-shaped valley (Fig. 1). All sampled soil profiles are within the Mediterranean sclerophyllous forest and outside of the area influenced by grazing. A perennial creek runs through the valley bottom, characterized by frequent granitic outcrops and at places shallow Quaternary fluvial deposits. A nearly straight hillslope connects the valley to a relatively flat, incised plateau. The four luminescence samples discussed here were taken from a hillslope soil profile (SC-9). The soil type here is a Cambisol, with a mean texture of 76.8% sand, 17.9% silt and 5.3% clay. The boundary between mobile regolith and the underlying

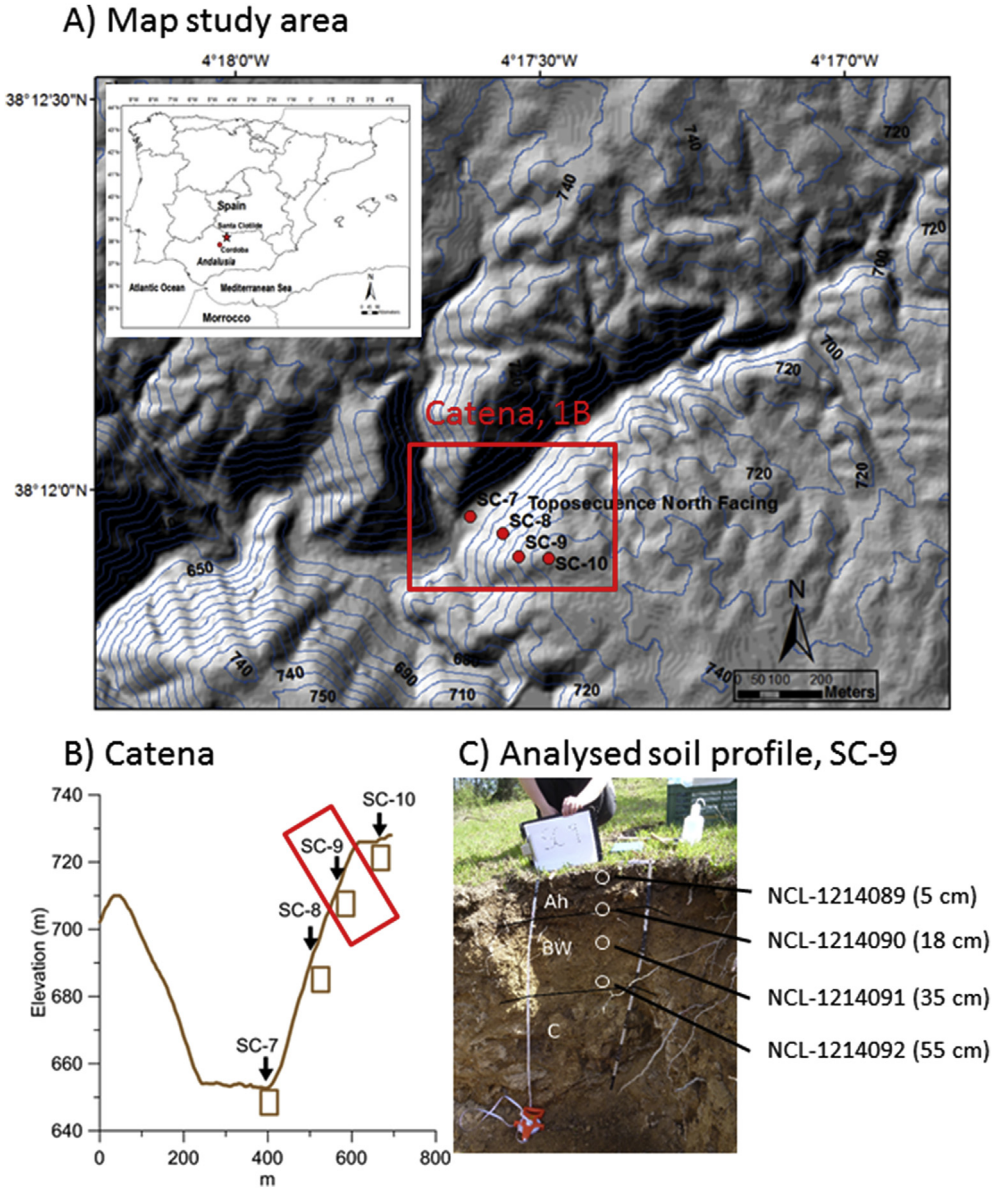

Fig. 1. Study area and setting. A map of the study area is shown in A). A profile of the soil catena and a description of the analysed soil profile (SC-9) are provided in B) and C), respectively. More details are provided in section 2.2.

saprolite layer is at 57 cm. We sampled at different depths from the soil surface to the bottom of the soil profile (or top of the in-situ saprolite layer): 5, 18, 35, 55 cm. In this way, only the mobile regolith layer, as identified during field observations, was sampled. More detailed textural and chemical analysis of the soil profile under investigation are provided in the electronic supplement. Results for the full catena and implications for soil and landscape evolution will be discussed in a separate paper (Roman-Sanchez et al., in prep.), here we focus on the method development and validation.

2.3. Experimental details

At the sample site a trench was dug, and four sample tubes of 5 cm diameter and 25 cm length were hammered horizontally into the fresh exposure at 5, 18, 35 and 55 cm depths. The sample tubes were opened and processed in the Wageningen luminescence laboratory under subdued orange light condition. Sand-sized material was sieved to 212–250 μm and subsequently cleaned using HCl and H_2O_2. K-rich feldspar and quartz extracts were separated using a heavy liquid (LST fastfloat®, 2.58 kg/dm^3). The quartz extract was furthermore etched for 40 min with 48% HF and subsequently washed with HCl; no etching was applied to the K-feldspar grains. More details on sample preparation and the separation of the K-rich feldspar and quartz fractions is provided in Kars et al. (2012) (their section 3.1). For the single-grain measurements the feldspar and quartz grains were loaded into aluminium single-grain discs with a 10 × 10 grid of 300 μm grain holes. The selected grain-size fraction for both feldspar and quartz was 212–250 μm to ensure that only one grain fits into each grain hole.

The external dose rate of our four samples was determined using laboratory high-resolution gamma spectrometry of material from the outer ends of the sample tubes and representative material from the sample surrounding. We measured the activity concentration of specific isotopes within the Uranium and Thorium decay chains as well as ^{40}K; these activity concentrations were converted into dose rates using the conversion factors of Guérin et al. (2011) and considering grain-size and soft-component (water and organic) attenuation effects (Mejdahl, 1979; Aitken, 1985). An additional dose rate contribution from cosmic radiation was calculated according to Prescott and Hutton (1994), taking into account location and altitude of the samples. For the K-rich feldspar extracts an additional dose rate from internal radiation sources (mostly ^{40}K and ^{87}Rb) was incorporated, assuming an internal K concentration of 10 ± 2% and Rb content of 400 ± 100 ppm as suggested by Smedley et al. (2012).

For the single-grain luminescence measurements an automated Risø TL/OSL reader (DA 15) fitted with a dual (red and green) laser single-grain attachment (Bøtter-Jensen et al., 2003; Duller, 2003) was used. The feldspar grains were stimulated for 1.68 s with a 150 mW 830 nm IR laser. All feldspar signals were detected through a LOT/Oriel D410/30 interference filter to select the K-rich feldspar emission around 410 nm. The quartz grains were stimulated for 0.83 s with a 10 mW Nd:YVO_4 solid-state diode-pumped laser

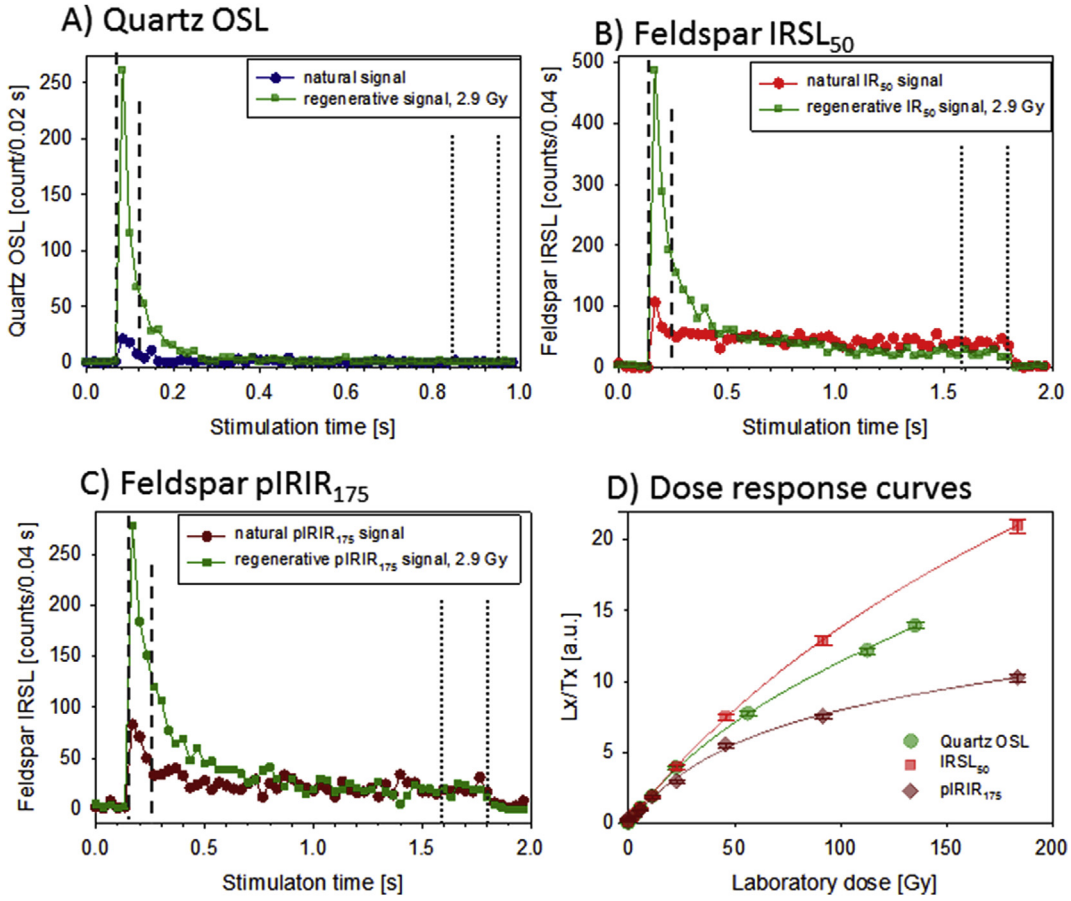

Fig. 2. Typical luminescence single-grain decay curves and dose response curves for sample NCL-1214089. Natural (dot) and regenerative dose (square; 2.9 Gy) luminescence decay curves of quartz OSL (A), feldspar $IRSL_{50}$ (B) and feldspar $pIRIR_{175}$ (C). The signal integration limits are shown as vertical dashed (initial) and dotted lines (background). Typical dose response curves for the three luminescence signals under investigation are shown in (D). The data were fitted using an exponential plus linear function. More details are provided in section 2.3.

emitting at 532 nm. The quartz OSL signal was detected through a 7.5 mm Hoya U-340 detection filter. The laboratory irradiations were made using a calibrated $^{90}Sr/^{90}Y$ beta source, at a dose rate of 0.113 ± 0.002 Gy/s to the single-grains.

For the quartz OSL single-grain measurements a measurement protocol similar to that of Reimann et al. (2012b) was employed, including a 10 s preheat at 220 °C and a cut-heat at 200 °C. The quartz OSL signal recorded at the time interval between 0.63 s and 0.83 s was subtracted from the initial 0.03 s of stimulation to obtain the net OSL signal (Fig. 2 A). For the feldspar luminescence measurements a combined single-grain IRSL/pIRIR protocol was employed using a relatively low preheat of 200 °C for 60 s, a cut-heat identical to this preheat (Blair et al., 2005), an single-grain IRSL stimulation at 50 °C and subsequent single-grain pIRIR stimulation at 175 °C. The signal of the first 0.07 s after the IR laser was switched on was used as the initial signal and the signal observed in the last 0.48 s of stimulation (1.20–1.68 s) was subtracted as background (Fig. 2B and C). To improve the reproducibility of our feldspar single-grain measurements especially at elevated temperature we modified the sample disc holding procedure as described in Smedley and Duller (2013). In this procedure, it is first searched for the single-grain position holes to identify the exact grain locations and subsequently the single-grain disc is raised to the measurement temperature. With this approach we ensure similar heat treatment for the stimulation of the natural IRSL/pIRIR signals and the following test dose and regenerative IRSL/pIRIR signals.

All dose estimates were derived by fitting the regenerated dose points by an exponential plus linear function using the Risø "Analyst 3.24 version 4.12" (Duller, 2007). For dose estimation each dose response curve was forced through the origin (Fig. 2D). The following criteria were used for accepting a grain for analysis:

i. A relative test dose error of less than 20% or 30% for feldspar and quartz, respectively.
ii. A natural test dose signal intensity (i.e. 0.07 s and 0.03 s for the feldspar and quartz signals, respectively), at least 3 times greater than the respective background signal measured on the same grain.
iii. Recycling ratios consistent with unity within 2σ.
iv. For quartz: absence of potential feldspar contribution, checked through the OSL IR depletion ratio (Duller, 2003).
v. Monotonically growing dose response curves.

The onset of the dose saturation of a grain was determined based on the D_0 criteria proposed by Wintle and Murray (2006) for single saturating exponential dose response. Accordingly, a grain is regarded as "in saturation" if its natural signal is larger than 2 times the D_0 value (~85% full saturation) of the exponential component of the dose response curve. Applying this criterion in combination with an exponential plus linear fitting results in a relative conservative threshold for the onset of saturation. We furthermore detected zero-dose grains, i.e. grains consistent with zero at 2 sigma, through the soil profile following the approach proposed in Gliganic et al. (2016) for quartz OSL. For the two feldspar data sets we had to slightly modify the analysis as modern (or very recently exposed) feldspar grains likely yield small un-bleachable or very hard-to-bleach IRSL and pIRIR remnant luminescence signals. Based on previous experience with similar luminescence dating protocols (Reimann et al., 2012a,b; Reimann and Tsukamoto, 2012) we estimate the remnant signals to amount for a remnant dose of 0.3 and 0.6 Gy (corresponding to 60 and 120 years) for the $IRSL_{50}$ and the $pIRIR_{175}$, respectively. Those remnants were incorporated in the zero-dose grain calculations by subtracting corresponding remnant doses from the D_e's.

2.4. Luminescence performance testing

To test the performance of the luminescence measurement protocols and the selected measurement parameters we carried out dose recovery experiments on sample NCL-1214089 (5 cm depth). For this purpose we first bleached a fraction of the prepared quartz or K-rich feldspar using either blue LED stimulation in the reader for two times 300 s (quartz) or a solar simulator bleach for 24 h (K-rich feldspar). After bleaching, the grains were loaded into single-grain discs, irradiated using the calibrated $^{90}Sr/^{90}Y$ beta source and the administrated beta dose (17 Gy) was subsequently measured. The dose recovery ratio (measured/given dose) was derived from the respective dose recovery distribution using the Central Age Model (CAM) of Galbraith et al. (1999).

For single-grain quartz OSL we obtained a CAM dose recovery ratio of 1.07 ± 0.05 (n = 24, out of 600 grains measured). The feldspar dose recovery estimates were corrected for laboratory residual doses as described in Reimann et al. (2012a), to avoid bias due to incomplete resetting of the signals prior to the experiment. The CAM residual doses were estimated to 0.74 ± 0.14 Gy and 1.77 ± 0.40 Gy for the $IRSL_{50}$ and the $pIRIR_{175}$, respectively. The CAM feldspar single-grain dose recovery ratios were calculated to be 0.96 ± 0.02 (n = 137, out of 200) and 1.00 ± 0.03 (n = 119, out of 200) for the $IRSL_{50}$ and the $pIRIR_{175}$, respectively. All dose recovery ratios are in agreement with unity within 2 sigma providing support for the use of these measurement protocols for dose estimation. The CAM also estimates the scatter in the dose recovery distribution that cannot be explained by the uncertainties of the individual single grain dose recovery estimates, the so called over-dispersion. For quartz single-grains the over-dispersion was

Table 1
Grain statistics for soil profile SC-9.

Sample ID	Signal	$n_{measured}$	$n_{luminescent}$	%	$n_{poor\ recylcing}$	$n_{no\ growth}$	%	$n_{Fsp\ contam.}$	%	$n_{accepted}$	%	$n_{non\text{-}sat.}$	$n_{above\ sat.}$	%
NCL-1214089	OSL	1600	74	5%	12	1	18%	9	12%	52	3.3%	52	0	0%
(depth 5 cm)	$IRSL_{50}$	300	219	73%	37	0	17%	–		182	61%	158	24	13%
	$pIRIR_{175}$	300	141	47%	25	3	20%	–		113	38%	103	10	9%
NCL-1214090	OSL	1400	77	6%	2	1	4%	35	45%	39	2.8%	34	5	13%
(depth 18 cm)	$IRSL_{50}$	300	232	77%	73	3	33%	–		156	52%	69	87	56%
	$pIRIR_{175}$	300	224	75%	58	10	30%	–		156	52%	78	78	50%
NCL-1214091	OSL	1400	46	3%	5	1	13%	29	63%	11	0.8%	9	2	18%
(depth 35 cm)	$IRSL_{50}$	300	182	61%	47	20	37%	–		115	38%	15	100	87%
	$pIRIR_{175}$	300	185	62%	91	29	65%	–		65	22%	7	58	89%
NCL-1214092	OSL	1200	482	40%	46	24	15%	385	80%	24	2.0%	2	22	92%
(depth 55 cm)	$IRSL_{50}$	300	227	76%	51	2	23%	–		174	58%	1	173	99%
	$pIRIR_{175}$	300	229	76%	84	14	43%	–		131	44%	0	131	100%

calculated to be 10.2 ± 6.2%; for the feldspar single-grains the over-dispersion was estimated to be 6.9 ± 1.0% and 15.9 ± 1.3% for the $IRSL_{50}$ and the $pIRIR_{175}$, respectively.

3. Results

3.1. Luminescence behaviour as function of depth below surface

We find that only a very small percentage of quartz grains (~1–4%) from our samples have luminescence properties suitable for equivalent dose (D_e) estimation (Table 1; Fig. 3A). This result

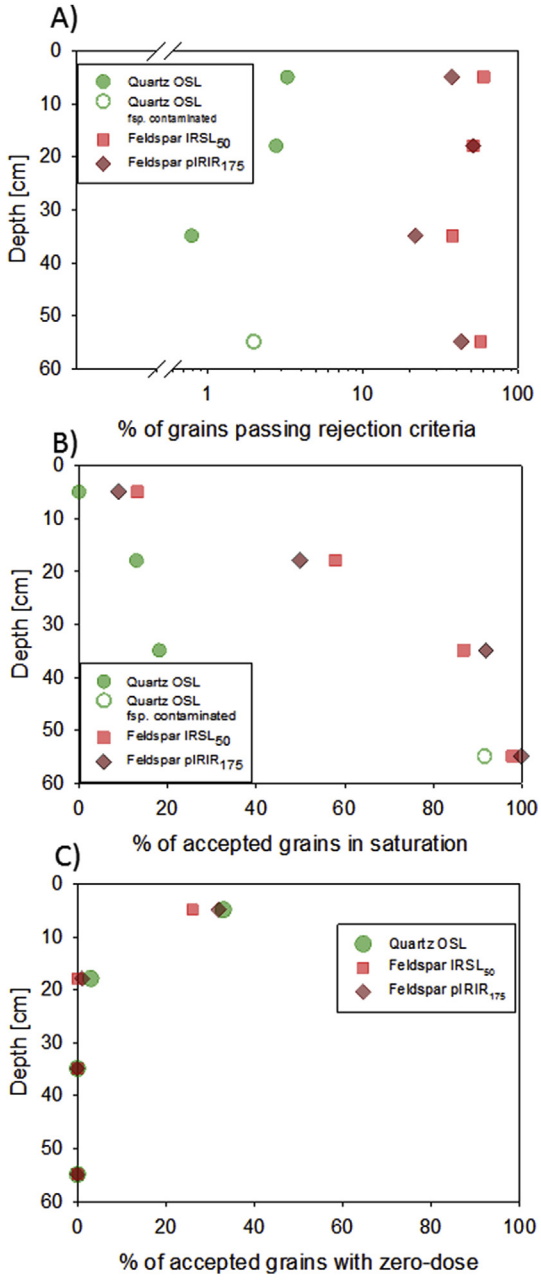

Fig. 3. Single grain luminescence behaviour as a function of sampling depth below the surface. The number of accepted mineral grains (i.e. grains that pass rejection criteria, section 2.4) for the different sample depths is plotted in A). Note that the x-axis of A) is logarithmic. The plot in B) is showing the percentage of accepted mineral grains above the saturation threshold The $2D_0$ criteria of Wintle and Murray (2006) was used as a limit for luminescence signal saturation. More details are provided in section 2.3.

corroborates similar findings by others from a wide range of geological and sedimentary settings (e.g. Duller et al., 2000; 2006; Lüthgens et al., 2011; Demuro et al., 2013; Reimann et al., 2012b). For the upper three samples, the main rejection reason is the luminescence sensitivity (i.e. rejection criteria (i) and (ii) see above). For the lowermost sample (NCL-1214092) the luminescence sensitivity seems better (40% of grains passing rejection criteria (i) and (ii)). This sample, however, shows a striking dominance of feldspar contamination (applying rejection criterion (vi)) possibly because it is closest to the saprolite (Table 1) and the quartz that is freshly converted from the underlying saprolite is not further purified yet by weathering processes. This puts a question to the reliability of the quartz OSL D_e estimate from NCL-1214092. With the exception of this questionable sample NCL-1214092 the percentage of quartz grains passing rejection criteria, and thus acceptable quartz grains, seems to decrease with depth (Fig. 3A, Table 1) The decrease of acceptable quartz luminescent grains from top to bottom possibly reflect maturing of quartz luminescence dosimetric properties mature during soil reworking and thus with increased residence time in the mobile regolith.

The percentage of suitable feldspar grains is more than an order of magnitude larger than for quartz (Fig. 3A), with 47–77% of the feldspar grains are luminescent (Table 1, rejection criteria (i) and (ii), see above) and many of these grains also meet the other two feldspar acceptance criteria. With regard to the $IRSL_{50}$ signal, 38–61% of the feldspar grains are suitable luminescence dosimeters. For $pIRIR_{175}$, 22–52% of the feldspar grains meet all acceptance criteria (Figs. 3A and 4, Table 1).

The percentage of accepted grains with luminescence signals above the saturation threshold (natural signal $>2^*D_0$, section 2.3) increases with depth for all three data types (OSL, IRSL, pIRIR; Fig. 3B). At 5 cm depth 0–13% of the accepted grains are above the saturation threshold whereas at 55 cm we consider 92% (quartz OSL), 98% (feldspar $IRSL_{50}$) or 100% (feldspar $pIRIR_{175}$) of the sand grains in saturation. Although quartz OSL displays a similar trend as the feldspar signals, the actual percentages, differ considerably (Fig. 3B, Table 1); plus we have to bear in mind that the quartz sample NCL-1214092 is questionable due to a significant feldspar contamination (see above). Possible reasons for quartz and feldspar differences are discussed in section 4.1.

The number of zero-dose grains for both feldspar signals and the quartz OSL signal drops dramatically from the uppermost sample NCL-1214089 at 5 cm depth (~30% zero-dose grains) to sample NCL-1214090 at a depth of 18 cm (0–3% zero-dose grains). For the two lower samples no zero-dose grain was found. All three datasets produce consistent trends through the soil profile with regard to zero-dose grains (Table 1, Fig. 3C). The distribution of the zero-dose grains through the soil profile suggests that present-day soil reworking, and thus the import of surface grains to the soil matrix, is limited to the uppermost part of the soil profile. Below 18 cm depth active soil reworking is currently not taking place.

3.2. Equivalent dose distributions and burial ages

Single-grain luminescence analyses have the advantage that we can distinguish between non-saturated (surface-visiting grains according to Heimsath et al., 2002) and saturated sand grains. The latter have most likely never been transported to the surface and thus they do not yield useful information with regard to the velocity of soil reworking processes. To account for this we excluded grains exceeding the saturation threshold (2^*D_0) from the calculations of the equivalent doses, corresponding apparent luminescence ages and apparent soil reworking rates.

The quartz D_e distributions peak at higher doses with increasing depth (Fig. 4). At 5 cm depth the majority of grains have doses close

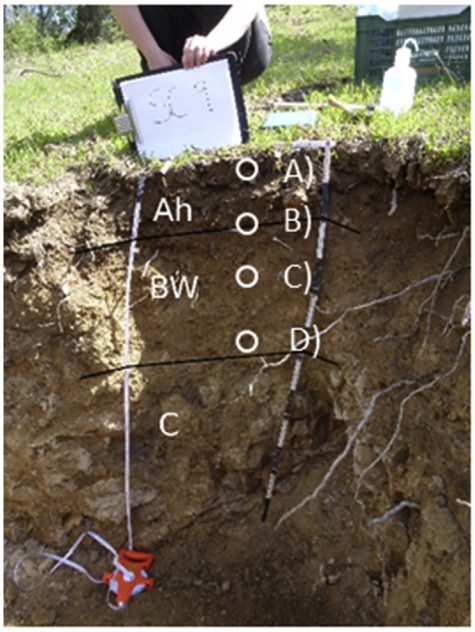

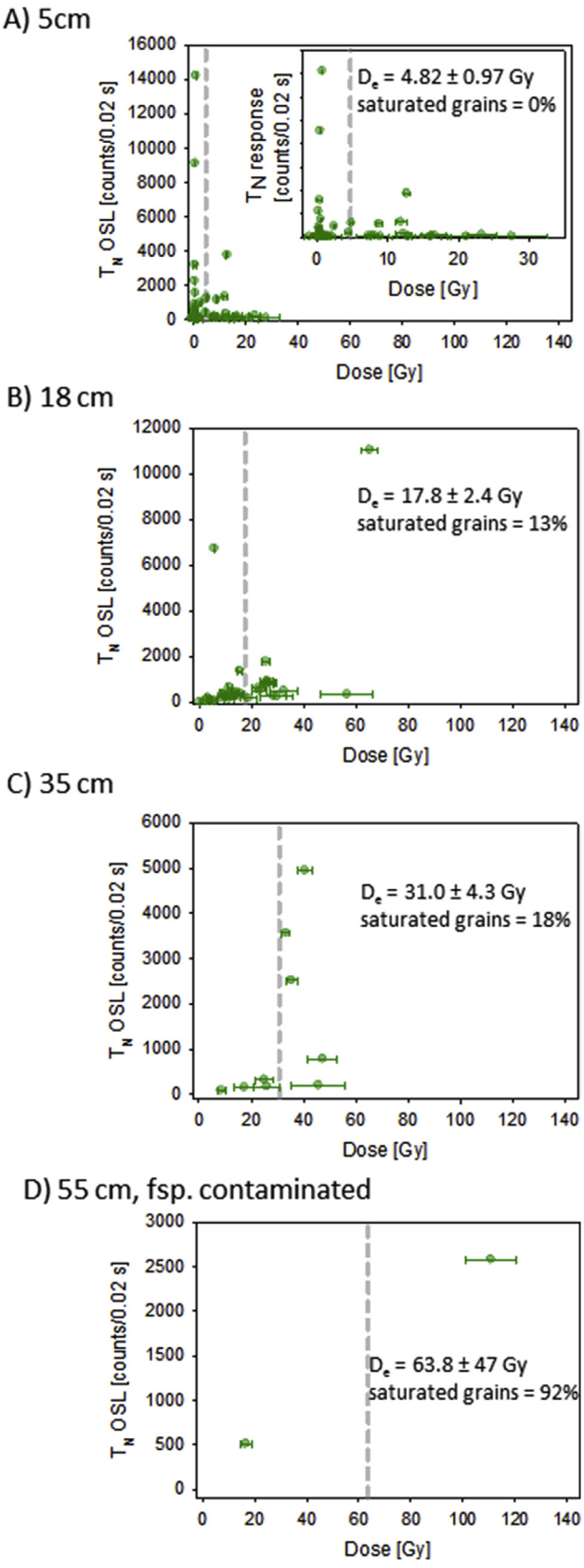

Fig. 4. Quartz OSL single-grain D_e distributions. Quartz OSL D_e vs T_N plots for the soil sample at 5 cm, 18 cm, 35 cm and 55 cm depth are shown in A), B), C), and D), respectively. Only grains below the saturation threshold (non-saturated) are plotted (see section 3.2). The percentage of grains with D_e above the saturation threshold (saturated grains), is indicated as well, and is shown to increase with sample depth. The shaded dashed line indicates the unweighted mean D_e estimate. On the left hand side the description of the corresponding soil profile is provided.

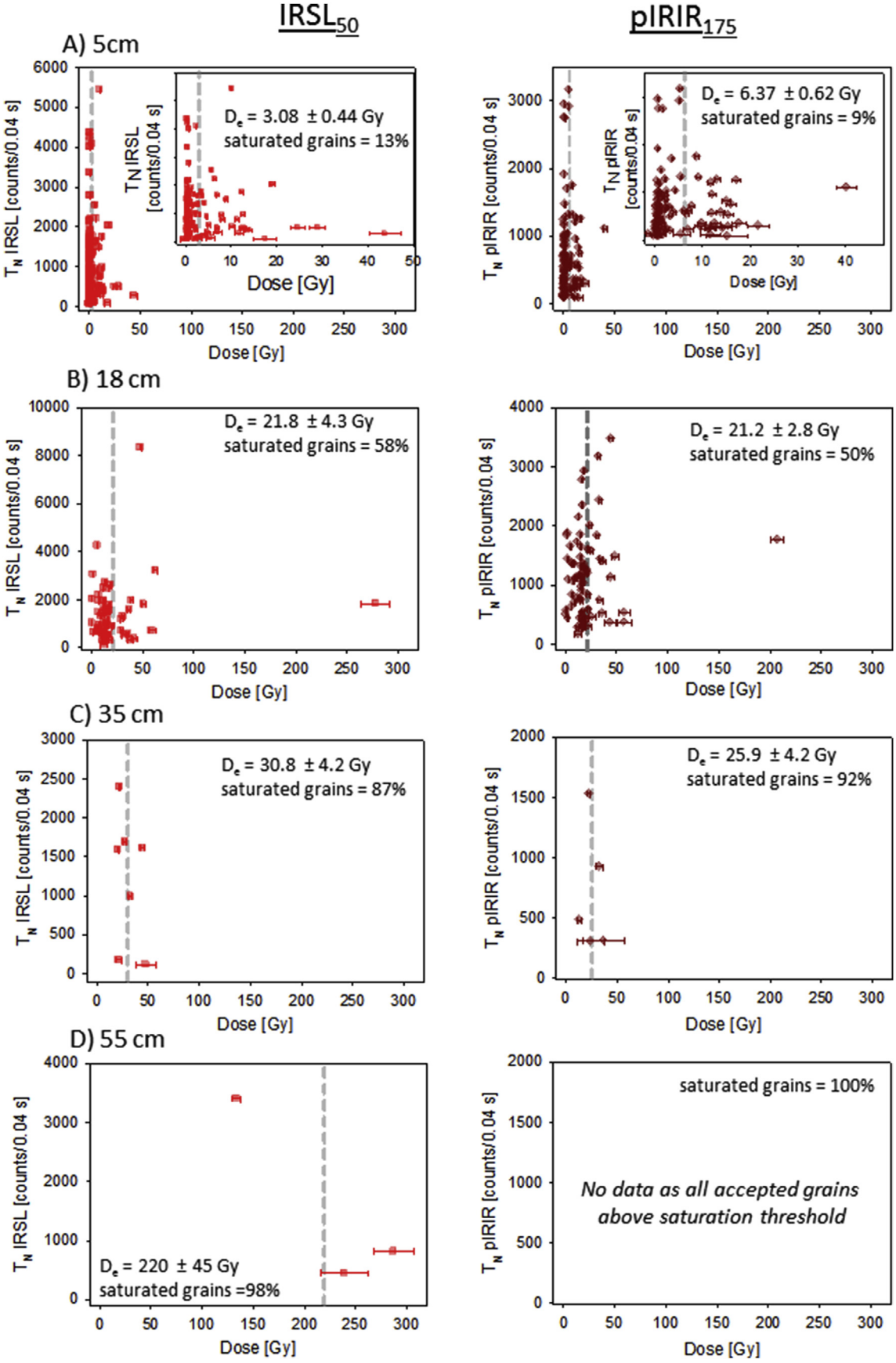

Fig. 5. Feldspar $IRSL_{50}$ (left column) and feldspar $pIRIR_{175}$ (right column) single-grain D_e distributions. $IRSL_{50}$ and $pIRIR_{175}$ D_e vs T_N plots for the soil sample at 5 cm, 18 cm, 35 cm and 55 cm depth are shown in A), B), C), and D), respectively. Only grains below the saturation threshold (non-saturated) are plotted (see section 3.2). The percentage of grains above the saturation threshold (saturated grains), is indicated as well, and increases with sample depth. The shaded dashed line indicates the unweighted mean D_e estimate. A description of the corresponding soil profile is provided in Fig. 4.

to zero suggesting recent resetting of those grains. The shape of the dose distributions changes from positively skewed close to the surface with an accentuated low D_e leading edge population to broad for the lower samples (Fig. 4). The percentage of accepted quartz grains above the saturation threshold increases with depth (Fig. 4, Table 1).

The feldspar dose distributions ($IRSL_{50}$ and $pIRIR_{175}$) also peak at higher doses with increasing depth (Fig. 5). For the sample in closest proximity to the surface the majority of grains reveal doses very close to zero for both signals. The shapes of the dose distributions of the two upper−samples (NCL-1214089 and NCL1214090) are positively skewed for both feldspar signals and show a clear low D_e leading edge population. The D_e distributions of the lower two samples show broad normal distributions.

The sample D_e is calculated based on the unweighted mean of the corresponding D_e distributions and the 1-sigma standard error is assigned as corresponding uncertainty. To allow comparison of the scatter in our distributions to previous OSL soil reworking studies and the modelling results of Heimsath et al. (2002) we furthermore report the ratio of the mean D_e and its standard deviation (N_s/S_s) (Table 2).

We divided the mean equivalent dose estimate by the total dose rate to calculate the apparent luminescence age of the samples, i.e. we estimate the time since grains last visit the surface. The informative value of the age estimates for the lowermost sample NCL-1214092 is limited as those ages are based upon a two quartz grains or three feldspar grains ($IRSL_{50}$) only. We are convinced, however, that it is important to show the age data of sample at 55 cm in the age comparison; the characterisation of this sample as likely being below the active soil reworking is consistent for all three singe-grain luminescence data sets as the vast majority (>90%) of all grains for this sample is above the saturation threshold and thus has likely never been exposed to daylight (for a more detailed discussion see section 4.1). All feldspar ages were corrected for anomalous fading using the fading rates measured on sample NCL-1214089 of 2.1 ± 0.2 and 1.3 ± 0.4%/decade for the $IRSL_{50}$ and the $pIRIR_{175}$, respectively using the method described in Auclair et al. (2003) and the fading correction model of Huntley and Lamothe (2001). The applied fading rates correspond to typical literature values for both signals (e.g. Reimann et al., 2011).

All apparent ages are listed in Table 2 and shown in Fig. 6. For samples NCL-1214090 and -091 all three data sets (quartz OSL, and feldspar $IRSL_{50}$ and $pIRIR_{175}$) agree with each other within uncertainties at the 1-sigma confidence level. For the topmost sample at 5 cm depth (NCL-1214089) $IRSL_{50}$ and quartz OSL data agree within 2-sigma uncertainties and quartz OSL and feldspar $pIRIR_{175}$ within 1-sigma. In summary, we obtained consistent apparent age results for all three single-grain data sets.

4. Discussion

4.1. Interpretation of the single-grain luminescence data

Our results have important implications regarding the use of luminescence data for the reconstruction of soil reworking processes. Below we discuss three main methodological aspects, namely: signal resetting & D_e distributions, zero-dose grains, maturing of grain luminescence properties, and saturated quartz & feldspar grains.

4.1.1. Signal resetting and D_e distributions

To calculate reliable rates of grain burial, i.e. soil reworking velocity, complete resetting of the luminescence signal at the surface is a crucial prerequisite. For the sample in closest proximity to the surface (NCL-1214089, 5 cm depth) the majority of quartz and feldspar grains reveal doses very close to zero (Figs. 4 and 5) suggesting that the signal resetting of the grains before re-burial was sufficient, i.e. most grains recently visited the surface. Thus, soil reworking, presumably by bioturbation, appears to be a process which transports sand particles to the surface where daylight sufficiently resets luminescence signals prior to re-burial; this confirms previous observations from quartz OSL soil reworking studies (e.g. Heimsath et al., 2002; Stockmann et al., 2013; Kristensen et al., 2015). Furthermore, all equivalent doses increase with increasing depth and corresponding quartz and feldspar apparent ages are consistent (Table 2, Fig. 6). The very good agreement of quartz and feldspar $pIRIR_{175}$ age estimates is an independent support of sufficient light exposure as these signals reset at significantly different rates, which can be used to infer the degree of signal resetting (e.g. Murray et al., 2012; Reimann et al., 2015).

The ratios of mean D_e to its standard deviation (N_s/S_s) are relative low for the upper two sample (0.55−0.73 and 0.52−1.26) and are increasing for the sample at 35 cm (1.99−2.72). This suggests that the relative standard deviation in the single-grain D_e distributions reduces down the soil profile and thus with increasing distance to the surface. This may suggest that the bleaching history of individual grains, which is dominantly driven by soil reworking in this setting, is more heterogeneous in the upper part of the soil profile.

4.1.2. Zero-dose grains

The presents of zero-dose grains in sufficient quantities is

Table 2
Age Table for soil profile SC-9.

Sample ID	Signal	Dose rate [Gy/ka]	Mean D_e [Gy]	N_s/S_s[a]	Uncorr. Age[b] [ka]	Apparent age [ka]
NCL-1214089	OSL	4.41 ± 0.22	4.82 ± 0.97	0.69		1.1 ± 0.2
(depth 5 cm)	$IRSL_{50}$	5.50 ± 0.29	3.08 ± 0.44	0.55	0.6 ± 0.1	0.7 ± 0.1
	$pIRIR_{175}$	5.50 ± 0.29	6.37 ± 0.62	0.73	1.2 ± 0.1	1.3 ± 0.1
NCL-1214090	OSL	4.13 ± 0.12	17.8 ± 2.4	1.26		4.3 ± 0.6
(depth 18 cm)	$IRSL_{50}$	5.08 ± 0.26	21.8 ± 4.3	0.62	4.3 ± 0.9	5.2 ± 1.2
	$pIRIR_{175}$	5.08 ± 0.26	21.2 ± 2.8	0.86	4.2 ± 0.6	4.7 ± 0.7
NCL-1214091	OSL	4.59 ± 0.22	31.0 ± 4.3	2.39		6.8 ± 1.0
(depth 35 cm)	$IRSL_{50}$	5.64 ± 0.29	30.8 ± 4.2	2.72	5.5 ± 0.8	6.6 ± 1.1
	$pIRIR_{175}$	5.64 ± 0.29	25.9 ± 4.2	2.78	4.6 ± 0.8	5.1 ± 0.9
NCL-1214092	OSL	4.22 ± 0.20	63.8 ± 47.0	0.96		15 ± 11
(depth 55 cm)	$IRSL_{50}$	5.12 ± 0.26	220 ± 45	2.79	43 ± 9	53 ± 11
	$pIRIR_{175}$	5.12 ± 0.26	–	–	–	–

[a] Ratio of mean D_e divided by its standard deviation. Adopted from Heimsath et al. (2002).
[b] Fading uncorrected feldspar ages. Details provide in section 3.

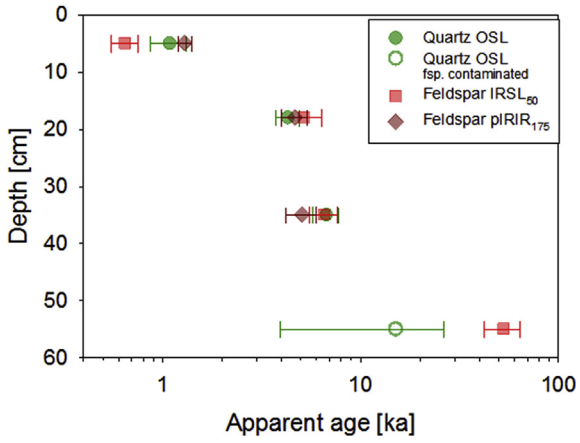

Fig. 6. Apparent ages. The apparent ages for three different luminescence signals (see legend) are plotted as function of soil depth. Data can be found in Table 2. Note that the x-axis is logarithmic.

restricted to the uppermost part of the soil profile (in the vicinity of the uppermost sample, Fig. 3C). Only this part is currently receiving grains form the surface and can be regarded as active reworking zone (see also Gliganic et al., 2016). Our data indicates that the lower boundary of this active reworking zone is between 5 and 18 cm depth. We tentatively suggest that soil reworking in the active reworking zone is characterised by continuous, low amplitude, mixing by typical soil microfauna (e.g. ants), while below this boundary soil reworking may be related to low frequency mixing events with higher amplitudes (e.g. tree-falls, macro fauna burrowing).

The number of zero-dose grains at a certain depth in the soil profile is used by Gliganic et al. (2016) to derive the time it takes until 100% of the soil matrix is replaced by grains from the surface, the so called replacement time. For our uppermost sample at 5 cm depth this replacement time is approximately 3.3 ka, corresponding to ~30% zero-dose grains within ~1000 years. Our replacement time of surface grains at a depth of 5 cm is comparable to replacement times at 25–30 cm depth reported in Gliganic et al. (2016) for a dune setting in SE Australia suggesting that the corresponding downward mixing rates in our Spanish hillslope setting are significantly lower.

4.1.3. Maturing of grain luminescence properties

It is very likely that the quartz luminescence signals experience a maturing process during repeated cycling (daylight exposure and radiation exposure). The quartz grains close to the saprolite zone boundary, reveal poor luminescence sensitivity, show a low number of accepted quartz grains (NCL-1214091), or a dominance of feldspar contamination (NCL-1214092). The luminescence sensitivity is better for the upper two samples, for which most grains likely experienced repeated surface exposure and re-burial by soil reworking. Sensitization of quartz OSL signals during cycles of exposure and burial has previously been reported for fluvial and coastal settings (e.g. Pietsch et al., 2008; Sawakuchi et al., 2012) but to our knowledge not in the context of soil reworking. Quartz freshly derived from plutonic or metamorphic bedrock, as analysed here, are typically luminescence insensitive (e.g. Guralnik et al., 2015a) and the number of luminescence emitting quartz grains is likely increasing by repeated cycling. This quartz luminescence maturing process implies that grains that have never been exposed to daylight, i.e. infinitely old or potentially saturated quartz grains, are likely to be luminescence insensitive. As a consequence, quartz grains with a surface exposure history are more likely to pass rejection criteria and thus the ratio of grains above the saturation threshold to non-saturated quartz grains will be biased towards the non-saturated grains.

In contrast to quartz and with the exception of the highly feldspar contaminated quartz sample NCL-1214092, the percentage of feldspar grains passing rejection criteria does not decrease down the profile (Fig. 3A). This finding is in line with previous work showing that feldspar minerals extracted from plutonic or metamorphic bedrock typically show satisfactory IRSL or pIRIR luminescence sensitivity (e.g. Sohbati et al., 2011; Guralnik et al., 2015b). We think that this explains the disagreement between quartz and feldspar saturation data (next subsection) as the latter is not biased towards the non-saturated (i.e. surface-visiting) grains.

4.1.4. Saturated quartz and feldspar grains

Our data (Fig. 3) suggests that the number of quartz and feldspar grains exceeding the saturation threshold, i.e. grains that have presumably never been exposed to daylight at the surface, increases with depth. Samples in close proximity to the saprolite (for example NCL-1214092) containing very few quartz grains or no feldspar grains that have been at the surface. This observation is in agreement with the pedological interpretation of the profile that the reworking intensity (e.g. by bioturbation) is highest in close proximity to the surface and drops significantly down the profile. The luminescence data therefore corroborate the field identification of the boundary between mobile regolith and the underlying saprolite or weathered bedrock.

Grains with luminescence signals above the saturation threshold yield no meaningful information regarding the velocity of soil reworking processes by themselves. However, the ratio of non-saturated grains to “saturated” grains provides useful information regarding the effectiveness of soil reworking. At larger depth soil reworking is less intensive which results in a decreasing percentage of grains that have experienced daylight exposure. This trend is reflected in all three luminescence data sets (Fig. 3B), and provides a powerful and novel means to investigate the intensity of soil reworking as a function of depth. Data by Heimsath et al. (2002), from a granite hillslope at the base of the Great Escarpment in Australia, also show how the proportion of quartz grains that never visited the surface increases with depth and varies from 29% at 20 cm depth to 72% at a depth of 50 cm (their Table 2). In contrast to our soil profile, Heimsath et al. (2002) found a significant amount of surface-visiting grains at lower depth near the soil base (between 33 and 56%, at depth between 80 and 60 cm), which is consistent with thorough soil reworking from the surface until within the base of the mobile regolith. However, these findings of Heimsath et al. (2002) are based on single grain-quartz measurements only, i.e. their ratio of surface to non-surface visiting grains is likely to be overestimated (see previous subsection).

Our quartz OSL data display a similar trend regarding the increasing proportion of saturated quartz grains with depth as both feldspar signals, the actual percentages, however, considerably differ with quartz OSL indicating a significantly smaller percentage of saturated grains (Fig. 3, Table 1). This disagreement between quartz and feldspar data most likely arises from the sensitisation of quartz during cycling and thus a bias in the quartz saturation grain data.

4.2. Soil reworking rates

Luminescence ages can be translated into soil reworking rates by dividing the sample depth by the luminescence age (Heimsath et al., 2002; Wilkinson and Humphreys, 2005; Stockmann et al., 2013). This rate indicates the average vertical burial rate of sand sized grains in the soil matrix by either vertical or lateral soil mixing

Table 3
Soil reworking rates for soil profile SC-9.

Sample ID	Signal	Depth [mm]	Apparent age [ka]	Apparent soil reworking rate, SR_{app} [mm/a]	NSF[a] [a.u.]	Effective soil reworking rate, SR_{eff} [mm/a]
NCL-1214089 (depth 5 cm)	OSL	50	1.1 ± 0.2	0.046 ± 0.009	1.00	0.046 ± 0.009
	$IRSL_{50}$	50	0.7 ± 0.1	0.077 ± 0.012	0.87	0.067 ± 0.010
	$pIRIR_{175}$	50	1.3 ± 0.1	0.038 ± 0.003	0.91	0.035 ± 0.003
NCL-1214090 (depth 18 cm)	OSL	180	4.3 ± 0.6	0.042 ± 0.006	0.87	0.036 ± 0.005
	$IRSL_{50}$	180	5.2 ± 1.2	0.035 ± 0.008	0.42	0.015 ± 0.004
	$pIRIR_{175}$	180	4.7 ± 0.7	0.038 ± 0.006	0.50	0.019 ± 0.003
NCL-1214091 (depth 35 cm)	OSL	350	6.8 ± 1.0	0.052 ± 0.008	0.82	0.042 ± 0.006
	$IRSL_{50}$	350	6.6 ± 1.1	0.053 ± 0.009	0.13	0.007 ± 0.001
	$pIRIR_{175}$	350	5.1 ± 0.9	0.069 ± 0.012	0.08	0.008 ± 0.001
NCL-1214092 (depth 55 cm)	OSL	550	15 ± 11	0.036 ± 0.027	0.08	0.0029 ± 0.0021
	$IRSL_{50}$	550	53 ± 11	0.010 ± 0.002	0.02	0.0001 ± 0.0000
	$pIRIR_{175}$	550	–	–	0.00	0.0000 ± 0.0000

[a] Non-saturation factor (NSF). Proportion of non saturated grains (i.e. number of non-saturated grains/number of accepted grains).

processes. The derived soil reworking rates for our profile are shown in Table 3. However, the derived soil reworking rates ignore information on the effectiveness of soil mixing as provided by the percentage of grains that have experienced daylight exposure (i.e. surface visiting grains). Thereby this 'rate' does not reflect the varying soil reworking intensity for different burial depths (Figs. 3A, 4 and 5). This is clearly illustrated by our data, which indicates similar soil reworking rates down the profile (~0.05 mm a^{-1}, Fig. 7A). Given the nature of soil reworking processes, it is evident that soil reworking intensity is a function of depth, and meaningful estimates should reflect this depth dependency. As a simple division of sample depth by apparent age is not capable to reproduce this, it should not be considered a good measure of soil reworking rate. We therefore refer to these soil reworking rates as apparent (SR_{app}).

As an alternative, we propose to use the proportion of non-saturated grains to the total number of accepted grains (non-saturation factor, NSF), i.e. the proportion of surface visiting grains, as a measure of the soil reworking effectiveness (see also section 4.1). Using this measure we can correct the apparent soil reworking rates by applying (Eq. (1)), to derive the effective soil reworking rate (SR_{eff}):

$$SR_{eff} = (\text{sample depth} / \text{apparent luminescence age}) \times NSF \quad (1)$$

Thereby, the effective soil reworking rate (SR_{eff}) determines the intensity of the soil-reworking based on the luminescence age of the non-saturated grains (apparent soil reworking rate) and uses the proportion of non-saturated grains as a correction factor to account for grains that have never visited the surface (or "out of competition" grains). Thus, one cannot use the SR_{eff} rates to directly back-calculate the residence time of the surface visiting in the soil profile. By applying the NSF we basically assign a reworking rate of zero (mm a^{-1}) to "out of competition" grains, i.e. for an increasing number of "out of competition" grains the effective soil reworking rate drops compared to the apparent soil reworking rate, the latter takes exclusively surface visiting grains into account. The non-saturation factors of the samples and the resulting SR_{eff} estimates are listed in Table 3 and shown in Fig. 7, together with conventional soil reworking rates (SR_{app}) for comparison. Contrary to previous studies we also calculate uncertainties relating to our soil mixing rate estimates (Table 3, Fig. 7) by using routine error propagation.

The quartz-based SR_{eff} yields similar values for the upper three samples and significantly drops for the lowest sample NCL-1214092. The SR_{eff} of feldspar, however, displays a different trend, with a clear decrease of the effective soil reworking rate with depth.

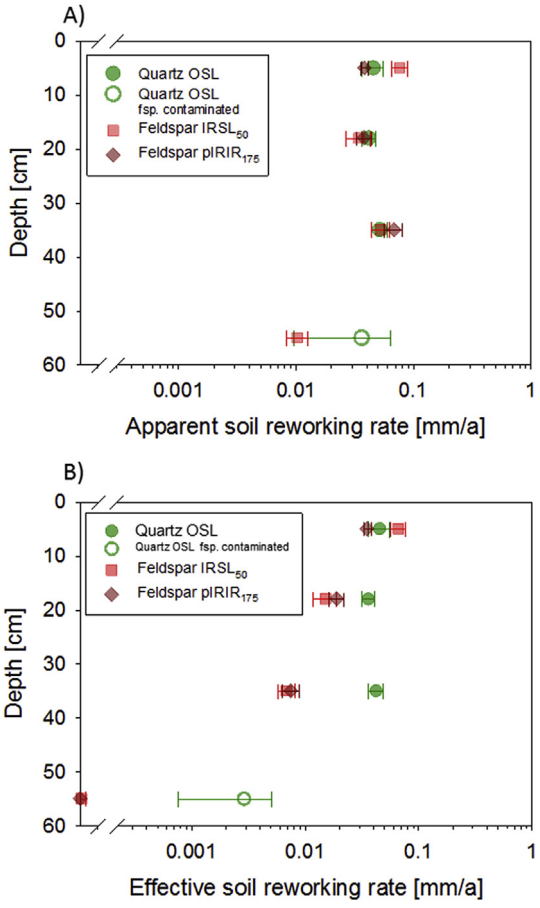

Fig. 7. Resulting soil reworking rates as a function of sample depth. The diagram A) shows the apparent soil reworking rates (SR_{app}). This metric is also used in previous studies (Heimsath et al., 2002; Stockmann et al., 2013) where it is referred to as reworking rate. The metric ignores grains that have not surfaced, and shows no decline of reworking rate with depth, which is highly unrealistic. The effective soil reworking rates (SR_{eff}, following eq. (1)) are shown in B). Here information about non-surfacing grains is incorporated, resulting in decreasing soil reworking rate as a function of depth for the feldspar based data. Quartz data cannot capture this trend, as discussed in the main text. Note that the x-axes are logarithmic.

At the surface we obtained rates of ~0.05 mm a^{-1} for both feldspar signals, whereas the SR_{eff} for the lower samples (at 35 and 55 cm depth) are orders of magnitude smaller (Table 3, Fig. 7B). This smaller feldspar SR_{eff}, results from the larger number of grains that

never visited the surface resulting in low NSF.

We have discussed in section 4.1 that owing to the maturing/sensitisation process of quartz luminescence, single-grain quartz OSL measurements preferably sample quartz grains with a reworking history and thus the quartz NSF is likely to be overestimated. This will result in biased quartz-based SR_{eff} estimates, which tend to be similar to the SR_{app} estimates. As feldspar luminescence signals do not sensitize during grain mobilisation and cycling, feldspar-based SR_{eff} estimates are not affected by such a bias and provide more meaningful estimates of soil reworking intensity than corresponding quartz rates. The feldspar SR_{eff} estimates are also better in line with the soil reworking pattern that is expected for this setting where soil reworking is most intense in close proximity to the surface and decreases with depth.

This holds important implications for linking bioturbation to creep rates. While the SR_{app} hold no relation to depth, the decrease of SR_{eff} with depth allows explaining convex-up creep profiles, typically observed in hillslopes and reproduced in models (Roering, 2004). The higher effective mixing rates for surface horizons will result in higher velocities of downhill creep, while the opposite is true for deeper horizons. Close to the saprolite, the velocity profile will drop to zero. The derivation of SR_{eff} therefore not only follows logically from taking into account the proportion of surface-visiting to "out of competition" grains but is also consistent with field observations and modelling results.

4.3. Quartz or feldspar grains as luminescence soil reworking tracer?

Our results confirm the potential of K-rich feldspars as an alternative soil reworking tracer and the suitability of the feldspar single-grain pIRIR measurement protocol for this kind of research. We obtained feldspar D_e distributions, apparent luminescence ages and apparent soil reworking rates which are consistent with single-grain quartz OSL data (Figs. 4–7A); the latter has been applied in other soil-reworking studies already (e.g. Heimsath et al., 2002; Stockmann et al., 2013; Kristensen et al., 2015). This provides us with confidence that neither the slower bleaching of the feldspar luminescence signals nor the necessary fading correction is a major source of inaccuracy for the samples under investigation.

One main advantage of the feldspar single-grain procedure is the much larger number of grains that can be used as potential soil reworking tracers (Fig. 3A, Table 1), greatly reducing measurement time and efficiency of data analysis. For our Spanish soil samples for example we had to analysed 1200–1600 quartz grains but only 300 feldspar grains for each sample, reducing measurement time significantly. An additional advantage of K-rich feldspar minerals especially in a soil settings is that a significant part of the dose rate (~20–40%) is provided from the internal potassium and rubidium, the so called internal dose rate. Purified quartz typically has an insignificant internal dose rate, thus the total dose rate is to ~100% provided by the external radiation field. The internal dose rate, however, is independent of some crucial but not un-problematic assumptions regarding the external radiation field. One assumption, is that the radiation surrounding/field has not been altered over the entire burial time, which is clearly a problematic assumption for mobile soil particles (e.g. Heimsath et al., 2002; this study).

Most importantly however, feldspar single-grain luminescence measurements enable us to reliably quantify the number of "out of competition" grains, i.e. grains that have never been exposed to daylight. These grains provide crucial information with regard to the soil reworking effectiveness which is needed to determine the soil reworking intensity as a function of depth. The maturing/sensitisation process in quartz (as described in section 4.1) results in systematic overestimation of effective soil reworking rates (SR_{eff}), especially for soil layers where a small part of the grains has experienced daylight exposure in the past (see section 4.2). This implies that in settings where the quartz experience sensitivity changes during repeated soil reworking, i.e. in settings with freshly weathered quartz from plutonic or metamorphic bedrock, feldspar minerals are more suitable soil reworking tracers.

5. Conclusions

This study presents a new method to determine soil reworking rates from feldspar single grain luminescence data obtained on samples taken at different depth below the surface. We tested this new method on a single soil profile from in Spain, and we used single-grain quartz luminescence analysis for comparison. We made use of a post-IR IRSL measurement protocol which harvest two single-grain feldspar luminescence signals ($IRSL_{50}$ and $pIRIR_{175}$) from one sand sized grain. We conclude that single-grain luminescence analysis of feldspar holds important advantages over quartz single-grain OSL:

i. Higher percentage of grains yielding suitable luminescence properties,
ii. More widely applicable due to more uniform luminescence properties in different locations and thus less dependent on mineral provenance,
iii. Absence of luminescence sensitivity change during soil reworking cycles and thus avoiding bias when determining soil reworking intensity.

Our analysis of single-grain feldspar luminescence allowed us to calculate a novel variable of effective soil reworking rate or soil reworking intensity, taking into account that many grains have never reached the surface. Based on our exploratory study, we propose that feldspar single-grain analysis has the potential to become the method of choice for investigating soil reworking rates.

Acknowledgement

We would like to thank five anonymous reviewers for the constructive feedback on the manuscript and previous versions. All participants of the HAZARD meeting 2016 in Wageningen are thanked for the active and inspiring discussion on our results.

Appendix A. Supplementary data

Supplementary data related to this article can be found at http://dx.doi.org/10.1016/j.quageo.2017.07.002.

References

Aitken, M.J., 1985. Thermoluminescence Dating. Academic Press Inc. Ltd, London.
Amundson, R., Berhe, A.A., Hopmans, J.W., Olson, C., Sztein, A.E., Sparks, D.L., 2015. Soil and human security in the 21st century. Science 348. http://dx.doi.org/10.1126/science.1261071.
Auclair, M., Lamothe, M., Huot, S., 2003. Measurement of anomalous fading for feldspar IRSL using SAR. Radiat. Meas. 37, 487–492.
Bateman, M.D., Boulter, C.H., Carr, A.S., Frederick, C.D., Peter, D., Wilder, M., 2007a. Detecting post-depositional sediment disturbance in sandy deposits using optical luminescence. Quat. Geochronol. 2, 57–64.
Bateman, M.D., Boulter, C.H., Carr, A.S., Frederick, C.D., Peter, D., Wilder, M., 2007b. Preserving the palaeoenvironmental record in Drylands: bioturbation and its significance for luminescence-derived chronologies. Sediment. Geol. 195, 5–19.
Bateman, M.D., Frederick, C.D., Jaiswal, M.K., Singhvi, A.K., 2003. Investigations into the potential effects of pedoturbation on luminescence dating. Quat. Sci. Rev. 22, 1169–1176.
Bøtter-Jensen, L., Andersen, C.E., Duller, G.A.T., Murray, A.S., 2003. Developments in radiation, stimulation and observation facilities in luminescence measurement. Radiat. Meas. 37, 535–541.

Blair, M.W., Yukihara, E.G., Mckeever, S.W.S., 2005. Experiences with single-aliquot OSL procedures using coarse-grain feldspars. Radiat. Meas. 39, 361–374.
Carracedo, M., Paquette, J.L., Alonso Olazabal, A., Santos Zalduegui, J.F., García de Madinabeitia, S., Tiepolo, M., Gil Ibarguchi, J.I., 2009. U–Pb dating of granodiorite and granite units of the Los Pedroches batholith. Implic. Geodyn. Models South. Central Iber. Zone Iber. Massif Int. J. Earth Sci. 98, 1609.
Demuro, M., Arnold, L.J., Froese, D.G., Roberts, R.G., 2013. OSL dating of loess deposits bracketing Sheep Creek tephra beds, northwest Canada: dim and problematic single-grain OSL characteristics and their effect on multi-grain age estimates. Quat. Geochronol. 15, 67–87.
Dietrich, W.E., Perron, J.T., 2006. The search for a topographic signature of life. Nature 439, 411–418. http://dx.doi.org/10.1038/nature04452.
Duller, G.A.T., 2003. Distinguishing quartz and feldspar in single grain luminescence measurements. Radiat. Meas. 37, 161–165.
Duller, G.A.T., 2006. Single grain optical dating of glacigenic sediments. Quat. Geochronol. 1, 296–304.
Duller, G.A.T., 2007. Assessing the error on equivalent dose estimates derived from single aliquot regenerative dose measurements. Anc. TL 25, 15–24.
Duller, G.A.T., Bøtter-Jensen, L., Murray, A.S., 2000. Optical dating of single sand sized grains of quartz: sources of variability. Radiat. Meas. 32, 453–457.
Duller, G.A.T., 2008. Single-grain optical dating of Quaternary sediments: why aliquot size matters in luminescence dating. Boreas 37, 589–612.
Gabet, E.J., Reichman, O.J., Seabloom, E.W., 2003. The effects of bioturbation on soil processes and sediment transport. Annu. Rev. Earth Planet. Sci. 31, 249–273.
Galbraith, R.F., Roberts, R.G., Laslett, G.M., Yoshida, H., Olley, J.M., 1999. Optical dating of single and multiple grains of quartz from Jinmium rock shelter, Northern Australia: part 1, experimental details and statistical models. Archaeometry 41, 339–364.
Gliganic, L.A., May, J.-H., Cohen, T.J., 2015. All mixed up: using single-grain equivalent dose distributions to identify phases of pedogenic mixing on a dryland alluvial fan. Quat. Int. 362, 23–33.
Gliganic, L.A., Cohen, T.J., Slack, M., Feathers, J.K., 2016. Sediment mixing in aeolian sandsheets identified and quantified using single-grain optically stimulated luminescence. Quat. Geochronol. 32, 53–66.
Godfrey-Smith, D., Huntley, D., Chen, W.-H., 1988. Optical dating studies of quartz and feldspar sediments extracts. Quat. Sci. Rev. 7, 373–380.
Guérin, G., Mercier, N., Adamiec, G., 2011. Dose rate conversion factors: update. Anc. TL 29, 5–8.
Guralnik, B., Ankjærgaard, C., Jain, M., Murray, A.S., Müller, A., Wälle, M., Lowick, S.E., Preusser, F., Rhodes, E.J., Wu, T.-S., Mathew, G., Herman, F., 2015a. OSL-thermochronometry using bedrock quartz: a note of caution. Quat. Geochronol. 25, 37–48.
Guralnik, B., Jain, M., Herman, F., Ankjærgaard, C., Murray, A.S., Valla, P.G., Preusser, F., King, G.E., Chen, R., Lowick, S.E., Kook, M., Rhodes, E.J., 2015b. OSL-thermochronometry of feldspar from the KTB borehole, Germany. Earth Planet. Sci. Lett. 423, 232–243.
Heimsath, A.M., Chappell, J., Spooner, N.A., Questiaux, D.G., 2002. Creeping soil. Geology 30, 111–114.
Huntley, D.J., Lamothe, M., 2001. Ubiquity of anomalous fading in K-feldspars and the measurement and correction for it in optical dating. Can. J. Earth Sci. 38, 1093–1106.
Jacobs, Z., Roberts, R.G., 2007. Advances in optically stimulated luminescence dating of individual grains of quartz from archeological deposits. Evol. Anthropol. Issues News Rev. 16, 210–223.
Johnson, M.O., Mudd, S.M., Pillans, B., Spooner, N.A., Fifield, L.K., Kirkby, M.J., Gloor, M., 2014. Quantifying the rate and depth dependence of bioturbation based on optically-stimulated luminescence (OSL) dates and meteoric 10Be. Earth Surf. Process. Landforms 39, 1188–1196.
Kaste, J.M., Heimsath, A.M., Bostick, B.C., 2007. Short-term soil mixing quantified with fallout radionuclides. Geology 35 (3), 243.
Kars, R.H., Busschers, F.S., Wallinga, J., 2012. Validating post IR-IRSL dating on K-feldspars through comparison with quartz OSL ages. Quat. Geochronol. 12, 74–86.
Kars, R.H., Reimann, T., Ankjærgaard, C., Wallinga, J., 2014. Bleaching of the post-IR IRSL signal: new insights for feldspar luminescence dating. Boreas 43, 780–791.
Keesstra, S.D., Bouma, J., Wallinga, J., Tittonell, P., Smith, P., Cerdà, A., Montanarella, L., Quinton, J., Pachepsky, Y., van der Putten, W.H., Bardgett, R.D., Moolenaar, S., Mol, G., Fresco, L.O., 2016. FORUM paper: the significance of soils and soil science towards realization of the UN sustainable development goals (SDGs). Soil Discuss. 2016, 1–28.
Klasen, N., Fiebig, M., Preusser, F., Reitner, J., Radtke, U., 2007. Luminescence dating of proglacial sediments from the Eastern Alps. Quat. Int. 164–165, 21–32.
Kristensen, J.A., Thomsen, K.J., Murray, A.S., Buylaert, J.P., Jain, M., Breuning-Madsen, H., 2015. Quantification of termite bioturbation in a savannah ecosystem: application of OSL dating. Quat. Geochronol. http://dx.doi.org/10.1016/j.quageo.2015.02.026.
Lukas, S., Spencer, J.Q.G., Robinson, R.A.J., Benn, D.I., 2007. Problems associated with luminescence dating of late quaternary glacial sediments in the NW Scottish Highlands. Quat. Geochronol. 2, 243–248.
Lüthgens, C., Böse, M., Preusser, F., 2011. Age of the Pomeranian ice marginal position in north-eastern Germany determined by Optically Stimulated Luminescence (OSL) dating of glaciofluvial (sandur) sediments. Boreas 40, 598–615.
Madsen, A.T., Buylaert, J.-P., Murray, A.S., 2011b. Luminescence dating of young coastal deposits from New Zealand using feldspar. Geochronometria 38, 379–390.
Madsen, A.T., Murray, A.S., Jain, M., Andersen, T.J., Pejrup, M., 2011a. A new method for measuring bioturbation rates in sandy tidal flat sediments based on luminescence dating. Estuar. Coast. Shelf Sci. 92, 464–471.
Mejdahl, V., 1979. Thermoluminescence dating: beta-dose attenuation in quartz grains. Archaeometry 21, 61–72.
Mudd, S.M., Yoo, K., Gabet, E.J., 2013. Influence of chemical weathering on hillslope forms. In: Shroder, John F. (Ed.), Treatise on Geomorphology, vol. 7. Academic Press, San Diego, pp. 56–65.
Murray, A.S., Thomsen, K.J., Masuda, N., Buylaert, J.P., Jain, M., 2012. Identifying well-bleached quartz using the different bleaching rates of quartz and feldspar luminescence signals. Radiat. Meas. 47, 688–695.
Murray, A.S., Roberts, R.G., 1997. Determining the burial time of single grains of quartz using optically stimulated luminescence. Earth Planet. Sci. Lett. 152, 163–180.
Murray, A.S., Roberts, R.G., 1998. Measurements of the equivalent dose in quartz using a regenerative-dose single aliquot protocol. Radiat. Meas. 29, 503–515.
Prescott, J.R., Hutton, J.T., 1994. Cosmic ray distributions to dose rates for luminescence and ESR dating: large depths and long-term variations. Radiat. Meas. 23, 497–500.
Pietsch, T.J., Olley, J.M., Nanson, G.C., 2008. Fluvial transport as a natural luminescence sensitiser of quartz. Quat. Geochronol. 3, 365–376.
Preusser, F., Degering, D., Fuchs, M., Hilgers, A., Kadereit, A., Klasen, N., Krbetschek, M., Richter, D., Spencer, J.Q.G., 2008. Luminescence dating: basics, methods and applications. Eiszeitalt. Ggw. Quat. Sci. J. 57, 95–149.
Preusser, F., Ramsmeyer, K., Schlüchter, Ch, 2006. Characterisation of low OSL intensity quartz from New Zealand Alps. Radiat. Meas. 41, 871–877.
Preusser, F., Chithambo, M.L., Götte, T., Martini, M., Ramseyer, K., Sendezera, E.J., Susino, G.J., Wintle, A.G., 2009. Quartz as a natural luminescence dosimeter. Earth Sci. Rev. 97, 184–214.
Preusser, F., Muru, M., Rosentau, A., 2014. Comparing different post-IR IRSL approaches for the dating of Holocene coastal foredunes from Ruhnu Island, Estonia. Geochronometria 41, 342–351.
Reimann, T., Notenboom, P.D., De Schipper, M.A., Wallinga, J., 2015. Testing for sufficient signal resetting during sediment transport using a polymineral multiple-signal luminescence approach. Quat. Geochronol. 25, 26–36.
Reimann, T., Thomsen, K.J., Jain, M., Murray, A.S., Frechen, M., 2012a. Single-grain dating of young feldspars using the pIRIR procedure. Quat. Geochronol. 11, 28–41.
Reimann, T., Lindhorst, S., Thomsen, K.J., Murray, A.S., Frechen, M., 2012b. OSL dating of mixed coastal sediments (Sylt, German Bight, North Sea). Quat. Geochronol. 11, 52–67.
Reimann, T., Tsukamoto, S., 2012. Dating the recent past (<500 years) by post-IR IRSL feldspar – examples from the North Sea and Baltic Sea coast. Quat. Geochronol. 10, 180–187.
Reimann, T., Tsukamoto, S., Naumann, M., Frechen, M., 2011. The potential of using K-rich feldspars for optical dating of young coastal sediments – a test case from Darss-Zingst peninsula (southern Baltic Sea coast). Quat. Geochronol. 6, 207–222.
Rink, W.J., Dunbar, J.S., Tschinkel, W.R., Kwapich, C., Repp, A., Stanton, W., Thulman, D.K., 2013. Subterranean transport and deposition of quartz by ants in sandy sites relevant to age overestimation in optical luminescence dating. J. Archaeol. Sci. 40, 2217–2226.
Roberts, R.G., Galbraith, R.F., Yoshida, H., Laslett, G.M., Olley, J.M., 2000. Distinguishing dose populations in sediment mixtures: a test of single-grain optical dating procedures using mixtures of laboratory-dosed quartz. Radiat. Meas. 32, 459–465.
Roering, J.J., 2004. Soil creep and convex-upward velocity profiles: theoretical and experimental investigation of disturbance-driven sediment transport on hillslopes. Earth Surf. Process. Landforms 29, 1597–1612. http://dx.doi.org/10.1002/esp.1112.
Sawakuchi, A.O., Guedes, C.C.F., DeWitt, R., Giannini, P.C.F., Blair, M.W., Nascimento, D.R., Faleiros, F.M., 2012. Quartz OSL sensitivity as a proxy for storm activity on the southern Brazilian coast during the Late Holocene. Quat. Geochronol. 13, 92–102.
Smedley, R.K., Duller, G.A.T., et al., 2013. Optimising the reproducibility of measurements of the post-IR IRSL signal from single-grains of K-feldspar for dating. Anc. TL 31, 49–58.
Smedley, R.K., Duller, G.A.T., Pearce, N.J.G., Roberts, H.M., 2012. Determining the K content of single-grains of feldspar for luminescence dating. Radiat. Meas. 47, 790–796.
Sohbati, R., Murray, A.S., Jain, M., Buylaert, J.P., Thomsen, K.J., 2011. Investigating the resetting of OSL signals in rock surfaces. Geochronometria 38, 249–258.
Stockmann, U., Minasny, B., Pietsch, T.J., McBratney, A.B., 2013. Quantifying processes of pedogenesis using optically stimulated luminescence. Eur. J. Soil Sci. 64, 145–160.
Spooner, N.A., 1994. The anomalous fading of infrared-stimulated luminescence from feldspars. Radiat. Meas. 23, 625–632.
Steffen, D., Preusser, F., Schlunegger, F., 2009. OSL quartz age underestimation due to unstable signal components. Quat. Geochronol. 4, 353–362.
Thomsen, K.J., Murray, A.S., Jain, M., Bøtter-Jensen, L., 2008. Laboratory fading rates of various luminescence signals from feldspar-rich sediment extracts. Radiat. Meas. 43, 1474–1486.
Tsukata, H., Takeda, A., Hisamatsu, S., Inaba, J., 2008. Concentration and specific activity of fallout ^{137}Cs in extracted and particle-size fractions of cultivated soils. J. Environ. Radioact. 99, 875–881.

van Gorp, W., Veldkamp, A., Temme, A.J.A.M., Maddy, D., Demir, T., van der Schriek, T., Reimann, T., Wallinga, J., Wijbrans, J., Schoorl, J.M., 2013. Fluvial response to Holocene volcanic damming and breaching in the Gediz and Geren rivers, western Turkey. Geomorphology 201, 430–448.

Wilkinson, M.T., Humphreys, G.S., 2005. Exploring pedogenesis via nuclide-based soil production rates and OSL-based bioturbation rates. Aust. J. Soil Res. 43, 767–779.

Wintle, A.G., Murray, A.S., 2006. A review of quartz optically stimulated luminescence characteristics and their relevance in single-aliquot regeneration dating protocols. Radiat. Meas. 41, 369–391.

Wallinga, J., Bos, A.J.J., Dorenbos, P., Murray, A.S., Schokker, J., 2007. A test case for anomalous fading correction in IRSL dating. Quat. Geochronol. 2, 216–221.

EVALUATING A SPATIAL SOIL WATER BALANCE MODEL UNDER MEDITERRANEAN CLIMATE AND INTERACTION WITH SOIL FORMATION

A. Román Sánchez[1], J. Vicente Giráldez[1,2] and T. Vanwalleghem[1]

[1] Dpto. of Agronomy, University of Córdoba, Ctra Madrid km 396, Córdoba, Spain o92rosaa@uco.es, ag1gicej@uco.es, ag2vavat@uco.es
[2] Institute of Sustainable Agriculture. CSIC, Alameda del Obispo, Córdoba, Spain.

ABSTRACT. Influence of the Mediterranean climate, relief and geology can shed light on the most important processes that affect the mechanisms and rate of bedrock weathering. This study presents a new spatially explicit model of soil water and temperature dynamics to explain the processes in soil formation. Several profiles along a catena located in Sierra Morena, Cordoba, S Spain.
This model also remarked the importance of soil water flow at different topographical positions, and other geomorphological processes on soil formation over long-term time scales.

RESUMEN. La influencia del clima mediterráneo, el relieve y la geología pueden aclarar los procesos más importantes que afectan a los mecanismos de meteorización de la roca madre y sus respectivas intensidades. Este estudio presenta un nuevo modelo espacial que evalúa la dinámica del agua del suelo y la temperatura para explicar los procesos de formación del suelo. En el área de estudio, situada en Sierra Morena, Córdoba, S España, se han analizado varios perfiles a lo largo de una catena.
Este modelo también permite evaluar la importancia del flujo de agua en el suelo en diferentes posiciones topográficas y otros procesos geomorfológicos en la formación del suelo a largo plazo.

1.- Introducción

It is well known that soil formation depends on factors such as bedrock, climate, relief, vegetation and time, of which hydrology and relief control strongly the spatial distribution of soil patterns within a catchment. However, despite the great effort dedicated to these processes, little is known about the quantitative relationship between geomorphological processes and soil formation, especially on long timescales. This work presents preliminary results of a larger study on soil forming processes in the South Central Sierra Morena area of SW Spain, Figure 1, where also shows the location of the study area with the soil pits along a typical catena. The soils formed on partially decomposed granite rock, show considerable differences in development stage, depending on the position in the catena.

Current available soil formation models range from simple mass-balance schemes, MILESD (Vanwalleghem *et al.*, 2013), to more complex systems models that include the dynamics of soil water and chemical processes, SoilGen (Finke *et al.*, 2013). LORICA (Arnaud *et al.* 2015) is a model that includes similar soil formation processes than MILESD, but considers more layers in the soil and the dynamic adaptation of the number of layer as a function of the soil profile's heterogeneity.

While the latter models have successfully described soil profile development, they are computationally demanding, and, therefore, difficult to apply at the landscape scale. The former models however, are too simple to include a closer representation of soil water and chemistry.

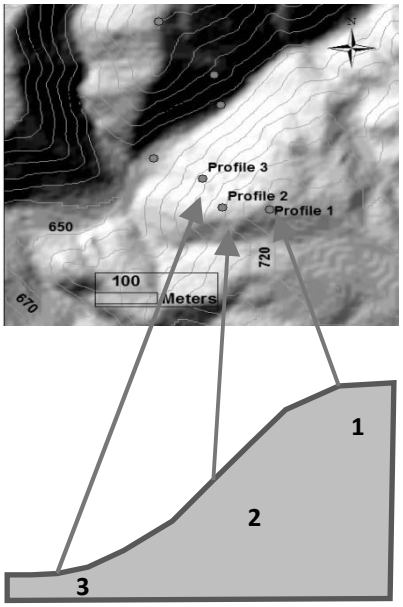

Fig. 1. Location of the study area and scheme of the catena

Therefore, this study proposes a long-term soil evolution spatially explicit model based on a simple soil water balance. The model uses as input data daily variations of temperature and rainfall. Usually paleoclimate data are available at the yearly or seasonal time scale only.

The objectives of this work are (i) to analyse and generate daily paleoclimate input data for the last 25.000 years (ii) to evaluate trends in soil moisture, deep percolation and infiltration and relate these with topographical variables like aspect, slope and to compare for different topographical positions along a catena, the importance of water and energy fluxes, erosion and soil formation.

2. Materials and Methods

2.1. Calibration with present-day data

The available daily rainfall, and maximum, average, and minimum temperatures taken from the Cordoba weather station (AEMET: 1959-2011) were used for the calibration of the weather generator.

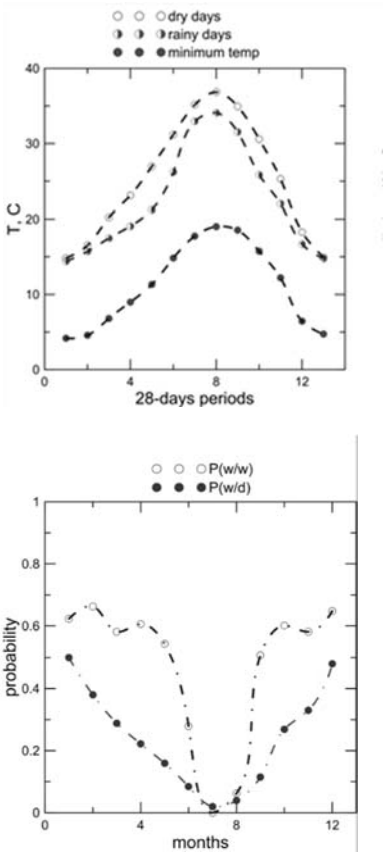

Fig. 2. Calibration of input parameters for the paleoclimate weather generation. P(w/w) and P(w/d) stand, respectively, for the probability of a rainy day occurring either after another rainy, or rainless, day.

2.2. Generation of palaeoclimate data

Originally, a random Monte Carlo approach was tested for generating temperature and rainfall, based on their respective probability distribution functions as suggested by Laio *et al.* (2001). However, problems with the phase angle distortion between rainfall and temperature data recommended the adoption of a Markovian scheme suggested by Matalas (1967), and incorporated by Richardson in his WGEN model (1981). The applicability of this model has been proved by several authors (*e.g.* Semenov *et al.*, 1998). The WGEN model calibrated for Córdoba, was coupled with rainfall and temperature anomalies presented by Combourieu Nebout *et al.* (2009) for a period of 25 000 years based on marine pollen records (Figure 3). The combined model was applied to the reconstruction of daily temperature and rainfall.

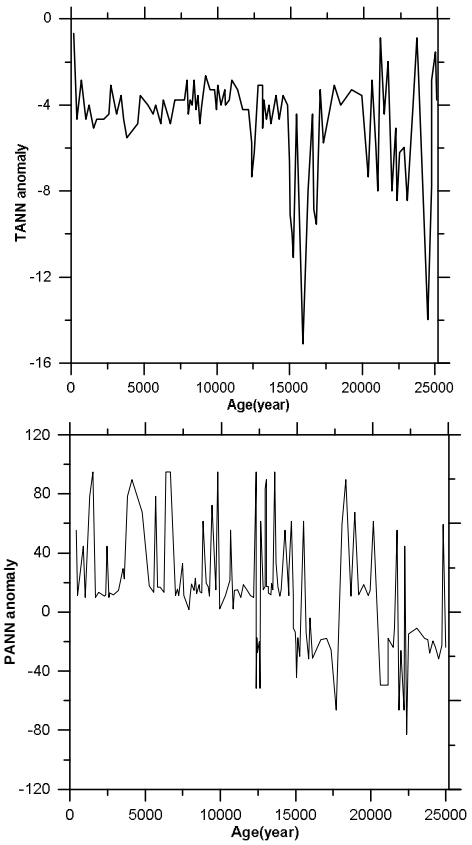

Fig. 3. Annual temperature and precipitation anomalies for a 25000 years period.

2.2.1. Estimation of potential evapotranspiration

To complete the water budget, the evapotranspiration rate, *ep*, for the study area was computed with the Hargreaves and Samani (1985) model. Potential evapotranspiration follows a sine-like trend.

2.2.2. Soil water balance model

The evolution of soil moisture is described with a simple model based on the scheme of Thornthwaite and Mather (Steenhuis and van der Molen, 1986) for the first order soil evaporation decay rate, and the treatment of the infiltration and percolation processes proposed by Brocca *et al.* (2008). In the latter model the infiltration rate, *f(t),* is equal to the rainfall rate corrected by a coefficient depending on the ratio between the actual soil moisture in the profile, *W(t),(3)* and its maximum value, W_{max}, *or cc*, wetness, with an exponent *m* that indicates the non-linearity of the process. The percolation rate, *g(t),* is equivalent to the value of the hydraulic conductivity, k_s, for the actual moisture content, assuming a unit hydraulic gradient, λ is the pore size distribution index linked to the structure of the soil layer and using the Brooks and Corey exponential function. In this case the flow is assumed to be gravity driven, with drainage consisting of deep percolation.

The actual evaporation rate, *ev*, is after the correction of *ep* with a factor, *cu*

$$ev = ep * cu \quad (1)$$

The water loss through evapotranspiration according to Thornthwaite and Mather is modified by the cumulative water loss, *Ph*, a time proxy

$$Ph(t) = Ph(t - \Delta t) + \Sigma ev - \Sigma p \quad (2)$$

The moisture in the profile, *W*, is expressed as a function of cumulative water loss

$$W(t) = cc * e^{-Ph(t)/cc} \quad (3)$$

The percolation rate is

$$g(t) = ks \left(\frac{W(t)}{Wmax}\right)^{3+(2/\lambda)} \quad (4)$$

Finally the infiltration rate is

$$f(t) = p(t)\left\{1 - \left(\frac{W(t)}{Wmax}\right)^{m}\right\} \quad (5)$$

To include the effect of the relief on the profiles along the catena, (1) plateau, (2) hillslope and (3) valley bottom, the profiles are linked by transferring runoff *(q)*, from the higher to the lower-lying profiles as runoff.

2.3. Calibration with observed runoff

To validate the model, historic runoff data from automatic hydrological information service, SAIH, of the Guadalquivir water district (1989-2011) will be used. Thereby, the model will be calibrated for our study area with a Mediterranean climate.

3. Results

The output of the model is a water balance dependent of the effect of the relief and the soil properties in the study area.

3.1. Water balance

Figure 4, shows the water balance in one of the three profiles, in this case profile 1 at the plateau.

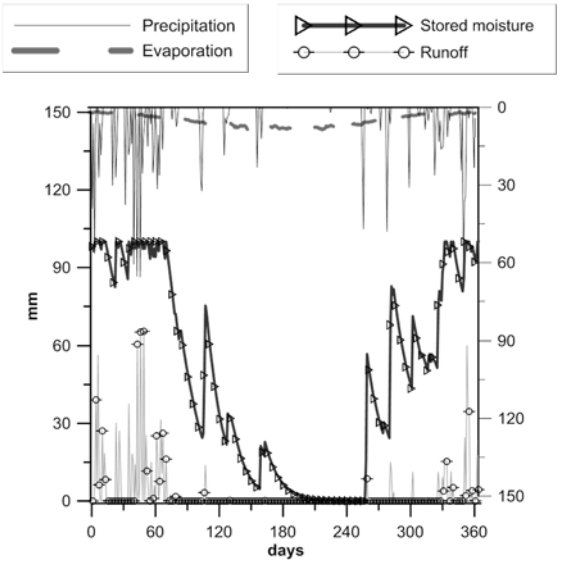

Fig. 4. Water balance in profile 1, at the plateau.

The relation between profile soil moisture, *W(t)*, runoff (*q*), precipitation (*p*) and potential evaporation (*ep*) for one model year is plotted in Figure 4.

This figure shows how the rain peaks quickly induce runoff maxima, once other water detention stores, as canopies, soil and surface depressions, are filled up. Interception on the vegetation and surface retention in pools, reduce the influence of the catchment contributing to the discharge at the runoff. The stored soil moisture reaches its maximum value, 100 mm in this case, during the winter months. After the first winter events there is usually a low rain period, but it disappears after a few weeks. The most frequent rains occur in spring and autumn. Some convective rains can appear in summer. There is a strong seasonal trend, as it can be expected in Mediterranean climate, with minimum values during summer.

During the winter rainy season, major runoff and percolation events occur. The computed cumulative percolation during one year appears in Figure 5.

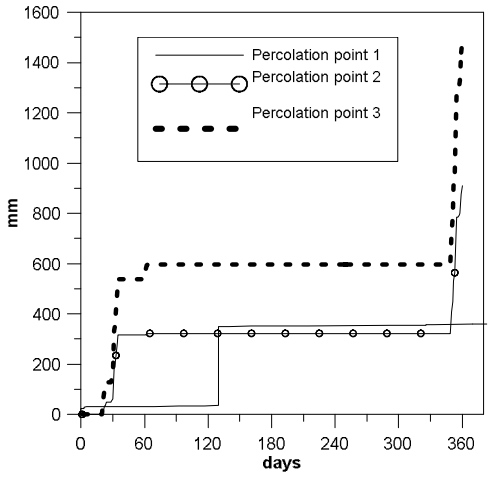

Fig. 5. Profile 1, 2, and 3, percolation accumulated throughout the year.

There is an evident relationship between the depth of each profile, its elevation, and the percolation volume. The plateau profile is more developed than the hillslope and valley bottom profile, although it is the shallowest.

The figures 6 and 7 represent the average soil moisture content and infiltration rate at the watershed. Light areas indicate greater average soil moisture contents and infiltration rates in the valleys and streams, what coincide with field observations.

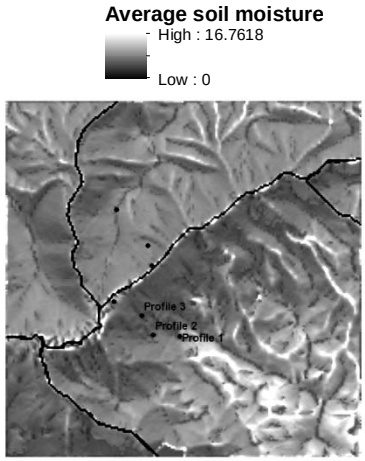

Fig. 6. Average soil moisture in the watershed

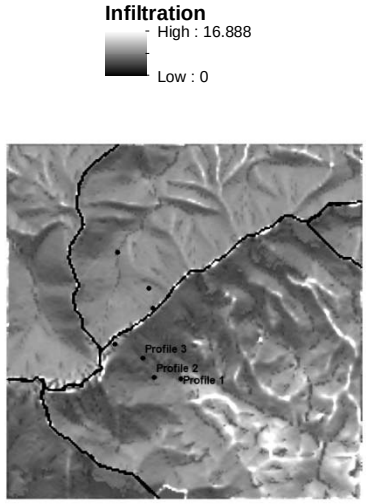

Fig. 7. Infiltration rates in the watershed. The higher values correspond to the plateau and watercourses

4. Conclusions

Simple models are useful tools to simulate seasonal water balance fluctuations, which are thought critical controls on soil formation in Mediterranean areas. The results of this model are oriented to calculate the water balance at the landscape scale and as the results show, large differences were found in the analysis of the different profiles. This model compares for different topographical positions the importance of water and energy fluxes, erosion and soil formation and incorporates in a simple way their interactions quantitatively. It is an efficient model; it can generate daily data along 1000 years in one hour.

Future work will now focus on to calibrate the model with observed runoff data in the study area and to introduce parameters that have influence on the weathering bedrock processes in order to generate a model of long timescales of soil formation and landscape-scale (25,000 years).

Acknowledgements. This study was funded by the research project AGL2012-40128-C03-02. Andrea Román is funded by predoctoral Fellowship Programme, Spanish Ministry of Science. Tom Vanwalleghem acknowledges funding by the Ramón y Cajal Fellowship Programme, Spanish Ministry of Science.

5. References

Brocca L., Melone F., Moramarco T. 2008. *On the estimation of antecedent wetness conditions in rainfall-runoff modelling. Hydrological Processes* 22, 629-642.

Combourieu-Nebout, N., Peyron, O., Dormoy, I., Desprat, S., Beaudouin, C., Kotthoff, U., Marret, F. 2009. *Rapid climatic variability in the west Mediterranean during the last 25 000 years from high resolution pollen data. EGU. Climate of the Past 5:* 503-521.

Finke P.A., Vanwalleghem T., Opolot E., Poesen J., Deckers J. 2013. *Estimating the effect of tree uprooting on variation of soil horizon depth by confronting pedogenetic simulations to measurements in a Belgian loess area. Journal of Geophysical Research, Earth Surface.* 118:2124-2139.

Hargreaves, G.H., Samani, Z.A., 1985. *Reference crop evapotranspiration from temperature. Applied Enineering. Agriculture,* 1: 96-99.

Laio F., Porporato A., Ridolfi L., Rodriguez-Iturbe I. 2001. *Plants in water-controlled ecosystems:active role in hydrologic processes and response to water stress. II Probabilistic soil moisture dynamics. Advances in Water Resources,* 24:707-723.

Matalas, N.C. 1967. *Mathematical assessment of synthetic hydrology. Water Resources Research.* 3:937, 945.

Richardson, C.W. 1981. *Stochastic simulation of daily precipitation, temperature, and solar radiation. Water Resources. Research.* 17:182-190.

Semenov, M.A., Brooks, R.J., Barrow, E.I., Richardson, C. W. 1998. *Comparison of the WGEN and LARS-WG stochastic weather generators for diverse climates. Climate Research.* 10:95-107.

Steenhuis, T.S, van der Molen, W.H. 1986. *The Thornthwaite-Mather procedure as a simple engineering method to predict recharge. Journal of. Hydrology.* 84:221-229.

Vanwalleghem, T., Stockmann U, Minasny B. and McBratney A.B. 2013 *A quantitative model for integrating landscape evolution and soil formation. Journal of Geophysical Research, Earth Surface* 118:331-347.

MEDITERRANEAN LANDSCAPE DYNAMICS: SOIL FORMATION PROCESSES LONG-TERM

ROMÁN SÁNCHEZ, ANDREA[1] (O92ROSAA@UCO.ES); GIRÁLDEZ, JUAN V.[1,2]; VANWALLEGHEM, TOM[1]

[1] University of Cordoba, Department of Agronomy, da Vinci Bldg, Cra Madrid km 396, 14071 Córdoba, Spain
[2] Institute of Sustainable Agriculture. CSIC, Alameda del Obispo s/n, Córdoba, Spain

Soil formation is a complex process that depends on factors such as bedrock, climate, relief, vegetation and time. Despite of the great effort dedicated to explore these processes, little is known there is not a precise about the quantitative relationship between geomorphology and soil formation, especially on long timescales. In order to understand this complex interaction is important to investigate some quantitative aspects of the processes that drive pedogenesis. The integration of quantitative aspects by means of modelling will help us to understand better the soil formation upscaling this information at large scales of time. In this study the effect of aspect and relative elevation on long- term soil formation has been studied on two converging slopes. The geometry generates microclimates that can structure ecosystems and affect depth and surface processes regimes.

In our study area, located in Sierra Morena, in Cordoba, S Spain, we studied 10 soil profiles along a catena distributed in various topographic conditions: plateau area, north and south facing slope. These profiles were sampled each 10-20 cm depth in order to study the quantitative differences in physical and chemical soil properties. A new, spatially explicit model is presented of water infiltration and redistribution, temperature coupled to soil forming processes as a function of properties such as topographical variables, like aspect, slope, climate variables and vegetation. This model is based on a simple soil water balance model and runs at a daily time step. As paleoclimate data for rainfall and temperature is generally only available at the yearly or seasonal time scale, a weather generator was used in order to generate the necessary input data. Model output, for example mean annual water percolation, are then compared against field observations to evaluate whether the model can explain important soil properties, such as for example total weathered soil depth or texture. This model allows to compare for different topographical positions the importance of water and energy fluxes, erosion and soil formation and incorporate in a simple way their interactions quantitatively.

SINGLE-GRAIN OSL AND IRSL DATING FOR RECONSTRUCTION OF SOIL FORMING PROCESSES IN A HILLSLOPE CATENA IN SIERRA MORENA, S SPAIN

ROMÁN SÁNCHEZ, ANDREA[1] (O92ROSAA@UCO.ES); REIMANN, TONY[2]; VANWALLEGHEM, TOM[1]; TEMME, ARNAUD J.A.M.[2]; GIRÁLDEZ, JUAN V.[1,3]

[1] University of Cordoba, Department of Agronomy, da Vinci Bldg, Cra Madrid km 396, 14071 Córdoba, Spain

[2] Soil Geography and Landscape group & Netherland Centre for Luminescence Dating (NCL). Wageningen University, Wageningen, Netherland

[3] Institute of Sustainable Agriculture. CSIC, Alameda del Obispo s/n, Córdoba, Spain

Soil formation depends on bedrock, climate, relief, vegetation and time. Bioturbation and colluvial soil re-location are important and significant processes that affect the mechanisms and rate of bedrock weathering. The estimation of the relative fraction of bedrock grains which has been mixed in the soil and transported either vertically or laterally to different depths gives an indication of the degree to which bedrock weathering is controlled by the latter processes. However, despite the great effort dedicated to the analysis of these processes, little is known about the quantitative relationship between geomorphological changes and soil formation, especially for long timescales. This study presents reconstruction of soil processes by single grain optically stimulated luminescence techniques (OSL) in several profiles sampled along a hillslope. The OSL analyses provide a direct measurement of soil forming processes (e.g. bioturbation, colluviation) and with them a more precise formulation of soil formation models at longer timescales.

Single-grain OSL techniques have been applied to quartz and feldspar minerals which were extracted from different soil horizons from a hillslope catena located in Sierra Morena, Córdoba, in the south of Spain. Four profiles were explored extracting twelve samples in order to study vertical and lateral mixing (e.g. soil creep, colluvial processes) of soils.

The suitability of three different OSL single grain approaches, quartz OSL, IRSL (infrared stimulated luminescence) and pIRIR (post-IRSL) feldspar, was tested on four samples. Statistical parameters deduced from single-grain OSL age distributions (e.g. number of zeroed grains, scatter and shape of the distribution) were used as indicators for bioturbation and/or soil-relocation. The most suitable approach was then applied to the several samples from hillslope catena. This study reveals the potential of OSL single-grain techniques in order to shed light on bioturbation and pedoturbation processes within soil formation and their interrelationship with geomorphological processes.

ESTIMACIÓN DE TASAS DE MEZCLA VERTICAL Y LATERAL DEL SUELO MEDIANTE UN MODELO ANALÍTICO

A. Román-Sánchez[1]*, A.M. Laguna[2], T. Reimann[3], A. Peña[4], J.V. Giráldez[1,5], J. Wallinga[3] y Tom Vanwalleghem[1]

[1]Dpto. de Agronomía, Universidad de Córdoba, Edif. Da Vinci, Ctra. Madrid km 396, 14071 Córdoba. e-mail: o92rosaa@uco.es
[2]Dpto. de Física Aplicada, Universidad de Córdoba, Edif. C2, Ctra. Madrid km 396, 14071 Córdoba.
[3]Soil Geography and Landscape group & Netherlands Centre for Luminescence dating, Universidad de Wageningen.
[4] Dpto. de Ingeniería Rural, Universidad de Córdoba, Edif. Da Vinci, Ctra. Madrid km 396, 14071 Córdoba.
[5] Instituto de Agricultura Sostenible, CSIC, Avda. Menéndez Pidal s/n. 14004 Córdoba

RESUMEN. Diferentes factores como el relieve, la roca madre, el clima, la actividad de los organismos y la vegetación intervienen en la formación del suelo. Tanto la bioturbación como el desplazamiento lateral del suelo por erosión ayudan a comprender la evolución conjunta del paisaje y del suelo. En este trabajo se propone una nueva solución analítica para la ecuación de la difusión y advección para estimar un valor de la difusividad y las intensidades de erosión o sedimentación a lo largo de una ladera. Se ha calibrado el modelo con datos de edad y profundidad obtenidos en perfiles de suelo.

ABSTRACT. Different factors such as relief, bedrock, climate, activity of the organisms and vegetation are involved in the soil formation. Both bioturbation and lateral movement of the soil by erosion help to understand the evolution of the landscape and the soil. An analytical solution for the diffusion-advection equation is proposed to estimate the values of diffusivity coefficient as well as of the erosion or deposition rates along a slope. The model is calibrated with age-depth data from soil profiles.

1. INTRODUCCIÓN

El suelo se forma cuando la roca madre se meteoriza y aparecen en ella materiales orgánicos. A pesar de su importancia

este proceso no se conoce muy bien en sí mismo, ni a escala de paisaje que co-evoluciona con el suelo (Heimsath 2002). Los procesos implicados dependen de las características de la zona como el clima, el relieve, la vegetación, el suelo. Stockmann et al. (2014) estimaron la intensidad de producción del suelo a través de la determinación de los radionucleidos cosmogénicos (TCN) sin detectar influencias de la litología o el clima. De todos los procesos que intervienen en la formación del suelo posiblemente se conozcan mejor los físicos y químicos, Sin embargo la influencia biológica en los procesos anteriores, siendo esencial es menos conocida. En particular el proceso conocido como bioturbación, la alteración física del material parental por micro- y macroorganismos, ya observado por Darwin en el siglo XIX, y patente en numerosas formas del relieve como termiteros o mimas, los montículos de Norteamérica atribuidos a castores y especies similares, y las consecuencias de la caída de árboles, es un tema importante de la investigación actual. (Gabet et al., 2003) analizaron la alteración del suelo producida por caída de árboles, termitas, lombrices, hormigas que causan la mezcla de partículas que estaban enterradas y son llevadas a la superficie.

Wilkinson et al., 2005 y Wilkinson et al., 2009 observaron una gran relación entre la alteración biológica del suelo y la formación de suelo y la evolución del paisaje.

Para describir de una forma sencilla la influencia de la bioturbación en la formación del suelo Johnson et al. (2014) propusieron una ecuación sencilla basada en la ecuación de difusión y advección.

Un aspecto importante en la formación del suelo es estimar la edad de los materiales que se modifican gradualmente con la profundidad bajo la superficie. Para ello la luminiscencia ópticamente estimulada (OSL) usando cuarzo o estimulada con Infrarrojo (IRSL, post IR IRSL) usando feldespato, puede detectar la edad de la alteración inicial, evaluando la energía que conserva el mineral (cuarzo o feldespato) desde la última vez que apareció en la superficie del suelo. Así pues, la edad del grano mineral es el tiempo transcurrido desde la última vez que estuvo en la superficie y posteriormente fue enterrado. Heimsath et al. (2002), Stockman et al., (2013); Johnson et al. (2014) evaluaron la edad de la muestra y la velocidad de mezcla del suelo usando esta técnica en granos de cuarzo. En este trabajo se introduce el uso de feldespato como trazador para determinar procesos pedogénicos. Reiman et al., 2017 aceptado, descubrió las ventajas del feldespato frente al cuarzo, con mayor porcentaje de granos luminiscentes y mayor eficacia en las medidas.

El objetivo de este trabajo es reconstruir los procesos de mezcla vertical y lateral y determinar las tasa de erosión superficial, depósito y bioturbación en perfiles de suelo a lo largo de una ladera.

2. MATERIALES Y MÉTODOS

2.1. Área de estudio

El área de estudio está localizada en el Parque Natural de Cardeña y Montoro, en la provincia de Córdoba. La precipitación media se sitúa en 545 mm con la estación húmeda en el invierno y las temperaturas varían entre 5 y 40 ºC. Este clima ha permitido el desarrollo de bosque mediterráneo esclerófilo representado por especies

arbóreas como *Quercus ilex* subsp. *Ballota*, *Quercus suber*, *Quercus faginea* y especies arbustivas como *Quercus coccifera, Pistacia lentiscus, Phlomis purpurea, Rubus ulmifolius*. A nivel geológico la zona en estudio está compuesta por granito y está integrada dentro del Batolito de los Pedroches. Los suelos están formados por Regosoles, Cambisoles y Pheozems. La zona muestreada se encuentra en un transecto lineal a lo largo de una ladera orientada al norte en la cabecera de la cuenca Martín Gonzalo. Se muestrearon cuatro perfiles de suelo: SC-10 (parte alta de la ladera), SC-9 (zona alta de la media ladera), SC-8 (zona baja de la media ladera), SC-7 (base de la ladera) a diferentes profundidades (5, 20,35 y 50 cm), (fig.1).

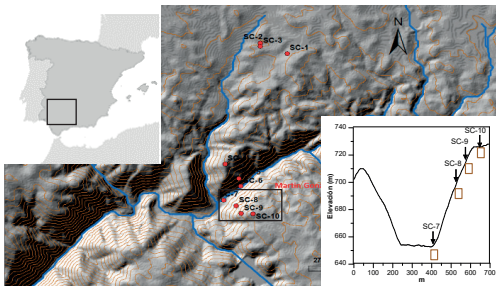

Fig. 1. Localización de la zona de estudio en el Parque Natural de Cardeña y Montoro (Córdoba, España). Perfiles de suelo SC-10, SC-9, SC-8 y SC-7 a lo largo de un transecto lineal en la ladera norte de la cabecera de la cuenca Martín Gonzalo.

2.2. Preparación de la muestra y medidas de luminiscencia

Se cogieron 15 muestras de suelo utilizando tubos metálicos de 5 cm de diámetro y 25 cm de largo clavados en cada uno de los perfiles a diferentes profundidades. Tras mantener las muestras selladas para impedir alteraciones por la luz solar, se enviaron al Netherland Centre for Luminescence dating (NCL) en la Universidad de Wageningen donde fueron preparadas y analizadas bajo luz tenue naranja. Una vez extraído el suelo de los tubos metálicos su contenido se dividió en dos partes, la primera para determinar la dosis absorbida por por unidad de tiempo, dose rate, (DR), y, la segunda, para estimar la paleodosis, equivalent dose (ED) o radiación absorbida desde la última vez que el grano estuvo expuesto a la luz.

Para determinar la DR, se separó 5 cm de suelo de cada extremo del tubo que posiblemente había estado expuesto a la luz de la superficie. Además, se tuvo en cuenta en el cálculo de la DR el contenido de humedad y materia orgánica de la muestra, determinándose mediante el secado en horno a 105 ºC para la humedad y a 500 ºC para la materia orgánica. La muestra se molió y se formaron discos prensados para así poder determinar mediante un espectrómetro de radiación gamma la dose rate. Para determinar la (ED) o paleodosis se utilizó el resto de la muestra contenida en el tubo y que no había estado expuesta a la luz. Esta muestra se tamizó a diferentes tamaños: <180 µm, >250 µm, 180-212 µm and 212-250 µm y se eligió el último para continuar con el tratamiento y medidas. La muestra elegida se trató con HCl y H_2O_2 para eliminar materia orgánica y los componentes de carbonatos. Seguidamente se separaron los minerales de feldespato y cuarzo con un líquido de densidad. Sólo el cuarzo fue tratado durante 40 minutos por 40% HF eliminando cualquier contaminación por feldespato.

Una vez realizado el pretratamiento químico tanto del feldespato como del cuarzo se procedió a las medidas de luminiscencia con un dispositivo Risø TL/OSL

reader DA 15 con una fuente de radiación beta $^{90}Sr/^{90}Y$ irradiando con 0.115 Gys^{-1} (Bøtter-Jensen et al., 2003; Duller, 2003). El protocolo seguido fue el de dosis regenerativa para la medida de la luminiscencia en la muestra. Para el cuarzo se llevó a cabo el método de luminiscencia estimulada ópticamente (OSL) y para el feldespato la luminiscencia estimulada por infrarrojo que a su vez se divide en dos metodologías: IRSL estimulada con 50 ºC y post-IR IRSL estimulada con 175 ºC. Los pasos a seguir en el protocolo de medida fueron: 1- Se extrajo la señal luminiscencia natural del grano mineral normalizada por la luminiscencia natural del siguiente test regenerado (L_N/T_N). 2- Se irradió cada grano mineral con varias dosis artificiales de radiación beta. 3- Se normalizó para cada grano la intensidad de luminiscencia de respuesta a cada dosis artificial irradiada con la señal del siguiente test (L_x/T_x). 4- Con este ratio se calculó una curva denominada dose response para ser ajustada a una función exponencial+lineal. 5- Se interpoló la luminiscencia natural de cada grano mineral en la dose response curve para obtener la dosis o (ED).

2.3.- Determinar la edad de la muestra y velocidad de mezcla en el suelo

La edad o tiempo desde la última vez que la muestra visitó la superficie del suelo se determinó dividiendo la ED entre la DR mediante la ecuación 1 (Reimann et al., 2017 aceptado; Román-Sánchez et al., 2017 en preparación)

$$Edad = \frac{ED\ (Gy\ \ a^{-1})}{DR\ (Gy)} \qquad (1)$$

Según, Stockman et al., 2013 Reimann et al., 2017 aceptado, Román-Sánchez et al., 2017 en preparación, la velocidad de mezcla del grano mineral en el suelo se puede calcular mediante la ecuación 2.

$$Ratio\ mezcla = \frac{Profundidad\ (mm)}{Edad\ \ (a)} \qquad (2)$$

2.4. Modelo analítico ecuación difusión-advección

Una vez calculada la edad de cada muestra a diferentes profundidades en cada perfil, se ajustó los resultados a un modelo que integra la ecuación de difusión-advección para hallar la constante de difusividad y el ratio de erosión-depósito a lo largo de la ladera.

Suponiendo que la bioturbación es el proceso esencial de alteración del regolito y que simultáneamente puede ser descrito mediante una ecuación de difusión, con D como la difusividad, que varía exponencialmente con la profundidad, z, en función de un parámetro de profundidad, z_b, y un valor de la difusividad, D_0

$$\frac{\partial A}{\partial t} = \frac{\partial}{\partial z}\left(D(z)\frac{\partial A}{\partial z}\right) \qquad (3)$$

$$D(z) = D_o e^{-z/zb} \qquad (4)$$

y que este proceso va acoplado con un proceso de erosión y depósito con intensidad constante, T ,o W, respectivamente (Johnson et al., 2014).

La ecuación completa para el caso de erosión es

$$\frac{\partial A}{\partial t} = \frac{\partial}{\partial z}\left(D(z)\frac{\partial A}{\partial z}\right) - T\frac{\partial A}{\partial z} + 1 \qquad (5)$$

Y para el caso de depósito

$$\frac{\partial A}{\partial t} = \frac{\partial}{\partial z}\left(D\frac{\partial A}{\partial z}\right) + W\frac{\partial A}{\partial z} + 1 \quad (6)$$

Suponiendo un sistema en equilibrio, en régimen permanente, bajo condiciones de contorno en superficie, $A=0$ y $z=0$, $D=D_o$, con la profundidad a la que aparece el regolito, z_o, y en la base del perfil, si no hay erosión, $T=0$, (z_{bp}), las ecuaciones 5 y 6 pueden resolverse con una solución analítica para la edad de la partícula en profundidad.

3. RESULTADOS Y DISCUSIÓN

3.1. Variación vertical y lateral de (ED)

La fig. 2 muestra los histogramas de frecuencia de ED para el feldespato $IRSL_{50}$ en cada una de las muestras a diferentes profundidades para cada perfil a lo largo de la ladera.

Como se observa en la fig. 2 para cada perfil, las muestras más someras, a 5 cm de profundidad, tienen mayor número de granos luminiscentes que las muestras más profundas. A medida que la profundidad aumenta el número de granos que ha sido expuesto a la superficie es menor. En el caso de los perfiles SC-8, SC-9 y SC-10 a partir de 35 cm de profundidad el número de granos que emiten luminiscencia es muy pequeño (entre el 2 y 15%). El resto de granos medidos, nunca ha visitado la superficie del suelo, lo que demuestra la presencia del límite entre el regolito y saprolito. Las muestras próximas a la superficie tienen una ED próxima a cero, una ED más pequeña.

En la fig. 2 se aprecia, también el trasporte ladera abajo. La fracción aguas arriba de la ladera tienen mayores valores de ED que los de aguas abajo.

Los resultados obtenidos con cuarzo y feldespato p-IR IRSL son similares. En este caso, sólo se midió con cuarzo el perfil SC-9 demostrándose con este perfil que el tiempo de medida era mayor y el porcentaje de granos luminiscentes era menor (Reimann et al., 2007 aceptado). Por este motivo, se optó por medir el feldespato para el resto de muestras, con mayores ventajas, un número mayor porcentaje de granos sensibles a la luminiscencia y mayor eficacia en el tiempo de medida.

3.2 Variación vertical y lateral de la edad

La fig.3 muestra importantes variaciones de la edad dentro de cada perfil y lateralmente a lo largo de la ladera. Por un lado, dentro de cada perfil, la edad aumenta exponencialmente con la profundidad. Estos resultados son consistentes con los observados en procesos de bioturbación, con una actividad mayor cerca de la superficie del suelo y disminuye a medida que profundiza en el suelo (Wilkinson et al., 2009). En el caso del perfil SC-10, la edad permanece casi constante a partir de 20 cm indicando que el proceso de mezcla del suelo permanece constante a partir de esa profundidad. Por otro lado, la edad disminuye a medida que se desciende en la ladera, siendo más baja en el perfil SC-7, en la base de la misma. Esto explica el movimiento lateral en la ladera producido por erosión superficial.

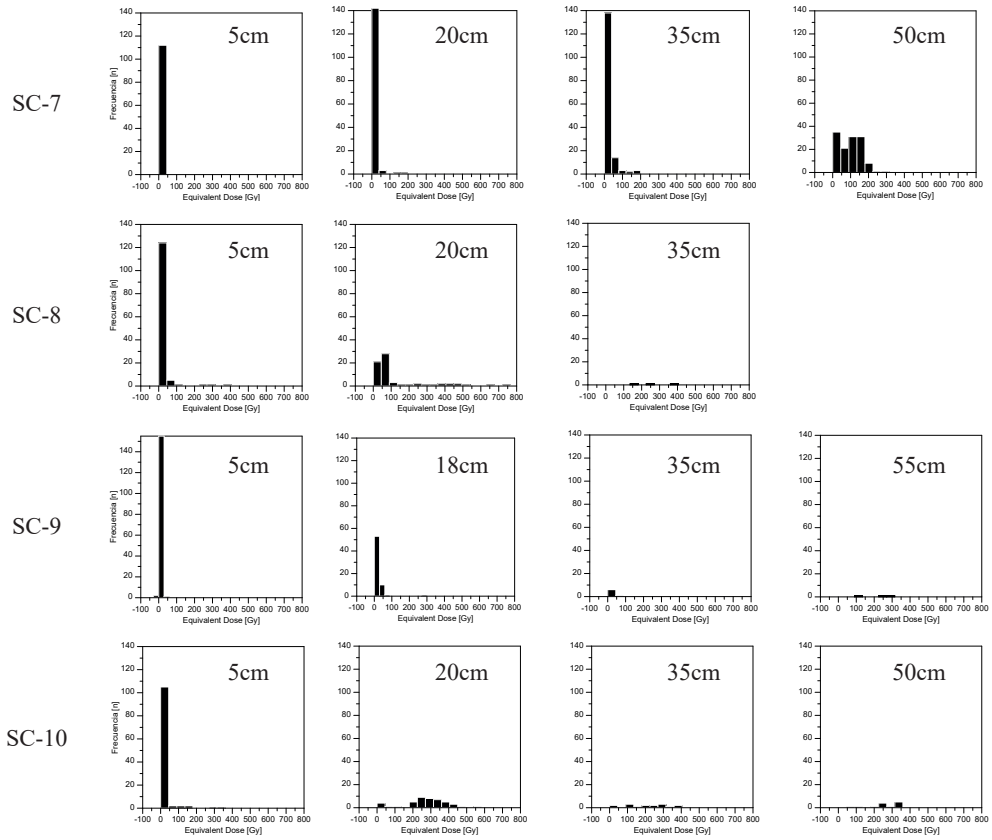

Fig. 2 Distribución de Equivalent dose (ED) en cada uno los perfiles.

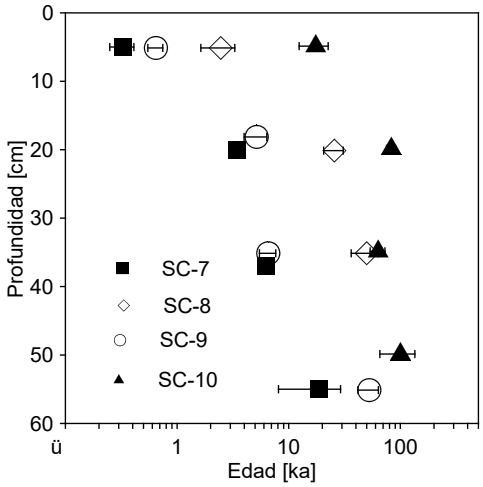

Fig. 3 Distribución de la edad en profundidad en cada perfil a lo largo de la ladera.

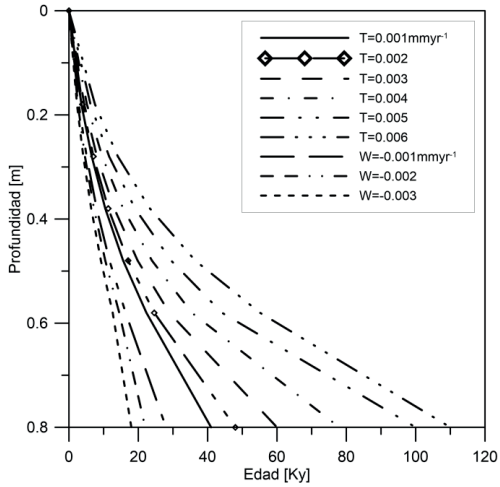

Fig. 4 Modelo teórico ecuación difusión-advección.

3.3 Solución analítica de la ecuación advección-difusión

Se han estimado los valores de los parámetros difusividad *Do*, e intensidades medias de erosión superficial *T* y depósito en ladera *W*.

La difusividad varía a 5 cm de profundidad entre 52 mm^2/año para el perfil situado en el fondo del valle (SC-7) y 12 mm^2 $año^{-1}$ para el perfil en la parte alta de la ladera (SC-10). A 50 cm de profundidad la constante de difusividad varía entre 34 y 0.7 mm^2 $año^{-1}$ para el perfil del valle (SC-7) y la cima (SC-10) respectivamente.

Los resultados indican que los valores óptimos de erosión son 0.008 mm a^{-1} para los perfiles SC-7 y SC-8, 0.004 mm a^{-1} para el perfil SC-10 y depósito -0.008 mm a^{-1} para el perfil SC-9.

La fig.4 representa la solución de la ecuación de advección y difusión, ecuación (5 y 6).

4. CONCLUSIONES

Los resultados concuerdan con los obtenidos por otros autores como Johnson et al., (2014) en otros ambientes. Este estudio permite conocer el control que ejerce la bioturbación y movimiento lateral sobre los procesos de formación de suelo, determinar las tasas de bioturbación, depósito y erosión empleando un nuevo modelo analítico sencillo a partir de la ecuación de difusión-advección, dilucidar el potencial de la técnica de datación por luminiscencia a través del feldespato en la geomorfología, y por último, identificar por primera vez, a través de esta técnica, el límite entre el regolito y saprolito permitiendo corregir el establecido previamente en campo.

Agradecimientos. Este estudio fue financiado por el proyecto de investigación AGL2012-40128-C03-02. Andrea Román está financiada por el Programa de Becas predoctorales del Ministerio de Economía y Ciencia de España.

5. BIBLIOGRAFÍA

Bøtter-Jensen, L., Andersen, C.E., Duller, G.A.T. y Murray, A.S., 2003. Developments in radiation, stimulation and observation facilities in luminescence measurements, in: Radiation Measurements. Presented at the Radiation Measurements, pp. 535–541. doi:10.1016/S1350-4487(03)00020-9

Duller, G.A.T., 2003. Distinguishing quartz and feldspar in single grain luminescence measurements. *Radiat. Meas. 37, 161–165. doi:10.1016/S1350-4487(02)00170-1*

Gabet, E.J., Reichman, O.J., Seabloom, E.W., 2003. The effects of bioturbation on soil processes and sediment transport. *Annu. Rev. Earth Planet. Sci. 31, 249–273. doi:10.1146/annurev.earth.31.100901.141314*

Gilbert, G.K., 1909. The convexity of hilltops. *J. Geol. 17, 344–350*

Heimsath, A.M., Chappell, J., Spooner, N.A. y Questiaux, D.G., 2002. Creeping soil. Geology 30, 111–114.

Johnson, M.O., Mudd, S.M., Pillans, B., Spooner, N.A., Keith Fifield, L. y Kirkby, M.J., Gloor, M., 2014. Quantifying the rate and depth dependence of bioturbation based on optically-stimulated luminescence (OSL) dates and meteoric 10 Be: Quantifying the rate and depth dependence of bioturbation. *Earth Surf. Process. Landf. 39, 1188–1196. doi:10.1002/esp.3520*

Reimann, T., Román-Sánchez.A, Wallinga, J. y Vanwallgehem, T., 2017. Getting a grip on soil reworking - single-grain feldspar luminescence as a novel tool to quantify soil reworking rates. *Quaternary Geochronology (aceptado)*

Román-Sánchez.A, Reimann, T., Wallinga, J. y Vanwallgehem, T., 2017. Bioturbation and erosion rates along the soil-hillslope conveyor belt, part 1: insights from single-grain feldspar luminescence. *En preparación*.

Román-Sánchez.A, Vanwallgehem, T., Reimann, T., Giráldez, J. V, Laguna, A., Peña, A., Wallinga, J., 2017. Bioturbation and erosion rates along the soil-hillslope conveyor belt, part 2: quantification using an analytical solution of the diffusion-advection equation. *En preparación*

Stockmann, U., Minasny, B., Pietsch, T.J. y McBratney, A.B., 2013. Quantifying processes of pedogenesis using optically stimulated luminescence. *Eur. J. Soil Sci. 64, 145–160. doi:10.1111/ejss.12012*

Stockmann, U., Minasny, B., McBratney, A.B., 2014. How fast does soil grow? *Geoderma 216, 48–61. doi:10.1016/j.geoderma.2013.10.007*

Wilkinson, M.T. y Humphreys, G.S., 2005. Exploring pedogenesis via nuclide-based soil production rates and OSL-based bioturbation rates. *Soil Res. 43, 767–779. doi:10.1071/SR04158*

Wilkinson, M.T., Richards, P.J. y Humphreys, G.S., 2009. Breaking ground: Pedological, geological, and ecological implications of soil bioturbation. *Earth-Sci. Rev. 97, 257–272. doi:10.1016/j.earscirev.2009.09.005*

THE POTENTIAL OF LUMINESCENCE TECHNIQUES IN GEOMORPHOLOGICAL PROCESSES

ROMAN-SANCHEZ, Andrea[1], LAGUNA, Ana[2], GIRALDEZ, Juan Vicente[1], REIMANN, Tony[3], PEÑA, Adolfo[4], WALLINGA, Jakob[5]and VANWALLEGHEM, Tom[6], (1)Department of Agronomy, University of Cordoba, Cordoba, Spain, (2)Applied Physic, University of Cordoba, Cordoba, Spain, (3)Netherlands Centre for Luminescence dating & Soil Geography and Landscape Group, Wageningen University, Wageningen, Netherlands, (4)Rural Engineering, Universidad de Córdoba, Cordoba, Spain, (5)Netherlands Centre for Luminescence dating (NCL), Delft University of Technology, Netherlands, (6)University of Cordoba, o92rosaa@uco.es

Soil formation includes important factors such as bioturbation and erosion-deposition. These geomorphological processes alter the soil properties and the soil production from saprolite. Both bioturbation and lateral movement are significant factors to understand the landscape evolution. In this study, we propose an analytical model for the diffusion-advection equation to quantify the bioturbation and erosion-deposition rates. The model is calibrated with age data from four soil profiles which have been obtained using Infrared Stimulated Luminescence techniques. The study area is located along a hillslope in a granite area in SE of Spain. A global sensibility analysis is applied to know the importance of the parameters in the model. An uncertainty analysis is performed to examine the better fit of the parameters in the model. The results reveal higher diffusivity constant at 20 cm in depth in the hill-base profile (47 mm^2/year) than in the hilltop profile (4.8 mm^2/year). The uncertainty in estimating the erosion and deposition rate is high. This study shows the capacity of the luminescence techniques in the geomorphological processes.
Session No. 195

T20. The Critical Zone As Heterogeneous Media: Implications for Physical, Chemical, and Biological Processes
Tuesday, 24 October 2017: 8:00 AM-12:00 PM
Room 618/619/620 (Washington State Convention Center)

Geological Society of America *Abstracts with Programs.* Vol. 49, No. 6
DOI: 10.1130/abs/2017AM-308541